11-2007

Damping and Fluidelastic Instability in Two-phase Cross-flow Heat Exchanger Tube Arrays

Joaquin Moran
Sheridan College, joaquin.moran@sheridancollege.ca

DAMPING AND FLUIDELASTIC INSTABILITY IN TWO-PHASE CROSS-FLOW HEAT EXCHANGER TUBE ARRAYS

DAMPING AND FLUIDELASTIC INSTABILITY IN TWO-PHASE CROSS-FLOW HEAT EXCHANGER TUBE ARRAYS

By

JOAQUIN E. MORAN

A Thesis
Submitted to the School of Graduate Studies
in Partial Fulfillment of the requirements
for the Degree of

Doctor of Philosophy

McMaster University

Doctor of Philosophy

McMaster University

Hamilton, Ontario

TITLE: Damping and Fluidelastic Instability in Two-Phase Cross-Flow Heat Exchanger Tube Arrays

AUTHOR: Joaquin E. Moran, M.Sc.

SUPERVISOR: Dr. David S. Weaver

NUMBER OF PAGES: 221 pages (i-xix, 1-200)

Abstract

An experimental study was conducted to investigate damping and fluidelastic instability in tube arrays subjected to two-phase cross-flow. The purpose of this research was to improve our understanding of these phenomena and how they are affected by void fraction and flow regime. The model tube bundle had 10 cantilevered tubes in a parallel-triangular configuration, with a pitch ratio of 1.49. The two-phase flow loop used in this research utilized Refrigerant 11 as the working fluid, which better models steam-water than air-water mixtures in terms of vapour-liquid mass ratio as well as permitting phase changes due to pressure fluctuations. The void fraction was measured using a gamma densitometer, introducing an improvement over the Homogeneous Equilibrium Model (HEM) in terms of void fraction, density and velocity predictions. Three different damping measurement methodologies were implemented and compared in order to obtain a more reliable damping estimate. The methods were the traditionally used half-power bandwidth, the logarithmic decrement and an exponential fitting to the tube decay response. The decay trace was obtained by "plucking" the monitored tube from outside the test section using a novel technique, in which a pair of electromagnets changed their polarity at the natural frequency of the

tube to produce resonance. The experiments showed that the half-power bandwidth produces higher damping values than the other two methods. The primary difference between the methods is caused by tube frequency shifting, triggered by fluctuations in the added mass and coupling between the tubes, which depend on void fraction and flow regime. The exponential fitting proved to be the more consistent and reliable approach to estimating damping. In order to examine the relationship between the damping ratio and mass flux, the former was plotted as a function of void fraction and pitch mass flux in an iso-contour plot. The results showed that damping is not independent of mass flux, and its dependency is a function of void fraction. A dimensional analysis was carried out to investigate the relationship between damping and two-phase flow related parameters. As a result, the inclusion of surface tension in the form of the Capillary number appears to be useful when combined with the two-phase component of the damping ratio (interfacial damping). A strong dependence of damping on flow regime was observed when plotting the interfacial damping versus the void fraction, introducing an improvement over the previous result obtained by normalizing the two-phase damping, which does not exhibit this behaviour. The interfacial velocity model was selected to represent the fluidelastic data in two-phase experiments, due to the inclusion of the tube array geometry and density ratio effects, which does not exist for the pitch velocity approach. An essential component in reliably establishing the velocity threshold for fluidelastic instability, is a measure of the energy dissipation available in the system to balance the energy input from the flow. The present analysis argues that the damping in-flow is not an appropriate measure and demonstrates that the use of quiescent fluid damping provides a better measure of the energy dissipation, which produces a much more logical trend in the stability behaviour. This value of damping, combined with the RAD density and the interfacial velocity, collapses the available data well and provides the expected trend of two-phase flow stability data over the void fraction range from liquid to gas flows. The resulting stability maps represent a significant improvement over existing

maps for predicting fluidelastic instability of tube bundles in two-phase flows. This result also tends to confirm the hypothesis that the basic mechanism of fluidelastic instability is the same for single and two-phase flows.

To God, my Family and my Country

Acknowledgements

I would like to thank the University of Zulia (Venezuela) for giving me the opportunity to come to McMaster and pursue my degree. Special mentions deserve Drs. Rafael Bravo and Jose A. Rincon. whom supported me from the beginning.

A special thanks to my Supervisor Dr. David S. Weaver, for his encouragement and assistance through the duration of my research. I could not have had a better advisor and mentor for my PhD. I would like to thank the other members of my Ph.D. committee for his valuable time and suggestions.

I would also like to express my gratitude to the administrative and technical staff of the Mechanical Engineering Department. To Betty-Ann Bedell-Ryc, Florence Rosato, Dave Schick, Ron Lodewyks and Joe Verhaeghe, thanks for your time and patience. To Dr. Paul A. Feenstra, thanks for instructing me in the meticulous art of engineering craftsmanship, and, above all, for being my friend along the way.

Thanks also to my fellow FIV group members for interesting discussions and many happy moments, particularly Bob Lumsden, Sherif Abdou, Kareem Aly, Atef Mohany and Ahmed Khalifa.

Last but not least, I would like to thank my Family in Venezuela for their continuous support. To my wife Liezka, thanks for taking care of me during all these years. This work is also a recognition to your love, patience and dedication. To All, Many Thanks.

Nomenclature

A	Upstream flow area [m^2]
Cap	Capillary number
C_i	Interfacial Coefficient
D	Tube diameter [m]
D_e	Effective tube diameter [m]
D_{ref}	Reference diameter, related to confinement [m]
D_w	Length scale of the flow [m]
f	Frequency of vibration [Hz]
f_a	Frequency of vibration in air [Hz]
f_l	Frequency of vibration in liquid [Hz]
f_R	Reduced frequency
FEI	Fluidelastic Instability
Fr	Froude number
g	Gravitational acceleration [m/s^2]
G_p	Pitch mass flux [kg/m^2s]
h	Specific enthalpy [kJ/kg]
HEM	Homogeneous Equilibrium Model
K	Fluidelastic constant in Connors equation
L	Tube length [m]
m	Lineal mass, including fluid added mass [kg/m]
m_a	Fluid added mass [kg/m]
m_h	Fluid added mass for two-phase flows [kg/m]
m_R	Hydrodynamic mass ratio
m_t	Lineal mass of the tube [kg/m]
N	Gamma count measured

q	Heat transferred to the Freon [kW]
Q	Total volumetric flow rate [L/s]
Re	Reynolds number
Ri	Richardson number
S	Slip Ratio
U_{ls}	Superficial Velocity of the liquid phase [m/s]
U_{gs}	Superficial Velocity of the gas phase [m/s]
U_l	Velocity of the liquid phase [m/s]
U_g	Velocity of the gas phase [m/s]
V	Flow velocity [m/s]
V_{eq}	Equivalent flow velocity [m/s]
V_i	Interfacial velocity [m/s]
V_p	Pitch flow velocity [m/s]
V_r	Reduced velocity
We	Weber number
x	Thermodynamic quality
α_H	Void fraction based on the HEM
δ	Logarithmic decrement of damping
γ	Confinement term
$\Phi(f_R)$	Dimensionless force spectrum
ρ	Fluid Density [kg/m^3]
ρ_g	Gas density [kg/m^3]
ρ_H	Fluid density based on the HEM [kg/m^3]
ρ_l	Liquid density [kg/m^3]
ρ_w	Density of liquid water [kg/m^3]
ρ_{tp}	Two-phase density [kg/m^3]
ρ_{RAD}	Fluid density based on the RAD void fraction [kg/m^3]

ζ_T Total damping ratio

ζ_v Viscous damping component

ζ_s Structural damping component

ζ_{tp} Two-Phase damping component

ζ_i Interfacial damping

ζ_F Fluid damping

ζ^f Fluid damping, Baj and de Langre (2003)

ζ_n^f Normalized fluid damping, Baj and de Langre (2003)

σ Surface tension [N/m]

μ_l Dynamic viscosity of the liquid phase [μ Pa s]

ν Kinematic viscosity [m^2 s]

ω_n Circular natural frequency [rad/s]

Contents

List of Tables

List of Figures

CHAPTER 1

Introduction

The interaction between fluid flow and structural dynamics is a common phenomenon both in nature and man-made devices. From the design of musical instruments to bridge decks, skyscrapers, electrical transmission lines, aircraft wings and heat exchanger tube arrays, the study of fluid-structure interaction plays an important role in a broad range of engineering applications.

When the fluid forces cause a continuous oscillation of the structure, the fluid-structure interaction is called flow-induced vibration. Typically, the effect of these vibrations degrade the performance of the system in consideration, leading to early failures that translate into additional maintenance and significant financial losses. For this reason, especially in the case of the power and process industries, understanding and consideration of flow-induced vibrations has become extremely important at the design stage (Païdoussis, 2006). In the past, most of the vibration problems were resolved by using exaggerated safety factors, which also had the collateral effect of requiring a much higher economic investment. Due to the progressive increase in

both production demand and fuel prices, increasing the efficiency of power plants has become a critical issue. The performance of plant devices now requires lighter structures and higher flow rates. For the specific case of heat exchangers, this translates into lower pressure drops and larger flow velocities, in order to achieve much higher heat transfer performance.

The use of two-phase shell-and-tube heat exchangers is a common practice in the power and process industries due to their thermal capabilities. In the nuclear industry, steam generators are particularly sensitive to flow-induced vibration problems, especially at the U-bend of the tube bundle, where cross-flow occurs. In this case, avoiding a potential failure is not only a financial concern, but also a matter of safety. In Canada, AECL (Atomic Energy of Canada Limited) developed the CANDU (Canada Deuterium-Uranium) reactor, which uses heavy water (D_2O) as the moderator (see Figure 1.1). Currently, there are more than 30 CANDU units in the world, with 18 of them located in Canada. With oil prices rising since the beginning of this decade, nuclear power is quickly recovering the attractiveness that it had in the past, with the additional advantage of not contributing to global warming. In 2004, 16 % of the electricity in the world (equivalent to 2,619 Billion kW/h) was produced by nuclear power plants. It is expected that nuclear energy sources will provide an additional 1,000 Billion kW/h by 2030 (EIA, 2007).

Figure 1.2 shows a recirculating type steam generator, used in CANDU nuclear reactors. The fluid on the tube side is heavy water that has been in contact with the radioactive source and carries its energy in the form of latent heat. On the shell side, the "light" water is evaporated as it moves from the bottom to the top of the heat exchanger, flowing in the axial direction relative to the tubes until it reaches the U-bend region of the tube bundle. Above this section, a set of centrifugal moisture separators ensure that only the vapor phase will exit the steam generator and flow through the turbine, while the liquid is recirculated. At the U-bend region of the bundle, the cross-flow configuration of the two-phase flow has the potential to produce high amplitude tube oscillations, especially at the outer tube spans where the stiffness

of the array is the lowest. If the amplitude of the vibrations becomes large enough, the tubes can be damaged by impact and fretting wear at the supports, thinning due to repeated mid-span collision or fatigue caused by high bending stresses (see Figure 1.3). Gamio and Pinto (1999) have identified tube fretting as one of the most common failure mechanisms in heat exchangers, often resulting in unplanned production interruptions. Green and Hetsroni (1995) reported that mechanical damage in the form of fretting affected more than half of the steam generators in the world during the last decade (see Table 1.1).

Since the early 60's, a lot of research has been carried out to both predict the conditions that will produce the vibrations in heat exchangers, and improve our understanding of the underlying physical mechanisms that take part in the phenomena. In single phase flows, the nature of the flow excitation mechanisms is relatively well understood (Païdoussis, 1982; Chen, 1984). The determination of the onset of fluidelastic instability, the most dangerous excitation mechanism in heat exchangers, is typically carried out by using empirical stability maps (see, for example, Weaver and Fitzpatrick (1988)). Fluidelastic instability can produce large oscillations and early failure of the tubes, and has been the main subject of attention from a research point of view. Numerous studies have investigated the effect of parameters such as tube diameter and frequency, pitch ratio of the array, mass ratio, and the physical properties of the fluids involved.

Gas-liquid flows are commonly encountered in heat exchangers such as condensers, evaporators, reboilers and steam-generators, which account for more than half of the process heat exchangers. However, the amount of research done in two-phase flow-induced vibration is small in comparison with the single-phase case. In two-phase flows, there are some additional factors to be considered, most of them related to the flow characterization. The first published data that presented a comprehensive analysis of the two-phase knowledge at the time was that of Pettigrew et al. (1989a), describing the vibration mechanisms present in two-phase cross-flow across tube arrays, and introducing some strategies aimed at predicting the fluidelastic instability.

As for the majority of the data published to date, this research was carried out using air-water mixtures due to the complexity and financial cost of steam-water experiments. The drawback of this fluid combination is that the density and viscosity ratios are very different than those in steam-water flows. In addition, the air-water mixtures does not allow for phase change or flashing, which occurs in single-component two-phase mixtures.

It has typically been assumed that in two-phase flow problems, fluidelastic instability can be predicted by using the same parameters (reduced velocity and mass-damping) as in single-phase flows. The fundamental difference is how the flow velocity, flow density, natural frequency and damping ratio are determined for two-phase flows. Two new parameters come into play: the void fraction (or fraction of the gas phase) and the flow regime (morphology of the phases). The introduction of the void fraction changes the way density, velocity and damping are defined in two-phase flows. Traditionally, the void fraction is calculated based on the Homogeneous Equilibrium Model (HEM), which assumes that there is no "slip" or relative velocity between the phases (that is, the liquid and gas phases move at the same velocity). With regard to the damping, the current practice relies on the half-power bandwidth method based on the averaged frequency spectrum of the tube, even when the flow excitation is not steady nor ergodic. This approach does not take into account that the change of added mass around the tubes may produce a continuous shifting of the natural frequency.

From the fluidelastic instability analysis point of view, the current design guidelines for two-phase flow across tube arrays suggest the use of the damping ratio measured at half the critical mass flux. The author believes that even when some estimate of damping is required for design purposes, there is no physical justification for this particular choice. At half the critical mass flux, the damping ratio is close to its maximum, leading to a non-conservative design.

The purpose of the research reported in this thesis is to develop a better understanding of damping and fluidelastic instability in heat exchanger tube arrays sub-

jected to two-phase flow. In order to improve the estimated values of reduced velocity and mass-damping parameter used in stability maps, an experimental program was undertaken, introducing a number of changes from the traditional approach in terms of measurement and data analysis. In this study, Refrigerant 11 (Freon) was used as the working fluid, allowing for a much better modelling of the real steam-water problem due to its phase change capability. In addition, the void fraction, usually based on the HEM model, was measured directly by using a gamma densitometer, eliminating the inaccuracies introduced by the no-slip assumption. A novel technique using an electromagnetic excitation device was designed and implemented to obtain more reliable damping estimates, minimizing the effect of the added mass fluctuation produced by the unsteady nature of the flow. It is hoped that a better understanding of the parameters governing fluidelastic instability in tube bundles exposed to two-phase flow will ultimately lead to improved design criteria for predicting the onset of these damaging vibrations.

1.1 Outline of the Thesis

This thesis is divided into 6 Chapters. Chapter 2 presents a review of the flow excitation mechanisms in single and two-phase cross-flows, including the measurement and analysis of the damping ratio to be used in fluidelastic analysis. A literature survey of the modelling techniques for two-phase flows across tube bundles is provided, including the important aspects of void fraction and flow regime. In Chapter 3, the experimental facility is presented and described, including the details related to the new electromagnetic excitation device for carrying out damping measurements. The preliminary testing of this tool and the post-processing methodologies for the data are also discussed. Chapter 4 presents the two-phase flow and damping results obtained in the experiments, and introduces a new approach for normalizing the damping data. The damping obtained by using the traditional half-power bandwidth method is compared to the exponential fitting to the decay trace, based on the results of the

new measurement device. The frequency shifting phenomenon is explained and verified. A clear relationship between the flow regimes observed during the experiments and the damping ratio is identified by using the new normalizing approach. Chapter 5 presents the fluidelastic instability results, and examines the effects of various parameter definitions on stability maps used for predicting this phenomenon. Recommendations are made based on parameters which provide the expected consistent transition from liquid, through two-phase, to gas flows. Chapter 6 summarizes the important novel contributions of this research and recommendations for future work.

Table 1.1. Steam-generator problems worldwide, Green and Hetsroni (1995).

Reported Problem	1977	1982	1992
Denting			
Tube support Corrosion	15	30	34
Tube-sheet corrosion	6	12	50
Tubing Corrosion			
Wastage	19	28	39
Pitting	0	3	14
ID Cracking	1	22	90
OD SCC/IGA	6	22	74
Mechanical Damage			
Fretting	9	15	117
Fatigue Cracking	3	4	10
Impingement	0	2	9
No Reported Problems	26	32	33
TOTAL UNITS	**52**	**99**	**205**

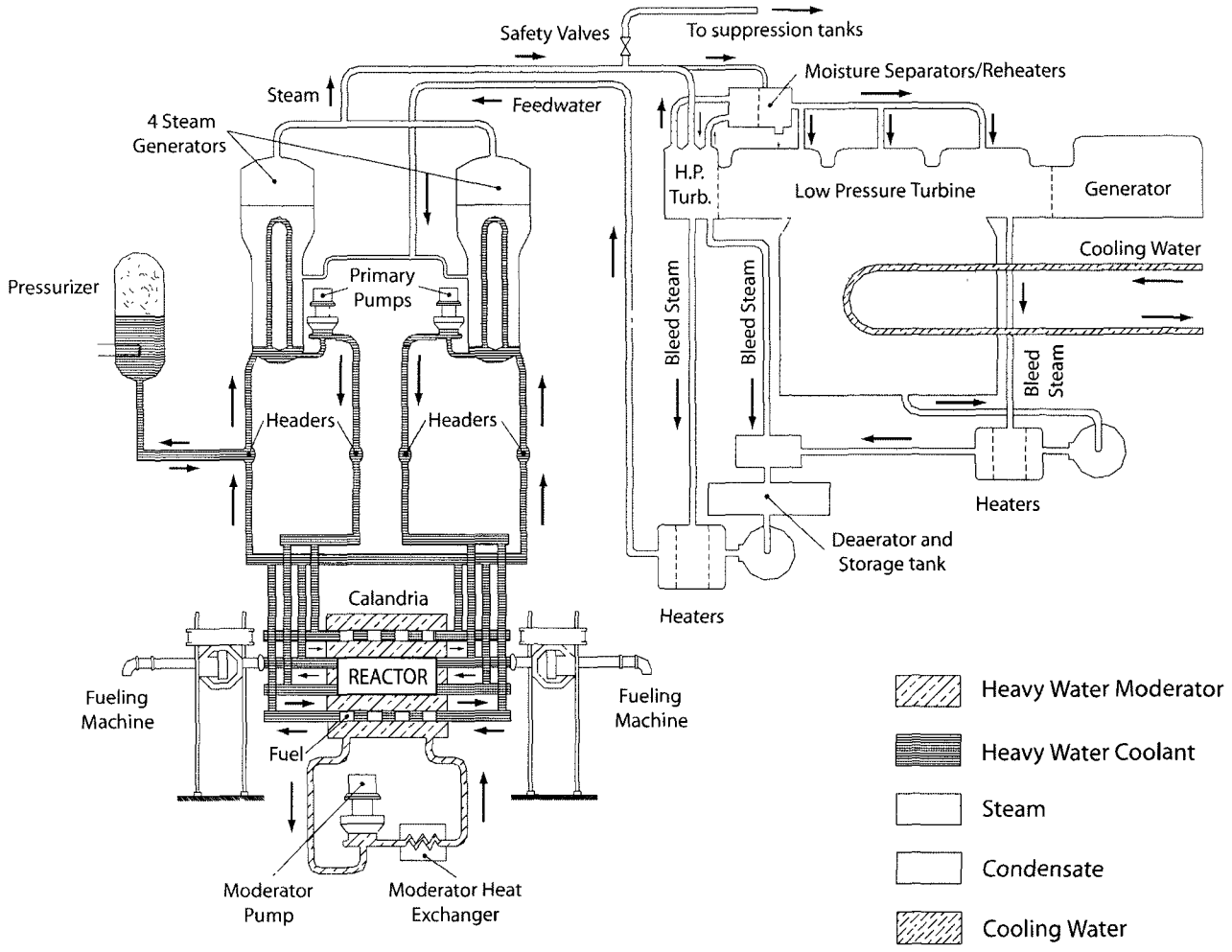

Figure 1.1. Schematic of a CANDU nuclear power system (Adapted from AECL).

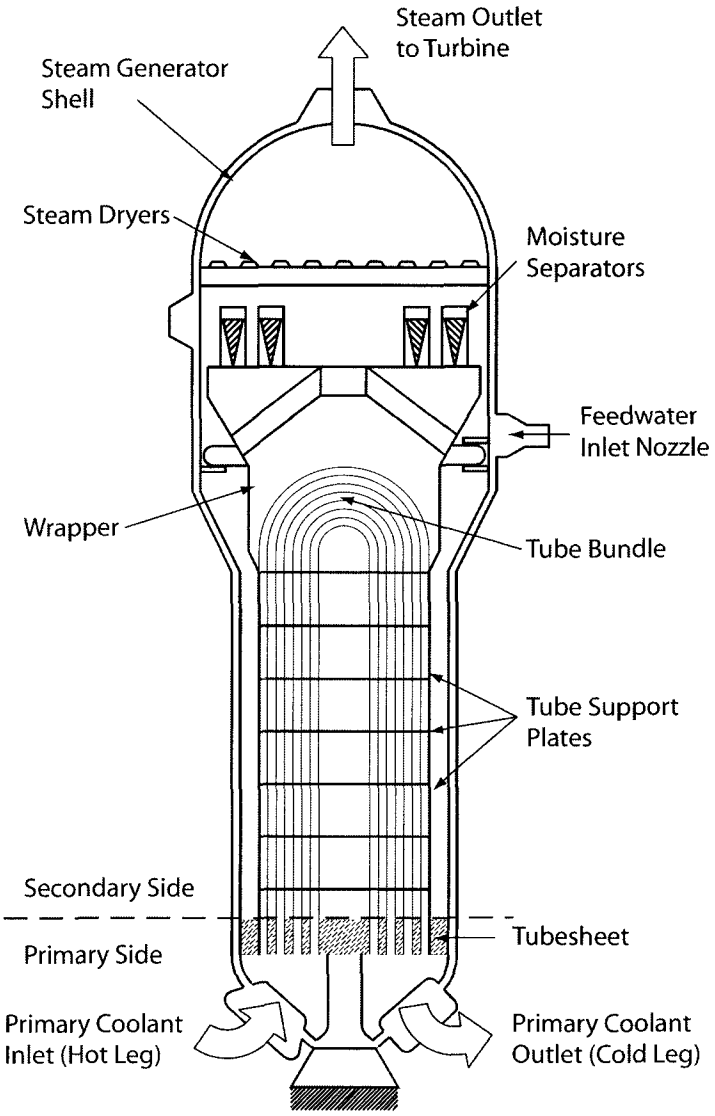

Figure 1.2. Diagram of a recirculating type CANDU steam generator (from Westinghouse).

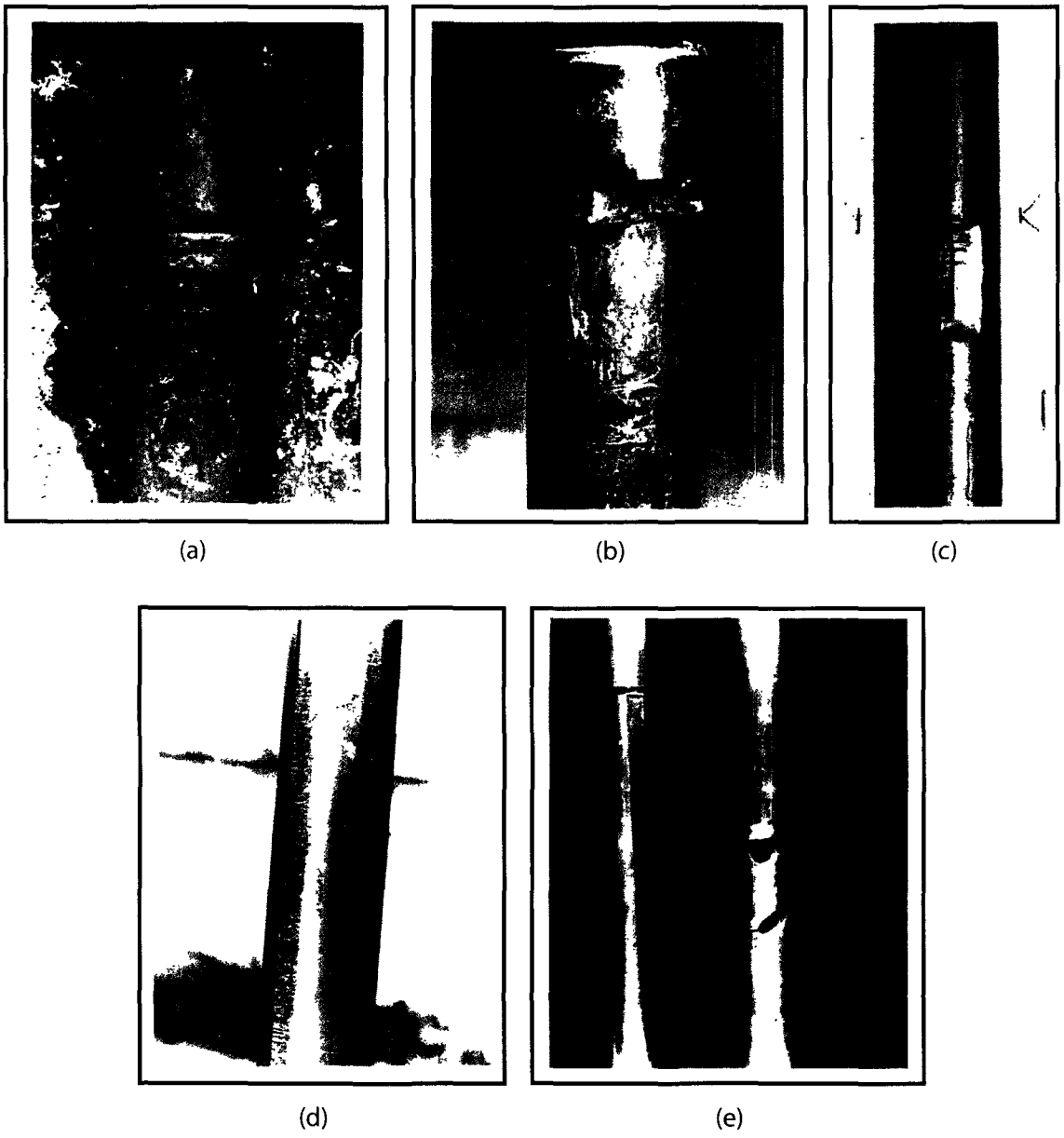

Figure 1.3. Tube damage caused by flow-induced vibration. (a), (b) and (c) show the effects of fretting wear at the supports, (d) tube-to-tube clashing at the mid-span between the supports and (e) damage caused by a broken piece of tube that hits other tubes in its path (pictures (a), (b), (c) and (d) were supplied by AECL, picture (e) by UKAEA Harwell - UK)

CHAPTER 2

Background - Review of Flow Excitation Mechanisms and Two-Phase Flow Modelling

As was discussed in the previous chapter, flow-induced vibrations in heat exchangers are an important concern due to their capability for generating tube failures in a relatively short time. As the increasing demand in the performance of heat exchangers requires lighter structures and higher flow rates, they become more prone to vibration problems, potentially leading to fretting wear at the tube supports and tube-to-tube clashing at the mid-span. Although the nature of the excitation mechanisms is relatively well understood in single-phase flows, some difficulties arise in two-phase flows, mainly related to the flow characterization. This Chapter presents a literature survey of the excitation mechanisms for single and two-phase flows across tube arrays. The existing models for analyzing fluidelastic instability and two-phase damping, as well as the current design guidelines, are introduced and discussed. The scaling parameters more commonly used in two-phase flow-induced vibration experiments are also presented. The last part of the chapter is dedicated to examining the existing models for determining the void fraction, flow regime and two-phase velocity.

2.1 Excitation Mechanisms in Single-Phase Flow

The flow-induced vibration mechanisms can be classified under three general categories: forced vibrations, self-controlled vibrations and self-excited vibrations, which correspond to steady state response, resonance and stability phenomena, respectively (Weaver, 2003). For the particular case of tube arrays, these mechanisms are commonly known as turbulence buffeting, vortex shedding (or Strouhal periodicity) and fluidelastic instability (FEI).

Figure 2.1 shows the relationship between the tube array response and the cross-flow velocity for single-phase flows. The excitation mechanisms that produce the oscillations are directly related to the flow velocity. When the flow has reached the velocity required for transition to turbulence, the random nature of the latter will produce a random dynamic pressure over the cylinder surface, inducing a random displacement. Commonly, these displacements are not large compared to the cylinder diameter. This forced excitation is known as "turbulence buffeting", and cannot be eliminated. However, turbulence is beneficial in heat exchangers, since it promotes mixing and maximizes the heat transfer coefficient. The effects of the small displacements produced by the turbulent buffeting must be estimated to determine the effective service life of the tube bundle.

Flow across the tubes also causes alternate vortex shedding, producing harmonic fluctuations of surface pressure. The "vortex shedding" or "Strouhal periodicity" is initially considered a forced vibration, because the fluid forces are independent of the structural displacement as long as the latter are small. If the displacements become sufficiently large, the vortex shedding process becomes locked onto the structural frequency and the phenomenon becomes "self-controlled". The resultant peak in amplitude is located in the vicinity of the structural natural frequency. In gas flows, when the vortex shedding frequency coincides with the natural frequency of the duct or container, acoustic resonance may be generated, producing intense noise and vibration. Excellent reviews of the vortex shedding mechanism and its effects on tube arrays can be found in Ziada et al. (989a), Ziada et al. (989b),Weaver (1993)

and Oengören and Ziada (1998).

At higher flow velocities there is an interaction between the flow field and the vibration response of the tube array. This produces an unstable condition known as fluidelastic instability, characterized by large amplitude oscillations which are extremely dangerous for any kind of device. In Figure 2.1, it is clear that at the fluidelastic instability threshold, a small increase in flow velocity produces a large increase in the tube response. When a cylinder in an array changes its position, the flow field around it also changes, affecting the fluid forces exerted on the cylinder and its neighbours. These fluid forces can induce instability if the energy input by the fluid exceeds the energy dissipated by damping. Due to the potential damage to the tube bundle caused by these large-amplitude oscillations, predicting the fluidelastic instability threshold has been the primary subject of attention during the last four decades from a research point of view.

2.1.1 Fluidelastic Instability in Single-Phase Flows

Fluidelastic instability is a self-excited vibration mechanism, i.e., the forces on the tube are path-dependent and hence non-conservative. In general, instability can be classified as being static or dynamic. Static instability occurs when the forces induced by the flow are in phase with the displacement of the structure, overcoming the structural stiffness and producing a static deflection (also known as divergence). However, if there is a phase difference between the tube motion and the induced fluid forces, the result is a dynamic instability. The tube will oscillate at or near its natural frequency according to the component of the fluid force in phase with the velocity (fluid-damping force). The amplitude of oscillation produced by the dynamic instability will increase until the overall damping of the system is capable of dissipating this energy, or until the motion is limited by some external constraint (i.e. spacing the between tubes). The fluidelastic instability that occurs in tube arrays is a dynamic instability.

The first studies carried out in order to better understand fluidelastic instability

and establish how to determine the fluidelastic instability threshold (or critical velocity of the flow), were those of Roberts (1966) and Connors (1970). Roberts (1966) performed experiments in single and double rows of tubes, and attributed the instability to a time lag between the tube displacement and the switching of jet-pairs issuing between the tubes. Connors (1970) carried out experiments in a single row of cylinders, subjecting the array to an air flow. He considered that the instability was the result of the interaction of the neighboring tubes as they vibrate in oval trajectories with specific phase relationships. As a result, he proposed a quasi-static semi-empirical model which yielded a stability prediction known as Connors equation, which was refined later by Blevins (1974). The equation expresses the relationship between two non-dimensional variables, known as the reduced velocity and the mass-damping parameter, and takes the general form:

$$\frac{V}{fD} = K\left(\frac{m\delta}{\rho D^2}\right)^n. \tag{2.1}$$

In equation 2.1, V is the pitch velocity, or average flow velocity in the gap between the tubes, D is the tube diameter, ρ is the fluid density, f is the tube natural frequency, m is the tube mass per unit length (including the fluid added mass) and δ is the logarithmic decrement of damping, which represents the energy dissipation in the system. The added mass (or hydrodynamic mass) is the mass of the surrounding fluid that has an inertial effect on the tube dynamics. Blevins (1974) also derived an equation similar to 2.1 for a single tube row, assuming that the fluidelastic instability forces were due to relative displacement between the tube and its neighbours. The constants K and n, initially equal to 9.9 and 0.5 respectively according to Connors, have been a topic of discussion during almost four decades. Although Connors' experiments were carried out for a single row of tubes, equation 2.1 is currently used for the design of heat exchanger tube bundles, which have multiple tube rows and different geometric configurations or array patterns (see Figure 2.2).

One of the consequences of Connors' theory is that the displacement of the neigh-

boring tubes is required for the instability to take place. However, it has been found that a single cylinder can become unstable even when surrounded by a rigid array (Weaver and Lever, 1977). This indicates that neither Roberts nor Connors theories explain completely the cause of instability. Blevins (1990) presented a more exhaustive dimensional analysis of the problem, showing that the onset of stability depends on the following dimensionless groups:

- Reduced velocity (V/fD)
- Reynolds number (VD/ν)
- Mass ratio ($m/\rho D^2$)
- Damping ratio (ζ)
- Array geometric configuration
- Tube spacing (Pitch over diameter ratio, P/D)
- Upstream turbulence

The pitch to diameter ratio is a very common parameter used to characterize tube arrays. The pitch P is defined as the distance center-to-center of the tubes. When large amounts of data were taken into account, the equation proposed by Blevins (1990) for the onset of fluidelastic instability took the same form as Connors equation, with the coefficients K and n depending on the tube array (geometric configuration, tube spacing) and fluid characteristics (liquid or gas). However, the physical nature of the instability is still hidden within those experimental factors. Weaver and El-Kashlan (1981a) showed that mass ratio and damping are not linearly dependent parameters, as is assumed by Connors. Weaver and Yeung (1984b) observed that the critical velocity was independent of the mass-damping for a parallel triangular array subjected to water flow. Price (2001) discussed the suitability of Connors equation for determining the occurrence of fluidelastic instability. Based on both theoretical models and experimental data. he concluded that "there are many deficiencies associated

with Connors equation", and therefore, its use was not justified. The combination of mass ratio and damping together as one non-dimensional parameter, the influence of damping on the critical velocity and an excessive conservatism are mentioned among other reasons for this conclusion.

Several approaches of the theoretical modelling of fluidelastic instability have been carried out to date. There are quasi-static models (Connors, 1970; Blevins, 1974), semi-analytical models (Lever and Weaver, 1982, 1986a; Yetisir and Weaver, 1993b), quasi-steady models (Blevins, 1979; Price and Païdoussis, 1986; Price, 1995), unsteady models (Chen, 983a) and even numerical models (Eisinger et al., 1995; Longatte et al., 2003). However, Connors equation is still widely used because of its simplicity and ease of application. For design purposes, the stability maps (see Figure 2.3) are another commonly used tool. They show graphically the relationship between the reduced velocity and the mass-damping parameter for each array geometry, allowing the designer to estimate if the bundle will be unstable for a given set of operating conditions. Excellent reviews on the subject have been presented by Païdoussis (1982), Chen (1984), Weaver and Fitzpatrick (1988), Price (1995) and Schröder and Gelbe (1999).

2.1.2 Models for Fluidelastic Instability

There is no consensus about a universal theory capable of predicting fluidelastic instability for all fluids and array geometries found in practical applications. However, most researchers agree on the existence of two main mechanisms: a displacement mechanism and a velocity mechanism.

The displacement (or stiffness-controlled) mechanism assumes that the fluid forces are linear, and that the flow reacts instantaneously as the tube moves (Blevins, 1990). The position of the tube and its neighbours affects the flow distribution within the array, changing the fluid forces on the tubes. It also assumes that the cylinders in adjacent rows vibrate out of phase, damping is the same in the transverse and streamwise directions, the fluid forces produced by the tube velocity are negligible, and the

vibration amplitude is an exponential function of time. For the particular case where all the cylinders have the same natural frequency, the displacement mechanism can be reduced to equation 2.1, introduced by Connors (1970). As mentioned above, one of the most important physical consequences of this mechanism is that a flexible tube surrounded by a rigid array will not become unstable. Weaver and Lever (1977) and Weaver and Yeung (1984a) observed the instability in the aforementioned configuration, suggesting that other mechanisms must be operating at the same time.

In reality, the fluid surrounding the tubes does not "feel" instantaneously the change in tube position. Instead, a finite time is required for the flow to react to the tube displacements, as was previously pointed out by Roberts (1966). The velocity (or negative-damping) mechanism establishes that the instability occurs when a time-lag exists between the cylinder displacement and the fluid forces. It also takes into consideration the damping provided by the fluid surrounding the tubes.

The existence of both the damping and stiffness controlled mechanisms was discussed by Chen (1983a), and taken into consideration in his unsteady model for determining the instability of tube arrays based on a previously developed theory (Chen, 1978). This mathematical model required the knowledge of unsteady fluid force coefficients, which were first measured by Tanaka and Takahara (1980) by using a single row of tubes and an in-line tube bundle with a single flexible tube. Their results showed that both the damping and stiffness force coefficients were dependent on the reduced velocity. Chen (1983b) used the coefficients presented by Tanaka and Takahara (1980) to predict the onset of fluidelastic instability and compared those results against previously published research. They found that different stability criteria had to be used depending on the values of the parameters considered (i.e. reduced velocity, damping) and proposed an expression equivalent to Connors' equation with k and n depending on cylinder arrangement, mass ratio, mass-damping parameter and turbulence characteristics. Price and Païdoussis (1982, 1983, 1986) introduced a linearized quasi-steady model based on two rows of cylinders, providing some insights into the physical mechanisms of fluidelastic instability. They concluded that the fluid

force coefficients based on measurements from two rows of cylinders were only applicable to tube arrays if the rows were surrounded by fixed tubes. They also attributed the instability to a phase-lag between the cylinder motion and the resulting fluid force. The stiffness-controlled mechanism was predominantly observed at high values of the mass-damping parameter (mainly due to the relative tube motion) while the instability was attributed to the damping-controlled mechanism for low mass-damping parameter values. Price (1995) pointed out that one of the disadvantages of this analysis was the amount of experimental input required.

Lever and Weaver (1982, 1986a,b) used the negative-damping approach in their semi-analytical model. They proposed an analytical formulation based on first principles, which required some empirical input to determine the flow resistance coefficient through the array and the positions of flow reattachment and separation from the tubes. The stability analysis was performed by considering a unit-cell within the array (see Figure 2.4a) and defining its boundaries based on the location of the cylinder, its neighbours, and the wake region behind the cylinder. The flow was assumed to be one-dimensional and inviscid. Using unsteady momentum and continuity equations, the unbalanced force on the cylinder was calculated by integrating the pressure profile over the tube surface where the flow was attached. A phase lag in the fluid force was introduced to take into account the inertial effects of the flow, and a resistance term was added to include the frictional losses. The predicted stability regions showed multiple bands for low values of the mass-damping parameter when plotted on a stability map, as shown in Figure 2.4b. According to Price (1995), the results of this model agreed very well with the predictions of Chen (983a) and Price and Païdoussis (1986).

Yetisir and Weaver (1993b,a) modified the model of Lever and Weaver to include the effects of multiple flexible cylinders. Li (1997) extended the work of Yetisir and Weaver to multi-span tube arrays, taking into account partial admission effects and using a linear disturbance decay function to obtain an explicit stability equation. This approach greatly improved the agreement of Yetisir and Weaver (1993b) model

with experimental results and minimized the multiple-stability-region phenomenon, caused in part by unrealistically large phase angles (see Figure 2.5).

The preceding review demonstrates that several theories and models have been developed for the prediction of fluidelastic instability. While none of them produces satisfactory results in every case, they have shed some light into the physics of the mechanisms involved and the parameters to be taken into consideration. For single-phase flows, the current design guidelines are based on abundant experimental data, and therefore can be considered as adequate as long as empirical data exists for the particular array geometry of interest.

2.2 Excitation Mechanisms in Two-Phase Flows

In two-phase flows, the excitation mechanisms are primarily turbulence buffeting and fluidelastic instability, as shown in Figure 2.6. The vortex shedding is unlikely to occur in gas-liquid two-phase flows, because the presence of bubbles apparently prevents this mechanism from appearing (Taylor et al., 1989; Pettigrew and Taylor, 1994; Feenstra, 2000). Due to the different nature of two-phase flows, the excitation mechanisms are present under different circumstances than in single phase flows.

2.2.1 Turbulence Buffeting

Wear due to buffeting in two-phase flows is especially important if the tubes are to be in service for long periods of time. Axisa et al. (1990) investigated turbulent buffeting in both single and two-phase flows. A theoretical framework was developed relating the amplitude of vibration and the dimensionless force spectrum of the flow, according to certain scaling parameters (see Appendix A). They proposed an upper bound of the force spectrum to be used for design purposes in single-phase flows. However, the scaling parameters chosen could not collapse the two-phase data available. Taylor et al. (1989) measured the fluctuating forces caused by water and air-water flows. They found that the buffeting forces were much higher in two-phase flows than

in the single-phase case. The expression used for calculating the dimensionless force spectrum in single-phase flows is:

$$\Phi(f_R) = \frac{\phi(f)}{\left(\frac{1}{2}\rho_w V_p^2 D\right)^2}\frac{V_p}{D}, \tag{2.2}$$

where $\phi(f)$ is the dimensional force spectrum, ρ_w is the density of liquid water and V_p is the pitch velocity. Equation 2.2 cannot be used in two-phase flow because the force spectrum is a function of void fraction. Taylor et al. (1996) developed a method for reducing two-phase data that is based on more physically sound scaling parameters. The bubble diameter was used as the length scale, while the flow regime was taken into account to define the force scale. More recently, de Langre and Villard (1998) presented a database of turbulence buffeting experimental data from direct and indirect force measurements, obtained from different researchers. Different tube array configurations and two-phase fluid combinations were considered (air-water, steam-water, refrigerants). They found that gravity forces were important in order to determine the appropriate dimensionless spectra, and other factors as surface tension, viscosity and dynamic pressure were not very significant. As a consequence, a good collapse was achieved for two-phase buffeting data, allowing for a better estimation of vibration amplitudes and therefore, a more accurate prediction of fretting wear rates in heat exchanger tubes. Figure 2.7 shows the relationship between the non-dimensional reference spectrum (N.R.E.S) and the reduced frequency (f_R). The reduced frequency is determined as

$$f_R = \frac{f D_w}{V_p}, \tag{2.3}$$

where D_w is a length scale of the flow based on the tube diameter and void fraction, the latter being calculated using the Homogeneous Equilibrium Model. The upper bound of N.R.E.S. proposed by de Langre and Villard (1998) allows estimation of the amplitude of vibration by using the random vibration theory (Appendix A). This

method of data reduction has been successfully implemented and used for comparison purposes by other researchers (Feenstra, 2000). Other important contributions have been presented by Pettigrew and Gorman (1978), Pettigrew and Taylor (1993) and Nakamura et al. (1995). Mureithi et al. (2002) found that the unsteady fluid forces induced on the tubes were not only a function of the reduced velocity, but of the void fraction, flow regime and other parameters. In addition, they observed that two-phase damping has a much more important role in turbulence buffeting than its single phase counterpart.

2.2.2 Fluidelastic Instability

During the last two decades, research devoted to two-phase flow induced-vibrations has increased, mainly driven by the nuclear industry. This is primarily due to the susceptibility of the U-bend region in nuclear steam generators to vibration, caused by the cross-flow of the steam-water mixture over the long-span and low-stiffness tubes. The phenomenon is very complex, and it depends on many different factors which are nonexistent in the single-phase flow situation. From a practical point of view, it has been postulated that the occurrence of fluidelastic instability can be predicted using the two non-dimensional parameters used for single-phase flows: the reduced velocity and the mass-damping parameter. However, in two-phase flows, additional parameters as void fraction, liquid-to-gas density ratio, surface tension and flow regime must be considered. Figure 2.8 shows a stability map where two-phase data has been plotted, based on the same analysis used in single-phase flows. The data points seem to follow neither the general trend observed in Figure 2.3 nor the predictions of the Connors equation. This behaviour suggests that more research is required to deal with the unique difficulties of scaling parameters and data analysis in two-phase flows.

One of the first attempts to study the fluidelastic instability in tube arrays subjected to two-phase flow was that of Heilker and Vincent (1981). They compared the two-phase response of a tube bundle subjected to an air-water flow, to that of the

single-phase case. Although they described the amplitude response in terms of a fluid pressure, they found that the incident flow direction was very important in terms of the instability threshold.

Axisa et al. (1985) presented results for fluidelastic instability in parallel triangular, normal triangular, normal square and rotated square arrays (P/D = 1.44), using air-water and steam-water mixtures. They found that using air-water data was reasonable to simulate steam-water mixtures in terms of fluidelastic instability predictions. Nakamura et al. (1986) also reported data for both air-water and steam-water flows. Pettigrew et al. (1989a,b) and Taylor et al. (1989) presented a series of three papers concerning two-phase turbulence buffeting, fluidelastic instability, hydrodynamic mass and damping. The four standard tube array configurations were investigated using cantilevered tubes: parallel triangular, normal triangular, normal square and rotated square arrays, with pitch over diameter ratios of 1.32 and 1.47. They found that the fluidelastic instability behaviour is different for continuous flow regimes than for intermittent flow regimes. Interestingly, they commented that the fluidelastic instability threshold does not appear to be greatly affected by changing the fluids. Also, a relationship between damping and void fraction was presented, showing a maximum damping ratio for void fractions from 40 to 80%. According to their research, the damping of the system is strongly influenced by the two-phase fluid used, and the air-water combination tended to provide larger damping than the steam-water experiments. This is primarily due to the differences in density ratio between the liquid and gas phases for different fluids. Pettigrew and Taylor (1994) presented a review paper discussing turbulence buffeting and fluidelastic instability in two-phase flows. Both the axial-flow and cross-flow configurations were considered, and design guidelines were proposed for hydrodynamic mass and damping.

The experiments of Pettigrew et al. (1989b) and Pettigrew and Taylor (1994) were carried out using air-water mixtures, with void fractions ranging from 5 to 99%. These values are based on the Homogeneous Equilibrium Model (HEM) in order to compute the "average" velocity and density of the mixture and allow for comparison

using stability maps. The HEM is a model for determining the void fraction of the two-phase flow that assumes no "slip" between the gas and the liquid, that is, both phases are moving at the same velocity. This assumption may be suitable for uniform flows, were the bubbles are small and evenly distributed. However, the use of the HEM for intermittent flows is not valid, since the distribution of void is not uniform and because of the "slip" or relative velocity between the phases.

Feenstra (1993) and Feenstra et al. (1995) presented one of the first experiments using a single component two-phase mixture of refrigerant 11. The fluidelastic instability threshold values obtained were less conservative than for previous experiments with air-water and, by using a gamma densitometer, it was shown that the real void fraction was considerably lower than the values predicted by the HEM.

Pettigrew et al. (1995) reported experiments using R-22. They found that the damping ratio is highly dependant on void fraction, with a maximum around 60-65%. They also reported that for voids of 65% and larger (based on HEM) the onset of instability decreases, that is, the larger the void fraction, the more prone is the array to becoming unstable. A direct explanation for this phenomenon was not provided and it was attributed to flow regime effects. It was also pointed out that the critical velocities for fully-flexible bundles are lower than for a single-flexible tube in a rigid array.

Feenstra (2000) carried out a series of experiments Refrigerant 11 as the working fluid, but in this case, a new void fraction model was implemented to account for the slip between the phases. Also, an alternate definition of two-phase velocity was presented (equivalent velocity), which accounted for the kinetic energy of each phase. He found that the fluidelastic instability threshold was slightly lower than for air-water mixtures. Comparing data from different researchers using his void fraction model, he found that the critical reduced velocity decreases with increasing mass damping parameter for an increasing void, as seen in Figure 2.8, suggesting that the reduced velocity and the mass damping parameter may be insufficient to describe two-phase flow-induced vibration for intermittent regimes. A study of the dependence of the

critical velocity on the flow regimes was also recommended.

Nakamura et al. (2002), presented a series of papers regarding unsteady forces, damping and fluidelastic instability in two-phase flow using steam-steam water cross-flow in an in-line array. It was found that the fluidelastic instability threshold was almost constant for void fractions from 70 to 96%, because of the invariance of the flow regime. However, it is also pointed out that even though the fluidelastic instability can be predicted with reasonable accuracy for homogeneous flows, a new approach is needed for non-homogeneous flows.

Weaver and Feenstra (2002) and Feenstra et al. (2003) investigated the onset for fluidelastic instability of a parallel triangular and a normal square array subjected to two-phase R-11 cross-flow. The parallel triangular configuration is particularly important because it is more susceptible to becoming unstable than the other array patterns for the same P/D ratio. For these studies, an "interfacial" velocity correlation, introduced by Nakamura et al. (2000), was used to compared the fluidelastic data from several researchers. There is a remarkable collapse in the data "in terms of the reduced velocity" (see Figure 2.9), and seems to be in agreement with the Connors theory for $K = 3.0$. However, the flow regime does not affect this collapse. It is important to remark that the maximum void fraction reached in these experiments was close to 65% (measured with a gamma densitometer) due to the rig limitations. Since the experiments carried out by Pettigrew have overestimated the void fraction because of the use of the HEM, there is scarce data available concerning the fluidelastic instability caused by high void fraction two-phase flows (>70%).

In recent reviews of flow-induced vibration mechanisms in two-phase flows across tube bundles (Goyder, 2002; Pettigrew et al., 2002; Pettigrew and Taylor, 2003a,b; Khushnood et al., 2004; Pettigrew and Taylor, 2004) the authors have stressed the need for more research regarding the physical mechanisms that play a role in two-phase flows, especially flow regime effects, void fraction distribution, damping and surface tension.

2.3 Overview of Damping

Damping is a key parameter in the analysis of flow-induced structural vibrations, because it is a measure of the ability of the system to absorb energy from the flow. The onset of fluidelastic instability will occur when the positive feedback between the fluid forces and the motion of the structure overcomes the capacity of the system to dissipate energy.

In tube arrays, more than one form of damping is acting as the tubes are surrounded by moving fluid and in contact with anti-vibration supports. According to Pettigrew et al. (1989a), the most important contributions to the total damping are

- Internal or material (structural) damping
- Viscous damping, between the fluid and the tube
- Flow-dependant damping, due to the flow velocity
- Squeeze-film damping, between the tube and the supports
- Damping due to friction or impacting at the tube supports

This particular research was focused on the first three categories. Additional information regarding the interaction between the tubes and supports can be found, for example, in Hassan et al. (2002, 2005). The relative importance of the friction and impacting between the tube and the supports depends on the media surrounding the tubes. If the bundle is exposed to an air flow, the viscous and flow-dependent contributions will be small compared to the dissipation caused by the tube-support interaction. If the flow is liquid, then the importance of the latter is reduced. In any case, this thesis will focus on the relationship between the flow and the tubes, represented by the first three components mentioned above.

Weaver and El-Kashlan (1981a) studied the effect of damping and added mass on the stability of a parallel triangular tube array. The bundle had a P/D ratio of 1.375, and was subjected to air flow. Damping was measured by plucking the tubes

and recording the decay response. Figure 2.10 shows the aerodynamic component of damping in the transverse direction as a function of pitch velocity. The aerodynamic component is equivalent to the sum of the viscous and flow-dependent components discussed above, and was obtained by subtracting the structural damping from the total measured damping. For flow velocities lower than 2 m/s (40 to 50 % of the critical velocity) damping seems to increase linearly. This agrees with the theoretical model introduced by Blevins (1979). After the fluidelastic forces become significant, damping reduces progressively, reaching zero at the critical velocity. The maximum damping seems to occur at about half the critical velocity.

The effect of increasing the damping ratio for the same array can be seen in Figure 2.11. Weaver and El-Kashlan (1981a) found that increasing the damping decreased the turbulence response, increased the instability threshold, and slightly reduced the slope of the post-stability region of the curve. They also pointed out that the critical velocity was substantially less dependent on damping or mass ratio than indicated in Connors equation. Therefore, the traditional form of the stability equation was inadequate as a general model of fluidelastic instability.

The variation of the different damping components is shown schematically in Figure 2.12. The structural damping is independent of flow velocity, and is the only mechanism of energy dissipation that still exists at the onset of stability. At zero flow velocity, the total damping is equal to the structural component plus the viscous damping. The viscous and velocity-dependant components increase linearly with flow velocity. This effect is eventually overcome by the fluidelastic damping (Price, 1995), which increases (negatively) as the critical velocity is approached. When fluidelastic instability occurs, the fluidelastic damping has overcome the positive components of damping and the net damping of the system is zero.

2.3.1 Hydrodynamic Mass

The hydrodynamic mass is defined as the mass of fluid which has the equivalent inertial effect as the fluid surrounding an accelerating body. If the hydrodynamic or

fluid added mass is defined as m_a, then the total effective mass of a vibrating body of mass m is

$$m + m_a \tag{2.4}$$

If the natural frequency of a body in a vacuum is known, f_a, and its natural frequency in the fluid is f, then the fluid added mass can be computed as

$$m_a = m\left[\left(\frac{f}{f_a}\right)^2 - 1\right]. \tag{2.5}$$

For two phase flows, Pettigrew et al. (1989a) has proposed the relation

$$m_h = \left(\frac{\rho_{tp}\pi D^2}{4}\right)\left[\frac{(D_e/D)^2+1}{(D_e/D)^2-1}\right], \tag{2.6}$$

where ρ_{tp} is the two-phase density, D_e is an equivalent diameter dependent on the flow confinement and D is the tube diameter. Pettigrew and Taylor (1994) reported that this approach was in reasonable agreement with the experimental results for void fractions below 80% based in the Homogeneous Equilibrium Model. They also attributed the discrepancies above 80% to flow regime effects, and stated that if the flow regime remained "continuous" for these void values, the model would be also suitable.

Carlucci and Brown (1983) and Pettigrew et al. (1989a) have plotted the hydrodynamic mass as a function of void fraction for air-water two-phase flows. The former authors performed experiments using a single cylinder subjected to two-phase flow, while Pettigrew et al. (1989a) studied cross-flow in tube arrays. Figures 2.13 and 2.14 show the relationship between the hydrodynamic mass ratio (m_R) and the void fraction based on the HEM. The quantity m_R is equal to the ratio of the actual added mass to the added mass of a tube surrounded by liquid. The continuous line represents the theoretical hydrodynamic mass ratio, which is the lineal mass of fluid displaced by the tube and corrected for confinement of the nearest tubes. It is defined

as:

$$m_{R,theor.} = \frac{[(D_e/D)^2 + 1]}{[(D_e/D)^2 - 1]} \left(\frac{\pi \rho D^2}{4} \right), \tag{2.7}$$

In both Figures, it is clear that the hydrodynamic mass ratio varies according to the void fraction. Figure 2.15 shows results by Feenstra (2000) obtained with Refrigerant 11. The HEM overestimates the void fraction, causing the data to shift to the right side of the figure. The RAD void fraction shows the different change rate in added mass as the void fraction increases. In one-component mixtures, the phase-change or "flashing" creates a vapour film around the tubes and tends to keep the hydrodynamic mass ratio constant above a certain void fraction. This effect cannot be reproduced when two-component mixtures (as air-water) are used to simulate steam-water two-phase flows. In addition, in two-phase flow problems the unsteadiness of the flow will contribute to changing the amount of liquid and gas that is in contact with the tube at a given time. The frequency of the tube will then fluctuate around a mean value, which is determined through an averaging process during a certain period of time. For lower void fractions. where the hydrodynamic mass ratio is strongly dependent on void fraction, the shifting is much more pronounced.

2.3.2 Damping in Two-Phase Flows

The first studies of two-phase flow damping were those of Carlucci (1980) and Carlucci and Brown (1983). Experimenting with vertical air-water flows passing a single cylinder, they found that the damping in two-phase flow was considerably higher than for single phase flows (either in liquid or gas). They also established a relationship between damping and void fraction. In order to take into account the additional damping in two-phase flows, they proposed an expression for the total damping ratio of the form

$$\zeta_T = \zeta_s + \zeta_v + \zeta_f + \zeta_{tp}, \tag{2.8}$$

where ζ_T represents the total damping ratio, ζ_s is the structural damping of the system, ζ_v is the viscous component due to the presence of the fluid, ζ_f corresponds

to the flow velocity dependant term and ζ_{tp} is the two-phase contribution. Figure 2.16 shows the variation of the fluid damping components with void fraction. It can be seen that the two-phase component of the total damping ratio is much larger than the other two, and much more dependant on void fraction. Pettigrew et al. (1989a) and Pettigrew and Taylor (1994) have used Carlucci's approach to analyze the behaviour of damping of tube bundles in two-phase flows. However, they considered that the flow-dependant term could be part of the two-phase damping. Consequently, equation 2.8 was rewritten as

$$\zeta_T = \zeta_s + \zeta_v + \zeta_{tp}, \tag{2.9}$$

The structural damping is commonly measured in air, and the viscous damping is determined using an expression proposed by Rogers et al. (1984) for single-phase flows

$$\zeta_v = \frac{\pi}{\sqrt{8}} \left(\frac{\rho D^2}{m} \right) \left(\frac{2\nu}{\pi f D^2} \right)^{0.5} \left\{ \frac{[1 + (D/D_e)^3]}{[1 - (D/D_e)^2]^2} \right\}. \tag{2.10}$$

In equation 2.10, ρ represents the fluid density, D is the tube diameter. m is the mass per unit length (including the fluid added mass), ν is the kinematic viscosity, f is the tube frequency and the bracketed term on the right side represents a confinement function. The two-phase component is calculated by subtracting the sum of ζ_s and ζ_v from the total damping ratio ζ_T, which is measured using the half-power bandwidth method based on the averaged frequency response of the tube. Even when equation 2.10 was originally formulated to estimate the "added damping" provided by a single-phase stagnant fluid, Pettigrew et al. (1989a) assumed that an analogous expression could be used in two-phase flow problems. They replaced the density and viscosity by two-phase quantities, with the density defined according to the HEM and the equivalent two-phase viscosity proposed by McAdams (Pettigrew et al., 1989a).

In order to compare damping data from different two-phase studies, Pettigrew et al. (1989a) and Pettigrew and Taylor (1994) proposed an expression to normalize damping. The objective was to develop design guidelines from experimental results obtained using different fluids and tube array configurations. The normalization was

applied only to the two-phase component of the total damping ratio.

$$(\zeta_{tp})_D = \zeta_{tp}\left(\frac{m}{\rho_l D^2}\right)\left\{\frac{[1-(D/D_e)^2]^2}{[1+(D/D_e)^3]}\right\}, \tag{2.11}$$

where $(\zeta_{tp})_D$ is the normalized two-phase damping and ρ_l is the density of the liquid phase. In equation 2.11, two terms are used for the normalization: the first is the mass ratio (based on the density on the liquid), which accounts for the added mass effects; the second, based on the tube diameter, represents the contribution of tube confinement. More recently, in an attempt to find a relationship between damping and other flow-related parameters, Pettigrew and Knowles (1997) reported results for a single cylinder subjected to two-phase axial flow. They concluded that the effect of surface tension on two-phase damping was strong, and tried to include it into the normalized form of the two-phase damping. However, the relationship between damping and surface tension was complex, and different for each flow regime. No relationship was found which generally accounted for the effects of surface tension.

Concerning the relationship between damping and void fraction, Hara (1987) established that the maximum damping ratio corresponded to a certain void fraction interval (30 to 60 % for his experiments). Axisa et al. (1988) presented experiments using steam-water mixtures. They found that damping is indeed related to void fraction, and that the values obtained for steam-water were considerably lower than those for air-water mixtures, at least for void fractions over 80% (based on the Homogeneous Equilibrium Model). This is an indicator of the significant differences which may be found between experiments carried out with air-water and those using one-component mixtures.

Nakamura et al. (2002) carried out experiments in in-line arrays to measure two-phase damping and added mass in two-phase flows. They used steam-water mixtures at high pressure (up to 5.8 MPa), and implemented an electromagnetic device to excite a metal block mounted on the tube support wires. They found that the damping ratio changes depending on the location of the tube within the array, and the inclination of

the bundle respect to the direction of the flow is also a factor to be considered. They also found that damping was larger in the lift direction than in the drag direction. In order to analyze and compare their results, they used the two-phase damping formulation proposed by Axisa et al. (1988).

In a recent paper, Anscutter et al. (2006) presented some results of two-phase internal flow in pipes, concerning the relationship between interfacial surface area, flow regimes and two-phase damping. They simulated bubbly flow using glass spheres suspended in water, and also performed experiments in air-alcohol and air-water mixtures. A simplified model was used to compute the interfacial area in slug flows, although the range of void fractions explored was up to 35%. They found that two-phase damping is strongly related to interfacial surface area, both in bubbly and slug/churn flows. They also observed that the maximum damping ratio occurred before the transition from bubbly to intermittent flow. While this study was for internal flow in pipes, it provides some potentially very useful insights into the physics of two-phase damping. Since interfacial area will be influenced by surface tension and bubble rise, slip and viscosity may be related to two-phase damping.

Due to the need for guidelines to be used in heat exchanger design, some quantitative expressions have been proposed to estimate two-phase damping. The design guidelines proposed by Pettigrew et al. (1989a) and Pettigrew and Taylor (1994) for the normalized two-phase damping can be seen in Figure 2.17. Different tube array configurations and P/D ratios were considered. The design guideline based on this plot corresponds to a maximum normalized two-phase damping ratio of 5, for a void fraction range from 40 to 70 % based on the HEM. However, Pettigrew et al. (1998); Pettigrew and Taylor (2003a, 2004) suggest a design envelope of $(\zeta_{tp})_D$ of 4 for the same void fraction range (see Figure 2.18). For fluidelastic analysis, Pettigrew et al. (1989a) proposed to use the damping at half the mass flux required for the instability to occur. As the available amount of damping data has been increasing during the last decade, it is expected that some of the proposed design guidelines will continue to change.

Baj and de Langre (2003) proposed a different approach for two-phase damping. They argued that the total damping ratio should be comprised of only two components, structural and fluid, the latter including all the effects related to the two-phase flow. Their normalization procedure replaced the liquid density used by Pettigrew et al. (1989a) with the two-phase density, based on the HEM void fraction. The resulting normalized fluid damping ratio is

$$\zeta_n^f = \zeta^f \left(\frac{m}{\rho_{tp} D^2} \right) \left(\gamma \frac{D}{D_{ref}} \right). \tag{2.12}$$

In equation 2.12, ζ_n^f is the normalized fluid damping, ρ_{tp} is the density of the two-phase mixture based on the Homogeneous Equilibrium Model and the terms D_{ref}/D and γ take into account the confinement effects. By extrapolating the values of the normalized fluid damping to zero reduced velocity, Baj and de Langre introduced the concept of "quiescent fluid damping" in two-phase mixtures as shown in Figure 2.21. The study showed that the quiescent fluid damping was lower than that recommended by the current design guidelines (which provide the damping measured at half the mass flux required for fluidelastic instability and assume that damping is independent of mass flux). In addition, the authors introduced a new "two-phase vibrational viscosity", arguing that the additional damping observed in two-phase flow is due to purely viscous effects. The new viscosity also proved to be much higher than the predictions of the existing models for two-phase mixtures (McAdams, Duckler and Cicchitti, see Collier and Thome (1996)).

In addition to the difficulties that arise from different normalization procedures, the way that damping is estimated from experimental data is also an important issue. Jauzen et al. (2005) demonstrated that there are differences in the damping values obtained by different measurement methods. They compared the logarithmic decrement, decay trace fitting and half-power bandwidth methods. It was observed that the half-power method produced higher damping values than the other two. Although the predictions using the decay trace fitting and the logarithmic decrement

were similar, the former proved to be more consistent. Chandler (2005) presented results of a series of experiments aimed to compare different damping measurement methodologies. A single tube was impacted with a calibrated force transducer hammer, and the responses were recorded and analyzed. The trend obtained by Janzen et al. (2005) was also observed in these experiments.

2.3.3 Two-Phase Damping and Mass Flux

Carlucci (1980) and Carlucci and Brown (1983) investigated the effect of flow velocity on two-phase damping in a single cylinder subjected to axial flow. They found that mass flux has little effect on two-phase damping for void fractions below 20%. However, they observed that the maximum two-phase damping ratio was a function of mass flux, and the damping data seem to broaden depending on flow velocity for HEM void fractions above 30%, as shown in Figure 2.19. This result was attributed to flow regime effects, introduced by the "gradual transition between annular and wispy-annular" flows. Pettigrew et al. (1989a) investigated damping of several tube bundles in two-phase cross flow. Damping measurements were taken with increasing mass fluxes up to the critical mass flux for fluidelastic instability, as shown in Figure 2.20. They stated that damping was "not too dependent on mass flux below two-thirds of the critical mass flux for instability". They also found that above half the mass flux for instability, damping generally tends to increase in the drag direction while it tends to decrease in the lift direction, promoting the occurrence of fluidelastic instability. They assumed that, from a practical point-of-view, mass flux was not an important parameter in the formulation of damping in two-phase flow. However, the mass flux combined with the void fraction defines the transition from one flow regime to the next. This feature is important because the current design guidelines (as shown in Figure 2.17) are based on damping results obtained at different mass fluxes.

Baj and de Langre (2003) also investigated the effect of flow velocity on damping. They found that the reduced velocity significantly affects damping over the whole range of reduced velocity studied (from 0 to 13). Even though two-phase fluid damp-

ing is often considered to be constant for low velocities according to Pettigrew et al. (1989a), Figure 2.21 shows that damping increases significantly at low reduced velocities. The maximum value of normalized fluid damping is obtained between one third and half of the critical velocity considered for each void fraction. This maximum value is typically twice the extrapolated value at zero velocity. The graphs on Figure 2.21 are reminiscent of those for gas flows as seen in Figure 2.10.

2.4 Scaling of Relevant Parameters

In any experimental study, it is common to find difficulties reproducing the exact characteristics of the problem at hand. Quantities like physical dimensions, flow velocities, fluid properties, etc., must be correctly scaled to be able to obtain reliable results and apply those to different scaled configurations. By using the Buckingham Pi Theorem, the relevant dimensionless parameters for studying fluidelastic instability in tube arrays include

Reduced Velocity : $(V_r = V_p/fD)$ is an important fluid-structure interaction velocity scale relating the flow velocity, V_p to structural velocity (tube frequency and diameter).

Reynolds Number : $(Re = \rho VD/\mu)$ is the ratio of the inertial forces to the viscous forces. This parameter is commonly neglected in tube bundle vibration since the Reynolds numbers in practical cases are relatively high, and the excitation phenomena do not appear to have a significant Reynolds number dependence.

Damping : (ζ) represents the capacity of the system to dissipate energy. The mechanisms of damping are not well understood and scaling is heavily based on empiricism.

Mass Ratio : $(m/\rho D^2)$ is the ratio of the vibrating mass to the mass of displaced fluid. It is important for scaling the amplitude response of the tube and is dominated by the fluid density ρ.

Geometry : The P/D ratio and layout pattern must be scaled accurately.

In many studies concerning flow-induced vibration, the scaling of all the fluid-mechanics and structure-mechanics related parameters is not always possible. In such cases, the most relevant parameters must be identified and scaled with judgement. By doing this, it is ensured as far as possible that any distortion in the model will produce conservative results, and therefore, the tendency of the model to vibrate under a certain flow will be amplified rather than suppressed.

2.5 Two-Phase Flow Modelling

When the flow under consideration has two phases (or physically homogeneous components), the dimensionless parameters that describe the onset of instability change. One of the difficulties of experimenting with two-phase flows is trying to define an equivalent flow velocity of the two-phase mixture so that flow-induced vibration data from various studies can be compared and scaled to prototypical applications. Defining the reduced velocity and mass-damping parameter in two-phase flows, raises at least two important issues:

1. How to define the fluid density
2. How to define the flow velocity

These are problematic because they require a good estimate of void fraction, as well as relative velocity between the phases. For the experimental modelling and simulation of two-phase flows some assumptions have to be made. In first place, it is expensive and complicated to use a steam-water mixture for these experiments due to the high temperatures and pressures required for the water to be evaporated. Secondly, the knowledge of the morphology of the flow or distribution of the phases (flow regime) is vital to estimate the density and velocity of the flow. The most common approach is to use air-water mixtures, which have the advantage of allowing

for better control of the void fraction (volume of gas present in the mixture) and flow regime, and does not require heating or high-pressure components. This reduces considerably the cost and complexity of the experiments, but at the expense of the physical modelling of the real problem. The drawback of this approach is the poor scaling capabilities of air-water in terms of density ratio and surface tension, when compared to the real fluids (steam-water). Also, the use of two-component immiscible mixtures does not allow for phase change or "flashing" within the tube bundle.

The use of one-component two-phase mixtures overcomes those deficiencies and produces more reliable results (Feenstra, 1993; Pettigrew et al., 1995; Feenstra, 2000). The possibility of phase change and the better scaling of density ratio and void fraction help us to gain insight into some aspects of the phenomenon which are not observable in two-component flows. Table 2.1 shows a comparison between some physical parameters for air-water, R-11 and R-22 refrigerants which have been used to simulate the two-phase flow in heat exchanger tube arrays (Feenstra, 2000).

Table 2.1. Typical properties of various fluids used to simulate steam-water mixtures. Adapted from Feenstra (2000).

Quantity	Steam Generator Conditions	Air-Water	R-11	R-22
Temperature, T (°C)	260	22	40	23.3
Pressure, P (kPa)	4700	101	175	1000
Liquid Density, ρ_l (kg/m^3)	784	998	1440	1197
Vapour Density, ρ_g (kg/m^3)	23.7	1.2	9.7	42.3
Liquid Viscosity, μ_l (μPa s)	103	959	356	139
Surface Tension, σ (Nm)	0.024	0.073	0.0167	0.0074

2.5.1 Void Fraction

The void fraction is a dimensionless quantity indicating the fraction of a geometry or temporal domain occupied by the gas phase, and it is probably the most significant

quantity one can measure in two-phase flow. It is very important when analyzing two-phase flow-induced vibrations because it affects how the flow velocity and two-phase density are determined. Since this parameter is strongly related to damping and the onset of instability, appropriate models must be implemented in its calculation. The most commonly used model to determine the void fraction has been the Homogeneous Equilibrium Model (HEM), due to its ease of application. The HEM assumes that the mixture can be considered "homogeneous", and the fluid properties can be defined depending on the proportion of the gas phase to the liquid phase. However, it is known that the HEM over-predicts the values of void fraction when compared to direct measurement methods. In addition, when the two-phase mixture is assumed to be homogeneous, the effect of flow regime is neglected. Direct measurement methods add complexity to the modelling, but overcome the deficiencies of the Homogeneous Equilibrium Model. Some of the existing models to calculate the void fraction in two-phase flows across tube arrays are presented in the next section.

2.5.1.1 Homogeneous Equilibrium Model (HEM)

In general, the void fraction can be determined from the combination of the continuity equations for each phase, as follows:

$$\alpha = \left[1 + S\frac{\rho_g}{\rho_l}\left(\frac{1}{x} - 1\right)\right]^{-1}, \tag{2.13}$$

where

$$S = \frac{U_g}{U_l}. \tag{2.14}$$

In equation 2.13, ρ_g is the gas phase density, ρ_l is the liquid density, x is the thermodynamic quality of the mixture and S is the velocity ratio or slip ratio, as defined in equation 2.14. The latter is a measure of the relative velocity that exists between the phases as they flow together, where U_g and U_l are the gas and liquid velocities respectively. Although it is well known that the density difference between the phases (particularly in vertical flow) will produce a relative velocity of the gas

phase respect to the liquid, other factors such as liquid viscosity, surface tension and average density of the mixture are considered key factors affecting the slip ratio. Since the relationship between these variables is not easy to devise, the Homogeneous Equilibrium Model assumes that the relative velocity is equal to zero. This implies that the slip ratio is equal to the unity. In other words,

$$U_l = U_g \tag{2.15}$$

The average two-phase density, ρ_{tp}, can be determined as

$$\rho_{tp} = \alpha\rho_g + (1-\alpha)\rho_l, \tag{2.16}$$

which can be reduced to the following expression for the fluid density, ρ_H, based on the HEM assumption

$$\rho_H = \left(\frac{x}{\rho_g} + \frac{1-x}{\rho_l}\right)^{-1} \tag{2.17}$$

Most of the research in two-phase flow-induced vibration has been carried out using the Homogeneous Equilibrium Model, even though the latter assumes that the liquid and gas phases are uniformly distributed and move with the same velocity (no slip). In general, this is not a valid assumption and it certainly does not provide for void segregation and different flow regimes, including intermittent flows. It also distorts the values assumed for effective flow velocity and two-phase density, which has a direct impact in fluidelastic instability analysis.

2.5.1.2 Feenstra's Model

Feenstra (2000) carried out a dimensional analysis of two-phase flow of refrigerant 11 passing a horizontal tube array, and combined it with experimental data. The result was a model for determining the slip ratio, allowing for the calculation of the void fraction based on equation 2.13. According to this model, the slip ratio can be

written as

$$S = 1 + 25.7\,(Ri * Cap)^{0.5} \left(\frac{P}{D}\right)^{-1}, \tag{2.18}$$

where P is the pitch of the array, D is the tube diameter and Ri and Cap are the Richardson and Capillary numbers respectively, given by the expressions:

$$\begin{aligned} Ri &= \frac{(\Delta\rho)^2 ga}{G_p^2} \\ Cap &= \frac{\mu_l U_g}{\sigma} \end{aligned} \tag{2.19}$$

As can be seen in equations 2.19, the liquid viscosity μ_l, density difference $\Delta\rho$, surface tension σ, mass flux (G_p), gravitational acceleration g, gap between tubes a and the gas velocity U_g are taken into account in this model. The model was the result of analyzing two-phase flow in tube bundles, while the majority of the existing models were obtained from circular pipe data. The prediction of void fraction obtained from this model is superior to that of other models when compared to gamma densitometry measurements (Khushnood et al., 2004; Consolini et al., 2006).

2.5.1.3 Other Void Fraction Models

The first void fraction models proposed for this kind of problem were those by Zuber and Findlay (1965) and Smith (1968). Zuber and Findlay developed a drift-flux formulation, taking into account the two-phase flow non-uniformity and the local differences in phase velocity. The slip ratio is then defined as a function of the phase densities, quality, void fraction based on HEM and some experimentally determined coefficients. The experiments were carried out in circular pipes using air-water mixtures. Smith (1968) assumed that the kinetic energy of the liquid is equivalent to that of the two-phase mixture, and a constant fraction of the liquid is entrained in the gas phase. Again, the experiments were carried out in circular pipes (vertical upward flow). The correlation proposed by Schrage et al. (1988) is based on void fraction measurements using a pair of quick-closing valves in a test section. It was developed

using air-water mixtures in circular pipes, and allows for the determination of void fraction as a function of quality and Froude number.

2.5.2 Flow Regimes

As mentioned above, the flow regimes represent the morphology of the phases, i.e. the phase distribution within the flowing conduit. They are strongly dependent on surface tension, viscosity of the fluids, flow area, pressure and temperature. Figure 2.22 shows schematically the flow regimes in evaporating vertical-upwards two-phase flow in circular pipes, while Figure 2.23 illustrates the flow regimes observed in tube arrays by Ulbrich and Mewes (1994). Numerous studies have been carried out to gain insight into the flow regime effects on the void fraction, most of them using air-water mixtures. The traditional approach has been to present a "flow regime map", allowing us to determine the flow regime based on some flow parameters (velocity, density, etc.). Other studies recommend the use of experimental correlations, valid only for a certain set of conditions.

It is generally agreed that three flow regimes exist on the shell side of heat exchangers: bubbly, intermittent and dispersed (as seen in Figure 2.23). At low void fractions, the gas phase appears as discrete bubbles transported by the continuous liquid phase. Initially, the bubbles are very small and there is no interaction between them, turning the mixture into a pseudo-homogeneous flow. As the void fraction increases, the bubbles become more numerous and ultimately will interact, producing void coalescence and larger bubbles. The size of these bubbles will depend to some degree on the mass flux and the tube array geometry. Up to this point, the flow is relatively steady and is commonly referred as "bubbly flow". For sufficiently high void fraction, the flow becomes unstable, with random temporal and spatial variations in phase distribution. This flow is characterized by unsteadiness and non-homogeneity in local void fraction and is referred to as "intermittent flow". At higher void fractions, the flow becomes more steady again. The "dispersed flow" regime is characterized by a high velocity gas phase core carrying liquid droplets.

The first flow regime maps were developed for two-phase internal flow in circular pipes (Taitel et al., 1980; McQuillan and Whalley, 1985; Barnea, 1987). Grant (1976) and Grant and Chisholm (1979) were the first to publish a flow regime map for two-phase flow across tube arrays, based on experiments using air-water mixtures. They visually observed three different flow regimes on the shell-side of a segmentally baffled heat exchanger: bubbly, intermittent and spray (or annular-dispersed). Ulbrich and Mewes (1994) identified the same general flow regimes and presented a flow regime map for vertical-upwards flow across an in-line tube bundle (see Figure 2.24). Their experiments were carried out using air-water adiabatic flow, and the parameters used for characterizing the flow regime were the superficial velocities. The superficial velocity of each phase is calculated as

$$U_{gs} = \frac{xG_p}{\rho_g} \quad , \quad U_{ls} = \frac{(1-x)G_p}{\rho_l}, \tag{2.20}$$

where U_{gs} is the superficial velocity of the gas phase, U_{ls} is the superficial velocity of the liquid phase, x is the thermodynamic quality of the mixture, G_p is the pitch mass flux and ρ_g, ρ_l are the densities of the gas and liquid phases respectively.

Noghrehkar et al. (1999) proposed flow regime maps based on results from both in-line and staggered tube arrays. They analyzed the probability density function of void fraction fluctuations, which were recorded by an electrical resistivity probe. According to the results of Noghrehkar et al. (1999), for in-line tube arrays the transition between bubbly and intermittent flows is very similar to that predicted by Ulbrich and Mewes (1994), but the intermittent flow regime remains to higher flow rates. They argued that the difference between the results was caused by the different measurement methodologies. By comparing the void fluctuations near the wall and deep into the bundle, they concluded that a visual observation from outside the test section could be misleading, because the void fluctuations were attenuated near the walls. In staggered arrays, they observed that the intermittent flow regime did not occur until higher gas flow rates when compared to in-line arrays, due to the breakup of large bubbles caused

by the bundle. Figure 2.25 shows the flow regime map presented by Noghrehkar et al. (1999) for staggered arrays.

2.5.3 Two-Phase Velocity

As noted above, a good estimate of both void fraction and flow velocity is required for analyzing fluidelastic instability in two-phase flows. The reduced velocity requires knowledge of the flow velocity, which is difficult to define when more than one phase is present. In two-phase flows, the velocity of the gas phase, the velocity of the liquid phase and the velocity of the interface between phases are all possible velocity measures. The relative importance of these velocities i.e., its impact on an "averaged" velocity of the mixture, will generally depend on the flow regime. For bubbly flows, the gas, liquid and interfacial velocities are very similar if the bubbles are very small. As the bubble size grows, the buoyancy effects accelerate the gas phase, creating the "slip" or relative velocity that will eventually produce a distortion of the interface. In the intermittent and dispersed flow regimes, a much higher slip ratio will further produce a difference between the velocities.

However, an estimate of the flow velocity is needed for design purposes. Three different velocity definitions have been proposed to scale two-phase flows:

- Pitch Velocity (Pettigrew et al., 1989b; Pettigrew and Taylor, 1994)
- Equivalent Velocity (Feenstra, 2000)
- Interfacial Velocity (Nakamura et al., 2000)

The pitch velocity for two-phase flows is defined as

$$V_p = \frac{G_p}{\rho_H}, \tag{2.21}$$

where ρ_H is the two-phase density based on the Homogeneous Equilibrium Model. This approach remains the most commonly used for fluidelastic analysis in two-phase

flows. However, as the HEM overestimates the void fraction (and hence underestimates the density), the use of this velocity can introduce errors in the prediction of fluidelastic instability.

The equivalent velocity (V_{eq}) was introduced by Feenstra (2000), and it takes into account the kinetic energy of the phases. It was thought to be a more physically reasonable estimate of the two-phase velocity than the pitch velocity, because it was developed from the continuity and energy equations and assumed that fluidelastic instability was related to the energy in the flow. It can be determined as

$$V_{eq} = \sqrt{\frac{\alpha\rho_g U_g^2 + (1-\alpha)\rho_l U_l^2}{\rho_{rad}}}. \tag{2.22}$$

In equation 2.22, ρ_{rad} represents the two-phase density based on gamma densitometer measurements, U_g is the velocity of the gas phase and U_l is the velocity of the liquid phase. If this approach is used for the calculation of the reduced velocity, a decreasing trend can be observed in the onset of instability when the mass-damping parameter is increased (Figure 2.9b). It seems that the equivalent velocity approach exaggerates the effects of flow regime change and fails to produce the desired data collapse.

The interfacial velocity (Nakamura et al., 1999) was the result of experimental measurements of bubble velocities using bi-optical probes. It comes from an expression originally developed by Nicklin et al. (1962) for the measurement of slug velocity that required some adjustments to make it suitable for tube arrays (Suzuta et al., 1999). The expression for the interfacial velocity is

$$V_i = C_i(U_{gs} + U_{ls}) + \sqrt{\frac{gD_e(\rho_l - \rho_g)}{\rho_l}}, \tag{2.23}$$

where U_{gs} and U_{ls} are the superficial velocities of the gas and liquid phases respectively. The interfacial coefficient C_i depends on the array pattern, and is equal

to 0.77 for parallel triangular arrays, 0.95 for a rotated square arrays and 0.73 for a normal square arrays. The use of this velocity in a stability diagram produces the collapse the two-phase fluidelastic data, regardless of the fluids used, array pattern or flow regime, as can be seen in Figure 2.9c.

2.6 Discussion

The analysis of damping and fluidelastic instability in two-phase flows is much more complex than in the single-phase case, due to the inclusion of void fraction and flow regime. The current design guidelines are based on the Homogeneous Equilibrium Model for the characterization of the two-phase mixture, overestimating the void fraction and completely neglecting the flow regime effects. Damping is commonly measured using the half-power bandwidth method, which is affected by the added mass fluctuations caused in part by the local changes in void fraction. For fluidelastic analysis, the damping used in the mass-damping parameter is traditionally taken at half the mass flux required for the instability to occur. In addition, it is assumed that damping is independent of mass flux. These are some of the aspects that must be studied and improved in order to better understand the mechanisms of flow excitation in two-phase flows, particularly fluidelastic instability.

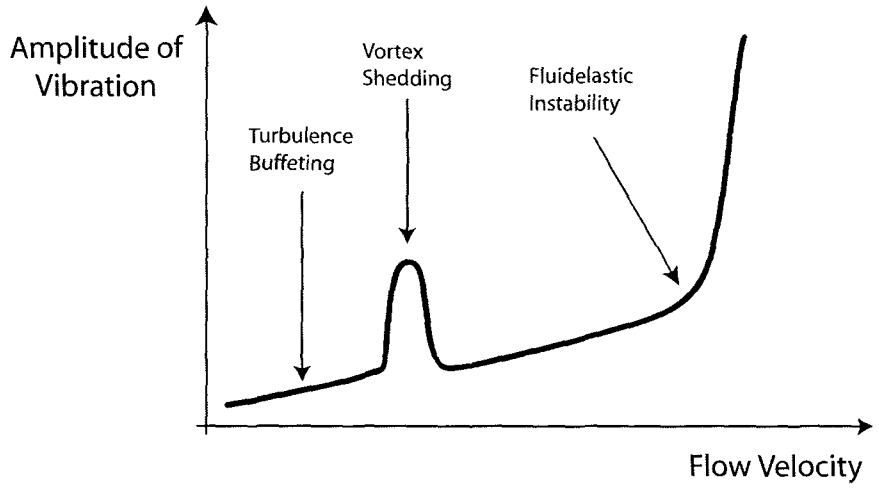

Figure 2.1. Idealized response of a tube array subjected to single-phase cross-flow, adapted from Païdoussis (1982).

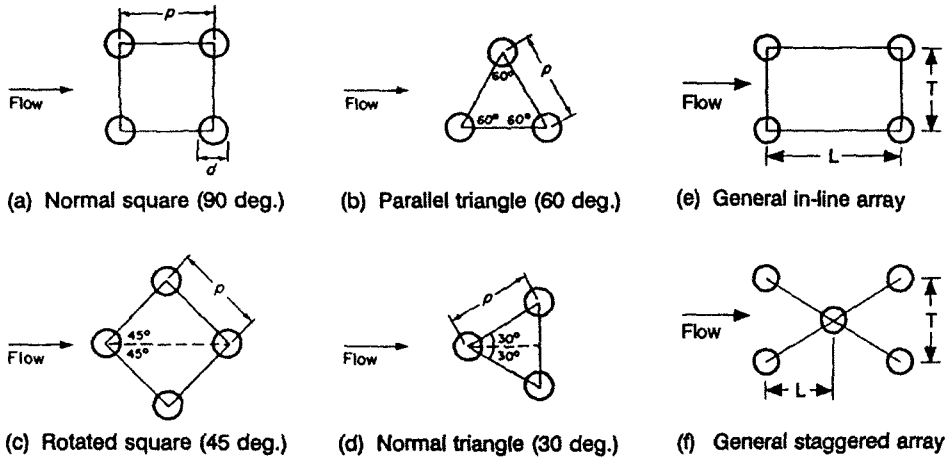

Figure 2.2. Different tube array configurations used in heat exchangers (Weaver, 1993).

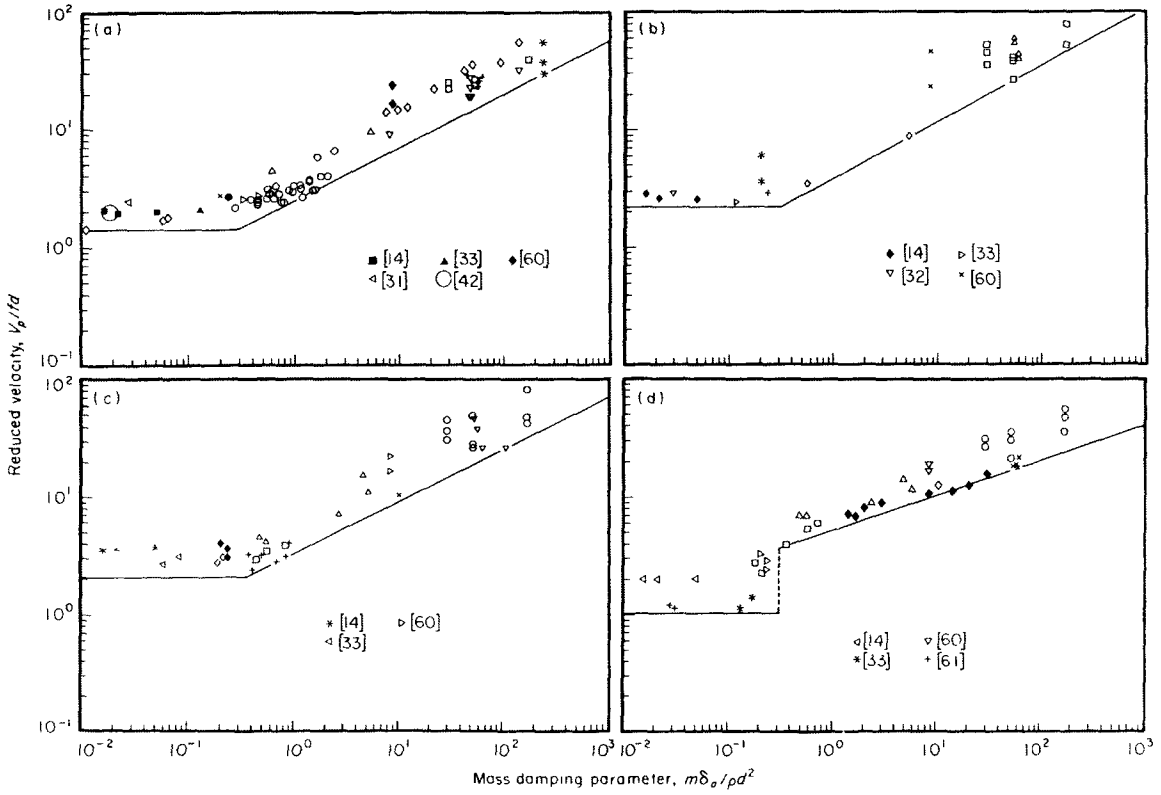

Figure 2.3. Stability maps proposed by Weaver and Fitzpatrick (1988) for different tube array geometric configurations (a) square, (b) rotated square, (c) normal triangular, (d) parallel triangular.

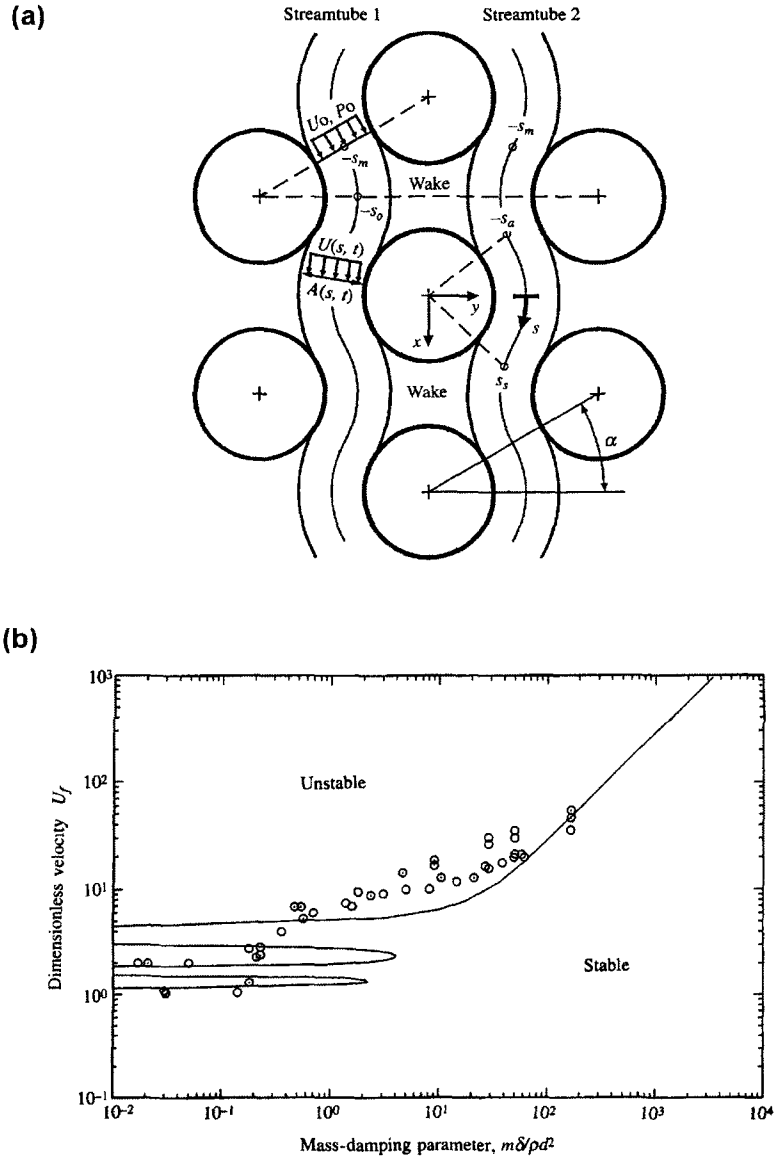

Figure 2.4. Semi-analytical model proposed by Lever and Weaver (1986a). (a) Typical unit-cell, (b) theoretical stability boundaries for a parallel triangular array with P/D = 1.35.

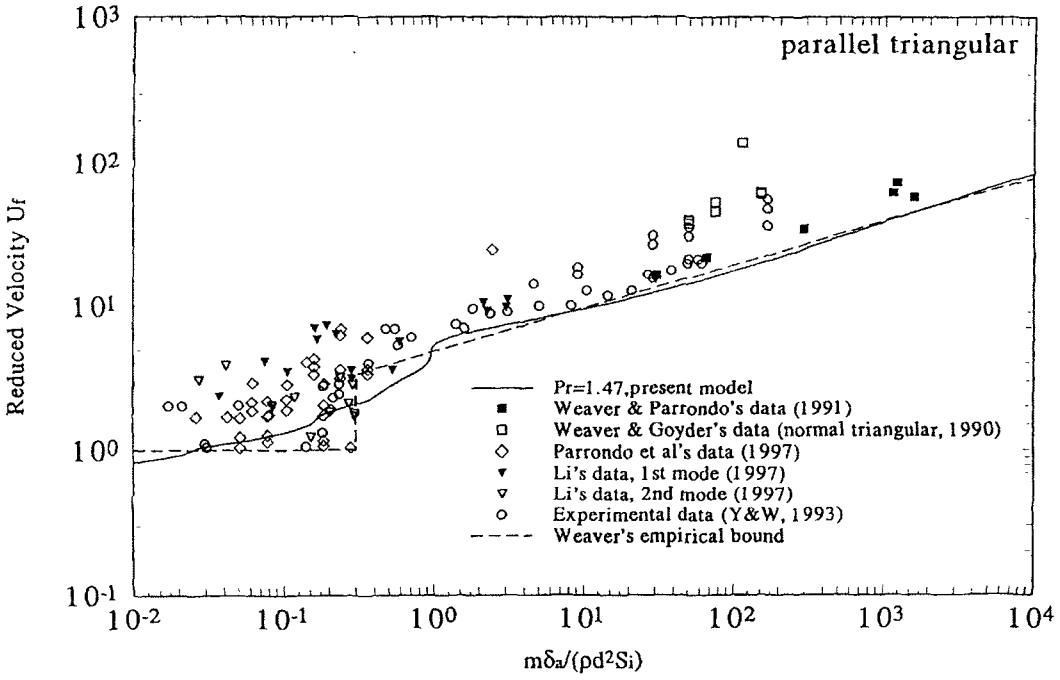

Figure 2.5. Comparison between empirical data, semi-empirical models and the theoretical model proposed by Li (1997) for a parallel triangular array. U_f is the reduced velocity based on the pitch velocity and S_i is the energy fraction, which represents the contribution of the partial admission effects.

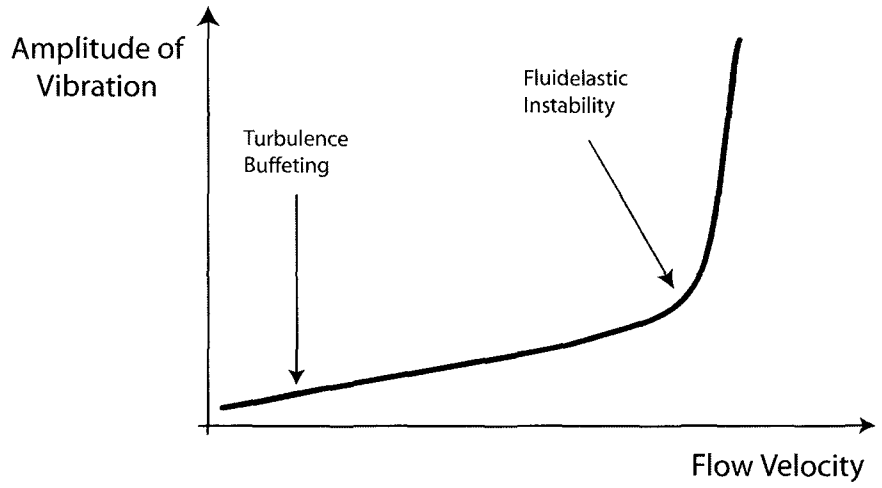

Figure 2.6. Idealized response of a tube array subjected to two-phase cross-flow.

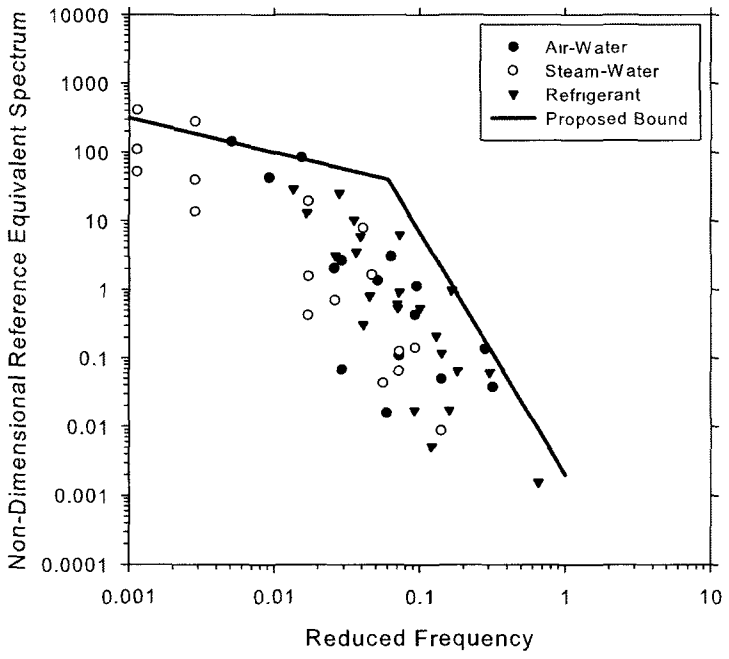

Figure 2.7. Reduced data for turbulence buffeting in two-phase flows. Adapted from de Langre and Villard (1998).

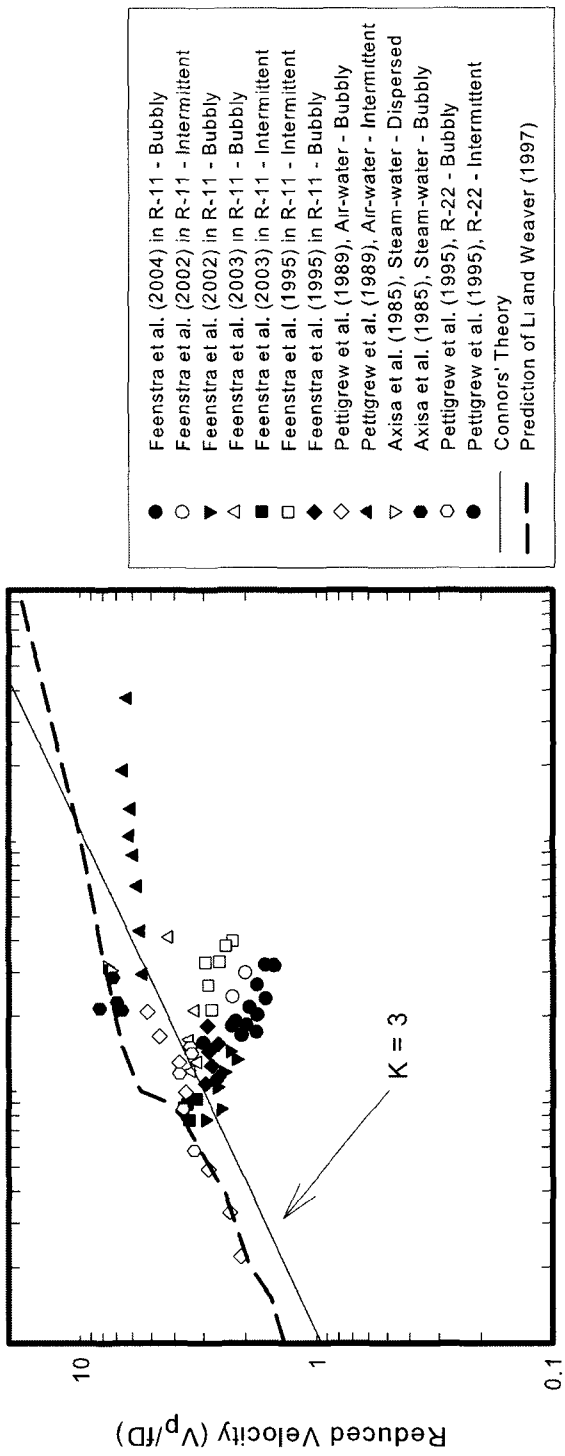

Figure 2.8. Critical velocities obtained from two-phase flow fluidelastic instability studies. The dashed line corresponds to the theoretical model introduced by Li (1997) for single-phase flows.

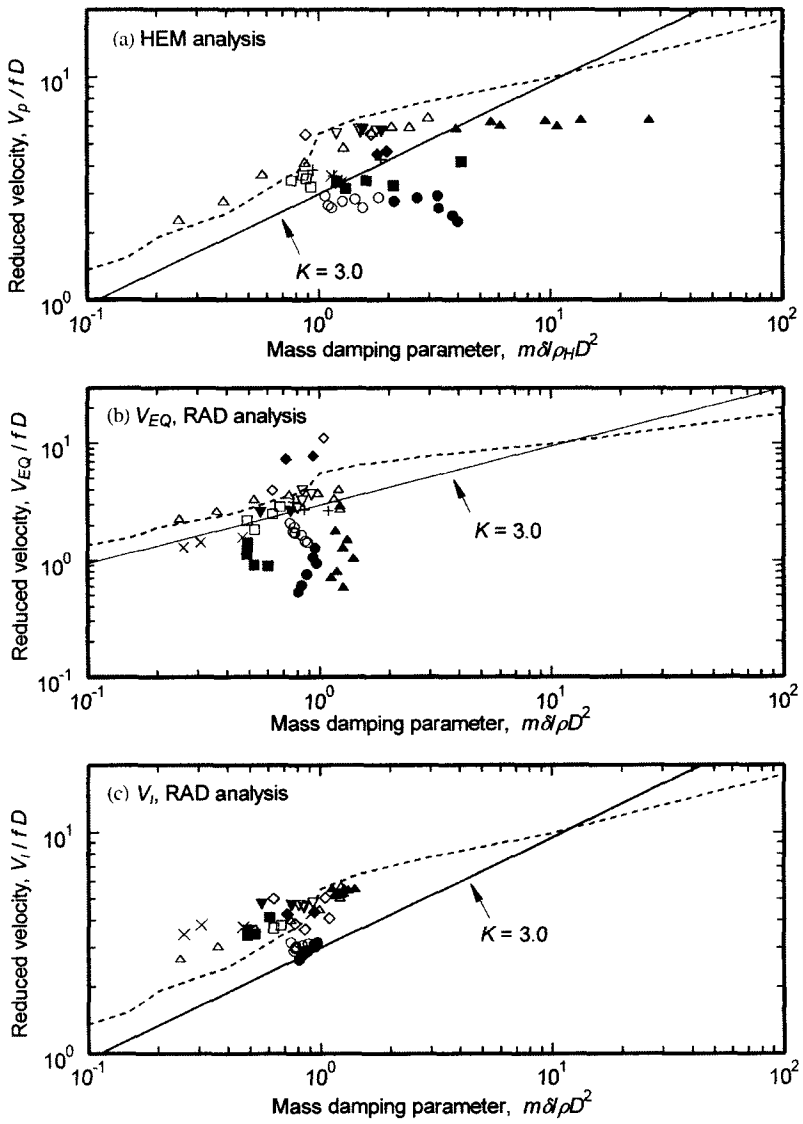

Figure 2.9. Critical flow velocities for fluidelastic instability of normal square tube arrays in two-phase cross-flows. Data analyzed by using (a) pitch velocity and HEM density, (b) equivalent velocity and RAD density, (c) interfacial velocity and RAD density (Feenstra et al., 2003). The dashed line corresponds to the theoretical model introduced by Li (1997) for single-phase flows.

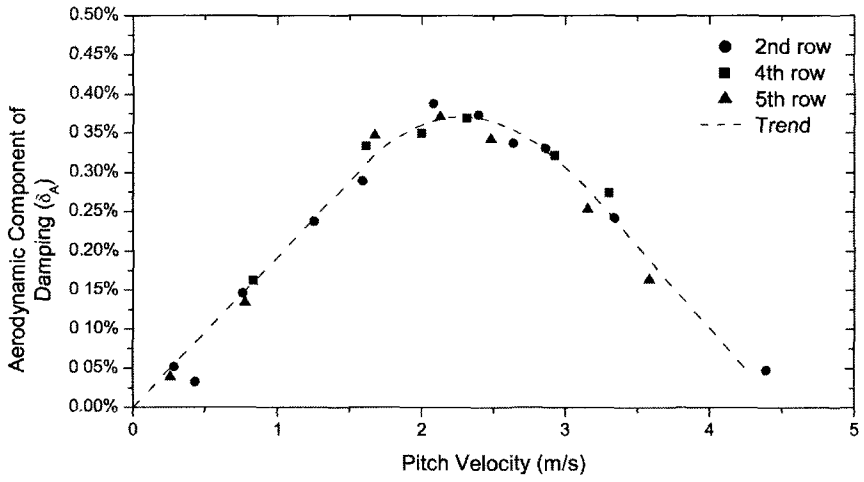

Figure 2.10. Aerodynamic component of damping as a function of pitch velocity. Adapted from Weaver and El-Kashlan (1981a).

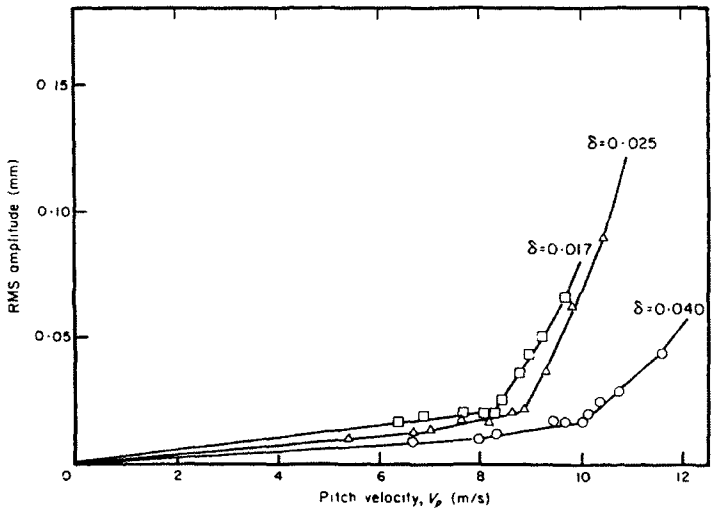

Figure 2.11. Amplitude response for different damping ratios (Weaver and El-Kashlan, 1981a).

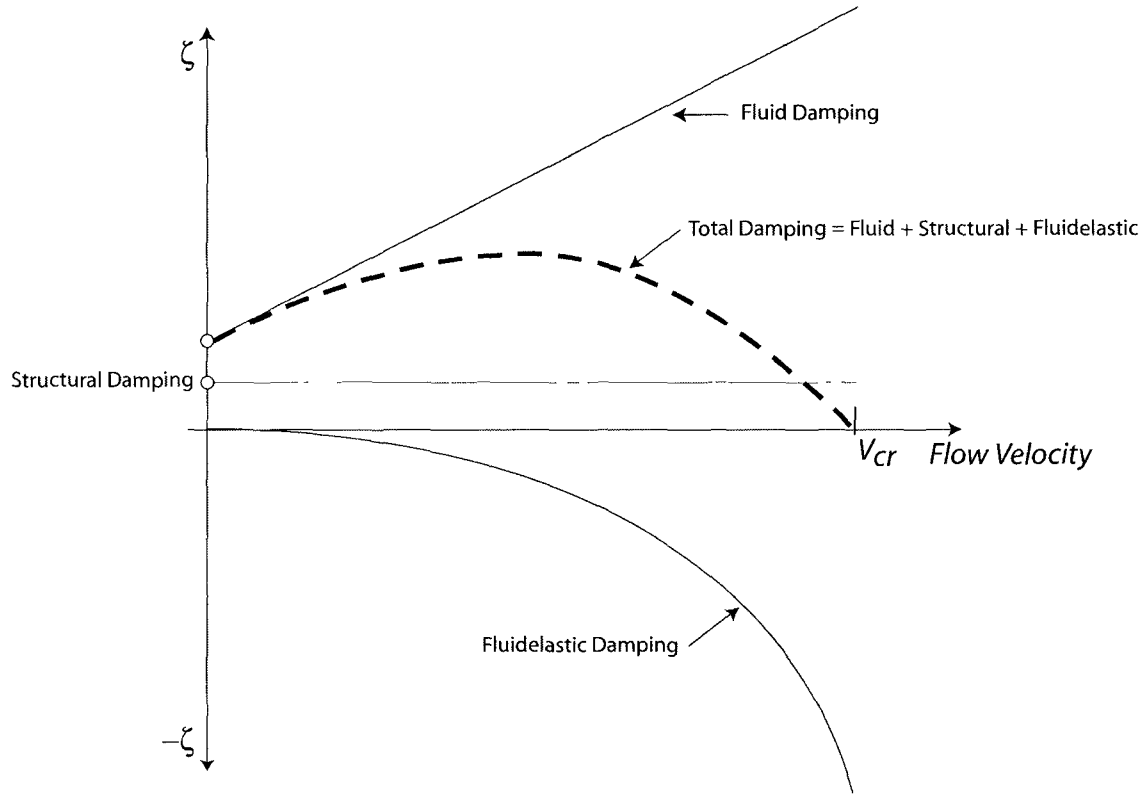

Figure 2.12. Conceptual variation of damping components with flow velocity. As the velocity increases, the fluidelastic forces overcome the effect of the fluid damping. At the critical velocity, the fluidelastic effects have equalized the sum of the structural and fluid contributions.

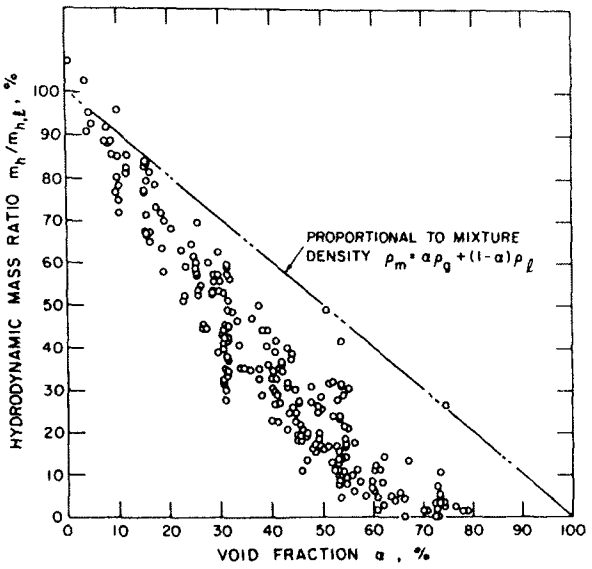

Figure 2.13. Hydrodynamic mass ratio vs. void fraction for mass fluxes of 500 to 5000 kg/m^{2}s in axial air-water flow over a single cylinder (Carlucci and Brown, 1983). The continuous line represents the theoretical hydrodynamic mass ratio.

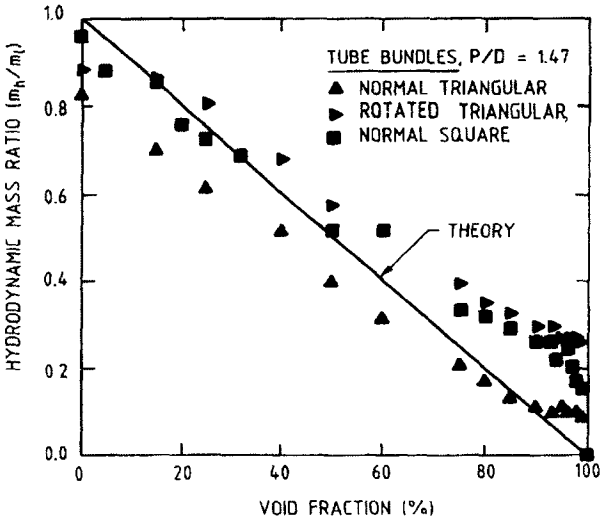

Figure 2.14. Hydrodynamic mass ratio vs. void fraction for different tube arrays subjected to air-water flows (Pettigrew et al., 1989a).

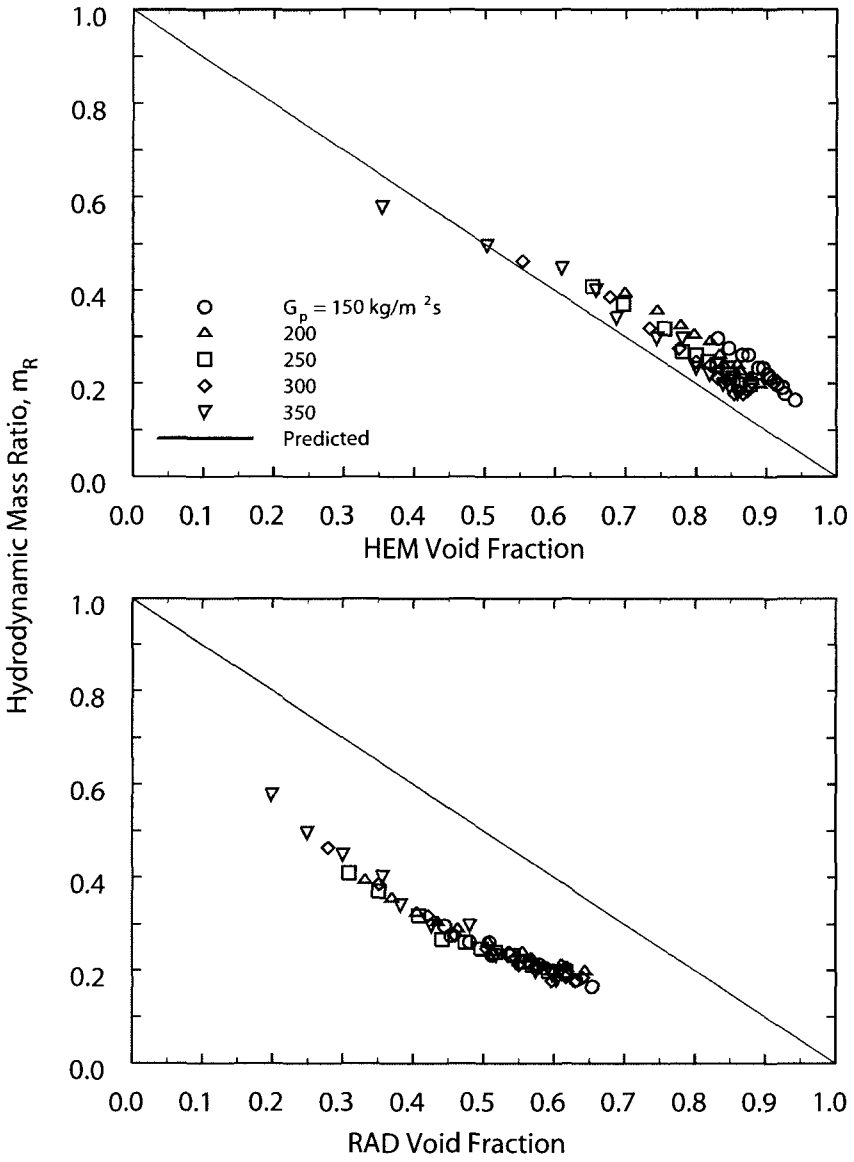

Figure 2.15. Added mass as a function of void fraction for various mass fluxes in R-11 (Feenstra, 2000). Above: Void fraction based on the HEM model; Below: void fraction based on gamma densitometer measurements.

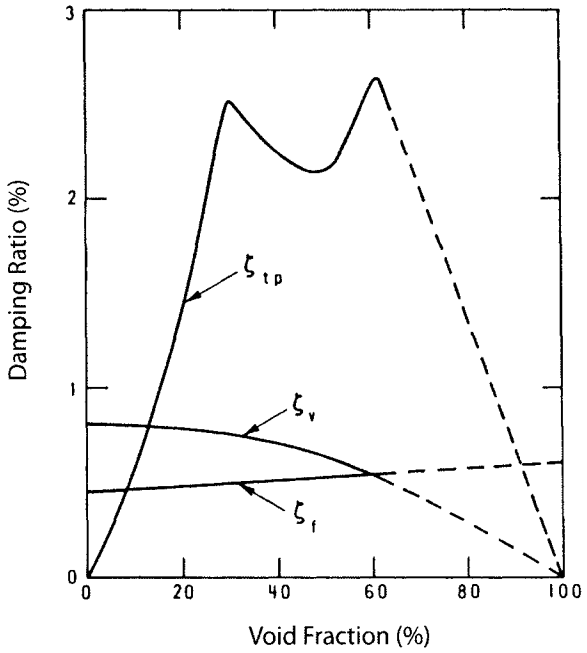

Figure 2.16. Variation of the components of the total fluid damping with void fraction (Carlucci, 1980).

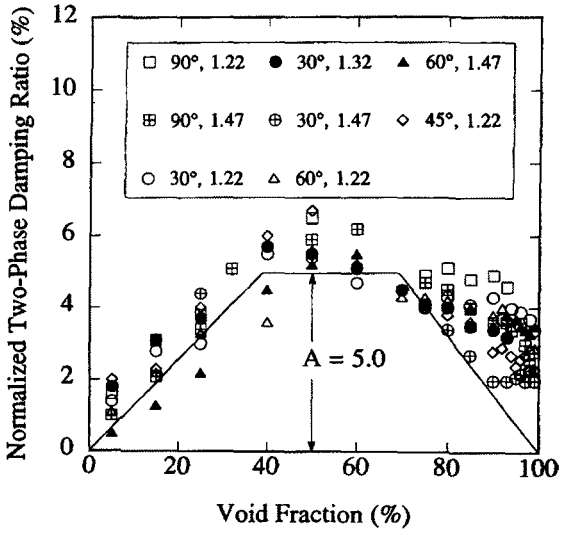

Figure 2.17. Dependence of normalized two-phase damping on void fraction: proposed design guideline (Pettigrew et al., 1989a).

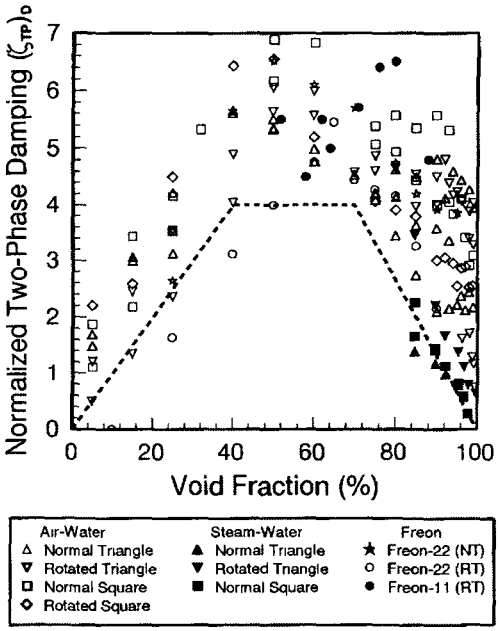

Figure 2.18. Comparison between design guideline and available damping data (Pettigrew and Taylor, 2004).

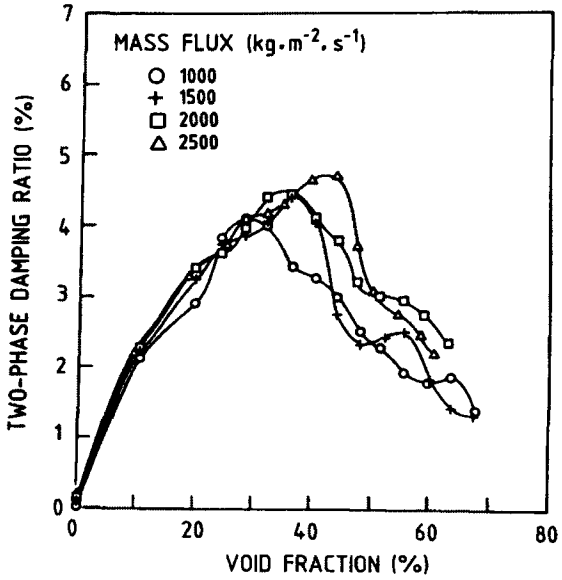

Figure 2.19. Effect of mass flux on two-phase damping ratio in axial flow (Carlucci, 1980).

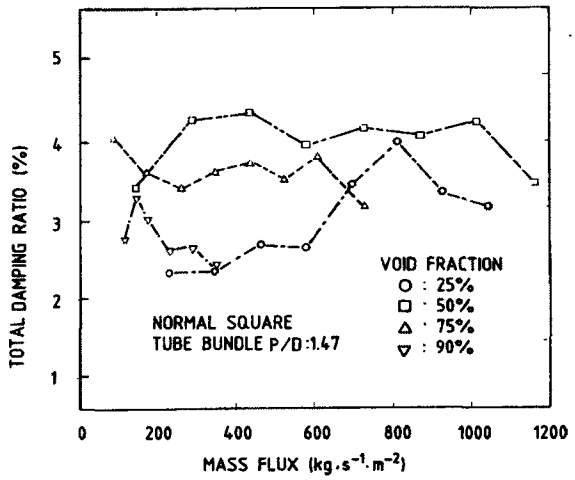

Figure 2.20. Effect of mass flux on tube damping ratio in two-phase cross-flow (Pettigrew et al., 1989a).

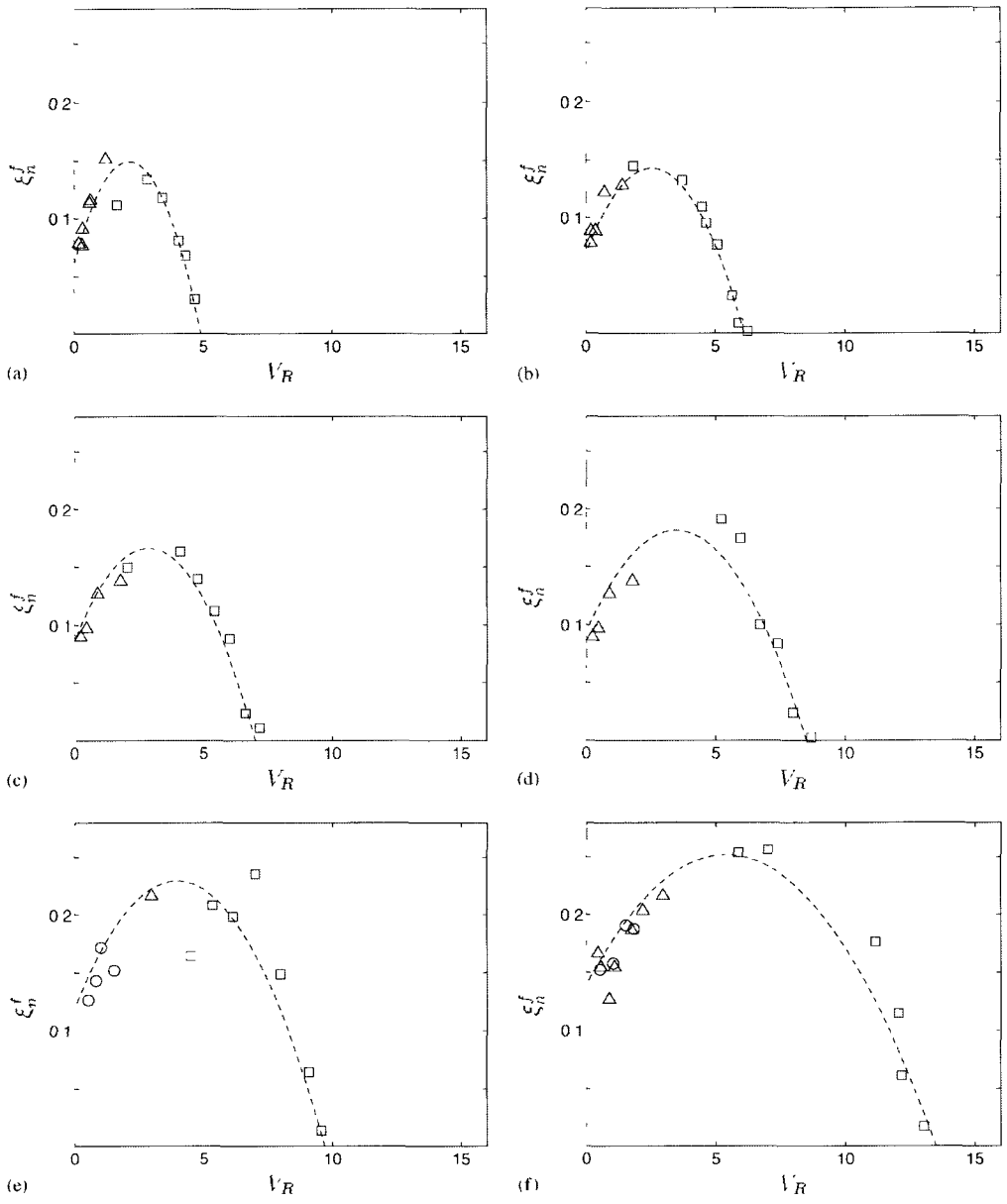

Figure 2.21. Normalized fluid damping versus reduced velocity for several ranges of HEM void fraction: (a) 20-30%; (b) 30-40%; (c) 40-50%; (d) 50-60%; (e) 60-70%; (f) 70-80% (Baj and de Langre, 2003)

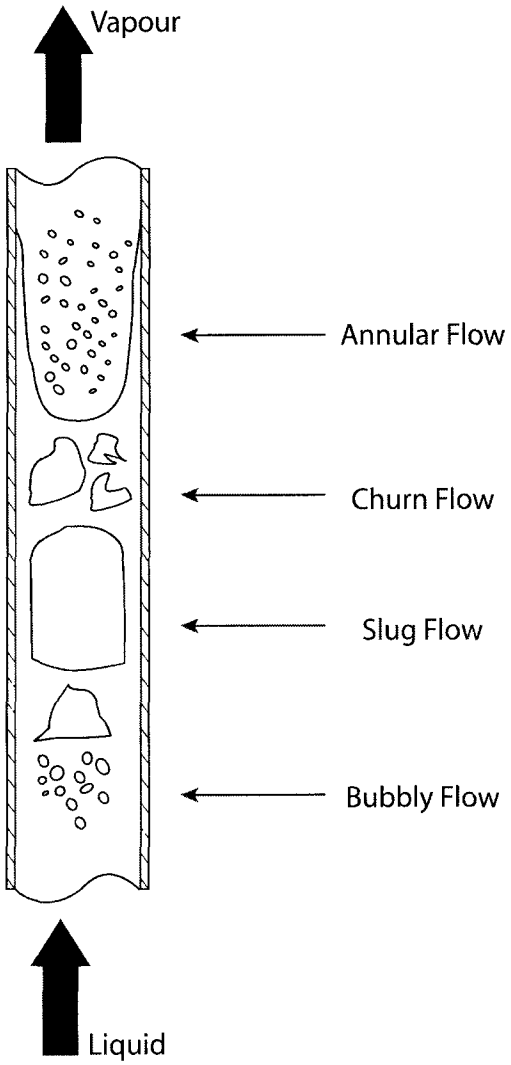

Figure 2.22. Schematic illustration of flow regimes in evaporating vertical-upwards two-phase flow in pipes.

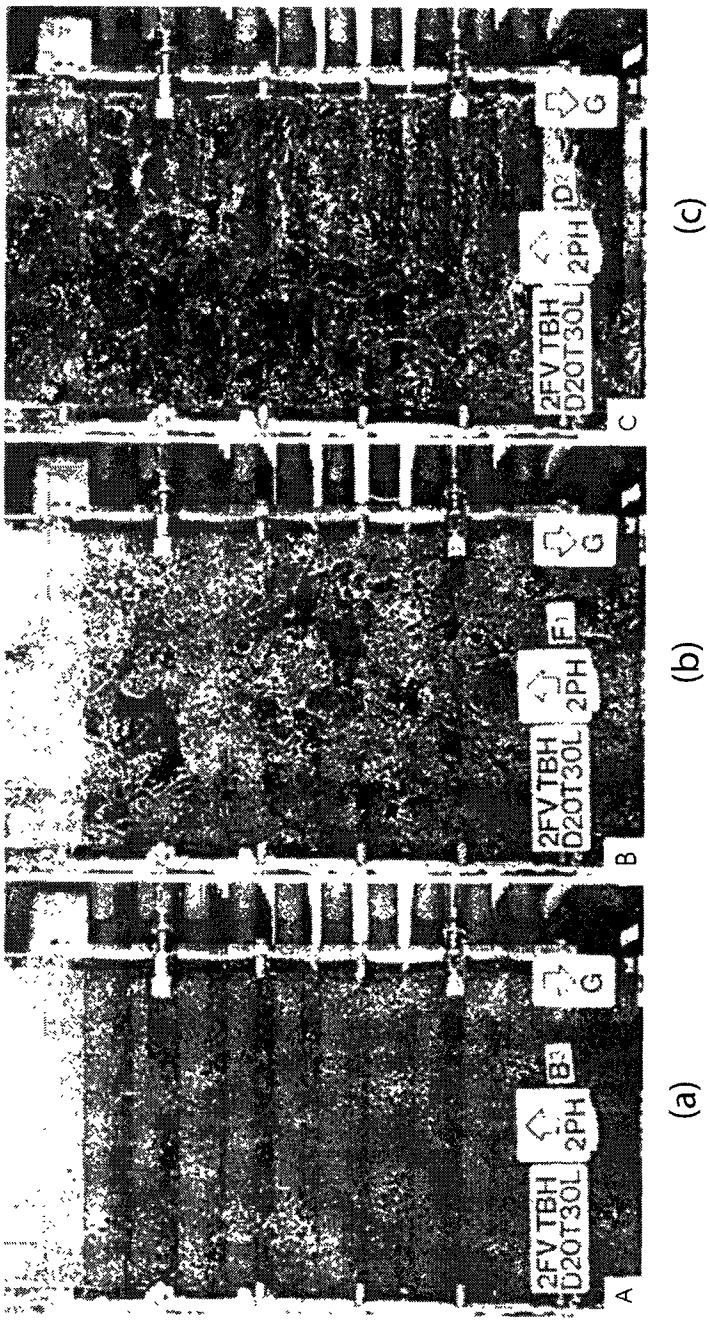

Figure 2.23. Flow regimes in vertical-upwards air-water two-phase flow in tube bundles: (a) Bubbly flow, (b) Intermittent flow and (c) Dispersed flow (Ulbrich and Mewes, 1994).

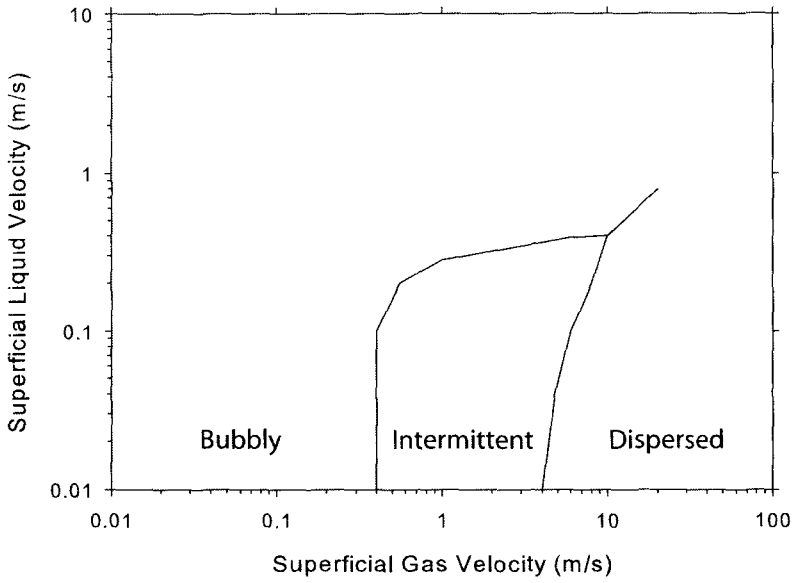

Figure 2.24. Flow regime map proposed by Ulbrich and Mewes (1994) for vertical-upwards two-phase flow in in-line tube arrays.

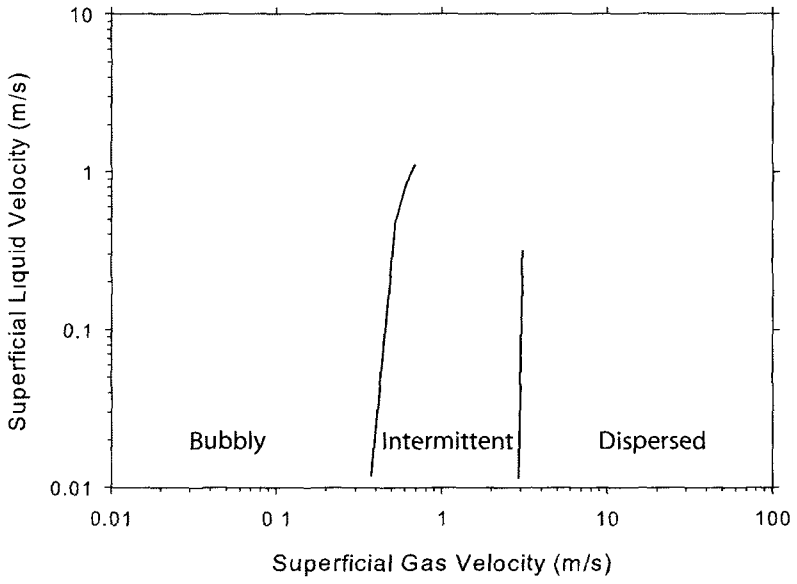

Figure 2.25. Flow regime map proposed by Noghrehkar et al. (1999) for vertical-upwards two-phase flow in staggered tube arrays.

CHAPTER 3

Experimental Facility and Methodology

An experimental program was designed and carried out to generate the damping and fluidelastic instability data required for this research. The steam generator conditions were simulated using a two-phase flow loop that operates with Refrigerant 11 as the working fluid. The flow loop was modified and a new tube bundle was designed, built and tested to study the effects of higher void fractions and flow velocities than previously possible. Two different sets of experiments were carried out. The first set was performed using a single-flexible tube in a rigid array, in order to obtain reliable estimates of the damping ratio which are not exaggerated by the hydrodynamic coupling between the tubes. Damping was measured using a novel technique that overcomes most of the limitations of the half-power bandwidth method. In the second set of experiments, a fully flexible array was used to determine the critical void fraction for fluidelastic instability over the range of mass fluxes studied.

This chapter provides a detailed description of the two-phase flow loop, as well as the measurement devices and data post-processing methodology. The design, testing and implementation of the electromagnetic device are also discussed.

3.1 Two-Phase Flow Loop

The facility used in this research was first designed, commissioned and tested by Westermann (1987) and Dam (1991). Additional improvements were introduced by Feenstra (1993, 2000) and Feenstra et al. (2003), in order to test different tube bundle geometries and extend the flow loop capabilities. The principal components of the flow loop are shown in Figure 3.1. As mentioned above, the working fluid is Trichlorofluoromethane (Freon 11), and is circulated throughout the loop by using a variable-speed gear pump. The main pump has a practical pumping capacity of 1.7 L/s, equivalent to a maximum single-phase pitch mass flux of 1000 kg/m^{2}s. The rotational speed of the pump is recorded by using a digital tachometer with a range from 0 to 1500 rpm and a resolution of 5 rpm. The flow rate through the flow loop is measured using orifice plates and is adjusted using control valves. Downstream of the main pump is the heating section, where the Freon is evaporated by the heat transferred from 15 U-bent heating coils. Prior to this research, the maximum capacity of the heating elements was 19.6 kW, corresponding to a maximum void fraction of about 60% (at a mass flux of 100 kg/m^{2}s). In order to generate the high-void fraction results required for this research, the heaters were rewired in order to extend their capacity to 46 kW. In terms of void fraction, the flow loop can now reach 90% (at 100 kg/m^{2}s).

Above the heaters, the two-phase mixture flows through a transition section (#2), before reaching the test section. The test section (#3) is the most important component of the flow loop, where the model tube bundle is located, and the void fraction is measured using a gamma densitometer. It has two glass windows on the sides as well as a frontal window, which allow for observation of the two-phase behaviour and the fluid-structure interaction. It is also equipped with pressure and temperature sensors for safety purposes. A tube-and-shell condenser located downstream the test section removes the heat from the mixture and allows for a better control of the thermodynamic parameters in the test section. A cooling water supply of 0.8 L/s was available (#4), although the maximum mass rate required for two-phase flow in the

experiments was around 0.6 L/s. The temperature of the cooling water ranged from 4°C in winter to 15°C in summer.

The temperatures along the flow loop were measured by six Type-E chromel-constantan thermocouples (Figure 3.1). The sensors were connected to a Phillips PM8237A temperature recorder, where an ice point reference was used to record the temperatures. The measurement resolution was 0.1 mV, equivalent to a precision of 0.3°C. An alarm was set-up in the recorder at a temperature of 70°C, using the sheath temperature of the heaters as a reference to prevent them from overheating in the event of a boiling crisis. The pressure in the test section was measured and controlled for safety purposes using a manometer. Due to the fact that the test section is the weakest component of the flow loop (due to the observation windows), the operation pressures were maintained below 270 kPa absolute (25 psia). However, due to the availability of a large mass flux of cooling water, the maximum pressures registered were around 140 kPa (20 psia) even when the void fraction reached up to 90% in some experiments.

3.2 Test Section and Model Tube Bundle

A schematic diagram of the test section is shown in Figure 3.2. It has a rectangular cross-section of 49.2 mm by 197 mm (1.94 by 7.76 in). In order to produce a relatively uniform two-phase flow along the length of the tubes, static mixers (flow homogenizers) were located upstream of the tube array as seen in Figure 3.3. The test section has half-tubes attached to the sides, in order to minimize the effect of the flat walls on the flow configuration. Downstream the tube bundle, splitter plates were installed to keep a constant solidity ratio and prevent the flow from recirculating within the test section and producing an artificially uneven distribution of void.

The model tube bundle consisted of ten cantilever-mounted brass tubes, with an external diameter of 9.525 mm (0.375 in). This represents a scale of about 3/4 the diameter of the tubes used in current CANDU steam generators. The geometric

pattern of the bundle is a parallel triangle with a pitch-over-diameter ratio of 1.49, also similar to that in CANDU steam generators (see Figure 3.4). The tubes were tuned to within ± 1 % of the average natural frequency measured in air by using variable end masses. Table 3.1 shows the geometric parameters of the tube bundle used in this study. Since the tube array was going to be subjected to high void fractions, heavy tubing was used to prevent the bundle from becoming unstable at undesirably low flow velocities. The monitored tube was located in the fifth row, which simulates the conditions of interior tubes in an array and permits a proper characterization of fluidelastic instability without upstream flow effects (Weaver and El-Kashlan, 1981b). A permanent magnet was attached to the free end of the monitored tube to facilitate the implementation of an electromagnetic plucking device for damping determination.

For the present research, it is assumed that the flow is perpendicular to the tube axis over most of the span, so that the straight tubes can be used instead of curved tubes. It is also assumed that the fluidelastic instability is more dependant on pitch ratio and array geometry than on the mode shape of vibration. This allows for the use of cantilevered tubes instead of the pinned-pinned boundary condition present in real steam generators. The fluidelastic instability is assumed to occur first in the transverse (lift) direction, which means that it is predominantly dependant on the transverse frequency. This consideration implies that the asymmetric stiffness characteristic of real tube bundles can be neglected. Weaver and Koroyannakis (1983) indicated that a symmetric-stiffness tube bundle (both the transverse and streamwise frequencies are the same) will have lower critical velocities than the asymmetric-stiffness prototype, hence producing conservative fluidelastic results. A summary of the scaling parameters values typical of CANDU steam generators and experimental research using air/water and Freon-11 are presented in Table 3.2. Note that especially with respect to density ratio and mass ratio, Freon 11 better simulates steam-water than air-water.

The vibratory response of the tube was measured by using two strain gauges, located on the cylindrical support between the tubes and the base plate of the array

Table 3.1. Geometric and dynamic properties for the model tube bundle.

Parameter	Tube Bundle
Geometric Configuration	Parallel Triangular
Tube Diameter (D)	9.525 mm
Tube Pitch (P)	14.20 mm
Natural Frequency in air (f_a)	48.5 Hz
Natural Frequency in liquid (f_l)	41.25 Hz
Lineal Tube Mass (m_t)	0.348 kg/m
Tube Length (L)	197.50 m
Structural Damping (ζ_a)	0.09 %
Damping in liquid (ζ_l)	0.50 %
Wall Thickness	1.60 mm
Upstream Flow Area (A)	9.69x10^{-3} m^2

Table 3.2. Scaling Parameters for Two-Phase flow-induced vibration experiments

Parameter	Definition	Steam Generator	Air-Water†	R-11
Pitch Ratio	P/D	1.3-1.5	1.47	1.44
Mass Ratio	$m/\rho D^2$	20-40	3-240	3-51
Reduced Velocity	V/fD	13-24	2.1-6.5	2.3-3.0
Damping (air)	ζ_{air}	0.16-0.45	0.2	0.1-0.16
Density Ratio	ρ_ℓ/ρ_g	33	830	150
Quality	x	0.12-0.22	0-0.093	0-0.1

†Pettigrew et al. (1989a).

(see Figure 3.5). These strain gauges were positioned at 90 degrees from each other, allowing for the measurement of displacement in both the transverse and streamwise directions. The strain gauges were calibrated in air, after the tube bundle was completely constructed (see Appendix B). Due to the solvent effects of the Freon 11, a special coating had to be carefully applied and cured.

The output signal from the strain gauges was collected using a dynamic analyzer

(HP 35670A), which calculated the rms amplitude and frequency spectrum in the frequency range from 0 to 100 Hz. The resultant averaged frequency spectrum was used to determine the natural frequency and the damping ratio based on the half-power bandwidth method (see Section 3.6.1). The rms amplitude was averaged over 100 samples with a resolution of 0.25 Hz. These values have proven to be adequate to provide repeatable data by previous research conducted in the same facility (see Feenstra (2000)).

3.3 Void Fraction Measurement

In this study, two values of the void fraction were determined. On one hand, the void fraction based on the Homogeneous Equilibrium Model (HEM) was calculated, in order to compare the present data with previous research and verify the over-prediction of void observed by Feenstra et al. (2002).

A direct measurement of the void fraction was also carried out using a single-beam gamma densitometer. This measurement is based on the Radiation Attenuation Determination (RAD) principle, in which the gamma ray flux that penetrates the test section will be attenuated differently depending on the density of the two-phase mixture that is flowing inside (Chan and Banerjee, 1981). The system consists of a Barium-133 gamma radiation source, a NaI scintillator and the equipment required for signal processing. Figure 3.6 shows the components of the gamma densitometer while Figure 3.2 shows the gamma beam area in a side view of the test section.

The measurement of void fraction provided by the gamma densitometer is a volumetric average. The void fraction recorded is an average of the concentration of the gas phase within the volume covered by the gamma rays, as they pass through the beam area in Figure 3.2. A lead collimator with a slit of 13 by 76 mm was used to concentrate the gamma flux in a portion of the test section located between the tube bundle and the homogenizers, seen as the space just below the half-tubes in Figure 3.3. The distance between the bundle and the homogenizers was maintained small

to ensure that the void distribution and volumetric void fraction measured by the gamma densitometer did not change and, therefore, were representative of those seen by the tube array. It was not desirable to pass the beam through the tube bundle since the displacement of the tubes could cause a deviation in the calibration of the densitometer. It is recognized that the local void distribution in the tube bundle may vary somewhat across the flow lanes or in the tube wakes. Thus, the RAD void fraction measured is the average value through the bundle. Prior to each experiment, the gamma densitometer was calibrated using the pure liquid and pure vapour cases (0 and 100% of void respectively, see Appendix A). The void fraction α can be calculated as

$$\alpha = \ln\left(\frac{N^*/N_l}{N_g/N_l}\right), \tag{3.1}$$

where N^* represents the gamma count obtained for the particular measurement and N_l and N_g are the gamma counts for the pure liquid and pure vapour cases respectively. The effect of temperature on the density change experienced by the freon throughout an experiment was also taken into account by introducing a correction factor. The measured gamma count N^* is determined from

$$N^* = N\sqrt{\frac{\rho_l}{\rho_{lc}}}. \tag{3.2}$$

In equation 3.2, N is the gamma count measured, ρ_{lc} is the liquid density at the time of calibration and ρ_l is the density of the liquid phase at the time of the data acquisition (Feenstra, 2000).

3.4 Electromagnetic Excitation device

Given the hypothesized limitations of the half-power bandwidth method for measuring damping in two-phase flows, it was postulated that more accurate damping measurements might be obtained using the decay response of the monitored tube instead of the frequency spectra. In order to study this possibility, it was necessary

to devise a method to produce an initial displacement of the tube and to capture the amplitude decay trace. The technique had to maintain the pressure integrity of the flow loop, and not disturb the flow distribution within the tube bundle. After various mechanical alternatives were evaluated, it was decided to implement an electromagnetic excitation device to initiate the tube oscillation. Since the force required to produce a significant static deflection of the monitored tube would require a very powerful magnetic field, an alternative approach would be to excite the tube at its resonance frequency. Given that the excitation comes from outside the test section, the method is non-intrusive, that is, it does not interfere with the two-phase flow distribution across the bundle or around the monitored tube.

Two electromagnetic coils were designed and built for this purpose (see Figure 3.7), and the polarity of these was changed at the natural frequency of the tube in order to produce resonance with a very low current (around 1 Ampere). A diagram of the equipment used is shown in Figure 3.8. A signal generator (Phillips PM-5165) was used to generate a sinusoidal wave at the natural frequency of the tube (determined from the averaged frequency spectra). The signal was fed into a two-channel amplifier (Panasonic RAMSA WP-1200) before circulating through the coils. Each coil was built by using a low-carbon steel rod with a diameter of 12.7 mm (0.5 in), and 28 AWG copper wire turned by hand some 400 times around each coil. The wire could withstand a maximum current of 2 A at 30°C, although the maximum used during the experiments was 1 A. The total resistance of each coil was about 4.5 Ω. This was designed to produce a magnetic field intensity equal to that of the permanent magnet mounted on the monitored tube, which was 3700 Gauss.

3.4.1 Preliminary Testing of Electromagnets

With the objective of testing whether the electromagnetic excitation device could produce the desired response of the monitored tube, a single-tube apparatus was utilized. An exact replica of the tube was used for these trials, in terms of mass per unit length, length, diameter and tube support (Figure 3.9). One strain gauge was

installed on the support to capture the response of the tube in the transverse direction, and a permanent magnet was fixed to the free end of the tube. The experiments were designed to evaluate the current required to make the tube oscillate with a certain amplitude, the influence of the distance between the electromagnets and the tube on the damping measured and the effect of coil misalignment. In order to have a reference value, an averaged value of the damping ratio was calculated by manually plucking the tube 10 times, with no electromagnets nearby.

The set-up was tested several times in air and with the tube submerged in water. It was important to verify that the magnetic field was strong enough to make the tube move in a fluid much denser than air. Figure 3.10 shows the typical responses obtained in air and water. The time required for the tube to reach a constant amplitude of vibration was observed to be less than 10 seconds for any value of the current less than 1 Ampere. It was determined that if the distance between the electromagnets and the monitored tube was more than 12.7 mm (0.5 in), the magnetic field did not have an effect on the damping measurements. Since the glass windows located in the test section are 12.7 mm thick, the minimum distance between the tube and the electromagnets was always adequate to ensure that the measured damping results were not affected by the presence of the electromagnets.

3.5 Experimental Program and Procedure

Two series of experiments, designated as A and B (see Table 3.3), were carried out in order to generate the data required for this study. Each series had a specific purpose:

- Series A - Damping ratio measurements
- Series B - Fluidelastic Instability data

The damping ratio measurements (Series A) where performed by fixing all the tubes in the array, with the exception of the monitored tube. The effect of hydrody-

namic coupling between the tubes, which is especially important at low void fractions, produces unreliable damping results. When a tube is plucked, the hydrodynamic coupling excites the neighbouring tubes to oscillate. Thus, the rapid amplitude decay of the plucked tube is due to transfer of kinetic energy to its neighbours rather than damping. A perforated plate was carefully attached to the free ends of the tubes in order to fix the neighbouring tubes (see Figure 3.11). In test series B, a fully flexible tube array was utilized. These experiments were specifically designed to determine the critical void fraction at which fluidelastic instability occurs for each one of the mass fluxes studied.

The gamma densitometer was calibrated at the beginning of each experiment. With the test section full of freon vapour, the averaged voltage produced by the scintillator was recorded at room temperature. After the voltage corresponding to the vapour phase was determined, the test section was filled with liquid freon and a new measurement was carried out. The effects of temperature change during the experiments were taken into account as described in the previous section. Flow regime also affects the accuracy of the single-beam gamma densitometer, mainly due to the change in the interface position respect to the beam. However, previous research has determined that in the worst case, the uncertainty of the gamma densitometer is less than 4% of the measurement (see Feenstra (2000)).

For both series, the mass flux was increased from 100 to 500 kg/m^{2}s in steps of 50 kg/m^{2}s. The objective was to observe the behaviour of the critical velocities in intermittent and dispersed flows. In Series B, an additional experiment with a mass flux of 77 kg/m^{2}s was carried out in order to increase the maximum critical void fraction observed.

3.5.1 General Procedure

In two-phase flow-induced vibration experiments, it has been shown that the two crucial parameters affecting the response of the tube are void fraction and mass flux. The traditional approach when doing experiments with air-water mixtures is to keep

Table 3.3. Summary of Test Series

	Series A	Series B
No of Flexible Tubes	1	10 (all)
Purpose	Damping	Fluidelastic Instability

the void fraction constant, while the mass flux is incremented via the volumetric flows of air and water. In this research, since we use a single-component two-phase freon flow, the mass flux is kept constant while the void fraction is increased by using the heating elements. This reduces the number of parameters that have to be adjusted (and controlled) between trials. The mass flux is first set by using speed control of the main pump and the readings from the orifice plates located downstream the pump. The void fraction or flow quality is then adjusted in the main heater control by using a rheostat. The scale of the rheostat goes from 0 to 100%, with the latter corresponding to approximately 46 kW. A digital powermeter with a resolution of 0.01 kW permitted the regulation of the power transferred by the heaters.

After increasing the heating power, the mass flux of cooling water had to be adjusted in order to keep the temperature and pressure of the test section constant during the experiment. This was done with the purpose of maintaining a constant density ratio between the liquid and vapour phases. The data acquisition started when the temperature measurements along the flow loop had been constant for about 10 minutes, indicating that a steady state condition had been achieved.

For both series of experiments, the variables recorded for each trial were:

- Temperature (at the points indicated in Figure 3.1), to verify the steady-state condition during the measurement
- Pressure (at the test section and upstream the main pump), to keep a constant density ratio between the liquid and gas phases in the test section.

- Pump speed and flow rate (measured at the orifice plates), to ensure that the mass flux was constant during the experiment
- Power transmitted by the heaters
- Flow rate of the cooling water, which was measured by two rotameters installed next to the condenser
- Averaged frequency spectrum in both the streamwise and transverse directions, captured by the HP dynamic analyzer.
- Void fraction, measured using the gamma densitometer.

The averaged frequency spectra and the void fraction measurements were carried out simultaneously. The scintillator was excited with 600 Volts by using a high voltage power source (Harshaw NV-25A). The number of counts was captured by a Tennelec Ratemeter (TC-527). A total of 300 averages of the void data were calculated from 10 samples acquired at 10 Hz. This choice of parameters was based on their proven reliability in previous studies that used the flow loop (see Feenstra (2000)).

In test series A, an additional measurement was performed. In order to capture the decay response of the monitored tube, the electromagnetic excitation device was utilized. The electromagnets were turned on for a period of 5 to 10 seconds, to ensure that the tube was vibrating at a constant amplitude. Then, the power was shut-off, and the tube decay response was captured by the strain gauges. This procedure was repeated three times and then the damping values were averaged to obtain a representative damping ratio for each value of heat flux (see next section). The frequency used to feed the electromagnets was the averaged tube natural frequency previously determined by the HP analyzer. The electromagnets were set-up to produce resonance in the lift direction, where fluidelastic instability generally occurs first. Hence, the damping measurements obtained in this research correspond to the direction transverse to the flow. The uncertainty analysis for all the measured quantities, damping and other fluidelastic parameters, is presented in Appendix C.

3.6 Analysis and Post-Processing of Data

In this section, it is shown how the variables measured during the experiments are converted into the parameters of interest in fluidelastic instability analysis. First, the dynamic response of the monitored tube will be examined, and, subsequently, the two-phase parameters will be determined from mass flux, temperature, pressure and void measurements.

3.6.1 Amplitude, Frequency and Damping

As mentioned above, the dynamic response of the monitored tube was captured by using two strain gauges, located at 90 degrees of each other. Although both the streamwise and transverse directions were recorded simultaneously using independent channels, only the frequency spectrum corresponding to the transverse direction was fully analyzed. The rationale behind this is that fluidelastic instability is generally expected to occur first in the lift direction, which indeed took place in all the experiments performed.

The frequency spectrum was acquired for a frequency range from 0 to 100 Hz, with a resolution of 0.25 Hz and averaged over 100 samples. The natural frequency was determined at the time of the measurement by visual observation of the spectra, and corroborated later using a MATLAB program. This program also determined the rms amplitude based on the integration of the frequency spectra for a preset range of frequency.

The averaged frequency spectra were also used to determine the damping ratio based on the half-power bandwidth method. This method assumes that the turbulent excitation due to the flow is broadband and random in the frequency range close to the natural frequency of the tube. Then, it can be considered that the frequency response of the tube is equivalent to the vibration response obtained from a frequency sweep. A FORTRAN program supplied by AECL was used to fit a curve to the frequency response by using a least-square regression technique. The program fits a frequency response of a single-degree of freedom system to the frequency data gathered during

the experiment, as shown in Figure 3.12. Initially, estimates of the damping ratio and the natural frequency are provided. The program then iterates to find the combination that will produce the best fitting to the experimental data. The value of the damping ratio at which the program converges is equivalent to that obtained by the half-power method. In this case, the damping ratio is a function of the width of the peak at an amplitude equal to $A_{max}/\sqrt{2}$, were A_{max} is the peak amplitude. For small damping ratios, we may write

$$\zeta = \frac{\Delta f}{2 f_n}, \tag{3.3}$$

where Δf is the frequency interval representing the width of the peak, and f_n is the natural frequency. The main disadvantage of this method is that, in two-phase flows, the continuous change in the average fluid density around the monitored tube produces a continually shifting frequency, artificially broadening the resulting response peak. This can potentially lead to an over-estimation of the damping ratio. The effect can be exacerbated by the varying added mass caused by different relative motion of a tube with its neighbours.

The damping ratio was also calculated based on the decay response of the monitored tube. The decay trace was captured three times for each void fraction studied by using the electromagnetic excitation device. During the testing stage of the electromagnets, it was determined that averaging the damping obtained from three decay traces was sufficient to produce a repeatable value. This was also verified with the full bundle installed during the experiments. The signal conditioner amplifier used in the experiments used capacitive coupling to eliminate the static component of the signal (DC offset). A MATLAB program was used to compute the damping ratio based on the decay trace. The program allowed the implementation of both the logarithmic decrement method, based on the magnitude of the peaks, and the fitting of an exponential function to the decay trace.

In this study, although the tube is forced to vibrate to about 10% of its diameter by the electromagnets, only the portion of the decay trace between 3% and 1% is

used for damping determination. By doing this, it is ensured that the response of interest is not so large that nonlinear effects are significant, and not so small that it is overwhelmed by the random turbulent excitation. The calculations were carried out varying the time interval slightly, in order to verify the independence of damping on the tube amplitude. For the implementation of the logarithmic decrement method, the decay response was divided in various sections, and the logarithmic decrement was computed for each one of them. The resulting values of damping ratio were averaged along the time interval considered (see Figure 3.13). For damping ratios below 4%, the damping ratio ζ can be approximated by

$$\zeta \approx \frac{\delta}{2\pi}, \quad \text{where} \quad \delta = \frac{1}{n} \ln \left(\frac{x_0}{x_n} \right). \tag{3.4}$$

In equation 3.4, n is the number of cycles between the peaks considered and x_0, x_n represent the peak amplitudes and δ is the logarithmic decrement.

The exponential fitting method simply fits an exponential function to the decay trace. This procedure produced a more consistent and reliable estimate of damping, especially when the void fraction fluctuations caused intense frequency shifting. In order to fit an exponential to the response, the program used the maxima of the peaks as shown in Figure 3.14. The function used was

$$y = Ae^{-Bt}, \quad \text{where} \quad B = \zeta \omega_n, \tag{3.5}$$

where ζ is the damping ratio and ω_n represents the circular natural frequency. The average and standard deviation of the three damping values were calculated for each void fraction.

The structural damping of the monitored tube was determined using the logarithmic decrement method. The monitored tube was manually plucked in air, while all the other tubes were held fixed to avoid any mechanical coupling, and the values cited are the average of 5 trials.

3.6.2 Properties of Freon-11

The thermodynamic properties of the R-11, as well as the viscosity of each phase, are determined by using a group of polynomial correlations developed by Feenstra (2000). The formulae were derived from least square fittings of the ASHRAE (1991) thermodynamic tables, for a temperature range of 20 to 60°C. Table 3.4 presents a summary of the correlations. The parameter T is the temperature based on the voltage reading from the thermocouples (EMF).

Table 3.4. R-11 property correlations

E Type Thermocouple	T[°C]	$= 0.82277+16.014\text{EMF}+0.10689\text{EMF}^2$
Liquid Viscosity	ν_l[μPa s]	$= 563.5 - 6.228T + 0.0262T^2$
Gas Viscosity	ν_g[μPa s]	$= 10.16 + 0.0356T$
Liquid Density	ρ_l[kg/m^3]	$= 1533.1 - 2.1962T - 0.003287T^2$
Gas Density	ρ_g[kg/m^3]	$= 2.8291 + 0.062313T + 0.0027383T^2$
Liquid Enthalpy	h_l[kJ/kg]	$= 199.92 + 0.87863T + 0.0003982T^2$
Vaporization Enthalpy	h_{lg}[kJ/kg]	$= 190.5 - 0.34876T - 0.00070376T^2$
Saturation Pressure	P_{sat}[MPa]	$= 0.048611 + 0.00087T + 5.689x10^{-5}T^2$
Surface Tension	σ[N/m]	$= 0.021 - 0.0001T$

3.6.3 Flow Parameters

This section provides an itemized description of the critical flow parameters that are needed to characterize the flow-induced vibrations.

3.6.3.1 Pitch Mass Flux

The pitch mass flux G_p is calculated based on the average velocity between the tube gaps and the density of the liquid freon, before circulating through the heaters section of the flow loop. It is determined as

$$G_p(kg/m^2s) = \frac{Q\ \rho_{l1}}{1000\ A}\left(\frac{P/D}{P/D-1}\right), \tag{3.6}$$

where Q is the total volumetric flow rate (L/s) of the freon measured by the orifice plates, ρ_{l1} is the density of liquid freon (kg/m^3) calculated at temperature T_1, right before circulating through the heaters (see Figure 3.1 and A is the upstream flow area of the test section (A=9.69 x10^{-3} m^2 in this research).

3.6.3.2 Enthalpy Increment

The energy gained by the two-phase freon as it flows through the heaters section can be calculated as

$$\Delta h = \frac{C_L \ q \ 1000}{\rho_{l1} \ Q}. \tag{3.7}$$

In equation 3.7, Δh is the enthalpy rise in kJ/kg, q is the heat transferred by the heaters (kW) and C_L is a correction coefficient that accounts for the heat lost due to convection to the room. The value of C_L was estimated to be 0.97 by Feenstra (2000).

3.6.3.3 Flow Quality

The thermodynamic quality was determined based on the temperature measurements along the flow loop. It represents the ratio of the vapour mass flux to the total mass flux of the mixture.

$$x = \frac{h_{l1} + \Delta h - h_{l2}}{h_{lg2}}. \tag{3.8}$$

The enthalpies h_{l1}, h_{l2} and h_{lg2} were calculated based on the correlations shown in Table 3.4 using the temperature measurements taken at the locations indicated in Figure 3.1.

3.6.3.4 Fluid Density based on the HEM

Assuming that the mixture is formed by fine bubbles well mixed with the liquid and there is no slip between the liquid and gas phases, the density of the two-phase

mixture can be estimated as:

$$\rho_H = \left(\frac{x}{\rho_{g2}} + \frac{1-x}{\rho_{l2}} \right)^{-1}. \tag{3.9}$$

3.6.3.5 Void Fraction based on the HEM

The volumetric ratio of the gas phase to the total volume of mixture can be determined by using the flow quality, the density ratio of the phases (measured upstream of the tube bundle) and assuming that the slip ratio is equal to unity.

$$\alpha_H = \left[1 + \frac{\rho_{g2}}{\rho_{l2}} \left(\frac{1}{x} - 1 \right) \right]. \tag{3.10}$$

3.6.3.6 Pitch Velocity based on the HEM

The averaged flow velocity in the gaps between the tubes can be estimated by using the mass flux, which is measured at the orifice plates, and the fluid density based on the Homogeneous Equilibrium Model.

$$V_p = \frac{Q \ \rho_{l1}}{1000 \ A \ \rho_H} \left(\frac{P/D}{P/D-1} \right) = \frac{G_p}{\rho_H}. \tag{3.11}$$

3.6.3.7 Separated Flow Quantities

In order to have a more realistic estimate of the flow density and other flow quantities, the void fraction was directly measured by using a gamma densitometer. The advantage of this method is that it takes into account the velocity ratio effects, caused by the density difference between the phases. The absolute velocities of the liquid and gas phases (U_l and U_g respectively) were also calculated by using the void fraction based on the Radiation Attenuation Determination (RAD).

RAD Void Fraction:

$$\alpha = \ln \left(\frac{N^*/N_l}{N_g/N_l} \right), \qquad \text{where} \qquad \mathrm{N}^* = \mathrm{N} \sqrt{\frac{\rho_{\mathrm{l}}}{\rho_{\mathrm{lc}}}}. \tag{3.12}$$

RAD Fluid Density (kg/m^3):

$$\rho_{RAD} = \alpha\rho_{g2} + (1-\alpha)\rho_{l2}. \tag{3.13}$$

Velocity of the Gas Phase (m/s):

$$U_g = \frac{x\ G_p}{\alpha\ \rho_{g2}}. \tag{3.14}$$

Velocity of the Liquid Phase (m/s):

$$U_l = \frac{(1-x)\ G_p}{(1-\alpha)\ \rho_{l2}}. \tag{3.15}$$

Velocity Ratio (Slip):

$$S = \frac{U_g}{U_l} = \left(\frac{1-\alpha}{\alpha}\right)\left(\frac{x}{1-x}\right)\left(\frac{\rho_{l2}}{\rho_{g2}}\right). \tag{3.16}$$

The Interfacial Velocity introduced in Chapter 2:

$$V_i = C_i(U_{gs} + U_{ls}) + \sqrt{gD_e(\rho_{l2} - \rho_{g2})/\rho_{l2}}, \tag{3.17}$$

where U_{ls} and U_{gs} are the superficial velocities of the liquid and gas phases respectively.

3.6.3.8 Other Dynamic Parameters

In addition to the previously described variables, there are some flow-induced vibration parameters that play an important role in the analysis of fluidelastic instability.

Hydrodynamic Mass:

$$m_h = m_t\left[\left(\frac{f_a}{f}\right)^2 - 1\right], \tag{3.18}$$

where m_t is the mass per unit length of the tube alone, f_a is the natural frequency of the tube in air and f is the in-flow frequency.

Total Mass per unit Length (Tube + Hydrodynamic Mass):

$$m = m_t \left(\frac{f_a}{f} \right)^2 . \tag{3.19}$$

Hydrodynamic Mass ratio:

$$m_R = \frac{m_h}{m_l} = \frac{(f_a/f)^2 - 1}{(f_a/f_l)^2 - 1}, \tag{3.20}$$

where m_l is the hydrodynamic mass in liquid flow and f_l is the tube natural frequency in liquid. The hydrodynamic mass ratio is assumed to be 1 in liquid flows, and 0 in gas flows.

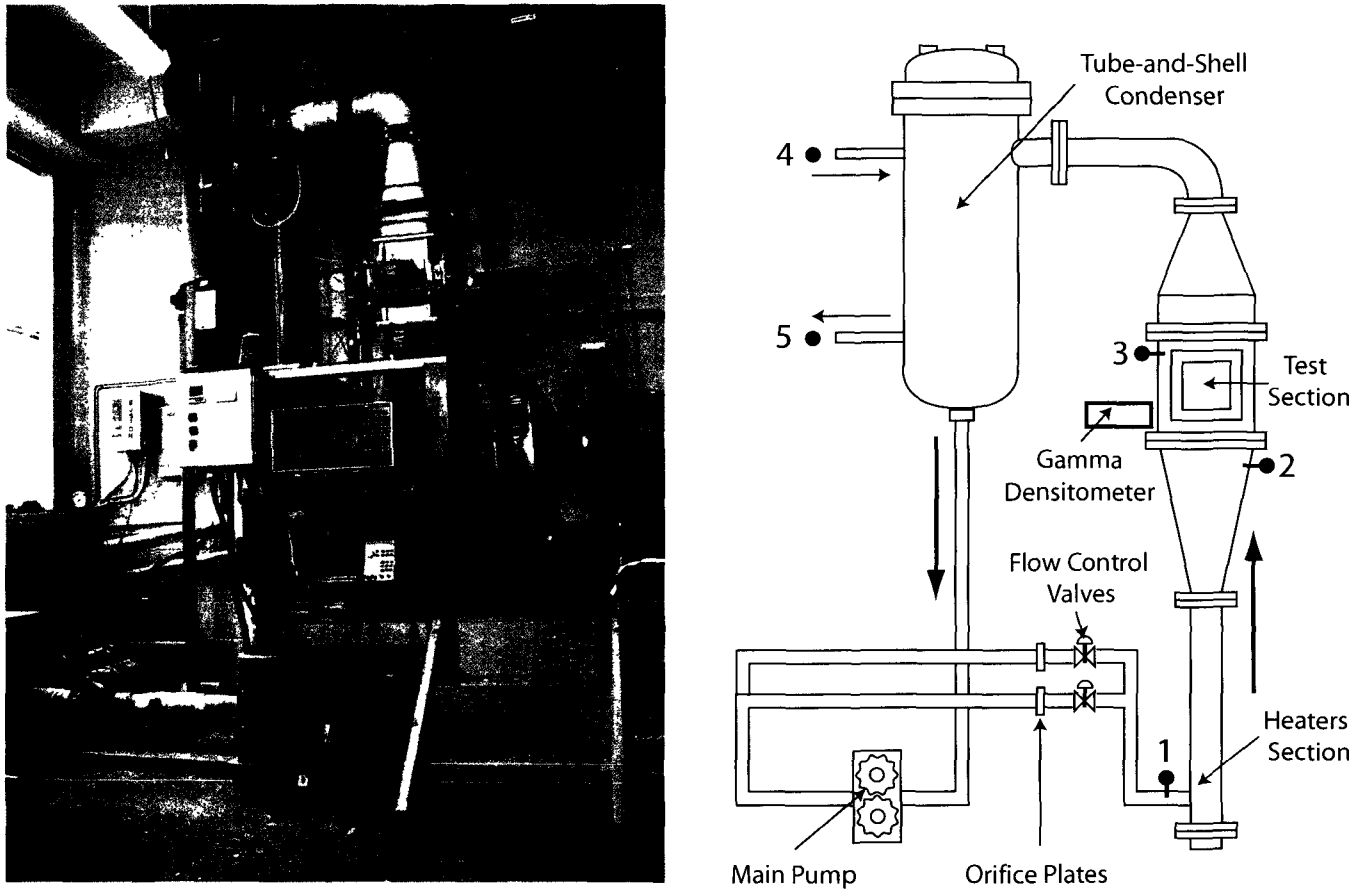

Figure 3.1. Picture and schematic diagram of the Two-phase flow loop located in McMaster University. The black circles indicate the number and location of the thermocouples.

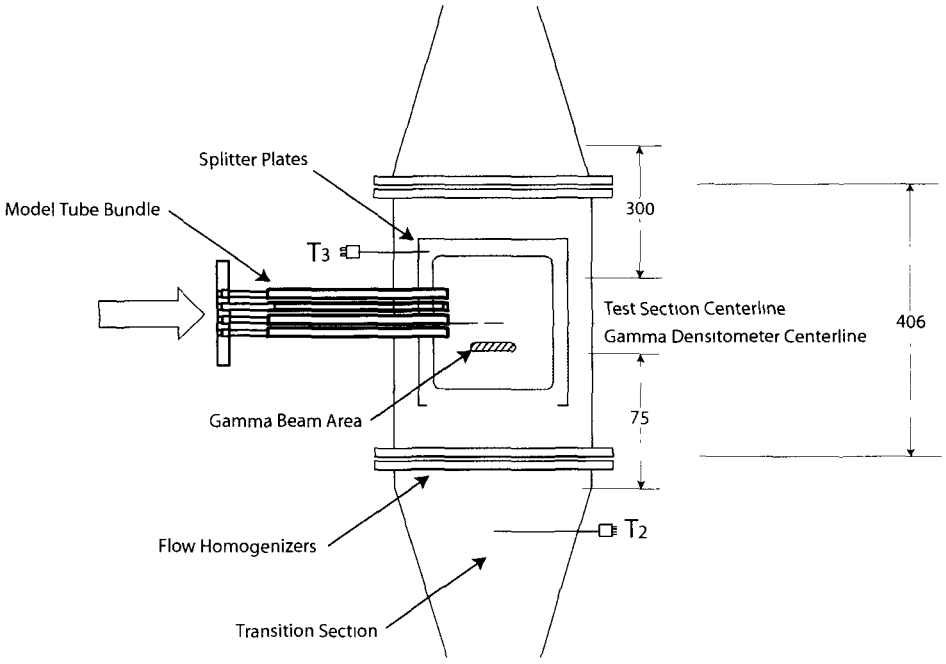

Figure 3.2. Schematic diagram of the test section (sideview), showing the location of the model tube bundle, flow homogenizers and splitter plates. The indicated dimensions are in mm. The thermocouples T_2 and T_3 are also shown. Adapted from Feenstra (2000).

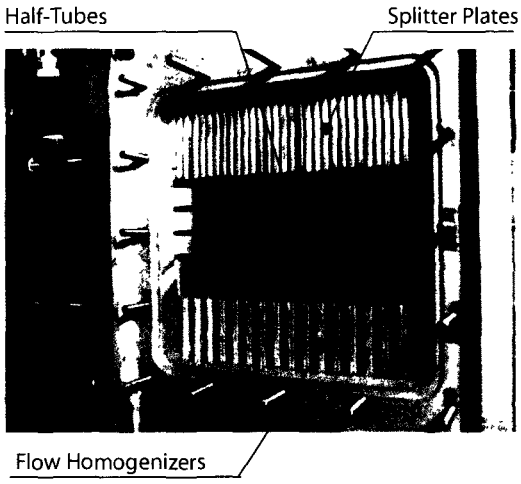

Figure 3.3. Picture of the test section showing the half-tubes attached to the wall, the flow homogenizers and splitter plates.

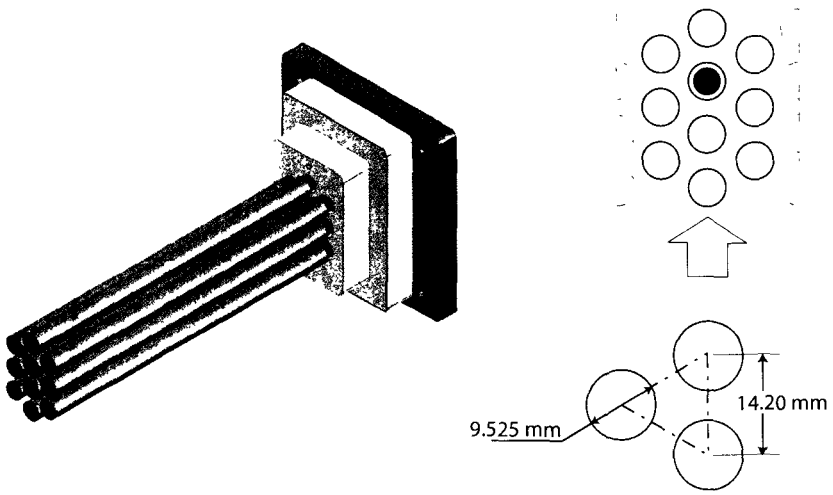

∴

Figure 3.4. A 3-D model of the tube array designed and built for this study. On the right side, a sketch of the installed bundle showing the half-tubes attached to the walls, the monitored tube and the flow direction.

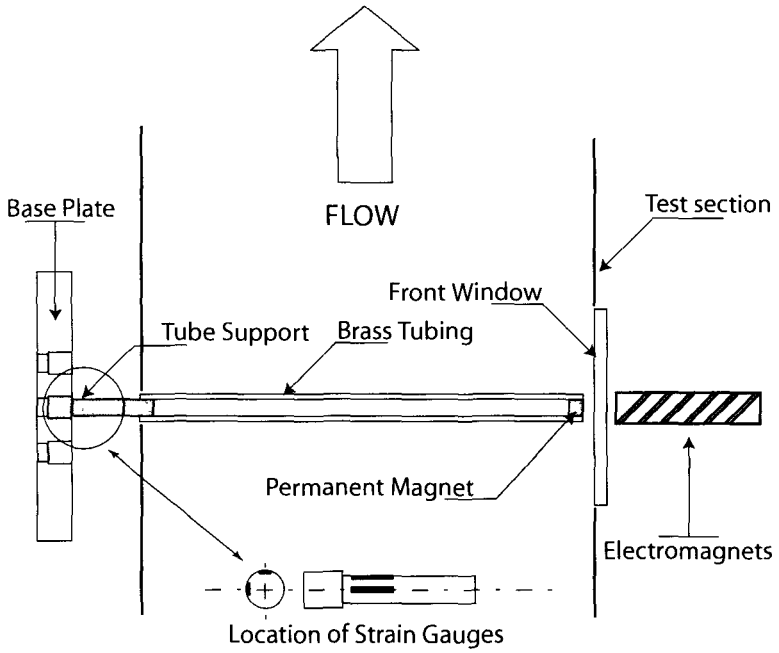

Figure 3.5. Side-view of the test section, showing a schematic diagram of the model tube bundle, the location of the strain gauges and the electromagnets.

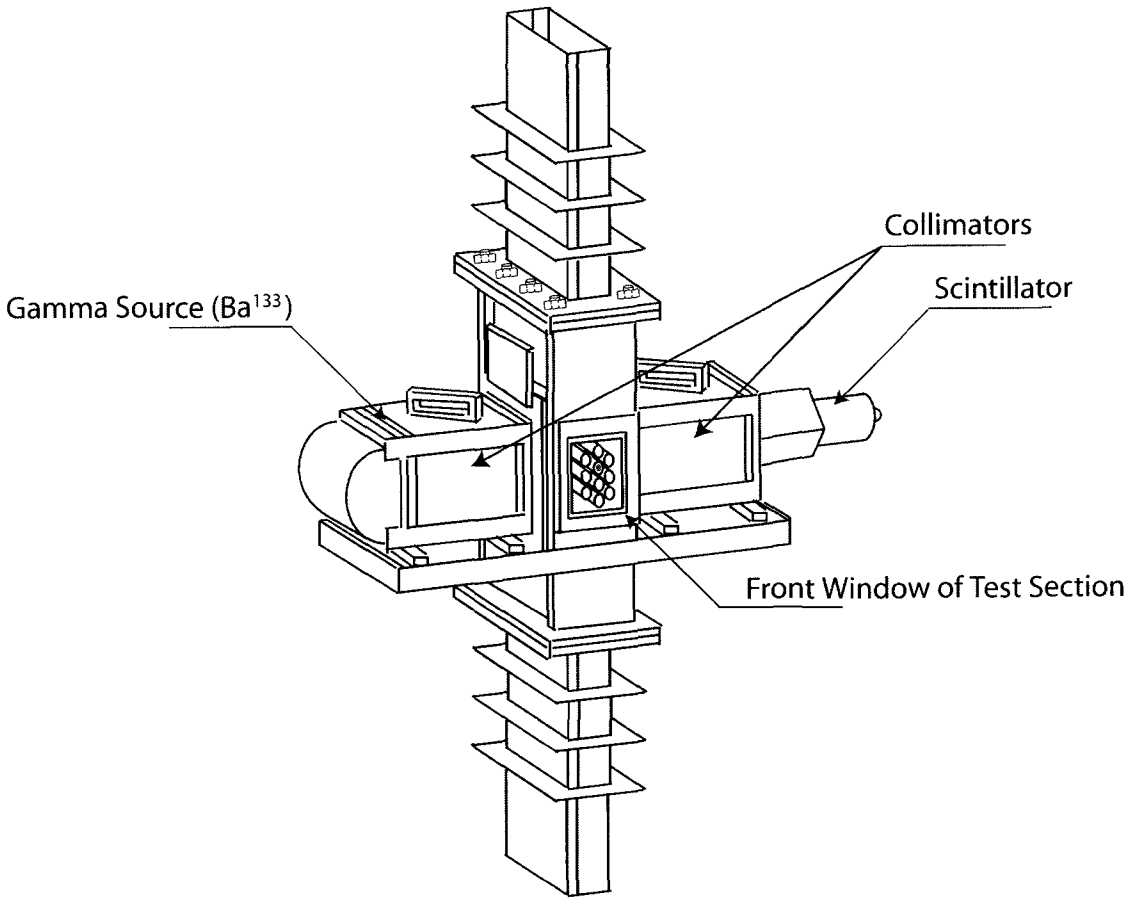

Figure 3.6. Set-up of the single-beam gamma densitometer on the test section. Adapted from Azzam (2004).

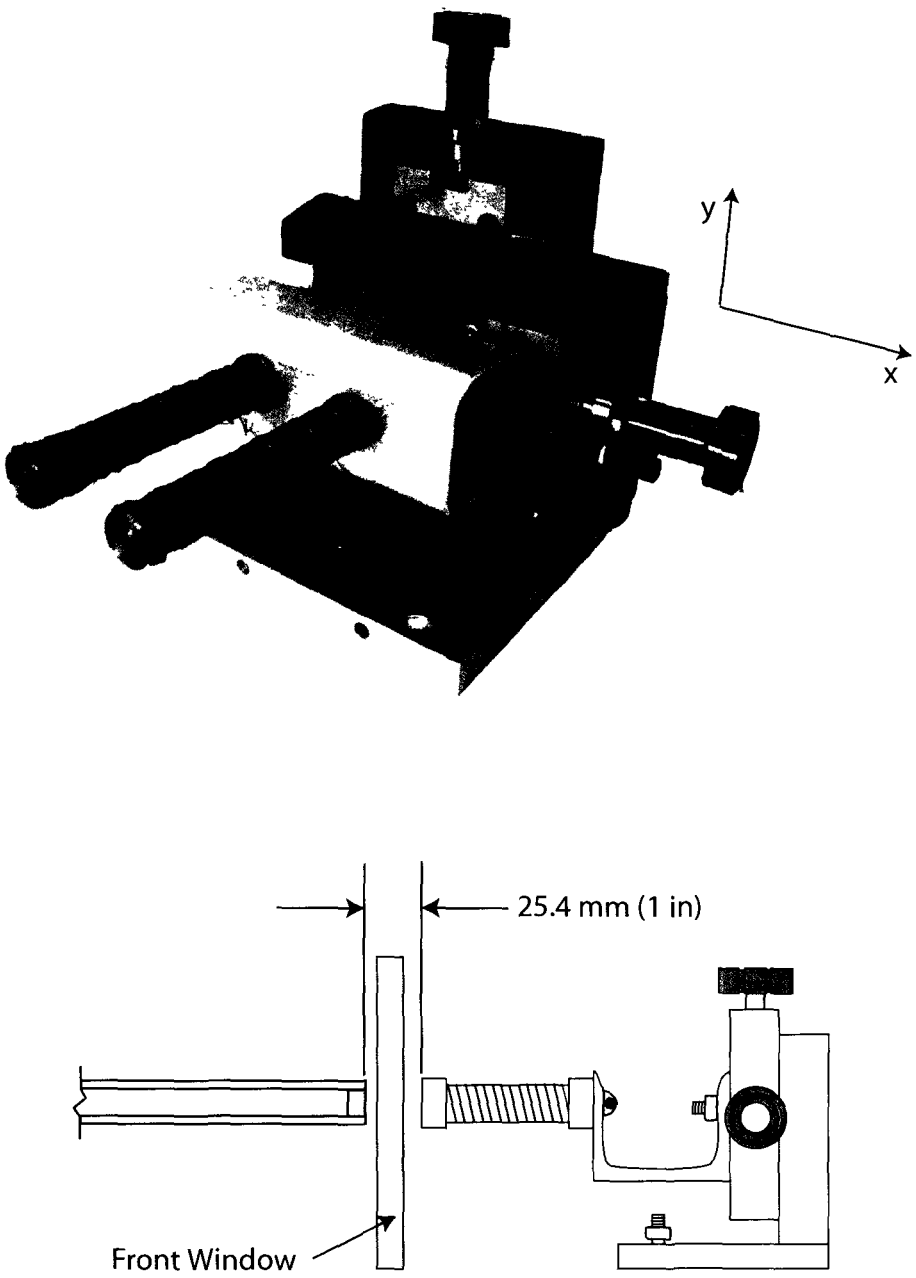

Figure 3.7. Electromagnetic device designed and built for this research. The coils are mounted on a special base that allows motion in the x and y directions, a plane orthogonal to the tube axis.

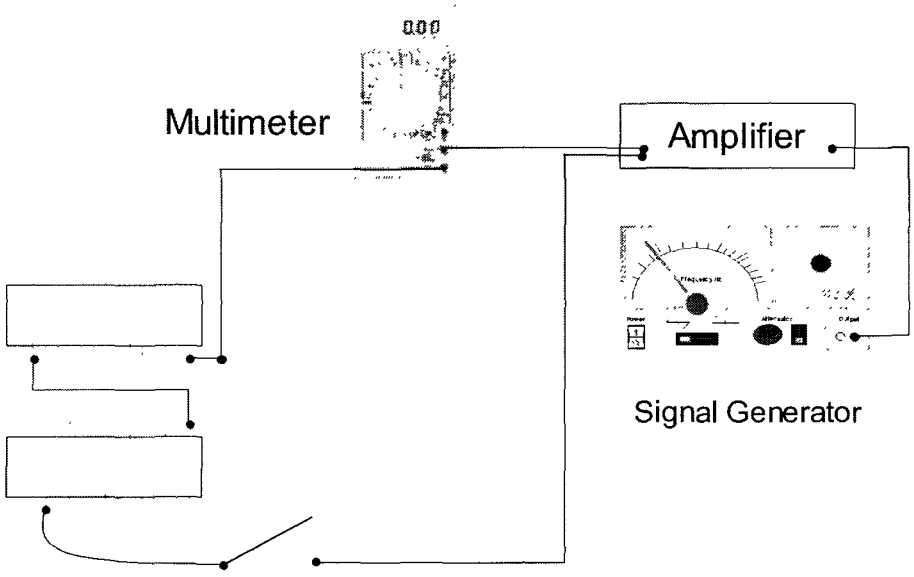

Figure 3.8. Diagram of the equipment required to excite the electromagnets at variable frequency.

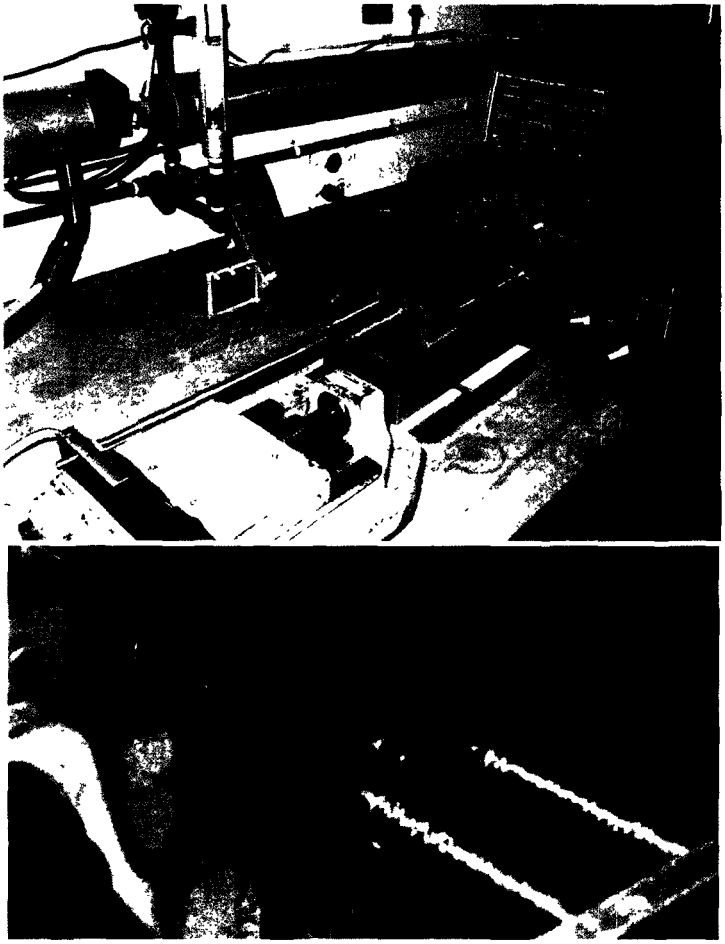

Figure 3.9. Single-tube testing set-up for the electromagnets.

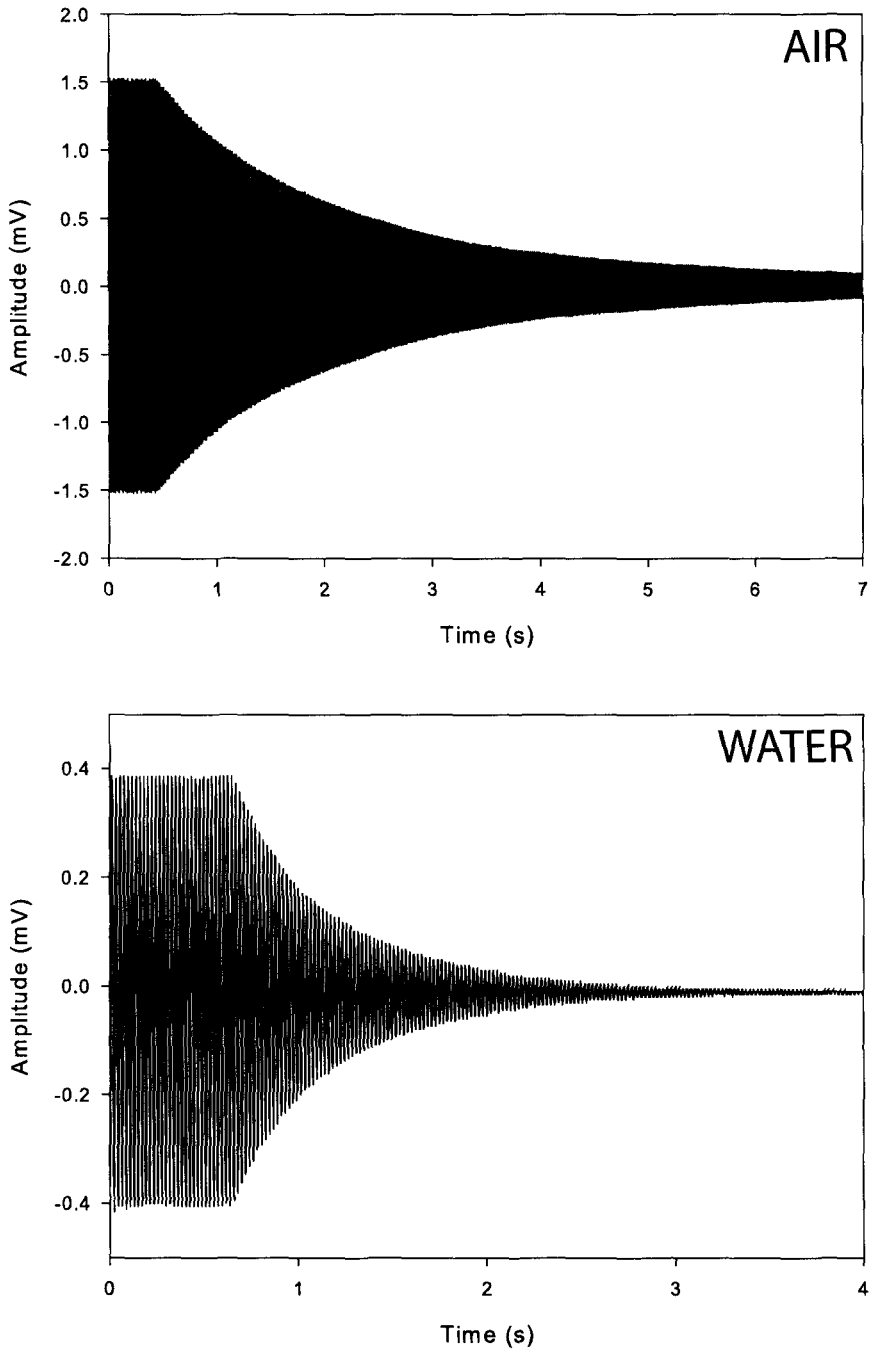

Figure 3.10. Decay response for the single-tube set-up in air and water. Note the constant amplitude oscillation produced by the electromagnets before they are shut-off.

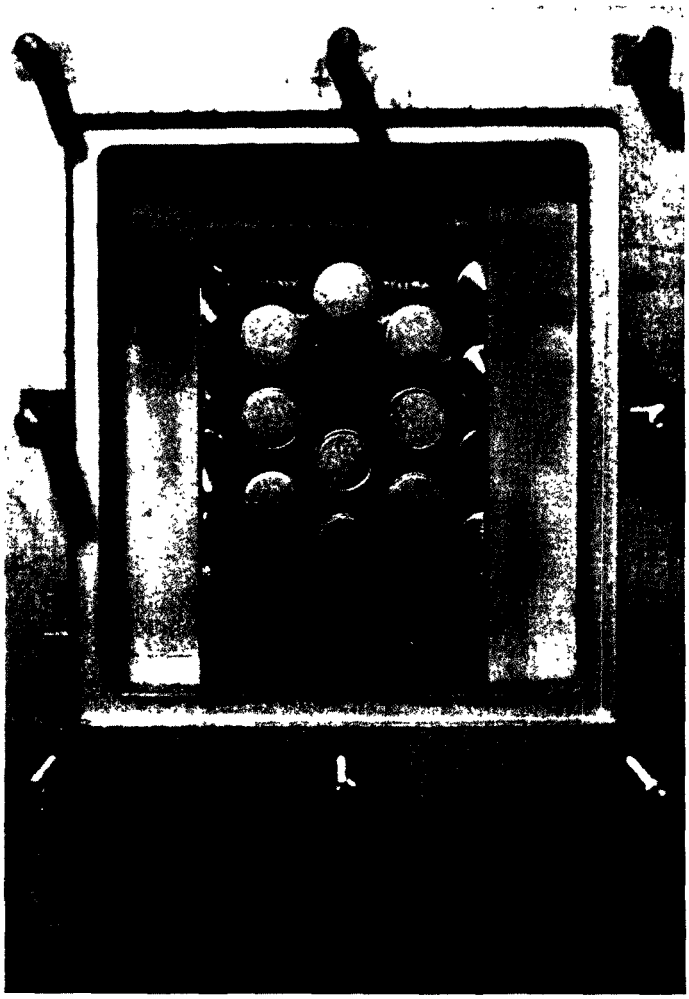

Figure 3.11. View of the model tube bundle with the perforated plate installed (single-flexible tube bundle). The front window of the test section has been removed. The half-tubes attached to the walls, the flow homogenizers (below the bundle) and splitter plates (above the bundle) are shown.

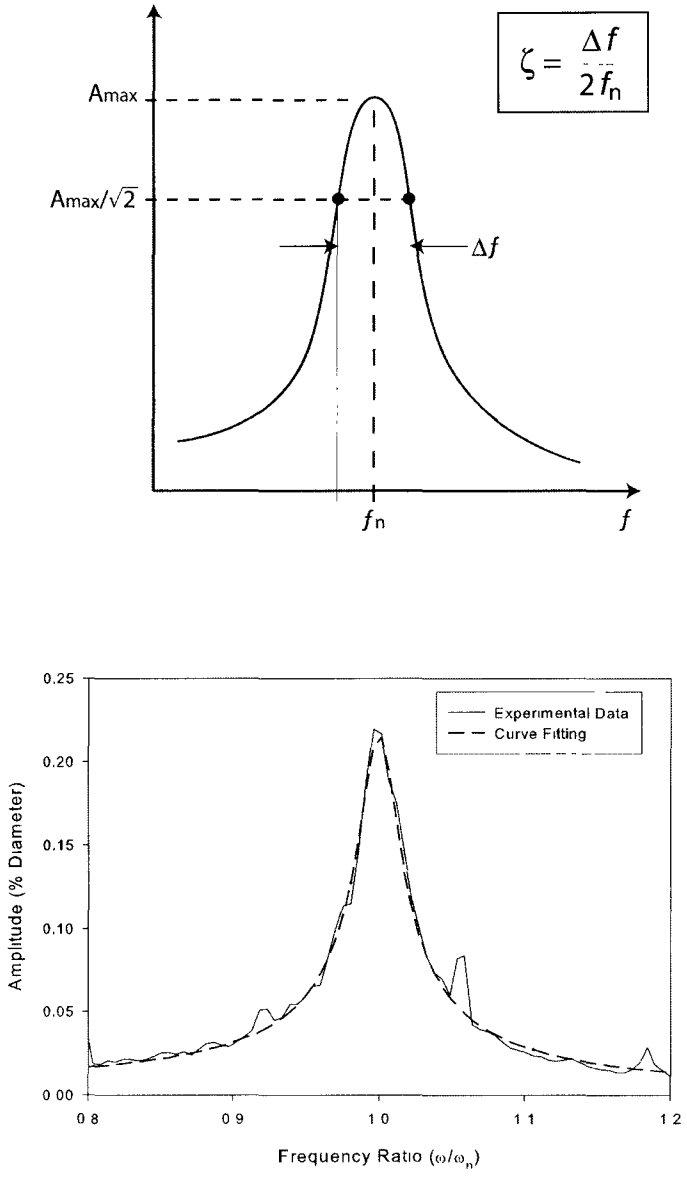

Figure 3.12. Half-power bandwidth method for calculating the damping ratio. The upper graph shows the theoretical concept of this procedure, based on the width of the peak at a certain amplitude. The plot on the bottom shows the fitting performed on actual data recorded during this research.

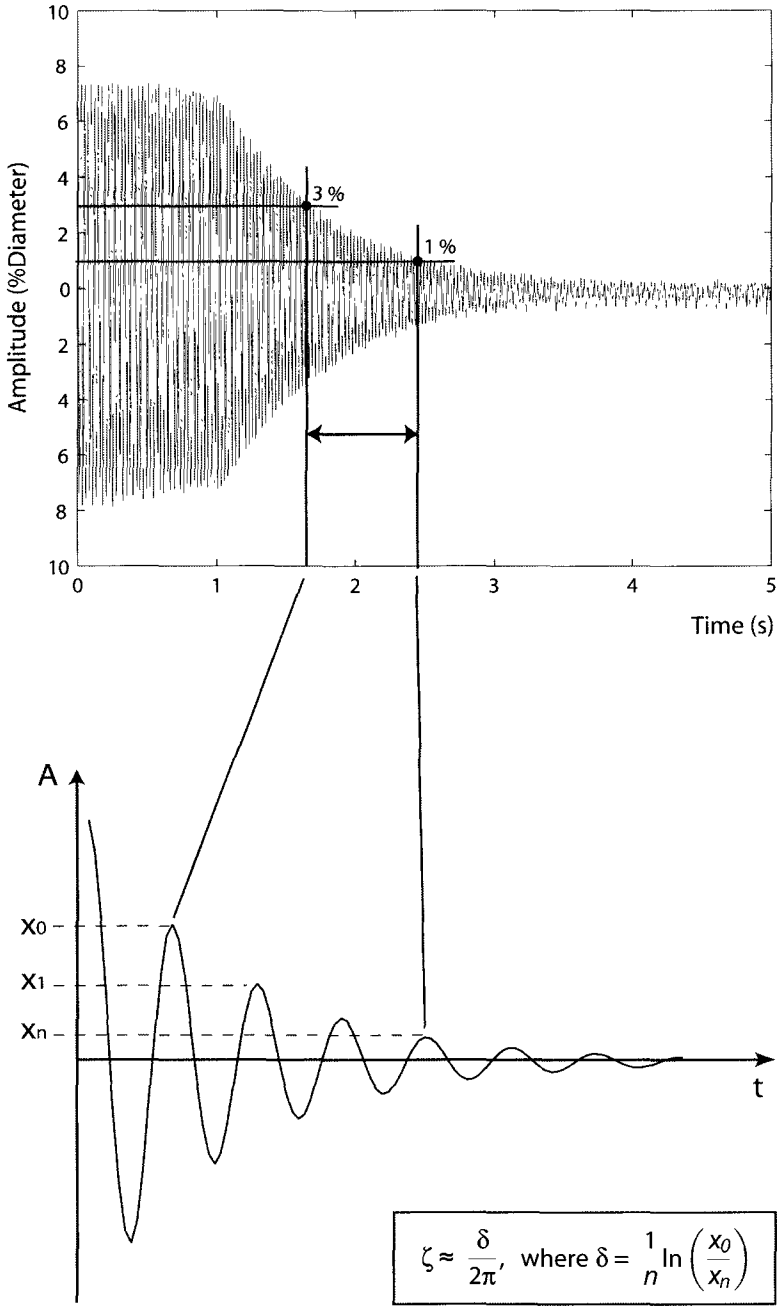

Figure 3.13. Procedure for the application of the logarithmic decrement method. The time interval was taken from 1 to 3% of the tube diameter (top). Then, the magnitudes of the peaks are used for determining the damping ratio (bottom).

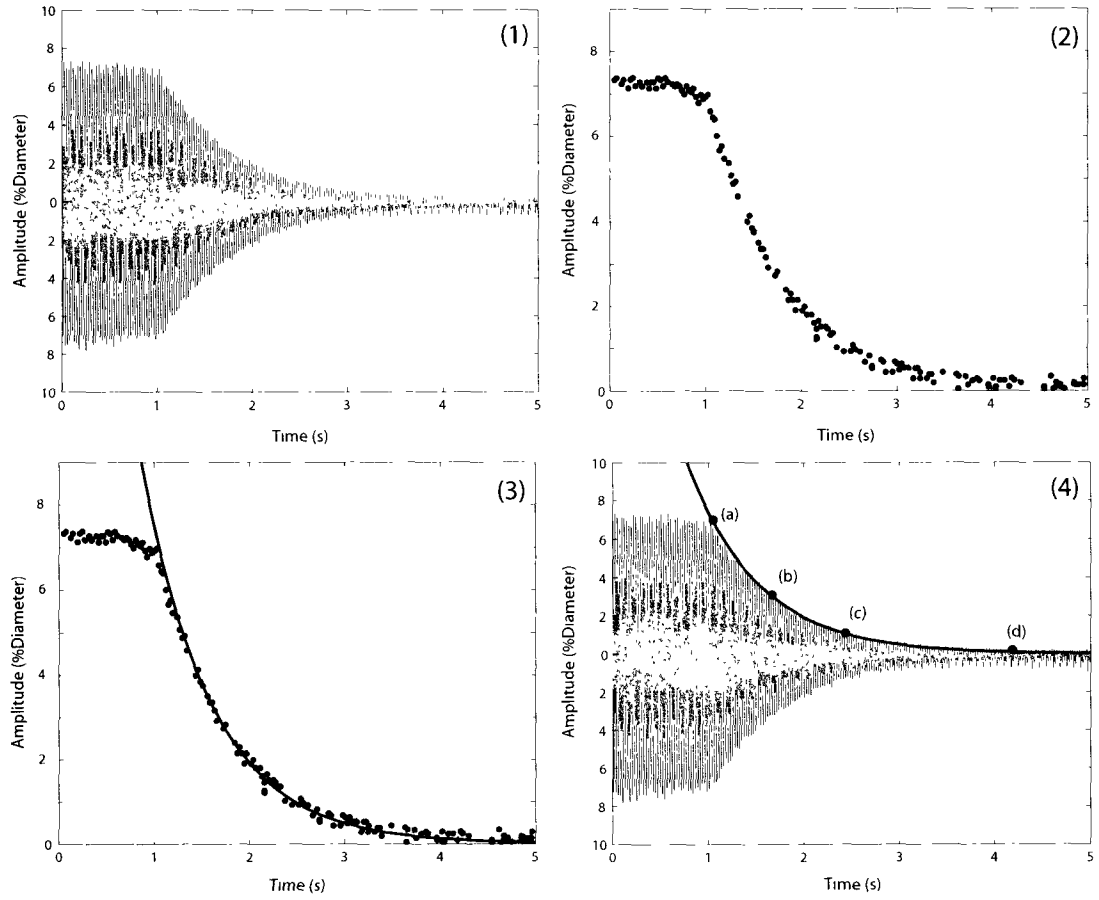

Figure 3.14. Procedure to fit an exponential to the decay trace. (1) Raw signal. (2) The maxima of the peaks have been separated for the upper part of the decay response. (3) An exponential is fitted to the maxima. (4) Final result, showing the points where the electromagnets were shut-off (a), the interval used for the fitting (b) to (c). The turbulent excitation has become significant before point (d).

CHAPTER 4

Two-Phase Flow and Damping: Results and Analysis

This chapter presents the two-phase flow and damping results and analysis obtained from test series A. The averaged tube frequency response spectra are first used to calculate the damping ratio based on the half-power bandwidth method, in order to establish a datum for comparing the present results against previously published data. Damping is then determined based on the decay response of the monitored tube, by employing the logarithmic decrement method and an exponential fitting to the decay response. The results from the three different damping measurement methods are then compared.

A dimensional analysis is carried out with the objective of identifying a relationship between damping and the fluid and flow properties. Using the results of the new measurement methodology, the effect of mass flux on damping is also explored. Finally, the dependence of damping on flow regime is examined by normalizing the two-phase component.

4.1 Two-Phase Flow Results

Due to the modifications performed on the flow-loop, the maximum void fraction measured with the gamma densitometer was about 90% for the lower mass fluxes (100 to 200 kg/m^{2}s), much higher than for previous research using the same flow-loop (Feenstra, 2000). These high-void experiments allowed the visualization of the three two-phase flow regimes: bubbly, intermittent and dispersed. This is very relevant, because it means that both damping and fluidelastic instability measurements have been obtained in every flow regime. The identification of the flow regimes was carried out by visual observation, and corroborated against the predictions of the flow regime maps introduced in Chapter 2. The experiments were carried out by setting the mass flux and heaters to obtain a certain void fraction. After establishing steady-state conditions, measurements were made of temperature, pressure and RAD void fraction. The frequency spectra, rms tube amplitude and three damping measurements based on the tube decay trace were also recorded. For each mass flux studied, the heat transfer to the fluid was increased to increase the void fraction and the whole process repeated until instability was reached.

The superficial velocities of the liquid and gas phases were calculated based on the RAD density by using Equations 2.20, and plotted on the maps proposed by Ulbrich and Mewes (1994) and Noghrehkar et al. (1999), as shown in Figures 4.1 and 4.2. In both figures, it is clear that the two-phase data spans across the three flow regimes. There are, however, some important differences. The Ulbrich and Mewes (1994) map shows that for all the mass fluxes studied the bubbly and intermittent flow regimes were present. The dispersed flow regime existed only for the experiments with mass fluxes equal to 100, and 150 kg/m^{2}s, although according to the observations carried out at 250 kg/m^{2}s dispersed flow was also exhibited. It should be noted that the Ulbrich and Mewes map was developed using air-water mixtures flowing across an in-line array. Regarding the transition from bubbly to intermittent flow, the Ulbrich and Mewes map and the visual observation agreed very well, especially for mass fluxes below 400 kg/m^{2}s (see Table 4.1). Interestingly, the transition void fraction between

bubbly and intermittent flow is generally around 40 to 60 %. For internal pipe flows, this transition usually occurs around 30% of void fraction, due to the inevitable interaction between the bubbles. The present experimental observations agree with those of Dowlati et al. (1992) and Noghrehkar et al. (1999), which suggests that the presence of the tube bundle creates a more efficient source for bubble breakup.

As discussed above, the transition between intermittent and dispersed flows was visually observed for only 4 out of the 9 experiments performed in test series A. Table 4.2 shows the transitional void fractions in this case. The mass fluxes above 300 kg/m^2s are not included in the table because dispersed flow was not observed during those experiments. The difference between the prediction of the Ulbrich and Mewes map and the visual observations are more pronounced in this case but the agreement still reasonably good. For the present results, Figure 4.1 shows that the liquid superficial velocity remains fairly constant for the experiments with mass fluxes over 250 kg/m^2s, while there is some change in this parameter for the experiments where dispersed flow was observed. This phenomenon is probably related to an increase in the slip ratio and the existence of flooding or down-wash of the liquid phase, which occur near the transition between intermittent and dispersed flows.

Concerning the flow regime map of Noghrehkar et al. (1999), the transition between bubbly and intermittent flows is similar to that suggested by Ulbrich and Mewes (1994), although the flow turns to intermittent earlier for the experiments with mass fluxes above 350 kg/m^2s. Noghrehkar et al. (1999) also suggests that the transition to dispersed flow starts at a gas superficial velocity of 3 m/s, much lower than the range 4 to 10 m/s suggested by the Ulbrich and Mewes (1994) flow regime map. This means that the dispersed flow regime was supposed to be observed in all the experiments. In the present study, dispersed flow was observed in only four of the nine mass fluxes investigated. It was decided that the results of Ulbrich and Mewes (1994) agreed better with the visual observations carried out during the present experiments. Therefore, it will be used as a reference in the following sections.

4.2 Damping Results

At each of the mass fluxes and void fractions represented by data points in the previous section, tube response frequency spectra and amplitude decay traces were obtained for estimating the damping using each of the three techniques described in Chapter 3 (see experimental results presented in Appendix E). In this research, the approach proposed by Baj and de Langre (2003) has been taken, i.e. the total damping ratio is considered to be the sum of only a structural component and a two-phase term,

$$\zeta_T = \zeta_s + \zeta_{tp}. \tag{4.1}$$

In equation 4.1, ζ_{tp} includes all the two-phase flow contributions: interfacial, viscous, and velocity dependent. The author agrees with Baj and de Langre (2003) that the fluid component of damping should include all the effects related to the particular flow characteristics (as in single-phase flow). This assumes that the fluidelastic instability is essentially the same phenomenon in single and two-phase flows, the primary difference being the way in which the determining parameters are scaled (de Langre, 2006). As pointed out in Chapter 2, the damping in two-phase flows is strongly dependent on void fraction. Figure 4.3 shows the total measured damping ratio, ζ_{tp}, versus the RAD void fraction for six of the nine mass fluxes studied. The values of damping used in these figures are based on the exponential fitting to the decay trace, and each data point corresponds to an average of the three traces collected for each value of the void fraction. The general behaviour of damping is similar to that exhibited in single-phase flows (see Figure 2.11). The damping ratio tends towards the value in-stagnant liquid when the void fraction approaches zero, increases with void fraction to reach a maximum and finally approaches zero as fluidelastic instability occurs. This behaviour is due to two effects taking place at the same time: the flow velocity increases the fluid component of damping, and the fluidelastic forces start diminishing the total damping present in the system (see Figure 2.12)). As the mass flux increases, the void fraction corresponding to the maximum damping

varies somewhat. The mechanism of energy dissipation is related to the flow regime attained by the two-phase mixture, and flow regime transition is a function of mass flux. Figure 4.3 also indicates the flow regimes observed for each experiment. The maximum damping ratio seems to occur close to the flow regime transition from bubbly to intermittent. A similar observation has been made by Anscutter et al. (2006) in internal two-phase vertical-upwards flow in pipes.

4.3 Datum Measurement of Damping using the Half-Power Method

A new method for measuring damping in two-phase flows was pursued in this research because it was thought that the traditional half-power bandwidth approach could have significant errors due to frequency variability during the period of data capturing. In order to establish a datum for comparison of results from the new methodology, as well as compare the present results using the half-power bandwidth with existing data, the half-power damping results obtained in this research were computed and normalized as described in Chapter 2, equations 2.9 to 2.11. The resultant normalized two-phase damping was compared against data previously presented by Axisa et al. (1988), Pettigrew et al. (1989a), Pettigrew et al. (1995) and Feenstra (2000). Figure 4.4 shows the relationship between the normalized two-phase damping ratio and the void fraction based on the Homogeneous Equilibrium Model. The continuous line represents the design guideline suggested by Pettigrew and Taylor (2004). The data points corresponding to this research are located on the high HEM void region ($\alpha_H > 40\%$). Noting the significant scatter in the existing data, the results obtained in this study generally agree well with those presented by previous researchers.

In Figure 4.4, there are two low data points at an HEM void fraction of about 0.5 that do not follow the expected trend. These points correspond to the experiments where the pitch mass flux was the lowest, between 100 and 150 kg/m^{2}s, and the

RAD void fraction measured for these points was less than 10%. This deviation from the expected trend is probably due to two factors. Firstly, the HEM over-predicts the void fraction, shifting the data to the right. This effect is more pronounced for low void fractions, as seen in Figure 4.5, where the HEM and RAD void fractions are plotted as a function of the HEM pitch velocity (used here for scale purposes). It can be seen that at the lowest velocities, the HEM void fraction predictions are up to 10 times larger than the gamma densitometer measurements. As the flow velocity increases, the two methods get closer to each other, with the HEM about 20% above the RAD void fraction at the highest measured HEM flow velocity. The HEM substantially over-predicts the void fraction over the entire pitch velocity range of the present experiments. The second possible explanation for those outlying data points is that the void fraction is a function of the thermodynamic quality, which has a considerable uncertainty for low mass-flux experiments. It is important to note that the values of damping plotted on this diagram by previous researchers are those used for fluidelastic analysis, that is, taken at half the critical mass flux. In this particular figure, all the damping values obtained during the present experiments have been plotted, and the agreement is still very good.

4.4 Comparison between the Damping Measurement Methods

Figure 4.6 shows a comparison between the results obtained using the exponential fitting to the decay response and the logarithmic decrement methods, for a pitch mass flux equal to 250 kg/m^{2}s. The data represent the average value of damping based on the three traces recorded for each void fraction (see Section 3.6.1, Chapter 3). It is observed that the logarithmic decrement method results have significant scatter, and do not indicate a clear trend over the range of RAD void fraction investigated. The logarithmic decrement approach is clearly too sensitive to the vibration amplitude peak-values used in the calculations, even when averaging is used. However, the

results based on the exponential curve fitting to the decay response are more consistent, not only over the void fraction range, but also between the three measurements performed for each value of void fraction. Apparently, the shifting frequencies caused by variation in fluid added mass and irregular response due to turbulent two-phase flow excitation make the logarithmic decrement approach rather unreliable for this application. These effects are minimized in the case of the exponential fitting method because of the smoothing obtained by fitting the decay curve instead of using the individual amplitude peaks. The differences between the two methods described above were observed for all the experiments over the range of mass fluxes studied. Based on this result, it was decided to use the exponential curve fitted damping results for comparison with the half-power bandwidth method in the discussion below.

Figures 4.7 and 4.8 show the damping measurements obtained using the half-power and exponential decay methods, plotted against the HEM and RAD void fractions respectively. The vertical dashed lines indicate transitions of flow regime based on the predictions of Ulbrich and Mewes (1994), as discussed in section 4.1. In both figures, the results based on the half-power bandwidth method are consistently higher than those from the exponential decay method. The void fraction model used makes an important difference concerning the location of the flow regime transition. In Figure 4.7, the flow regime changes occur at high HEM void fractions, and are relatively close to each other. However, as seen in Figure 4.8, the flow regime zones are actually more spread out, enduring over a larger range of void fraction. The trends observed in Figures 4.7 and 4.6 were detected in all of the mass fluxes studied.

The differences in damping values obtained between the half-power and the exponential fitting methods is the greatest in the bubbly flow regime, and reduce as the flow moves into the intermittent and dispersed flow regimes. The effect of varying void distribution on fluid added mass, and therefore on tube natural frequency, reduces as the void fraction increases. Figure 4.9 shows error bars on the exponential fitting results, representing the standard deviation of the three measurements performed for each void fraction. No error bars are shown for the half-power results

because only one averaged spectrum was captured for each void fraction. It can be seen that for bubbly flows, the difference between the methods is much larger than the range defined by standard deviation. During the transition from bubbly to intermittent flow, the standard deviation of the damping data remains substantial due to the temporal and spatial unsteadiness exhibited by the flow. It seems that the half-power bandwidth method is more sensitive to the effects of frequency shifting at lower void fractions than the exponential decay curve fitting approach. This explains why the former method gives much larger values of damping at lower void fraction than the latter method, and why the difference in results between the two methods reduces with increasing void fraction. Interestingly, the effects of intermittent flow on damping measurements appear to be less important than those of variations in fluid added mass. For higher void fractions, the standard deviation of the exponential fitting results diminish. Above a void fraction of about 0.6, the damping values obtained by the two methodologies are relatively close but the half-power values still consistently higher than those obtained by the exponential fitting method. This agrees with the results reported by Janzen et al. (2005) and Chandler (2005).

4.5 Frequency Shifting Phenomenon

It was proposed that the change in added mass around the monitored tube produces a shifting frequency and that this phenomenon may artificially broaden the averaged peak observed in the tube frequency response spectrum, leading to unreliable damping results. This effect can be quantified using equation 4.2

$$\omega_n = \sqrt{\frac{k}{m_s + m_a}}, \tag{4.2}$$

where ω_n is the natural frequency of the tube, k is the stiffness, m_s represents the mass per unit length of the tube and m_a is the hydrodynamic mass or fluid added mass. The sum of m_s and m_a is the total mass that has inertial effect on

the dynamics of the tube. If the tube is surrounded by vapour or air, the effect of m_a is negligible, and the total mass approaches that of the tube alone. When the tube is surrounded by liquid, the total mass is larger, contributing to a decrease in natural frequency. For an isolated cylinder, the added mass has a unique value and the cylinder's natural frequency is well defined. For a cylinder in a closely space group of cylinders, there are multiple values of the added mass depending on the relative motions of the various cylinders in the group. Thus, the cylinders exhibit a cluster of closely spaced natural frequencies with the cylinders' motion being hydrodynamically coupled to its neighbours'.

In two-phase flow problems, the unsteadiness of the flow will contribute to changing the amount of liquid and gas that is in contact with the tube at a given time, thus, exacerbating the fluctuations in added mass. The frequency of the tube will then fluctuate around a mean value, which is determined through an averaging process during a certain period of time. The distribution of the phases around the tube is related to the flow regime and void fraction. As the void fraction increases, the added mass effect reduces. Figure 4.10 shows the relationship between the void fraction and the hydrodynamic mass ratio (m_R) for both the HEM and RAD void estimations. The quantity m_R is equal to the ratio between the actual added mass and the added mass of a tube surrounded by liquid, as discussed in Chapter 2. The continuous line represents the theoretical hydrodynamic mass ratio, which is the lineal mass of fluid displaced by the tube and corrected for confinement of the nearest tubes. It can be calculated as:

$$m_{R,theor.} = \frac{[(D_e/D)^2 + 1]}{[(D_e/D)^2 - 1]} \left(\frac{\pi \rho D^2}{4} \right), \tag{4.3}$$

Since the HEM over-predicts the void fraction, the results based on this model are shifted to the right hand side of the figure, the same effect observed in Figure 2.15. On the other hand, the more realistic RAD void measurements show that the real values of added mass are lower than expected, and tend to level off at void fractions larger than about 75%. The hydrodynamic mass ratio must approach zero when the

void fraction is equal to unity. The choice of HEM or RAD does not directly affect the calculation of the fluid added mass, since the latter is based on the ratio of the in-flow tube natural frequency to the natural frequency in liquid. To explain the small change in m_R for high voids, it has been postulated that a vapour film is formed around the tube and the effective fluid added mass becomes insensitive to further increases in void fraction. The present experimental rig does not permit RAD void fractions above 90% (equivalent to a HEM void fraction of about 99%).

If the fluid added mass remains constant, there is no frequency shifting. For lower void fractions, where the hydrodynamic mass ratio is significant, the shifting is very pronounced. Having observed this behaviour, a new experiment was devised and carried out in order to demonstrate that the large difference in the damping values obtained from the different measurement methodologies was caused by frequency shifting. Instead of performing a long-time averaging process to estimate the natural frequency (3 minutes, 100 averages), a series of short one-average samples was recorded (4 seconds per average). To be able to verify the repeatability of this results, two independent experiments were performed using this methodology, taking 100 and 200 samples respectively in each experiment. Four void fractions were studied, corresponding to the bubbly, transitional (bubbly-intermittent), intermittent and dispersed flow regimes. The frequency distributions corresponding to each experiment are shown in Figures 4.11 and 4.12 in the form of histograms. Both figures show the number of counts at a specific frequency plotted over the natural frequency bandwidth in Hz. In Figure 4.11, it is seen that the mean tube natural frequency increases from 45.5 Hz to 47.8 Hz as the void fraction increases, which is expected since added mass reduces with increasing void fraction. Interestingly, the standard deviation of the frequency results reduces as the flow goes from bubbly to dispersed. For void fractions of 26 and 41%, which correspond to the bubbly flow regime, the standard deviation is similar (0.67 Hz), and much higher than for intermittent flow (void fraction of 58%, $\sigma = 0.40$) or dispersed flow (74%, 0.23). It is clear that as the void fraction increases, the frequency shifting phenomenon reduces its intensity,

going from about ±2.0 Hz in bubbly flow to ±0.5 Hz in dispersed flow (4.40% to 1.01% of the corresponding natural frequencies respectively). In Figure 4.12, which provides the histogram for 200 samples, the same trends are observed. The values of the mean natural frequencies are a little different due to the slightly different void fractions used. The standard deviation for each flow regime also agree well with the results of the previous experiment using 100 samples.

The results of the experiments show clearly that, at low void fractions, significant frequency shifting occurs. Thus, the frequency response curve fitted to long time averaged spectra will exhibit an artificially widened half-power bandwidth and, therefore, an exaggerated measure of the damping. The exponential decay fitting approach does not suffer this deficiency and therefore provides a more accurate measure of damping at low void fractions. At higher void fractions, the frequency shifting reduces and the results from the two methods become similar. Note that even after the flow has departed from the bubbly regime, the half-power bandwidth results are always slightly above the exponential fitting results. This agrees with previous results presented by Janzen et al. (2005) and Chandler (2005), who have found systematic small differences between the methods, not related to frequency shifting. The half-power bandwidth method systematically gives slightly larger values of damping ratio than the logarithmic decrement approach.

4.6 Damping and Mass Flux

Previous research carried out by Carlucci (1980) and Carlucci and Brown (1983) explored the relationship between the flow velocity (mass flux) and two-phase damping. Although they concluded that the flow velocity had little effect on the damping ratio, the experimental set-up they used was not a tube bundle in cross-flow, but a confined array in axial flow. Pettigrew et al. (1989a) also evaluated the effect of mass flux on damping, concluding that it was not dominant away from the fluidelastic stability threshold, and for this reason was not a significant parameter in the

formulation of damping in two-phase flow. The results presented by Pettigrew et al. (1989a) were obtained from experiments carried out using a normal-square tube bundle. In order to investigate the relationship between two-phase flow damping and mass flux, iso-contours of the total damping ratio have been plotted by using the data obtained from the exponential fitting method on a grid of RAD void fraction and pitch mass flux (see Figure 4.13). The mass flux seems to have little influence on the total damping ratio for void fractions lower than 15% and higher than 60%. However, between 15 and 60% of void fraction, the damping ratio is clearly dependant on mass flux, with a maximum located near 250 kg/m^{2}s. This range of void contains part of both the bubbly and intermittent flow regimes, including the transition, where the maximum damping ratio should occur according to the present results (see Figure 4.3). Interestingly, a very similar behaviour was observed by Baj and de Langre (2003) when they plotted two-phase damping as a function of reduced velocity for different void fractions, as shown in Figure 2.21. It can be seen from the Baj and de Langre (2003) experiments that the maximum damping ratio increases as we increase the void fraction, and this effect seem to be less important at low voids. Feenstra (2000) also reported similar results, especially for HEM void fractions lower than 80% (approximately 55-60% in terms of RAD void).

The results obtained in this research show that the assumption that damping is independent of mass flux is not valid. In two-phase flows, the mass flux, void fraction and possibly other fluid properties have a strong effect on the flow regime transition, which also seems to affect the damping, as seen in Figure 4.3.

4.7 Dimensional Analysis of Damping

With the objective of investigating a scaling relationship for the damping present in the system in terms of the two-phase flow parameters, a dimensional analysis was carried out for the damping ratio. As a first step, the total damping ratio in a tube

bundle was assumed to be a function of the following flow variables:

$$\zeta = \zeta\left(\alpha, S, G_p, \mu_l, \rho_{tp}, \Delta\rho, P, D, \sigma, g\right), \tag{4.4}$$

where S is the slip ratio (U_g/U_l), G_p is the mass flux, σ is the surface tension, $\Delta\rho$ is the density difference between the liquid and gas phases, P is the array pitch, D is the tube diameter and g is the gravitational acceleration. The resulting dimensionless parameters were combined and rearranged to reduce its number, obtaining the following groups:

$$\begin{aligned}
\Pi_1 &= We/Re = Cap = \mu_l U_{gs}/\sigma \\
\Pi_2 &= P/D \\
\Pi_3 &= Fr = V_p^2/Dg \\
\Pi_4 &= \Delta\rho/\rho_{tp} \\
\Pi_5 &= \alpha \\
\Pi_6 &= S.
\end{aligned} \tag{4.5}$$

In equation 4.5, Cap is the Capillary number, the ratio of the Weber number to the Reynolds number. The mass flux G_p has been substituted by the superficial velocity of the gas phase. The other parameters are the Froude number (Fr), the density ratio $\Delta\rho/\rho_{tp}$, the pitch ratio P/D, the slip ratio S and the void fraction α, which were originally dimensionless. The Capillary number has a special significance in two-phase flow across tube bundles. It was first introduced by Feenstra (2000) in order to calculate the slip ratio and determine void fraction. In Feenstra's void fraction model, the Capillary number represents the ratio of viscous forces to surface tension (interfacial) forces, which affect the development and transition between flow regimes. We know that surface tension has a strong influence on two-phase damping Pettigrew and Knowles (1997) and, as the liquid phase carries much of the flow momentum, the liquid viscosity was included instead of using a two-phase value. The viscosity of the

liquid is also relevant in vertical-upwards two-phase flow because it affects the degree of coalescence of the bubbles, playing an important role in flow regime transition. Since Feenstra's void fraction model has proven to be very effective in reproducing the behaviour of two-phase mixtures (Consolini et al., 2006), both for single-component (steam-water mixture, refrigerants) and two-component flows (air-water), it seems reasonable to assume that the use of the Capillary number will allow us to capture some of the physics involved. In this study, the viscosity of the liquid phase and the surface tension were determined based on the temperature of the mixture, measured just upstream of the tube bundle. The superficial velocity of the gas was calculated as

$$U_{gs} = \frac{xG_p}{\rho_g}, \tag{4.6}$$

where x is the thermodynamic quality and ρ_g is the density of the gas phase.

4.8 Interfacial Damping and Flow Regime

The two-phase damping (in this case defined as $\zeta_{tp} = \zeta_T - \zeta_s$, equation 4.1) can be combined with the Capillary number as a normalization parameter, since this has proven to be a useful scaling parameter for two-phase flows. Figure 4.14 shows the combination of the two-phase damping ratio and the Capillary number versus the RAD void fraction for all the mass fluxes studied. This normalized damping is called here Interfacial Damping ($\zeta_i = \zeta_{tp}Cap = \zeta_{tp}\frac{\mu_l U_{gs}}{\sigma}$) due to its dependence on surface tension, an interfacial property. As indicated above, the flow regimes were determined based on the flow regime map proposed by Ulbrich and Mewes (1994) and corroborated by visual observation. These transitions are not sharp. Additionally, at different mass fluxes, the transition between flow regimes will not occur at the same void fraction. With this in mind, an estimated range of transition is indicated in Figure 4.14 by using shaded bands.

For the first time is it shown clearly how flow regime affects the damping. For the bubbly flow regime, we can observe a remarkable collapse of the damping data, even

when the recent experiments described in section 4.6 and Figure 4.13 have shown that damping is dependent on mass flux for a certain range of void fractions. After the two-phase flow becomes intermittent, the trend becomes less apparent, while for dispersed flows the collapse is improved. The large scatter observed during the intermittent flow regime is undoubtedly due to the flow instability, which is characterized by large random spatial and temporal changes in local void fraction. On the other hand, the good agreement observed in the bubbly and dispersed flow regimes suggests that the Capillary number is successfully scaling the physical phenomenon causing damping in these flow regimes.

With the objective of extracting more information from this particular plot, a statistical procedure known as LOESS (locally weighted polynomial regression) was implemented. A detailed explanation of this procedure is presented in Appendix D. The LOESS procedure is especially useful to find trends in large clouds of data points (Cleveland, 1994). The result is shown by the solid line in Figure 4.15. As mentioned above, the trend is clear for bubbly and dispersed flows. For the intermittent flow regime, the interfacial damping parameter is hugely scattered, but not strongly dependent on the void fraction. At this stage, the damping is diminishing due to the reduction in the averaged density of the mixture, as well as the reduction in interfacial surface area due to void coalescence. At the same time, the superficial gas velocity is increasing, and these effects apparently tend to offset one another in the intermittent flow regime. In the dispersed flow region, the flow is more steady, the interfacial area is substantially reduced as is the averaged fluid density and the fluidelastic forces are increasing.

Since Figure 4.15 shows a clear relationship between damping and flow regime, it was decided to fit functions to the smoothed lines obtained from the LOESS. The fitting curve is different for each flow regime, as shown in Figure 4.16. For bubbly flows, a quadratic function is used, while the intermittent flow regime was approximated using a straight line. The dispersed flow is approximated by a third

order polynomial. The functions obtained were

$$\begin{aligned} \zeta_i &= 0.16\alpha^2 + 0.015\alpha, & 0 \leq \alpha < 0.45 \quad \text{(Bubbly)} \\ \zeta_i &= 0.045, & 0.45 \leq \alpha < 0.75 \quad \text{(Intermittent)} \\ \zeta_i &= -3.02(\alpha - 1)^3 + 3.51x10^{-4}, & 0.75 \leq \alpha \leq 1 \quad \text{(Dispersed).} \end{aligned} \tag{4.7}$$

In previous studies (Pettigrew et al. (1989a), Pettigrew and Taylor (1994)) it was observed that the normalized two-phase damping varied linearly with the void fraction between 0 and 45%. In the present data, the relationship is quadratic for the same range of void fraction. This is explained in part by the parameters used in the normalization of two-phase damping. The normalized damping presented in this study is based primarily on the superficial gas velocity, which is a direct function of the density of the mixture. The relationship between density and void fraction is nonlinear, especially for low values of void fraction. It is thought that the present plot of damping versus void fraction represents a substantial improvement over the traditionally used plots (Figures 2.17, 2.18). This is because the RAD void fraction better represents the actual void fraction than the HEM, the present normalization procedure appears to better capture the physics by including the surface tension and viscosity, and the distinct effects of flow regime are accounted for.

4.9 Discussion

A set of experiments was conducted to study the effect of the measurement methodology and the influence of two-phase parameters on the two-phase damping ratio. Previous studies carried out in single phase media (Chandler, 2005; Janzen et al., 2005) have shown that the damping results can be affected by the measurement method and the postprocessing techniques. In the present study, three different methods were investigated based on the same experiments: the traditionally used half-power bandwidth method, the logarithmic decrement method and an exponential fitting to the

decay trace of the tube. Due to the unsteady nature of two-phase flow and its impact on the tube response, the implementation of the logarithmic decrement method using vibration peak amplitudes produced much more scattered results than the exponential fitting to the decay trace. Consequently, only the latter was compared against the half-power bandwidth method.

For all three methods, the dynamic system was considered linear and of a single degree of freedom. However, the use of the half-power bandwidth method relies on the frequency response of the tube, requiring that the flow excitation be broadband random near the natural frequency of the the tube, as well as steady and ergodic. In two-phase flow across tube arrays, especially when the density of the media is high (low void fraction region), the hydrodynamic mass changes are more intense due to the presence of the neighbouring tubes. This behaviour has been observed and acknowledged by Pettigrew et al. (1989a) and Pettigrew and Taylor (1994). In tube bundles with a single flexible tube, the influence of the neighbouring tubes is minimized, but the effects of tube motion relative to its neighbours and local void changes still exist. Figure 4.9 shows the difference between the results based on the half-power and exponential fitting methods. It is evident that, for low void fractions predominantly in the bubbly flow regime, the half-power bandwidth method gives much higher values of the damping ratio. This behaviour persists at higher void fractions, but the difference in results becomes quite small.

It was postulated that the primary reason for the half-power method's much higher estimates of the damping ratio was the frequency shifting caused by added mass fluctuations. Since the density of the media is constantly changing around the tubes, the natural frequency of the monitored tube will shift accordingly, artificially widening the peak observed in the averaged frequency response spectra. In order to quantify these effects, an experiment was devised in which the averaging time was reduced and a large number of samples was recorded for selected void fractions. The results shown in Figures 4.11 and 4.12 prove that the frequency shifting is a function of void fraction, and the effect minimizes as the void fraction is increased. Figure 4.10 illustrates the

same phenomenon by using the hydrodynamic mass ratio as an indicator. At low void fractions, the dependence of hydrodynamics mass ratio on the void fraction is strong, but as the void increases, the hydrodynamic mass ratio stabilizes. The author believes that, at high void fractions, tube vibration produces a vapour film around the tube, preventing it from "sensing" the small local changes of the density.

Based on the damping results obtained using the exponential fitting to the decay traces, the effect of flow velocity (mass flux) on the damping ratio was evaluated by plotting iso-contours of damping on a grid of RAD void fraction and pitch mass flux (Figure 4.13). Although previous studies concluded that the mass flux had little or no effect on the damping ratio (Carlucci, 1980; Carlucci and Brown, 1983; Pettigrew et al., 1989a) it is shown that the effect of mass flux is strong for a range of void fraction between 15 and 60%. The mass flux seems to have little influence on the total damping ratio for void fractions lower than 15% and higher than 60%. Similar behaviour have been observed by Feenstra (2000) and Baj and de Langre (2003). The present results show that damping is not independent of mass flux, and therefore, valid damping measures should not be obtained or compared using such an assumption.

A dimensional analysis was applied to the two-phase damping with the objective of investigating the relationship between the latter and two-phase flow related parameters. As a result, the inclusion of surface tension in the form of the Capillary number appears to be useful when combined with the two-phase component of the damping ratio (interfacial damping). However, it is important to note that this concept has not truly been tested in these experiments because some fluid properties do not change much (liquid viscosity, surface tension, density of liquid and gas phases). Further research is necessary to properly evaluate this approach. Figure 4.14 demonstrates for the first time a strong dependence of damping on flow regime. When the data is smoothed by using statistical analysis (Figure 4.15), the change of the interfacial damping as a function of flow regime becomes more evident. At low void fractions (bubbly flows), the collapse of the damping data is very good, even when different mass fluxes have been plotted at the same time. In the dispersed flow region, a similar

behaviour is observed. Notably, in the intermittent flow regime the damping data is highly scattered due to unstable flow and the random temporal and spatial local void fluctuations. Overall, it appears that for intermittent flows the interfacial damping does not show a clear dependence on void fraction. This analysis has shown a clear variation of damping with flow regime, introducing an improvement over the previous results (Figure 2.18) which do not include the effects of flow regime and do not properly account for void fraction and the physical parameters governing two-phase flows.

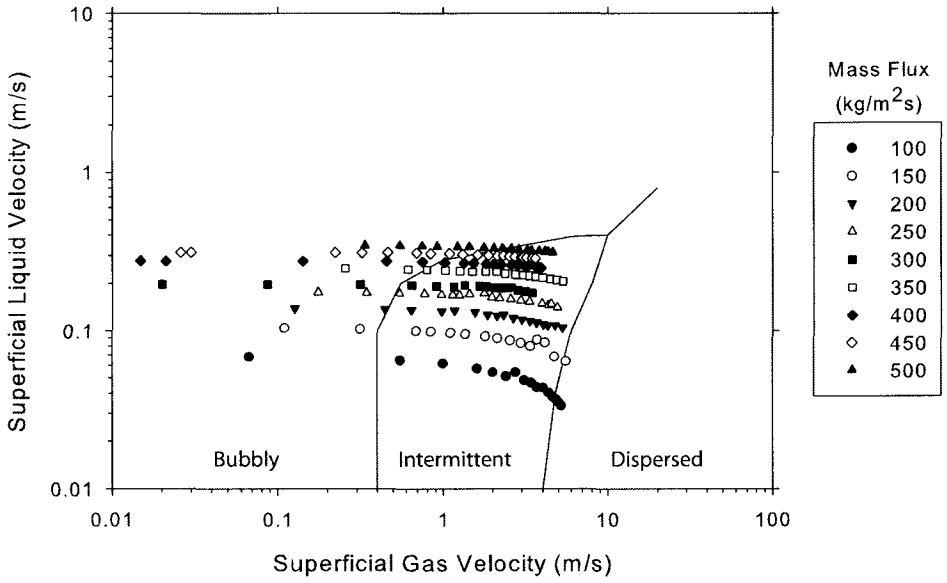

Figure 4.1. Flow regime data for the test series A based on the map by Ulbrich and Mewes (1994).

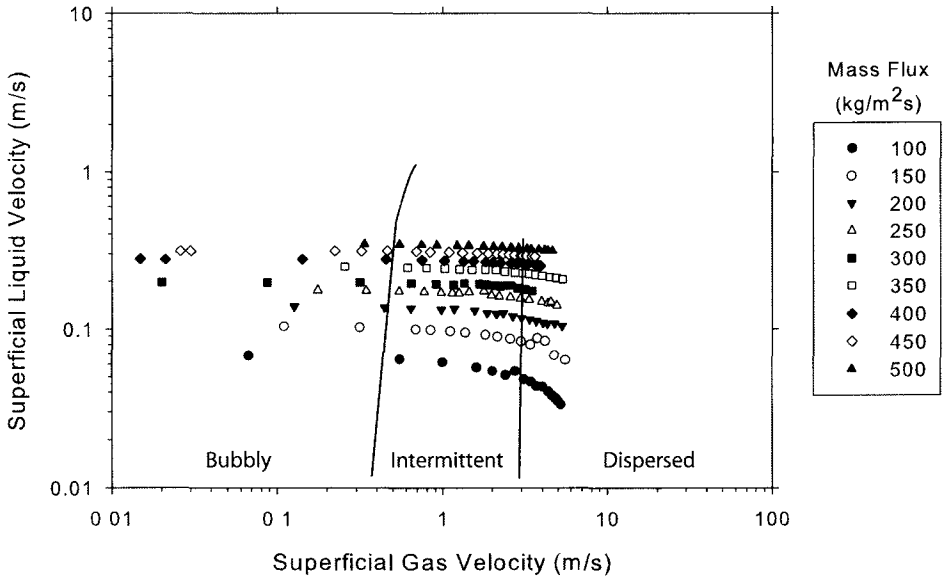

Figure 4.2. Flow regime data for the test series A based on the map by Noghrehkar et al. (1999).

Table 4.1. Comparison between the transitional void fractions between *bubbly and intermittent* flow obtained from the Ulbrich and Mewes (1994) flow regime map and visual observation.

Mass Flux (kg/m^2s)	Void - Map (%)	Void - Visual (%)
100	49.3	49
150	41.8	42
200	37.5	38
250	40.4	46
300	42.5	43
350	43.4	47
400	44.9	45
450	52.3	43
500	59.3	40

Table 4.2. Comparison between the transitional void fractions between *intermittent and dispersed* flow obtained from the Ulbrich and Mewes (1994) flow regime map and visual observation.

Mass Flux (kg/m^2s)	Void - Map (%)	Void - Visual (%)
100	80.8	80
150	83.3	78
200	-	75
250	-	75

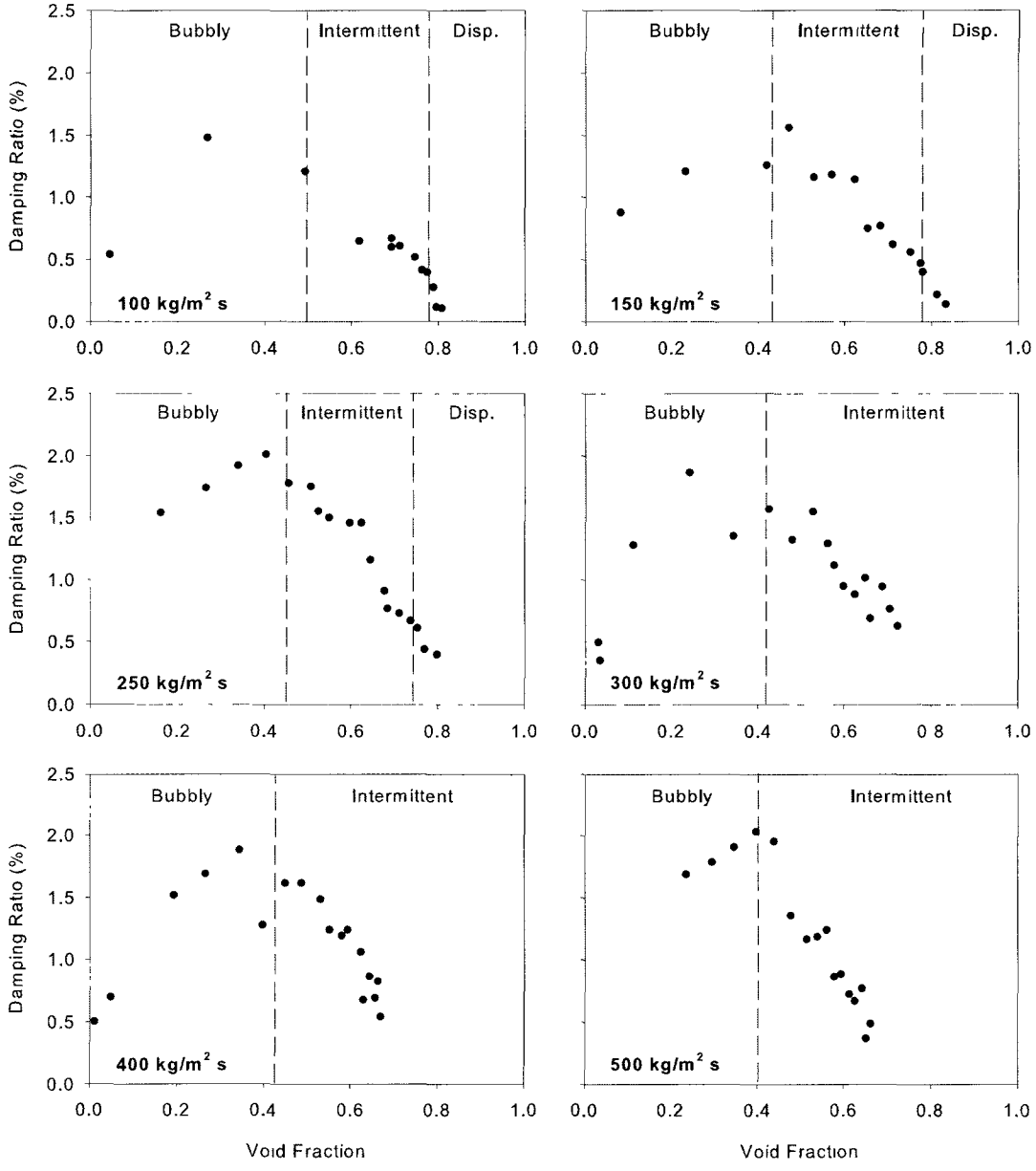

Figure 4.3. Total damping ratio, ζ_T, versus RAD void fraction. The mass fluxes and flow regimes observed are indicated in each plot.

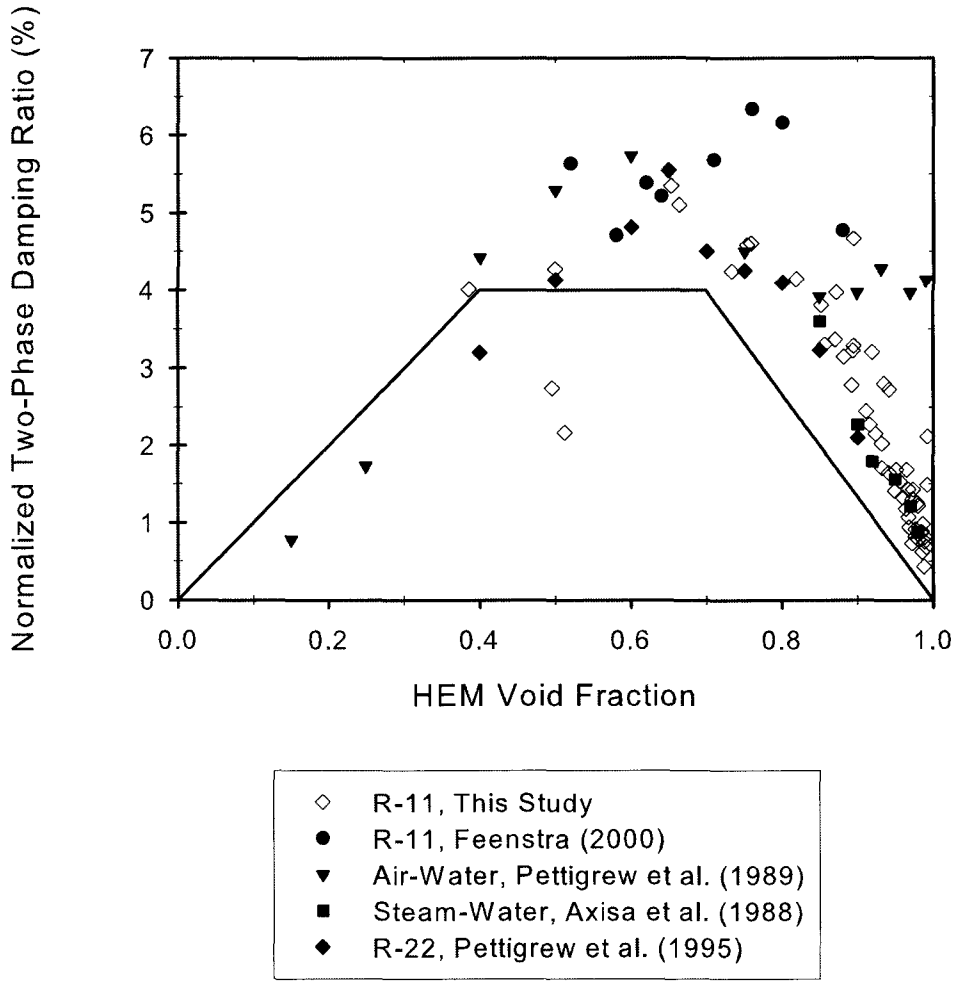

Figure 4.4. Normalized two-phase damping ratio vs. HEM Void fraction. The continuous line shows the design guideline suggested by Pettigrew and Taylor (2004).

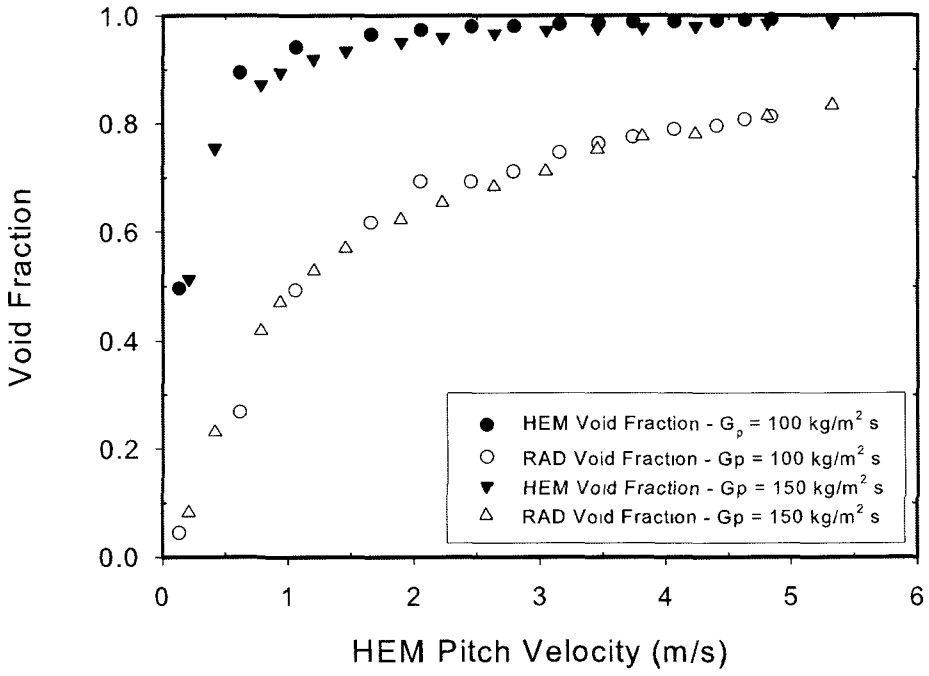

Figure 4.5. Comparison between the void fraction predicted by the HEM and the gamma densitometer measurements, as a function of HEM pitch velocity.

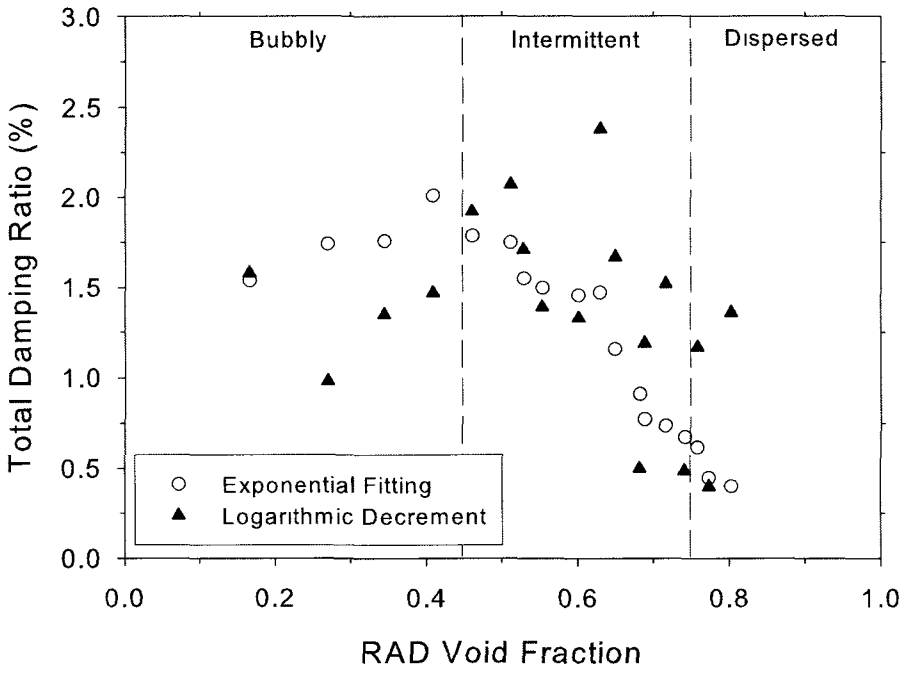

Figure 4.6. Comparison between the exponential fitting and the logarithmic decrement methods for a mass flux of 250 kg/m^{2}s. The bubbly, intermittent and dispersed flow regions are indicated.

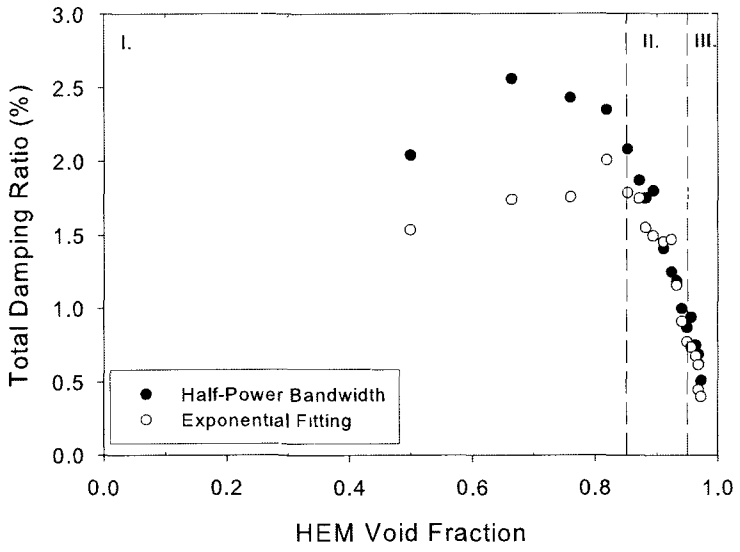

Figure 4.7. Damping based on the half-power bandwidth and exponential fitting methods versus the HEM void fraction for a pitch mass flux of 250 kg/m^{2}s. The areas labeled I, II and III represent the bubbly, intermittent and dispersed flow regimes respectively.

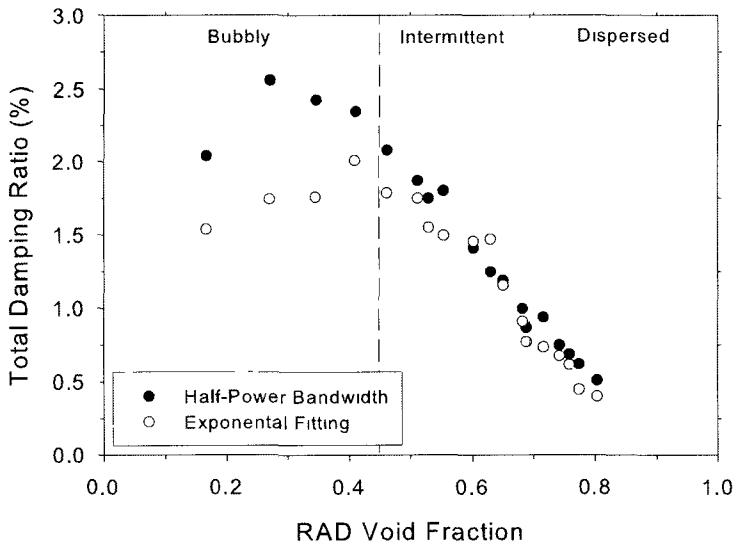

Figure 4.8. Damping based on the half-power bandwidth and exponential fitting methods versus the RAD void fraction. The pitch mass flux was 250 kg/m^{2}s.

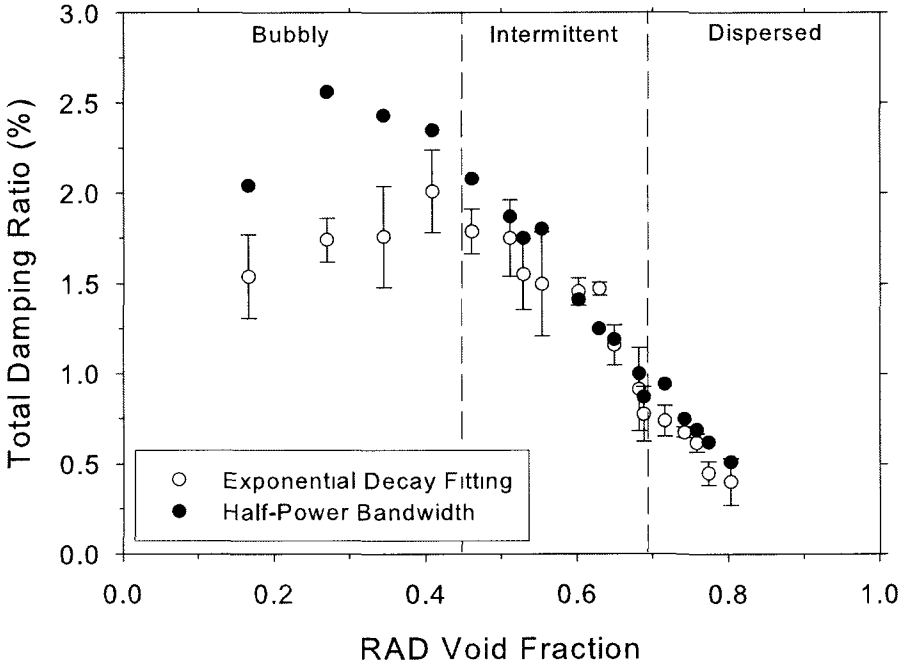

Figure 4.9. Comparison between the half-power bandwidth method and the exponential fitting to the decay trace. The pitch mass flux was 250 kg/m^{2}s. The error bars indicate one standard deviation, calculated using the three decay responses acquired for each void fraction.

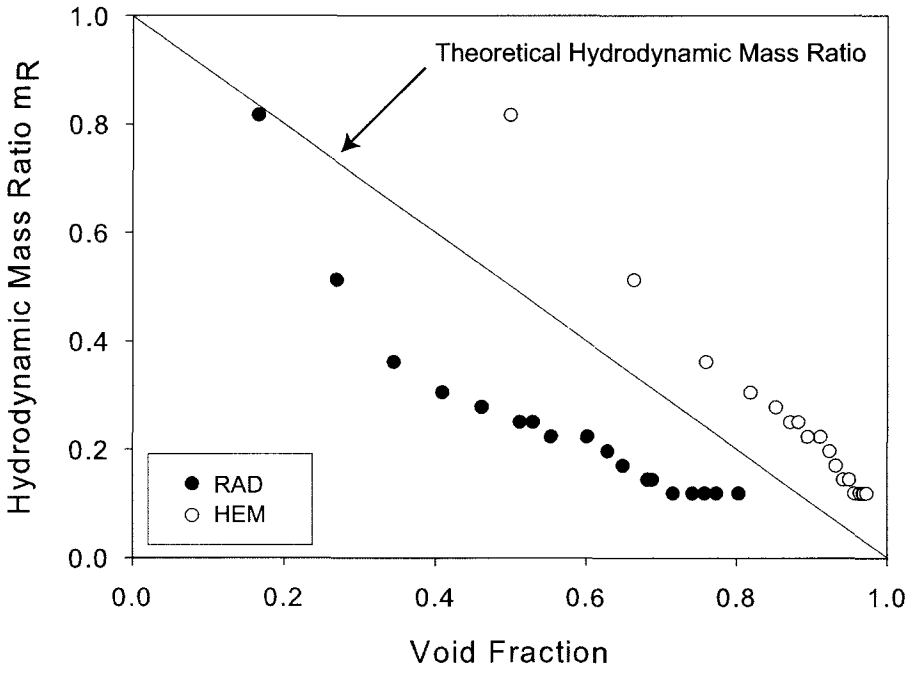

Figure 4.10. Hydrodynamic mass ratio vs. void fraction for a mass flux of 250 kg/m^2 s. The continuous line represents the theoretical hydrodynamic mass ratio.

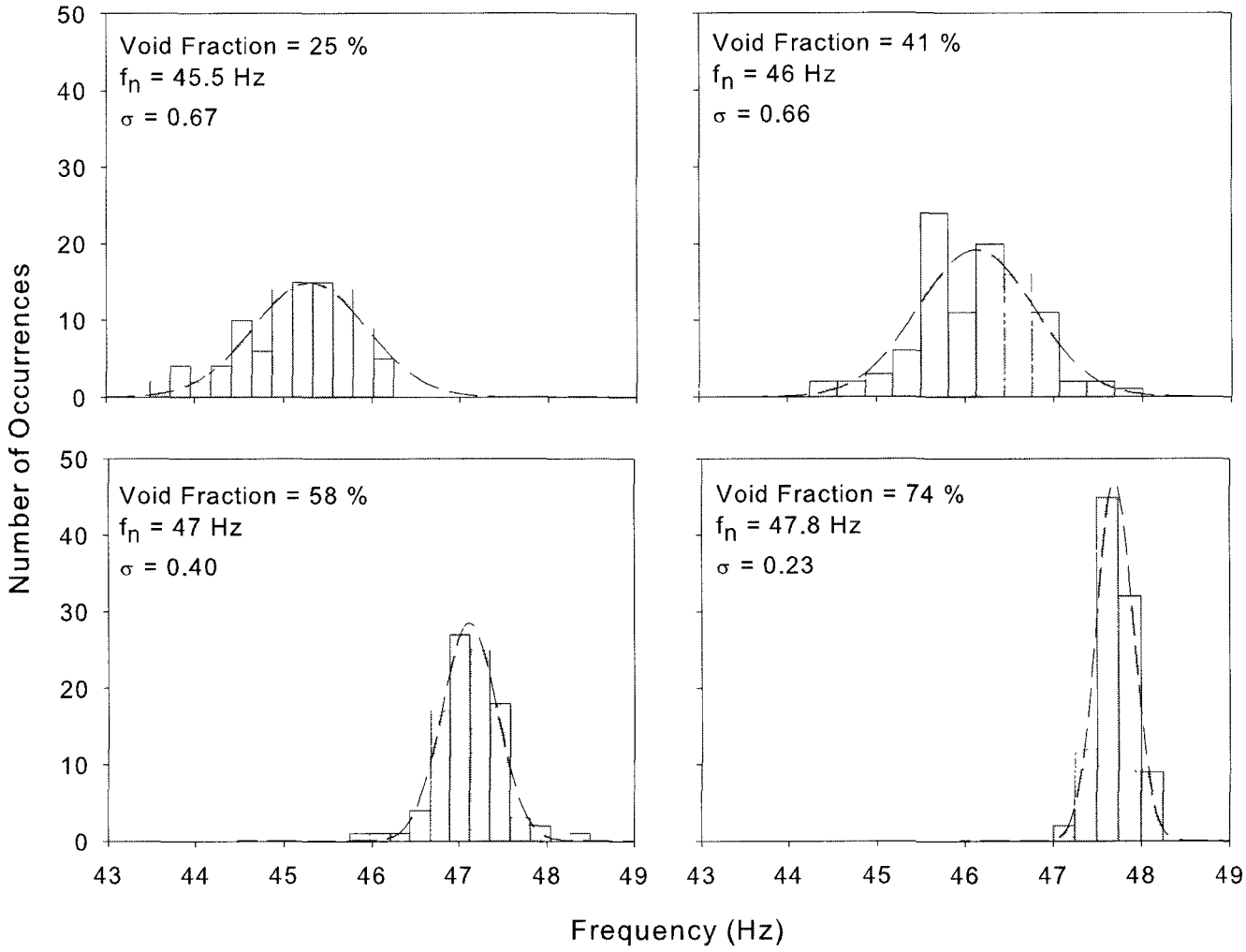

Figure 4.11. Histogram of frequency (100 samples) showing the magnitude of the shifting phenomenon for different void fractions. The mass flux was 200 kg/m^{2}s. The dashed line representing a gaussian approximation to the data is shown only as a reference.

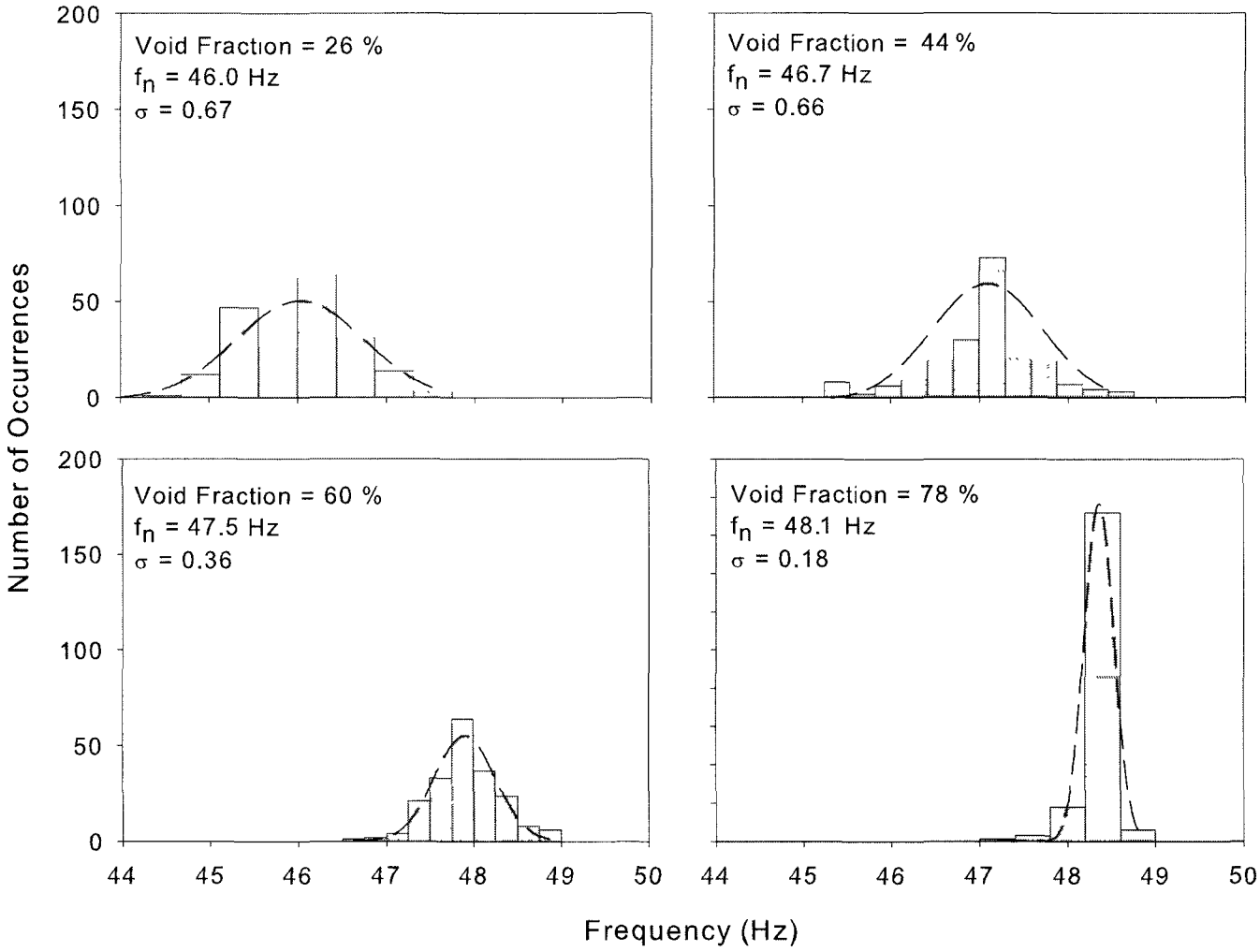

Figure 4.12. Histogram of frequency (200 samples) showing the magnitude of the shifting phenomenon for different void fractions. The mass flux was 200 kg/m^{2}s. The dashed line representing a gaussian approximation to the data is shown only as a reference.

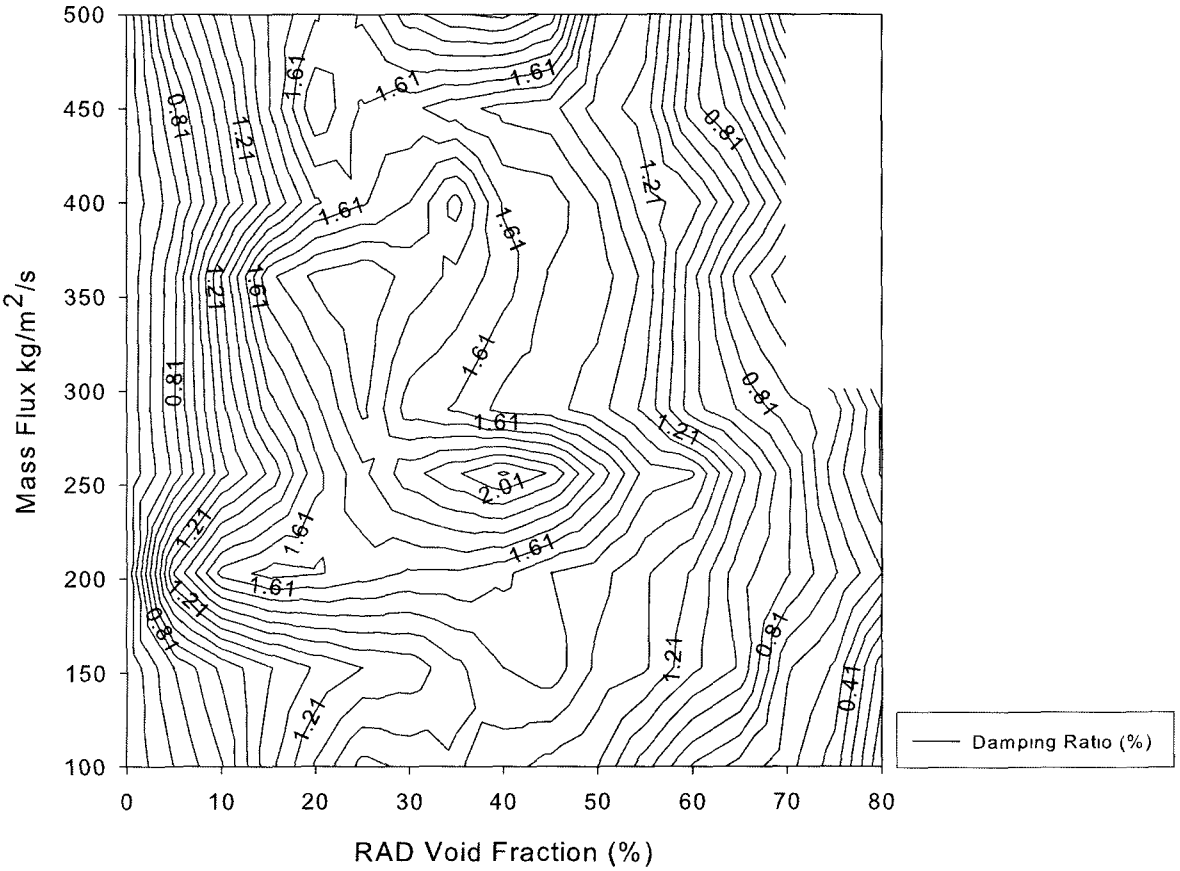

Figure 4.13. Iso-contours of damping on a grid of void fraction and mass flux. The effect of mass flux on damping is stronger for a void fraction range from 15 to 60 %, coinciding with the bubbly-intermittent flow transition, the point of maximum damping. The blank rectangle on the upper-right hand side indicates that void fractions above 70% were not observed for mass fluxes from 300 to 500 kg/m^{2}s.

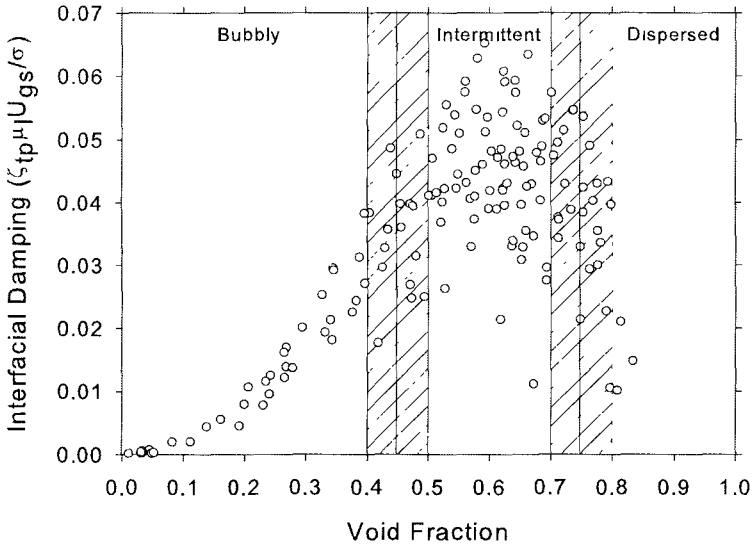

Figure 4.14. Interfacial damping as a function of void fraction for all the mass fluxes studied. The shaded bands indicate the change of flow regime zones for the different mass fluxes

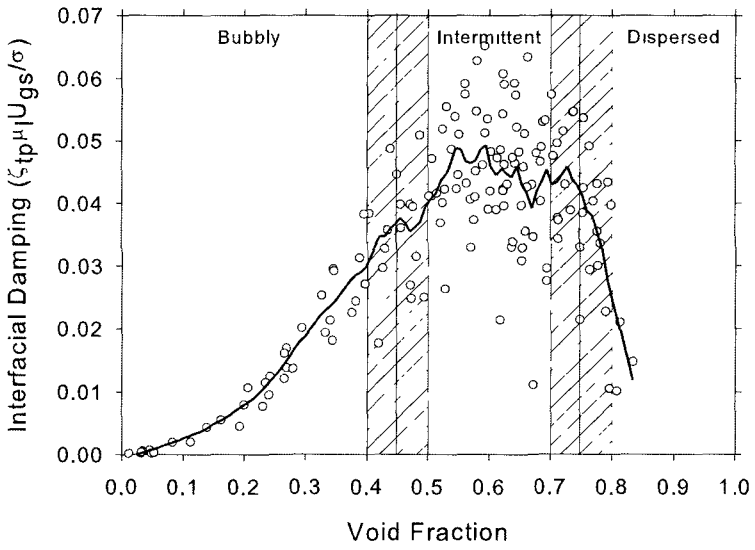

Figure 4.15. LOESS methodology applied to the interfacial damping. The shaded bands indicate the change of flow regime zones for the different mass fluxes.

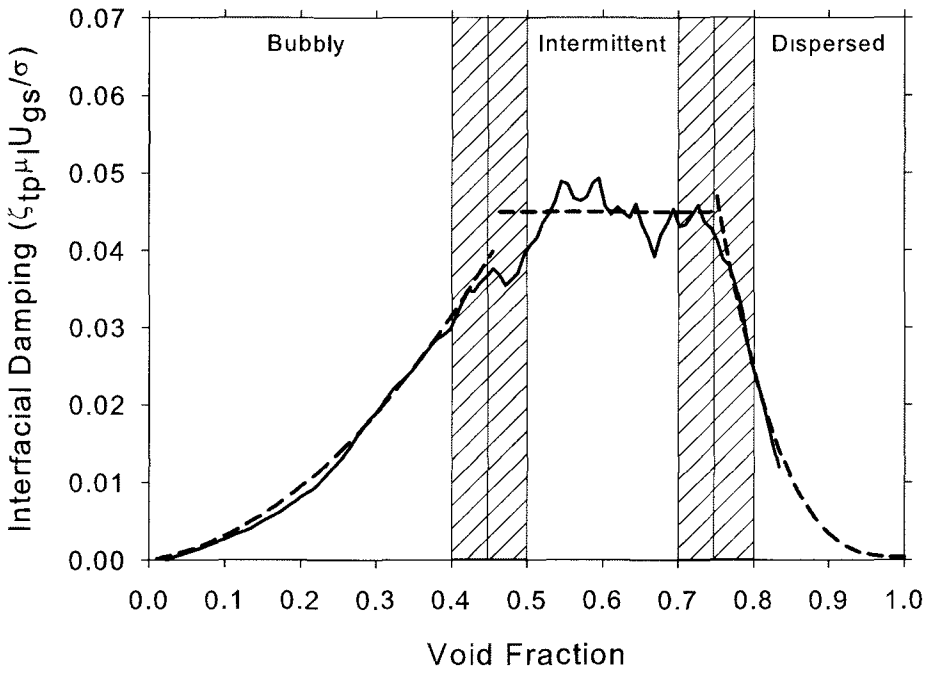

Figure 4.16. Approximation of the interfacial damping behaviour based on the LOESS. The shaded bands indicate the change of flow regime zones for the different mass fluxes. —— LOESS fit, - - - - - Equations 4.7.

CHAPTER 5

Fluidelastic Instability Analysis

In this Chapter, the experimental results from test series B are presented and the parameters used for modelling fluidelastic instability in two-phase flows are presented and discussed. The tube response amplitude is plotted as a function of flow velocity, using the interfacial velocity and the RAD and HEM pitch velocities, allowing for the comparison between these velocity models. The data is then plotted on a stability map, in order to evaluate the effect of using the in-flow damping calculated from the exponential fitting to the decay trace. The inclusion of the flow regime effects is attempted by using a term representing the energy dissipation for each flow regime. The stagnant fluid damping is also used for plotting the fluidelastic data. This approach, applied to the results obtained on a parallel triangular array, is generalized to the normal triangular, normal squared and rotated squared configurations.

5.1 Critical Velocity Results for the Fully-Flexible Tube Bundle

As mentioned in Chapter 3, the two-phase flow loop was modified to increase the maximum void fraction obtainable during the experiments. The heat flux transferred to the Freon was taken from 19.2 to 46 kW, producing RAD void fractions up to 92% for a pitch mass flux of 100 kg/m^{2}s, much higher than the previous maximum of 65% obtainable by Feenstra (2000) and Feenstra et al. (2003). Since the maximum possible void fraction has been substantially increased, the flow velocity is also much higher, going from 1 m/s to more than 5 m/s at a mass flux of 100 kg/m^{2}s (HEM pitch velocities).

For tests series B, a total of 10 experiments were carried out, varying the mass flux from 100 to 500 kg/m^{2}s in steps of 50 kg/m^{2}s and including an additional experiment at 77 kg/m^{2}s. For each experiment, the mass flux was set using the velocity control of the main pump. Then, for each trial, the heat transferred to the fluid was increased to change the void fraction. The temperatures along the flow loop were constantly monitored, in order to establish that the flow was steady before data acquisition commenced. For each trial, the averaged frequency spectrum of the monitored tube was recorded, providing the frequency and amplitude information required for the fluidelastic analysis. At the same time, the gamma densitometer was utilized to capture the RAD void fraction upstream of the tube array. Based on the measured void fraction, the flow density, the HEM and RAD pitch velocities and the Interfacial velocity were calculated. The RAD pitch velocity is defined as

$$V_{rad} = \frac{G_p}{\rho_{rad}}, \tag{5.1}$$

where ρ_{rad} is the two-phase flow density based on the RAD void fraction (see equation 2.17). The HEM and the Interfacial velocities were computed using equations 2.21 and 2.23, presented in Chapter 2. After the data is acquired, the void fraction is

increased using the heaters, and the process is repeated until high amplitude tube vibrations are observed.

Figure 5.1 shows the RMS amplitude of the monitored tube (as a percentage of tube diameter) versus the HEM pitch velocity for a mass flux of 100 kg/m^{2}s. The solid circles represent the tube response in the direction transverse to the flow, whereas the empty circles show the tube response in the streamwise direction. For low flow velocities, turbulence buffeting produces small amplitude oscillations that vary approximately linearly with velocity. When the stability threshold is reached, the response of the tube suddenly changes, steadily increasing its amplitude for small increments of velocity. The determination of the critical velocity is carried out by fitting smooth curves or lines to the pre-instability and post-instability regions, as shown in Figure 5.1. The stability threshold is taken at the intersection between the curve fittings, and is indicated by a vertical line marked "critical velocity".

A summary of such curves for different mass fluxes is presented in Figure 5.2. In this Figure, only six of the ten experiments are shown for the sake of brevity. However, mass fluxes representing the lowest, medium and highest values studied have been included. As with Figure 5.1, the vertical lines indicate the estimated location of the critical velocity, determined by using the methodology described above. In some cases, the determination of the critical velocity requires some judgement, as shown in Figure 5.2 for a mass flux of 300 kg/m^{2}s. Here, the tube response does not exhibit such a clear slope change. Thus, the critical velocity is taken immediately after the amplitude starts increasing, to ensure a conservative estimate of the stability threshold. In general, the critical velocity is well defined for the range of mass fluxes studied.

It can be seen that the effect of increasing the mass flux from 77 to 150 kg/m^{2}s is to increase the critical velocity slightly, then generally decrease it for further increase in mass, similar to the results presented by Feenstra (2000) and Feenstra et al. (2002). From a physical point of view, having a lower fluidelastic threshold at higher mass fluxes is a consequence of the density of the mixture. As the mass flux increases,

the void fraction observed at the critical velocity will be lower, because for the same heat flux transferred to the fluid, the larger mass fluxes have the lower void fractions (see Table 5.1). In addition, the inertial effects of the predominant liquid phase are stronger than for the case of gases, causing the fluidelastic threshold to occur earlier than for low mass fluxes. It is also important to consider the hydrodynamic coupling between the tubes, which becomes a key factor in predominantly liquid flows, producing a lower fluidelastic threshold. The difference between the displacements in the transverse and streamwise directions is not very important for the mass fluxes studied, except at the stability threshold, where the transverse amplitude increases more rapidly. This trend agrees with previous results presented by Pettigrew et al. (1989b), Feenstra et al. (1995) and Feenstra et al. (2002).

These results are re-plotted using the pitch velocity computed from the RAD measurements and are shown in Figure 5.3. It is seen that the trend indicated is opposite to the results shown in Figure 5.2. In this case, the critical velocity seems to increase as the mass flux increases. The reason is that the RAD void fraction is much lower than the predictions of the homogeneous model, resulting in a higher two-phase effective density. This result can also be explained from the perspective of the void fraction. As the critical void fraction increases, the critical RAD pitch velocity is lower. The consequence of this result is observed in Figure 2.8, where the reduced velocity decreases dramatically as we increase the void fraction (move from the liquid to the gas region). A similar behaviour has been observed by Feenstra (2000) when the reduced velocity plotted in a stability map was calculated using the equivalent velocity, as seen in Figure 2.9b.

The interfacial velocity introduced by Nakamura et al. (2000) behaves similarly to the HEM pitch velocity in terms of the trend in fluidelastic stability threshold versus mass flux, in the sense that for higher mass fluxes the critical velocity is lower (Figure 5.4). However, the interfacial velocity takes into account the buoyancy effects and the geometric configuration of the tube bundle, which are neglected or simply not considered in the Homogeneous Equilibrium Model. The trend indicates

that the critical velocity increases with void fraction, as is observed in any single-phase stability map when we go from the liquid (low mass-damping parameter) to the gas (high mass-damping parameter) zones. The interfacial velocity results seem to provide the expected trend in stability behaviour over the transition from liquid to gas flows. Hence, the interfacial velocity will be used for plotting and comparing the fluidelastic results obtained in this research. A summary of the HEM, RAD and Interfacial critical velocities and void fractions is presented in Table 5.1.

5.1.1 Comparison with Single-Flexible Tube in Rigid Array

Figure 5.5 shows the comparison between the amplitude response of the monitored tube in the single-flexible and fully-flexible tube arrays for 100, 250 and 500 kg/m^{2}s. As the mass flux increases, the dynamic behaviour of the tube bundle is different. For 100 kg/m^{2}s. both arrays become unstable at nearly the same interfacial velocity. This results agree with the research of Lever and Weaver (1986a), which found that for parallel triangular arrays subjected to air flow, the stability threshold was nearly the same for single and fully flexible arrays. For the other two mass fluxes shown (250 and 500 kg/m^{2}s) the fully flexible bundle clearly became unstable earlier than the single-flexible array. As the mass flux increases the void fraction at instability is lower, and it appears that the mechanism of fluidelastic instability becomes more dominated by the fluid stiffness, that is, the motion of the neighbouring tubes has an effect on the fluidelastic forces. This phenomenon was also observed by Scott (1987). who performed experiments using several tube bundle configurations subjected to water flows. For the case of parallel-triangle tube arrays. he investigated two P/D ratios: 1.375 and 1.730. He observed that the single-flexible bundle had a higher fluidelastic instability threshold than the fully flexible tube bundle. However, the difference in critical velocities was a function of the tube spacing, being larger for the larger spacing (1.73).

The magnitude of the turbulence buffeting seems to increase slightly as we increase the mass flux. This is expected, since the forces applied by the flow are a function of

the momentum of the liquid phase. For each of the mass fluxes studied, the turbulence buffeting results of both the single and fully flexible arrays are very similar, supporting the suitability of our use of the single-flexible results for damping data.

5.2 Fluidelastic Instability Results

Due to the modifications performed to the flow loop, new critical velocity data at higher void fractions was gathered during test series B. As a first step, these values were compared to previously published results by using the traditional approach for calculating the reduced velocity and mass-damping parameter. This implies that the Homogeneous Equilibrium Model was used to compute the flow density and velocity. In addition, the damping ratio was determined based on the half-power bandwidth method and taken at half the critical mass flux, as suggested by Pettigrew et al. (1989a) and Pettigrew and Taylor (2003a). Figure 5.6 illustrates this comparison. It can be observed that the present data agrees well with previously published results. For a given data set at lower mass-damping parameter values, the reduced velocity increases with the mass-damping parameter, and the trend is similar to the prediction of Connors' equation for a value of K equal to 3.0. The range of mass-damping parameters investigated goes up to 12, indicating a void fraction much higher than the majority of the previous studies using two-phase single-component fluids.

One of the features observed in Figure 5.6 is that as the void increases, the critical reduced velocity seems to decrease, deviating from the behaviour suggested by Connors' model (also see Figure 2.8). As the void fraction increases, its density reduces, increasing the value of the mass-damping parameter. If fluid density were the only parameter being changed, one would expect a monotonic increase of critical reduced velocity with increasing mass-damping parameter. Surprisingly,the opposite trend is observed, shown by the arrows in Figure 5.6 . This behaviour is still unexplained and has been attributed to flow regime affects, more particularly, the consequence of intermittent flows. It is this unexplained behaviour which motivated the flow loop

modifications in the present study to achieve higher void fractions. The observed trend downward with increasing void fraction must ultimately reverse its direction to approach the data for gas flows at very high void fractions. However, the fluidelastic data obtained in this research shows the same trend as the previous results, even when the fluidelastic instability was observed in dispersed flows for four of the ten experiments. It can be concluded that there must be a problem with the trend exhibited by the results, and this may be a consequence of the choice of parameters used to characterize the phenomenon.

Figure 5.7 shows the stability map produced using the damping value obtained by the exponential fitting method rather than the half-power bandwidth method. In this case, two separate clusters of data points are observed. The lower cluster represents the experiments where the instability took place in the intermittent flow regime. As in the previous figure, the reduced velocity decrease slightly as the void fraction increases. The data points representing the upper cluster correspond to the experiments where the fluidelastic instability occurred in dispersed flow. Since for dispersed flows the density of the mixture is low compared to intermittent and bubbly flows, the data is much closer to the gas region of the stability map as expected. Although there appears to be a slight improvement in this plot over Figure 5.6, the results obtained in the fluidelastic analysis are very similar, because the differences between the exponential fitting and half-power methods are significant primarily at low void fractions (bubbly flow).

The stability results can also be plotted based on the RAD void fraction (see Figure 5.8). In this case, both the pitch velocity and the two-phase density were calculated using the gamma densitometer measurements. The HEM density data reported by Pettigrew et al. (1989b, 1995) and Axisa et al. (1988) was converted into a more realistic density value by using the void fraction model introduced by Feenstra (2000). The iterative process required to carry out this conversion has been explained in detail in Feenstra (2000) and Feenstra et al. (2002). For this particular choice of parameters, the fluidelastic data does not indicate a progressive change from liquid to

gas, and neither does it follow the trend indicated by Connors equation. A reasonable data collapse is achieved, but the downward trend with increasing mass-damping parameter cannot be correct. This observation suggests that the pitch velocity based on the RAD density may not be appropriate to capture of fluidelastic instability phenomenon.

If the interfacial velocity is used to compute the reduced velocity and the RAD density is taken for calculating the mass-damping parameter, the data collapses as seen in Figure 5.9. This collapse is mainly due to the implementation of the measured void fraction as the HEM significantly over-predicts the actual void fraction. In addition, the results seems to follow Connors prediction for K = 3.0, coinciding with the behaviour observed by Feenstra et al. (2003). The latter also observed that the flow velocity determined by this model showed close agreement with that of the HEM. The definition of interfacial velocity proposed by Nakamura et al. (2000) is given by

$$V_i = C_i(U_{gs} + U_{ls}) + \sqrt{gD_e(\rho_l - \rho_g)/\rho_l}. \tag{5.2}$$

The superficial velocities U_{gs} and U_{ls} are defined according to the equations:

$$U_{gs} = \frac{xG_p}{\rho_g} \quad , \quad U_{ls} = \frac{(1-x)G_p}{\rho_l} \tag{5.3}$$

Substituting equations 5.3 into 5.2, we have

$$V_i = C_i\left[\frac{xG_p}{\rho_g} + \frac{(1-x)G_p}{\rho_l}\right] + \sqrt{gD_e(\rho_l - \rho_g)/\rho_l} \tag{5.4}$$

Simplifying,

$$V_i = C_iG_p\left[\frac{x}{\rho_g} + \frac{(1-x)}{\rho_l}\right] + \sqrt{gD_e(\rho_l - \rho_g)/\rho_l} \tag{5.5}$$

According to the Homogeneous Equilibrium Model, the two-phase density can be

calculated as

$$\rho_H = \left(\frac{x}{\rho_g} + \frac{1-x}{\rho_l} \right)^{-1} \tag{5.6}$$

Hence

$$V_i = C_i V_p + \sqrt{g D_e (\rho_l - \rho_g)/\rho_l} \tag{5.7}$$

In equations 5.2 to 5.7, D_e is an effective diameter calculated as $2(P-D)$, and g is the gravitational acceleration. Based on equation 5.7, it is clear that the interfacial velocity is a function of the HEM pitch velocity V_p. However, it incorporates two additional terms: one coefficient that varies depending on the tube array geometric configuration (C_i), and a buoyancy term that reflects the density difference between the liquid and gas phases. When used in the stability map, this approach removes the apparent change in stability behaviour seen in the conventional HEM analysis when the flow regime changes from bubbly to intermittent, where the reduced velocity seem to diminish when the mass-damping parameter increases (see Figures 5.6 and 5.8). The author believes that the inclusion of the buoyancy and bundle geometry effects into the determination of flow velocity introduces physical parameters that are relevant in the fluidelastic phenomena and were not considered in the past.

The interfacial damping discussed in Chapter 4 was also used to plot the fluidelastic data. Based on the void fraction observed at the critical velocity, the interfacial damping was calculated using equations 4.7 and then utilized to determine the mass-damping parameter (Figure 5.10). The data for intermittent flow shows the same downward trend seen in a number of the cases considered about. On the other hand, the data for dispersed flow has the opposite trend and shows increasing critical reduced velocity with increasing void fraction. This peculiar behaviour is the result of the significant reduction in damping observed for high void fractions, suggesting that interfacial damping is not a suitable scaling parameter for fluidelastic instability.

If the mechanism of fluidelastic instability is considered to be the same for single and two-phase flows as discussed with de Langre (2006), the data is expected to proceed smoothly from the critical velocities in liquids (void fraction equal to zero)

to those in gases (void fraction equal to 1). Thus, there is a need for better parameter definitions to characterize fluidelastic instability in two-phase flows, based on improved values for density, velocity and damping.

5.3 Proposed Approach for Fluidelastic Instability Analysis

Even though the measured values of void fraction, damping, and the calculation of flow velocity have been improved in this research, the trends observed in the stability maps still do not reflect the expected smooth transition from liquid to vapour. However, the RAD void fraction and interfacial velocity seem to introduce a considerable improvement over the HEM density and pitch velocity.

On the other hand, the values of damping used for fluidelastic analysis should be seriously questioned. It is clear from Baj and de Langre (2003) and Weaver and El-Kashlan (1981a) that the net damping must be zero at the critical velocity. Thus, it appears logical that all damping due to the flowing fluid should be neglected in the parameters characterizing fluidelastic instability. Therefore, only the total damping with no-flow represents a logical measure of the energy dissipation which must be overcome by the flow effects in order to produce fluidelastic instability.

An logical alternative to the use of the in-flow damping is the in-vacuo or structural damping, since it is the only component of system damping that must be overcome to produce fluidelastic instability. Typically, damping in air is very small compared to the structural damping, so that the damping in air is not significantly different from that in-vacuo. In single-phase flows, the damping in air has been used to plot fluidelastic data for both liquid and gas flows (Weaver and Fitzpatrick, 1988). However, it would be logical to use the total damping measured in no-flow condition as a measure of the energy dissipation in the system which must be overcome by the flow to produce instability. In two-phase flows, measurement of no-flow damping would appear impossible because of buoyancy of the gas phase. However, Baj and de Langre

(2003) extrapolated damping data, plotted as a function of flow velocity, back to the zero flow datum, and such an approach seems reasonable. Unfortunately, such data does not exist for the present study and it was decided that, in the absence of reliable no-flow damping data, a conservative estimate would be the damping measured in vapour with no flows.

If the structural damping (in vapour) is used for the calculation of the mass-damping parameter, the result is the stability map shown in Figure 5.11, where single-phase data has also been plotted. In this figure, the reduced velocity has been calculated using the pitch velocity for single-phase data and the interfacial velocity for the two-phase results. As in previous figures, the density of the two-phase data taken from previous studies based on HEM have been corrected based on Feenstra's void fraction model. By using this approach, the two-phase data is collapsed much better than with the traditional in-flow approach. As the void fraction is increased, this change produces a larger value of the mass-damping parameter, due to the reduction in flow density. However, the structural component of damping is very small if compared with the total damping measured in two-phase flows. For this research, the maximum damping observed was 2.1%, while the structural damping of the monitored tube was 0.09%, only 4% of the maximum total damping when subjected to two-phase flow.

When the tubes are surrounded by liquid, the viscous damping observed when the flow velocity is zero is generally much larger than the structural component. The total damping in the system at this point is very similar to the viscous component alone. For the case of tubes surrounded by air, the viscous damping is very small, and the total damping can be considered as equal to the structural damping. Based on these ideas, it was decided to use the damping in quiescent fluid as the reference value for fluidelastic instability analysis. This means that for results in air (or vapour), the damping in-air was used to calculate the mass-damping parameter. For two-phase and liquid data, the damping in stagnant pure liquid was utilized. The in-flow damping was not used because of the lack of data, as stated above. Figure 5.12 shows how

this approach collapses the two-phase data and shows a progressive transition from the liquid to the gas data. The use of the higher value of damping for the liquid and two-phase results have shifted these to the right on the stability map. Thus, the two-phase data follows the design guidelines proposed by Weaver and Fitzpatrick (1988) for single-phase flows very well. If it is accepted that the basic mechanism of fluidelastic instability is the same in single and two-phase flows, then it appears that the choice of proper scaling parameters is a crucial factor to developing a reliable stability map.

This last combination of parameters seems to be the best for producing the expected behaviour in transition from liquid to gas flows. Arguably, these parameters must also best capture the physics involved. The use of the RAD density, interfacial velocity and quiescent-fluid damping collapses the available data well and provides the expected trend of two-phase flow stability data over the void fraction range from liquid to gas flows. The resulting stability map represents a significant improvement for predicting fluidelastic instability of tube bundles in two-phase flows. This result also tends to confirm the hypothesis that the basic mechanism of fluidelastic instability is the same for single and two-phase flows.

5.3.1 Generalization to Other Tube Array Geometries

This approach can be applied to the other tube array geometries, as shown in Figure 5.13. For these figures, the reduced velocity is based on the pitch velocity for the single-phase results and on the interfacial velocity for the two-phase data. The collapse observed for all the geometric configurations is evident, even when limited two-phase data is available in some cases. Again, the two-phase results follow the trend indicated for Weaver and Fitzpatrick (1988), showing a higher critical reduced velocity than the pure-liquid data.

5.4 Discussion

The fluidelastic stability threshold of the tube array used in this research, was determined for a range of mass fluxes in test series B. The relationship between the monitored tube amplitude and different flow velocity models was presented and discussed. These models were the pitch velocities based on the HEM and RAD densities, and the interfacial velocity correlation introduced by Nakamura et al. (2000). The interfacial velocity model was selected to represent the fluidelastic data in two-phase experiments, due to the inclusion of the tube array geometry and density ratio effects which does not exist for the pitch velocity approach. The single-flexible and fully-flexible tube bundle responses were compared for various mass fluxes, showing that at higher void fractions (lower mass fluxes) the behaviour of both configurations is similar. At lower voids (larger mass fluxes), the hydrodynamic coupling causes the fully flexible array to become unstable earlier.

The present results were plotted in a stability map by following the current design guidelines. These included using the half-power bandwidth method for the damping ratio, the Homogeneous Equilibrium Model for the void fraction and flow velocity, and taking the damping at half the critical mass flux to calculate the mass-damping parameter. The results agreed with previously published data. However, the trends observed in the stability maps were similar to those obtained in the past by Pettigrew et al. (1989a) and Feenstra (2000), in the sense that the reduced velocity decreased when the void fraction was increased. This effect has been attributed to intermittent flow regime effects, although it could be caused by the use of incorrect scaling parameters to represent two-phase flow fluidelastic results. The use of the RAD pitch velocity does not introduce any improvements over the current analysis methodologies, exaggerating the effect described above.

The use of the interfacial velocity seems to collapse the two-phase data, and introduces the tube bundle configuration and the effects of buoyancy. However, the fluidelastic data does not clearly follow the expected trend from the liquid to the vapour critical values.

Since the net damping must be equal to zero when the critical velocity is reached, is was decided that the in-flow damping values were not appropriate for correctly scaling the fluidelastic instability phenomenon. As an alternative, the structural damping was used for the calculation of the mass-damping parameter, as has been done by some authors in single-phase flows. Using this approach, the two-phase data collapsed much better than when using the traditional in-flow damping. As the void fraction is increased, this change produces a larger value of the mass-damping parameter, due to the reduction in flow density. Given that the structural component of damping is very small if compared with the total damping measured in two-phase flows, the damping in quiescent fluid was used as the reference value for fluidelastic instability analysis. This means that for results in air, the damping in-air was used to calculate the mass-damping parameter. For two-phase and liquid data, the damping in stagnant liquid was utilized. This approach collapses the two-phase data and shows a progressive transition from the liquid to the gas results. The two-phase data follow the design guidelines proposed by Weaver and Fitzpatrick (1988) for single-phase flows, suggesting that the mechanism of fluidelastic instability is the same in single and two-phase flows, as suggested by de Langre (2006)

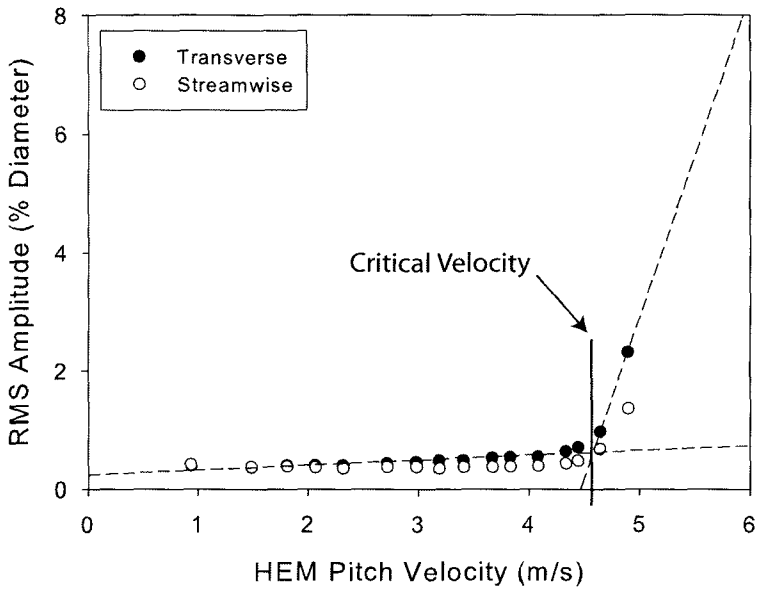

Figure 5.1. Typical RMS tube amplitude response as a function of HEM pitch velocity.

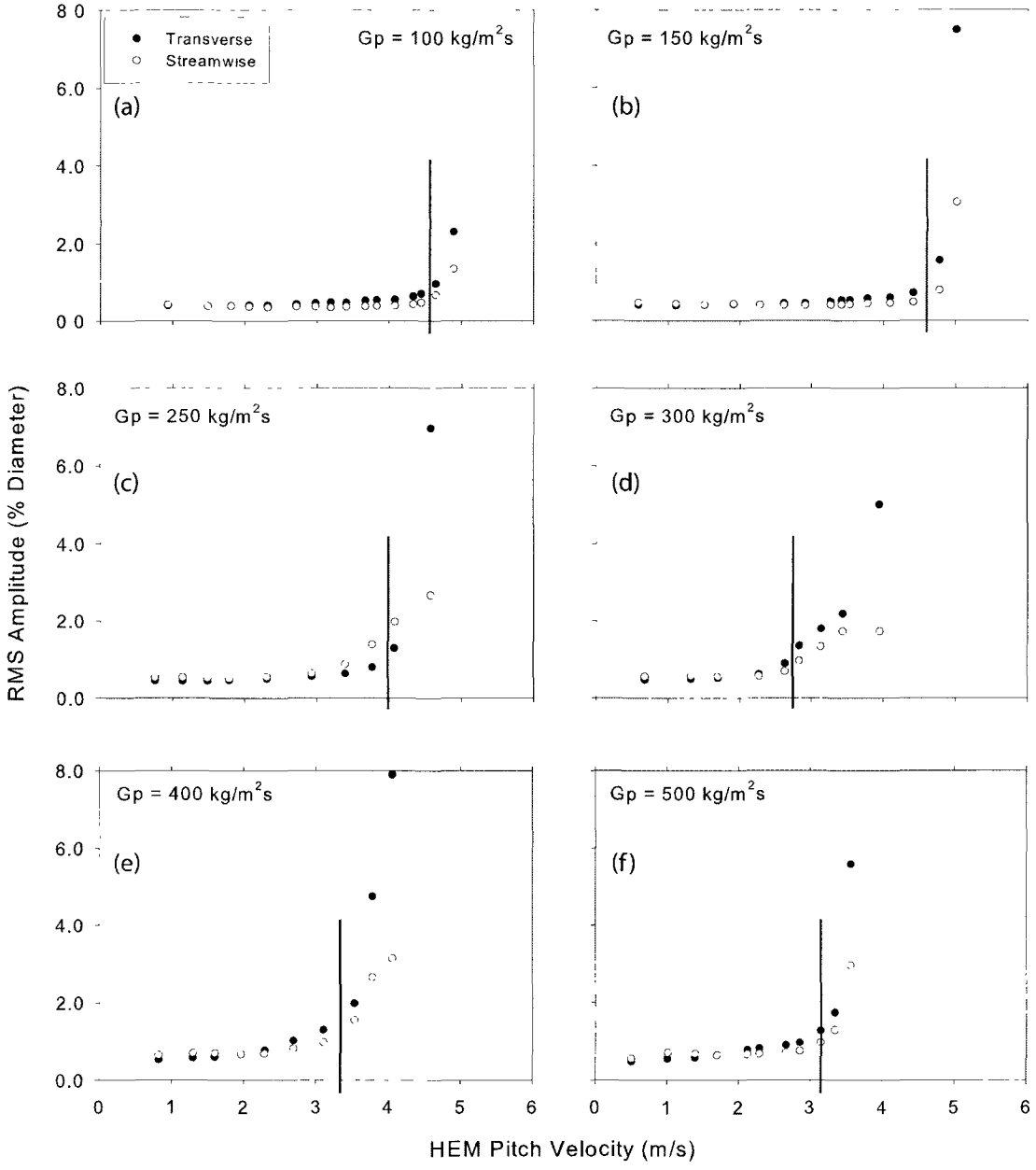

Figure 5.2. RMS amplitude of the monitored tube as a function of HEM pitch velocity.

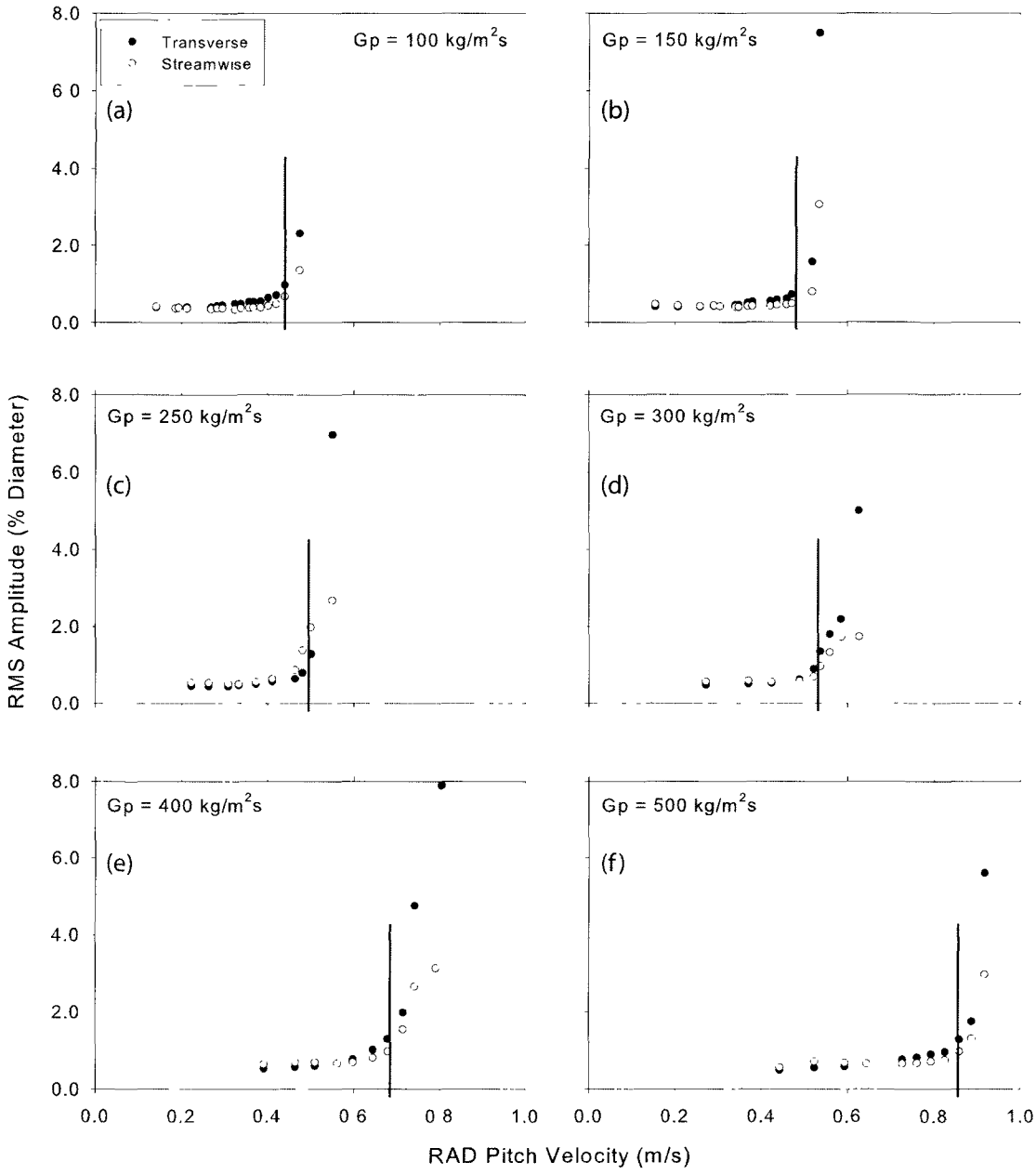

Figure 5.3. RMS amplitude of the monitored tube as a function of RAD pitch velocity.

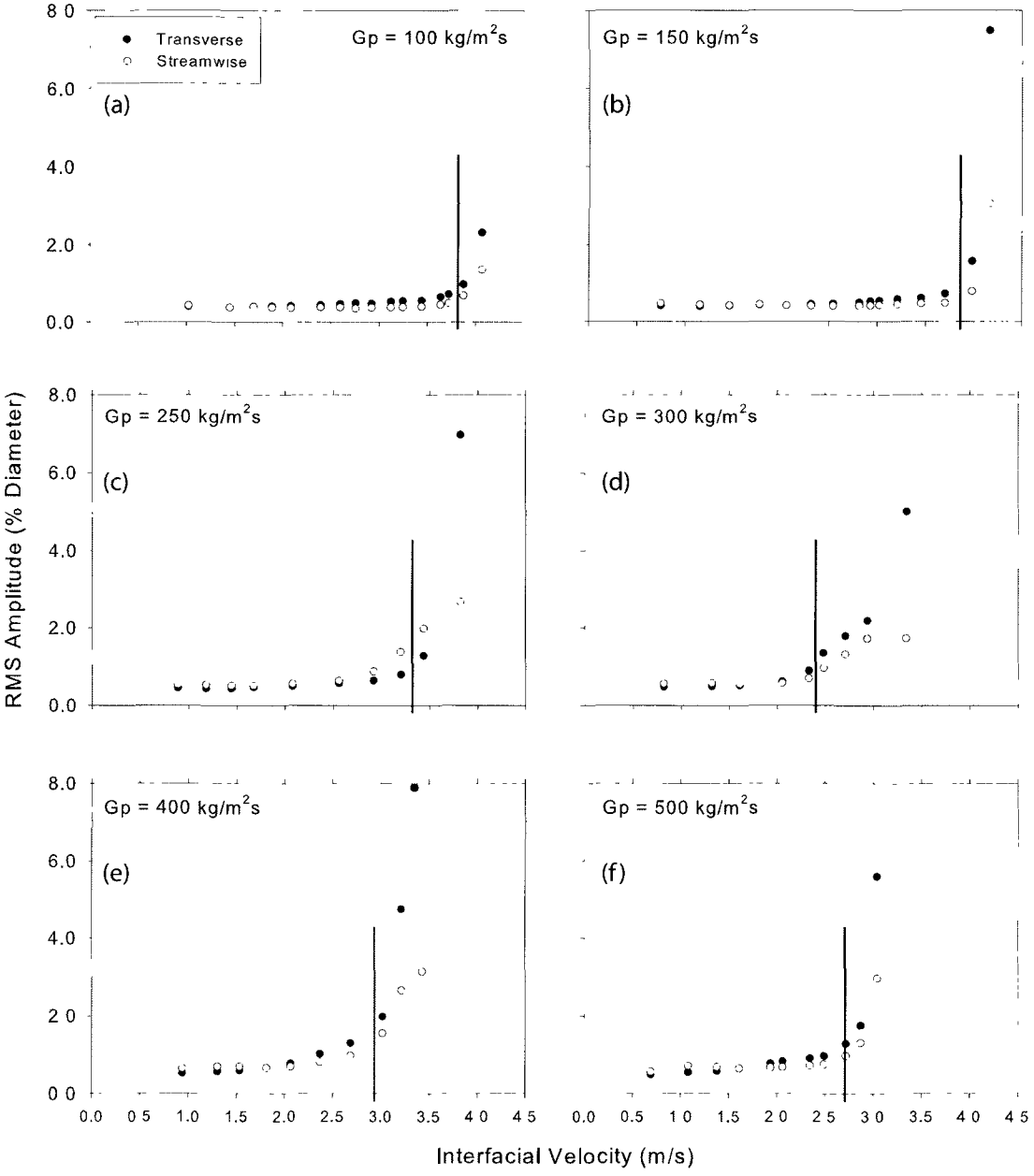

Figure 5.4. RMS amplitude of the monitored tube as a function of interfacial velocity.

Table 5.1. Critical velocity data from test series B (Fully-flexible array).

Mass Flux (kg/m^2s)	Frequency (Hz)	HEM Void Fraction	RAD Void Fraction	Critical Velocity (m/s) Pitch HEM	Pitch RAD	Interfacial
77	47.75	0.996	0.865	4.38	0.40	3.63
100	47.75	0.991	0.824	4.52	0.44	3.80
150	47.75	0.985	0.794	4.65	0.47	3.88
200	47.75	0.972	0.722	4.07	0.50	3.40
250	47.75	0.948	0.640	4.00	0.51	3.30
300	48.00	0.947	0.650	2.75	0.53	2.38
350	47.75	0.938	0.641	3.00	0.62	2.50
400	48.00	0.928	0.615	3.30	0.68	2.90
450	48.00	0.913	0.575	3.36	0.74	2.80
500	48.50	0.902	0.609	3.15	0.85	2.70

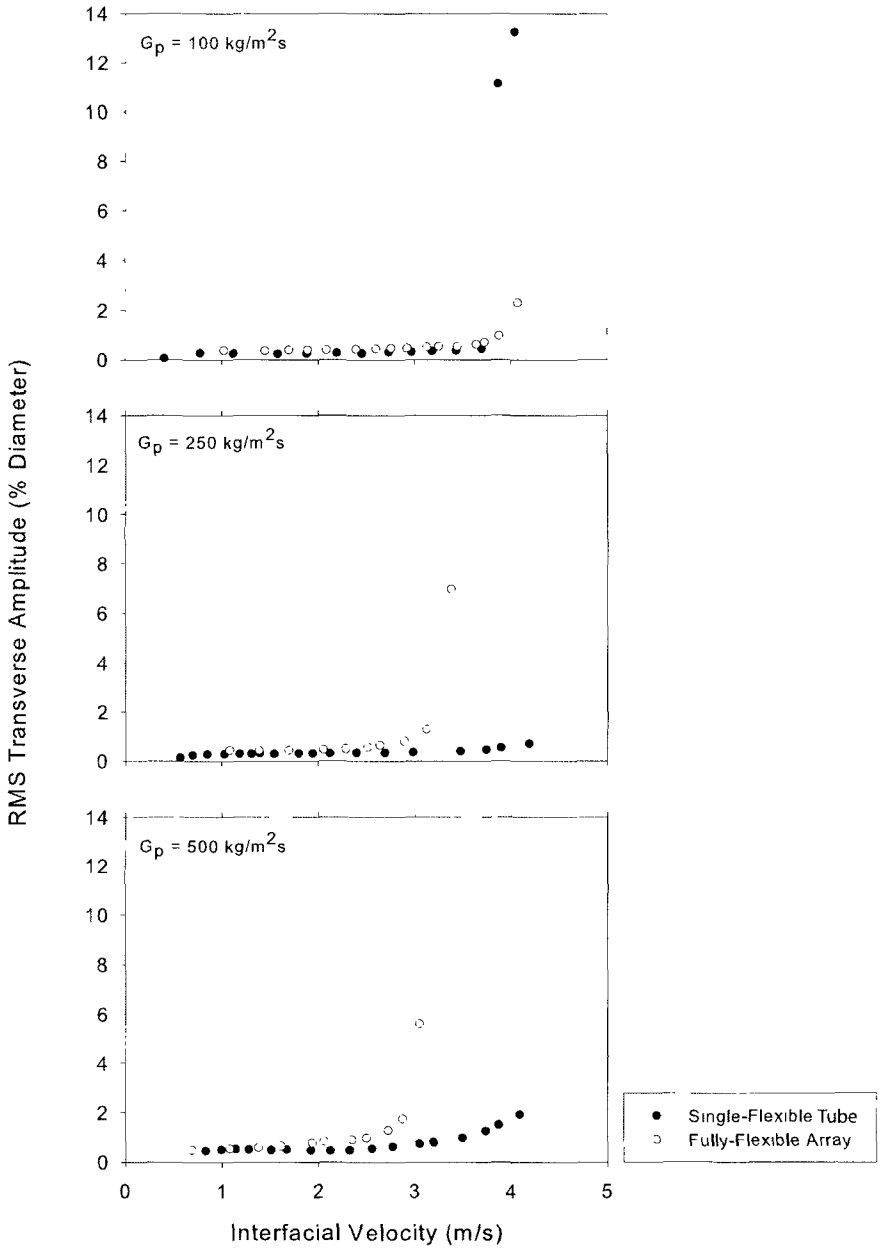

Figure 5.5. Comparison of the RMS amplitude response of the monitored tube in the single-flexible and fully-flexible cases.

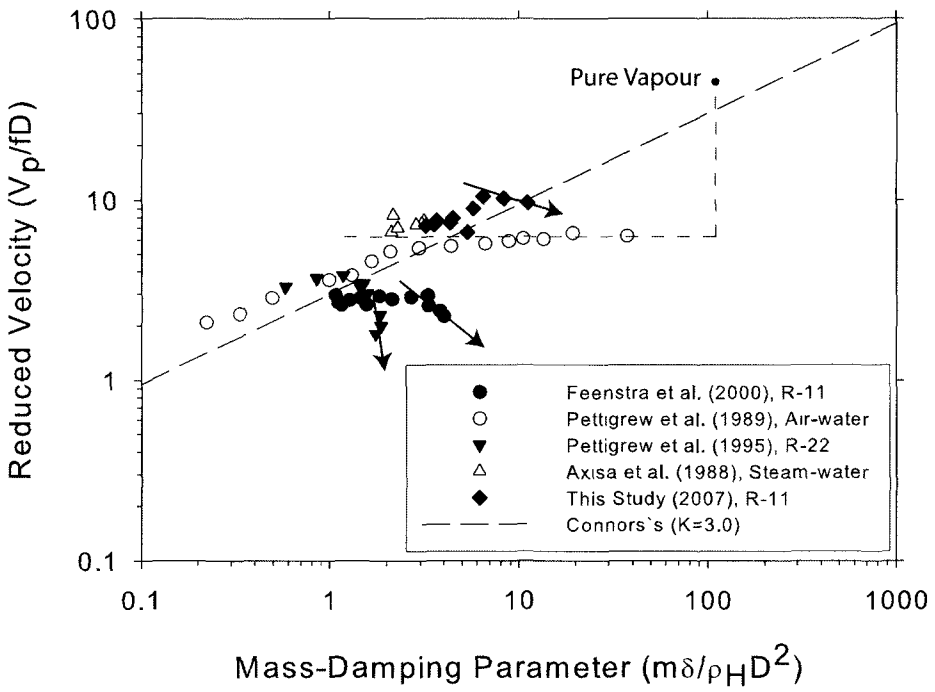

Figure 5.6. Stability map showing the fluidelastic instability results based on the traditional criteria. The reduced velocity and the mass damping parameter are based on HEM density. The half-power bandwidth method was used for the damping.

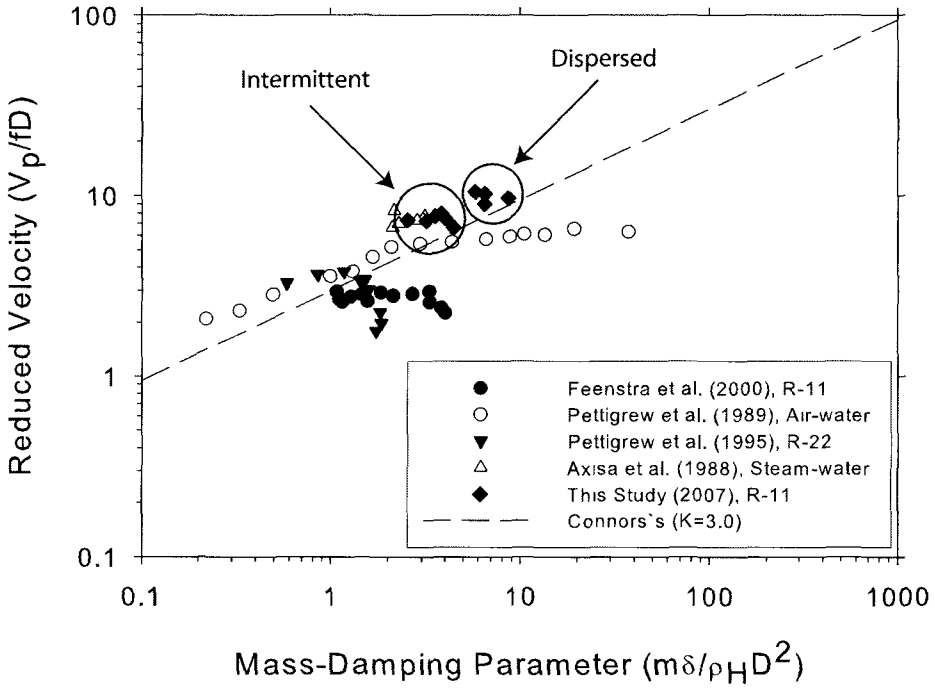

Figure 5.7. Fluidelastic instability results with the damping based on exponential fitting to the decay trace. The circles represent the experiments where the instability occurred in intermittent flow and dispersed flow.

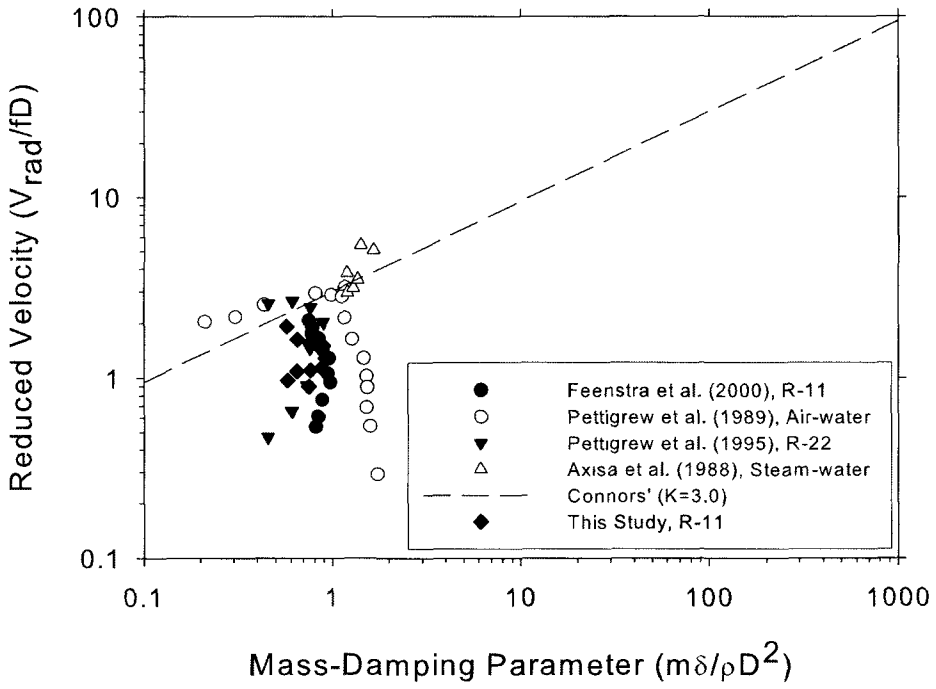

Figure 5.8. Stability map based on the RAD pitch velocity and RAD void fraction.

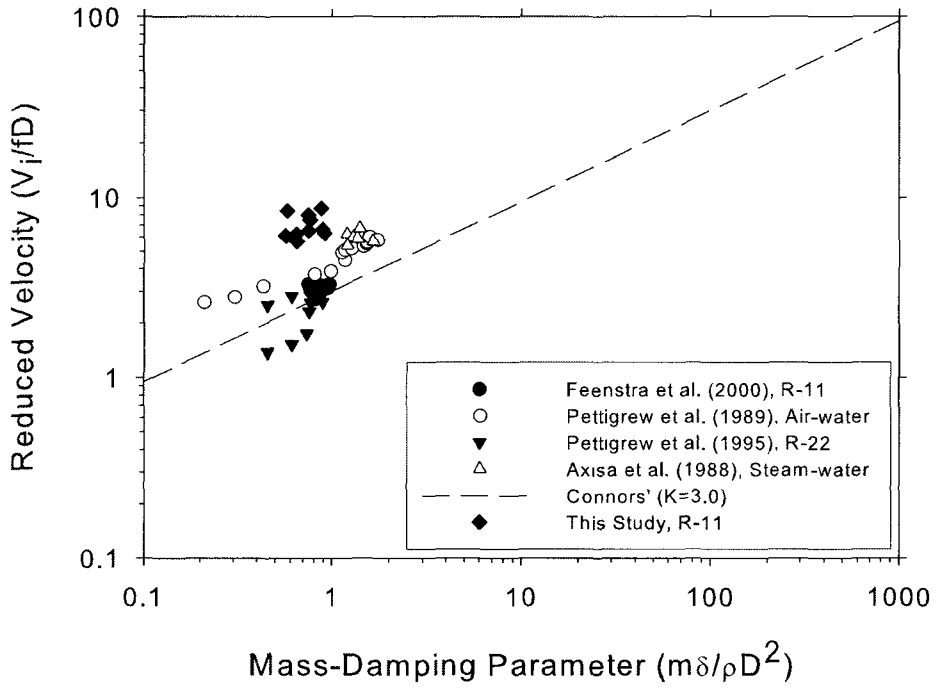

Figure 5.9. Stability map based on the Interfacial velocity and RAD void fraction.

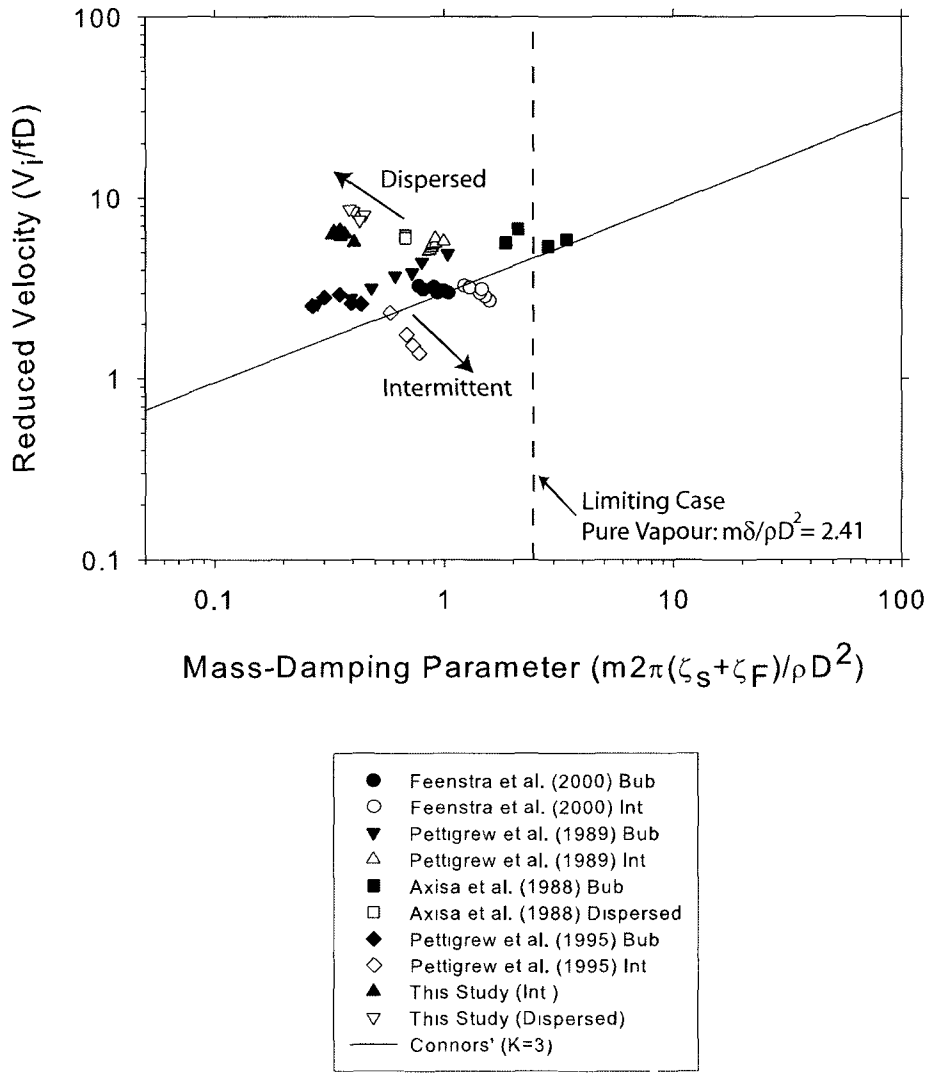

Figure 5.10. Stability map based on interfacial damping. For the case of dispersed flow, the mass-damping parameter shows unexpected results. The term ζ_F is calculated as ζ_i/Ca_p.

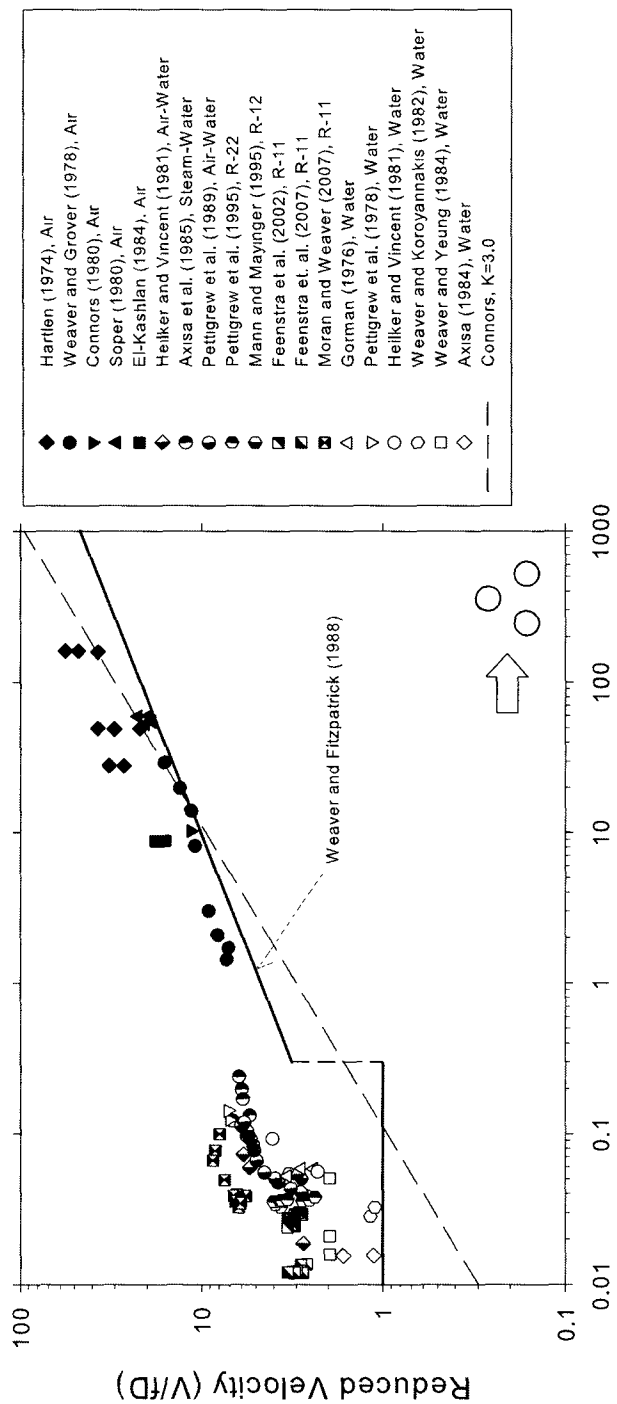

Figure 5.11. Stability map for two-phase data based on damping in air (Parallel Triangular Array). The reduced velocity is based on the pitch velocity for single-phase data and the interfacial velocity for two-phase data.

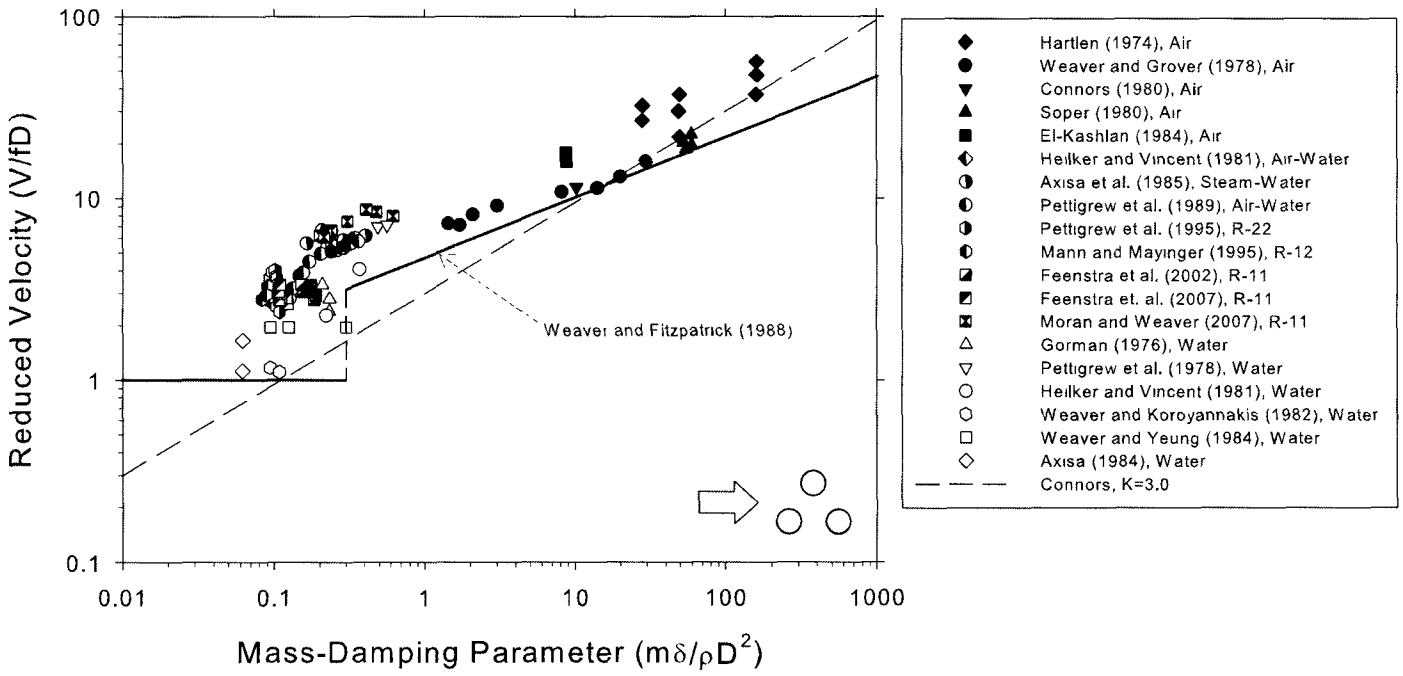

Figure 5.12. Stability map based on damping in stagnant fluid. The in-air damping is plotted based on the structural damping. The liquid and two-phase damping are plotted based on the damping in stagnant liquid. The reduced velocity is based on the pitch velocity for single-phase data and the interfacial velocity for two-phase data.

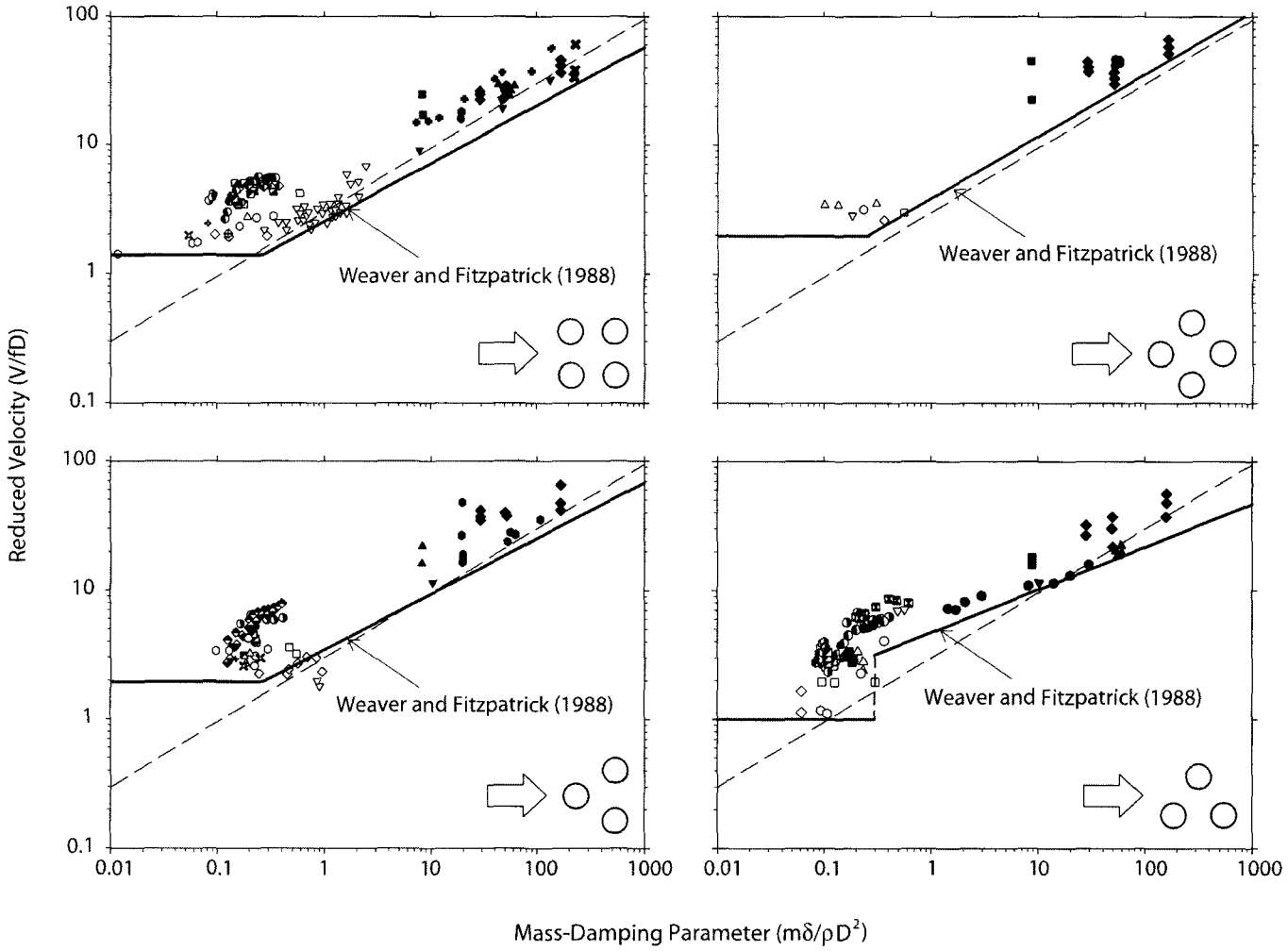

Figure 5.13. Stability maps for several bundle configurations based on stagnant-fluid damping. The reduced velocity is based on the pitch velocity for single-phase data and the interfacial velocity for two-phase data.

CHAPTER 6

Conclusions and Recommendations

Flow-induced vibration experiments were conducted to study the response of a parallel triangular tube array subjected to two-phase cross-flows. In the nuclear industry, steam generators are particularly sensitive to flow-induced vibration problems, especially in locations where two-phase cross-flow occurs. Avoiding a potential failure is a serious concern in terms of cost and safety.

The primary intent of this work was to improve our understanding of the physical mechanisms that play a role in damping and fluidelastic instability in two-phase flows. The characteristic unsteadiness of the latter makes this a very complex problem, influenced by a large number of parameters. In order to improve the estimated values of reduced velocity and mass-damping parameter used in stability maps, an experimental program was undertaken introducing a number of changes from the traditional approach in terms of measurement and data analysis. Some of the current design guidelines developed for heat exchangers are based on simplified and rather inaccurate models. In this study, we used a different approach to obtain more ac-

curate estimates of void fraction, flow density, flow velocity and damping. A single-component mixture was used as the working fluid, allowing for a better modelling of the real steam-water problem than air-water mixtures, due to its phase change capability. The void fraction, usually based on the HEM model, was measured directly by using a gamma densitometer, eliminating the inaccuracies introduced by the no-slip assumption. A new technique was developed and implemented to obtain more reliable damping estimates, minimizing the effect of the added mass fluctuation produced by the unsteady nature of the flow. The contributions to the current body of knowledge in the field of two-phase flow-induced vibrations in tube arrays that were produced by this experimental study, are summarized as follows:

1. A new method was developed for improved and more reliable damping measurements in two-phase flow across tube bundles. A pair of electromagnets was used to "pluck" the monitored tube from outside the test section, allowing for the capturing of the decay trace response in a non-intrusive fashion. Damping was calculated using the logarithmic decrement method and an exponential fitting based on the tube decay response. The results were compared against the half-power bandwidth method, which uses the tube averaged frequency response spectrum to compute the damping ratio. The results show that the half-power method substantially over-predicts the damping for low void fractions (bubbly flows). It was demonstrated that the differences between the methods are caused by natural frequency fluctuations, triggered by local void changes and relative tube modes. The frequency shifting phenomenon was observed to be a function of void fraction, being stronger at low voids. At higher void fractions, where the flow regimes are intermittent or dispersed, the fluid added mass effects are not important, reducing the difference in results between the exponential fitting and the half-power bandwidth method.

2. The present results show that damping is not independent of mass flux as previously assumed. Based on the damping results obtained by using the exponential

fitting to the decay trace, the effect of flow velocity (mass flux) on the damping ratio was evaluated by plotting iso-contours of damping on a grid of RAD void fraction and pitch mass flux. Although previous studies concluded that the mass flux had little or no effect on the damping ratio (Carlucci, 1980; Carlucci and Brown, 1983; Pettigrew et al., 1989a) it has been discovered that the effect of mass flux is strong for a range of void fraction between 15 and 60%. The mass flux seems to have little influence on the total damping ratio for void fractions lower than 15% and higher than 60%. Damping values based on the assumption that they are independent of mass flux may be significantly in error over the void fraction range from 15 to 60%.

3. A dimensional analysis was carried out to investigate the relationship between damping and two-phase flow related parameters. It is shown that the inclusion of surface tension through the Capillary number appears to be useful when combined with the two-phase component of the damping ratio (interfacial damping). A strong dependence of damping on flow regime has been clearly established by plotting the interfacial damping versus the void fraction. This is a distinct improvement over the previous approach, which does not distinguish the effects of flow regime. When the data is smoothed using statistical analysis, the change of the interfacial damping as a function of flow regime becomes more evident. At low void fractions (bubbly flows), the collapse of the damping data over a range of void fractions and mass fluxes is very good. In the dispersed flow region, a similar behaviour is observed. For the intermittent flow regime, the damping data is very scattered due to flow instability characterized by large random temporal and spatial local void fluctuations. However, it seems that for intermittent flows the interfacial damping does not show a clear dependence on void fraction.

4. An essential component in reliably establishing the velocity threshold for fluidelastic instability, is a measure of the energy dissipation available in the system

to balance the energy input from the flow. Traditionally, the damping measure used has been the half-power bandwidth value obtained at half the critical mass flux. The present analysis argues that this is not an appropriate measure and demonstrates that the use of quiescent fluid damping provides a measure of the energy dissipation, which produces a much more logical trend in the stability behaviour.

5. It is proposed that the interfacial velocity be used with the RAD density and quiescent fluid damping in the traditional parameters used to define the fluidelastic instability, i.e. reduced velocity and the mass-damping parameter. This approach collapses the available data well and provides the expected trend of two-phase flow stability data over the void fraction range from liquid to gas flows. The resulting stability maps represent a significant improvement over existing maps for predicting fluidelastic instability of tube bundles in two-phase flows. This result also tends to confirm the hypothesis that the basic mechanism of fluidelastic instability is the same for single and two-phase flows.

Recommendations:

Based on some of the difficulties and questions that arose during this research, there are clearly a number of areas that warrant further research. Among those are:

1. Void fraction distribution: The RAD void fraction used in the present research is considered superior to the traditional HEM model because it accounts for the difference in velocity between the phases. However, this measurement of void fraction is an average value obtained immediately upstream of the bundle. It seems likely that the average void fraction is not the same down the flow lanes between the tubes as it is in the tube wakes. This uneven local void distribution is likely to be dependent on mass flux, average void fraction and tube array geometry. It would be very interesting to carry out a detailed study of void fraction distribution in tube bundles and the determine its potential effects on damping, tube response and fluidelastic instability.

2. Physics of damping in two-phase flows: The present research showed that two-phase damping increases in the bubbly flow regime, has wide scatter but is relatively independent of void fraction in the intermittent flow regime, and decreases rapidly in the dispersed flow regime. It seems that interfacial area and flow steadiness are important factors in determining the damping, but the physics are not really understood. Additionally, the present normalization of damping includes the surface tension through the Capillary number, but more data is required to fully establish the validity of this scaling parameter. Further research is required to improve our understanding of the physics and scaling of damping in two-phase flows.

3. Interfacial Velocity: The present as well as other recent research, has shown that interfacial velocity apparently provides the best measure of two-phase flow velocity for scaling fluidelastic instability in tube arrays subjected to two-phase cross-flow. However, the reason for this is not clear. Basic research which studies the details of local void and interfacial velocity and their effects on tube response and the fluidelastic instability threshold could help our understanding of these parameters and, perhaps, provide further confidence that interfacial velocity is the most appropriate characteristic velocity measure in two-phase flows.

References

Anscutter, F., Béguin, C., Ross, A., Pettigrew, M., and Mureithi, N. (2006). Two-phase damping and interface surface area in tubes with internal flow. In *ASME Pressure Vessels and Piping Conference (PVP2006)*, volume 4A, Paper No. 93878, Vancouver, BC, Canada.

ASHRAE (1991). *ASHRAE Handbook: Fundamentals - SI Edition.* American Society of Heating, Refrigeration and Air-Conditioning Engineers, Atlanta, Georgia.

Au-Yang, M. K. (2001). *Flow-Induced Vibration of Power and Process Plant Components: A Practical Workbook.* ASME Press, New York.

Axisa, F., Antunes, J., and Villard, B. (1990). Random Excitation of Heat Exchanger Tubes by Cross-Flows. *J Fluid Struct*, 4(1):321- 341.

Axisa, F., Boheas, M. A., and Villard, B. (1985). Vibration of tube bundles subjected to steam-water cross-flow: A comparative study of square and triangular arrays. In *8th International Conference of Structural Mechanics in Reactor Technology*, number B1/2, Brussels.

Axisa, F., Wullschleger, M., and Villard, B. (1988). Two-phase cross-flow damping in tube arrays. In *ASME PVP Conference*, volume 133, pages 9–15, Pittsburgh PA, USA. ASME, ASME Publications.

Azzam, Z. Z. (2004). Development of an optical technique for measuring void fraction. Master's thesis, McMaster University, Hamilton, Canada.

Baj, F. and de Langre, E. (2003). Scaling of damping induced by bubbly flow across tubes. *J Fluid Struct*, 17:351-364.

Barnea, D. (1987). An Unified Model for predicting Flow-Pattern transitions for the whole range of pipe inclinations. *Int J Multiphase Flow*, 13(1):1 12.

Blevins, R. D. (1974). Fluidelastic whirling of a tube row. *J Press Vess Tech*, 96:263 267.

Blevins, R. D. (1979). Fluid damping and the whirling instability of tube arrays. In *3rd National Congress on Pressure Vessel and Piping Technology (PVP)*, San Francisco CA, U.S.A. ASME.

Blevins, R. D. (1990). *Flow Induced Vibration*. Krieger Publishing Company, Malabar, Florida, second edition.

Blevins, R. D. (2001). *Formulas for Natural Frequency and Mode Shape*. Krieger Publishing Company, Malabar, Florida, first (revised) edition.

Carlucci, L. N. (1980). Damping and Hydrodynamic Mass of a Cylinder in Simulated Two-Phase Flow. *J Mech Design*, 102:597–602.

Carlucci, L. N. and Brown, J. D. (1983). Experimental studies of Damping and Hydrodynamic Mass of a Cylinder in Confi"Nucl Eng Des" Two-Phase Flow. *J Vib Acoust Stress*, 105:83–89.

Chan, A. M. and Banerjee, S. (1981). Design aspects of gamma densitometers for void fraction measurements in small scale two-phase flows. *Nucl Instrum Methods*, 190:135–148.

Chandler, C. (2005). Methods of determining a damping ratio from a single impact test. In *ASME PVP Conference*, Paper No. 71041, Denver, U.S.A.

Chen, S. S. (1978). Cross-flow-induced vibrations of heat exchanger tube banks. *Nucl Eng Des*, 47:67 86.

Chen, S. S. (1983a). Instability mechanisms and Stability criteria of a group of Circular Cylinders Subjected to Cross-Flow. Part I -Theory. *J Vib Acoust Stress*, 105:51-58.

Chen, S. S. (1984). Guidelines for the Instability Flow Velocity of Tube Arrays in Cross-Flow. *J Sound Vib*, 93(3):439–455.

Cleveland, W. S. (1994). *The elements of graphing data*. Hobart Press, revised edition.

Collier, J. G. and Thome, J. R. (1996). *Convective Boiling and Condensation.* Clarendon Press, third edition.

Connors, H. J. (1970). Fluidelastic vibration of heat exchanger tube arrays excited by crossflow. In *Flow-Induced Vibration in Heat Exchangers*, pages 42 56. ASME.

Consolini, L., Robinson, D., and Thome, J. R. (2006). Void fraction and two-phase pressure drops for evaporating flow over horizontal tube bundles. *Heat Transfer Engineering*, 27(3):5 21.

Dam, R. F. (1991). Two-phase flow-induced vibrations for tube banks in cross flow: Creating an experimental facility. Master's thesis, McMaster University, Hamilton, Canada.

de Langre, E. (2006). Private Communication.

de Langre, E. and Villard, B. (1998). An upper bound on random buffeting forces caused by two-phase flows across tubes. *J Fluid Struct*, 12:1005–1023.

Dowlati, R., Chan, A. M. C., and Kawaji, M. (1992). Hydrodynamics of Two-Phase flow across a horizontal in-line and staggered rod bundle. *J Fluids Eng*, 114:450–456.

EIA (2007). Energy Information Administration: Annual energy outlook, DOE/EIA-0383. www.eia.doe.gov.

Eisinger, F. L., Rao, M. S. M., Steininger, D. A., and Haslinger, K. H. (1995). Numerical simulation of cross-flow-induced fluidelastic vibration of tube arrays and comparison with experimental results. *J Press Vess Tech*, 117:31–39.

Feenstra, P. A. (1993). Two-phase flow-induced vibration in heat exchanger tube arrays: An experimental investigation. Master's thesis, McMaster University, Hamilton, Canada.

Feenstra, P. A. (2000). *Modelling Two-Phase Flow-Excited Fluidelastic Instability in Heat Exchanger Tube Arrays.* PhD thesis, McMaster University, Hamilton, Canada.

Feenstra, P. A., Judd, R. L., and Weaver, D. S. (1995). Fluidelastic Instability in a Tube Array subjected to Two-Phase R-11 CrossFlow. *J Fluid Struct*, 9:747- 771.

Feenstra, P. A., Weaver, D. S., and Judd, R. L. (2002). Modelling Two-Phase Flow Excited Damping and Fluidelastic Instability in Tube Arrays. *J Fluid Struct*, 16(6):811 840.

Feenstra, P. A., Weaver, D. S., and Nakamura, T. (2003). Vortex Shedding and Fluidelastic Instability in a normal square tube array excited by Two-Phase Cross-Flow. *J Fluid Struct*, 17:793-811.

Gamio, C. and Pinto, W. (1999). Shell and tube exchanger failures spur reliability programs. *Oil and Gas J*, pages 71 74.

Goyder, H. (2002). Flow-induced vibration in heat exchangers. *Inst of Chem Eng*, pages 226–323.

Grant, I. (1976). Pressure drop on the shell side of shell-and-tube heat exchangers in single and two-phase flows. Technical report, HTFS, Design Report No. 16.

Grant, I. and Chisholm, D. (1979). Two-phase flow on the shell side of a segmentally baffled shell-and-tube heat exchanger. *J Heat Transfer*, 101:38–42.

Green, S. J. and Hetsroni, G. (1995). PWR Steam Reactors. *Int J Multiphase Flow*, 21:1–97.

Hara, F. (1987). Vibrations of Circular Cylindrical Structures subjected to Two-Phase CrossFlows. *JSME Int J*, 30(263):711–722.

Hassan, M. A., Weaver, D. S., and Dokainish. M. A. (2002). A simulation of the turbulence response of heat exchanger tubes in lattice-bar supports. *J Fluid Struct*, 16(8):1145–1176.

Hassan, M. A., Weaver, D. S., and Dokainish, M. A. (2005). A new tube/support impact model for heat exchanger tubes. *J Fluid Struct*, 21:561–577.

Heilker, W. J. and Vincent, R. Q. (1981). Vibration in Nuclear Heat Exchangers due to Liquid and Two-Phase Flow. *J Eng Power*, 103:358–365.

Janzen, V. P., Han. Y., Smith, B. A., and Fluit, S. M. (2005). Vibration damping of stabilized steam generator tubes. In *ASME PVP Conference*, Paper No. 71666, Denver, U.S.A.

Khushnood, S., Khan, Z. M., Malik, M. A., Koreshi, Z. U., and Khan, M. A. (2004). A review of heat exchanger tube bundle vibrations in two-phase cross-flow. *Nucl Eng Des*, 203:233–251.

Lever, J. H. and Weaver, D. S. (1982). A Theoretical Model for Fluidelastic Instability in heat exchanger tube bundles. *J Press Vess Tech*, 104:147–158.

Lever, J. H. and Weaver, D. S. (1986a). On the stability behaviour of heat exchanger tube bundles: Part 1 – modified theoretical model. *J Sound Vib*, 107:375–392.

Lever, J. H. and Weaver, D. S. (1986b). On the stability behaviour of heat exchanger tube bundles: Part 2 - numerical results and comparison with experiments. *J Sound Vib*, 107:393–410.

Li, M. (1997). *An Experimental and Theoretical Study of Fluidelastic Instability in Cross Flow Multi-Span Heat Exchanger Tube Banks.* PhD thesis, McMaster University, Hamilton, Canada.

Longatte, E., Bendjeddou, Z., and Souli, M. (2003). Methods for numerical study of tube bundle vibrations in cross-flows. *J Fluid Struct*, 18:513–528.

McQuillan, K. W. and Whalley, P. B. (1985). Flow Patterns in Vertical Two-Phase Flow. *Int J Multiphase Flow*, 11(2):161–175.

Mureithi, N. W., Nakamura, T., Hirota, K., Wanatabe, Y., Kusanabe, T., and Takamatsu, H. (2002). Dynamics of an in-line tube array subjected to Steam-Water Cross-Flow. Part II: Unsteady fluid forces. *J Fluid Struct*, 16(2):137–152.

Nakamura, T., Fujita, K., Kawanishi, K., and Saito, I. (1986). A Study on the Flow-Induced Vibration in a Tube Array by Two-Phase Flow: 2nd. Report. *JSME Int J*, 52(473).

Nakamura, T., Fujita, K., Kawanishi, K., Yamagushi, N., and Tsuge, A. (1995). Study on the vibrational characteristics of a tube array caused by two-phase flow. Part I: Random vibration. *J Fluid Struct*, 9:519–538.

Nakamura, T., Hirota, K., and Tomomatsu, K. (2000). Some problems on the estimation of flow-induced vibration of a tube array subjected to two-phase flow. In Ziada, S. and Staubli, T., editors, *Flow-Induced Vibrations*, The Netherlands. A. A. Balkema.

Nakamura, T., Hirota, K., Tomomatsu, K., Kasahara, J., and Takamatsu, H. (1999). On positional effect of flexible tubes in a square array subjected to freon two-phase flow. In *ASME PVP Conference*, volume 389, pages 73–80, Boston, U.S.A.

Nakamura, T., Hirota, K., Wanatabe, Y., Mureithi, N. W., Kusanabe, T., and Takamatsu, H. (2002). Dynamics of an in-line tube array subjected to Steam-Water Cross-Flow. Part I: Two-phase damping and added mass. *J Fluid Struct*, 16(2):123–136.

Nicklin, D. J., Wilkes, J. O., and Davidson, J. F. (1962). Two-phase flow in vertical tubes. *Trans Inst Chem Engrs*, 40:61–68.

NIST/SEMATECH (2007). *National Institute of Standards and Technology: e-Handbook of Statistical Methods.* http://www.itl.nist.gov/div898/handbook/.

Noghrehkar, G. R., Kawaji, M., and Chan, A. M. C. (1999). Investigation of two-phase flow regimes in tube bundles under cross-flow conditions. *Int J Multiphase Flow*, 25:857–874.

Oengören, A. and Ziada, S. (1998). An In-depth Study of Vortex Shedding, Acoustic Resonance and Turbulent Forces in Normal Triangle Tube Arrays. *J Fluid Struct*, 12:717–758.

Païdoussis, M. P. (1982). A Review of Flow-Induced Vibrations in Reactors and Reactor Components. *Nucl Eng Des*, 74:31–60.

Païdoussis, M. P. (2006). Real-life experiences with flow-induced vibration. *J Fluid Struct*, 22:741–755.

Pettigrew, M. J. and Gorman, D. J. (1978). Vibration of heat exchanger tube bundles in liquid and two-phase cross-flow. In *Proceedings B. E. N. S. International Conference on Vibration in Nuclear Plants*, volume Paper 2.3, Keswick, UK.

Pettigrew, M. J. and Knowles, G. D. (1997). Some Aspects of Heat-Exchanger Tube Damping in Two-Phase Mixtures. *J Fluid Struct*, 11:929–945.

Pettigrew, M. J. and Taylor, C. E. (1993). Two-Phase Flow-Induced Vibrations. In Au-Yang, M. K., editor, *Technology for the 90's*, chapter 7, pages 812–864. ASME Press, New York.

Pettigrew, M. J. and Taylor, C. E. (1994). Two-Phase Flow-Induced Vibration: An Overview. *J Press Vess Tech*, 116:233–253.

Pettigrew, M. J. and Taylor, C. E. (2003a). Vibration analysis of shell-and-tube heat exchangers: An overview – Part 1: Flow, damping, fluidelastic instability. *J Fluid Struct*, 18:469–483.

Pettigrew, M. J. and Taylor, C. E. (2003b). Vibration analysis of shell-and-tube heat exchangers: An overview – Part 2: Vibration, response, fretting wear, guidelines. *J Fluid Struct*, 18:484–500.

Pettigrew, M. J. and Taylor, C. E. (2004). Damping of heat exchanger tubes in two-phase flow: Review and design guidelines. *Journal of Pressure Vessel Technology*, 126:523–533.

Pettigrew, M. J., Taylor, C. E., Fisher, N. J., Yetisir, M., and Smith, B. A. W. (1998). Flow-Induced Vibration: Recent findings and open questions. *Nucl Eng Des*, 185:249–276.

Pettigrew, M. J., Taylor, C. E., Janzen, V. P., and Whan, T. (2002). Vibration Behavior of Rotated Triangular Tube Bundles in Two-Phase Cross-Flows. *J Press Vess Tech*, 124:144–153.

Pettigrew, M. J., Taylor, C. E., Jong, J. H., and Currie, I. G. (1995). Vibration of Tube Bundles in Two-Phase Freon Cross-Flow. *J Press Vess Tech*, 117:321–329.

Pettigrew, M. J., Taylor, C. E., and Kim, B. S. (1989a). Vibration of Tube Bundles in Two-Phase Cross-Flow. Part I: Hydrodynamic Mass and Damping. *J Press Vess Tech*, 111:466–477.

Pettigrew, M. J., Tromp, J. H., Taylor, C. E., and Kim, B. S. (1989b). Vibration of Tube Bundles in Two-Phase Cross-Flow. Part II: Fluidelastic Instability. *J Press Vess Tech*, 111:478–487.

Price, S. J. (1995). A Review of the Theoretical Models for Fluidelastic Instability of Cylinder Arrays in Cross-Flow. *J Fluid Struct*, 9:463–518.

Price, S. J. (2001). An Investigation on the use of Connors' Equation to predict Fluidelastic Instability in Cylinder Arrays. *J Press Vess Tech*, 123:448–453.

Price, S. J. and Païdoussis, M. P. (1982). A theoretical investigation of the parameters affecting the fluidelastic instability of a double row of cylinders subject to cross-flow. In *3rd International Conference on Vibrations in Nuclear Plants*, pages 107–119, Keswick, U.K.

Price, S. J. and Païdoussis, M. P. (1983). Fluidelastic instability of a double row of ciscular cylinders subject to cross-flow. *J Vib Acoust Stress*, 95:59–66.

Price, S. J. and Païdoussis, M. P. (1986). A single flexible cylinder analysis for the fluidelastic instability of an array of flexible cylinders in cross-flow. *J Fluid Eng*, 108:193–199.

Roberts, B. W. (1966). Low frequency aeroelastic vibrations in a cascade of circular cylinders. *I. Mech. E. Mechanical Engineering Science Monograph*, (4).

Rogers, R. G., Taylor, C. E., and Pettigrew, M. J. (1984). Fluid effects on multi-span heat exchanger tube vibration. In *Pressure Vessel and Piping Technology (PVP)*, number H00316, San Antonio, Texas. ASME.

Schrage, D. S., Hsu, J. T., and Jensen, M. K. (1988). Two-phase pressure drop in vertical cross flow across a horizontal tube bundle. *AIChE J*, 34(1):107–115.

Schröder, K. and Gelbe, H. (1999). New Design Recommendations for Fluidelastic Instability in Heat Exchanger Tube Bundles. *J Fluid Struct*, 13:361–379.

Scott, P. M. (1987). Flow visualization of cross-flow induced vibrations in tube arrays. Master's thesis, McMaster University, Hamilton, Ontario, Canada.

Smith, S. (1968). Void fractions in two-phase flow: A correlation based upon an equal velocity model. *Proc. Inst. Mech. Eng.*

Suzuta, T., Ueno, T., Hirao, Y., and Tomomatsu, K. (1999). Measurement of interfacial velocities in gas-liquid upward two-phase flow across tube bundle. In *7th International Conference on Nuclear Engineering (ICONE-7).*

Taitel, Y., Barnea, D., and Dukler, A. E. (1980). Modelling Flow Pattern Transitions for Steady Upward Gas-Liquid Flows in Vertical Pipes. *AIChE J*, 26(3):345–354.

Tanaka, H. and Takahara, S. (1980). Unsteady fluid dynamic forces on a tube bundle and its dynamic effect on vibration. In Au-Yang, M. K., editor, *Flow-Induced Vibration of Power Plant Components - PVP*, volume 41, pages 77–92, New York. ASME.

Taylor, C. E., Currie, I. G., Pettigrew, M. J., and Kim, B. S. (1989). Vibration of Tube Bundles in Two-Phase Cross-Flow: Part III Turbulence Induced Excitation. *J Press Vess Tech*, 111:488 500.

Taylor, C. E., Pettigrew, M. J., and Currie, I. G. (1996). Random Excitation Forces in Tube Bundles subjected to Two-Phase Cross-Flows. *J Press Vess Tech*, 118:265–277.

Ulbrich, R. and Mewes, D. (1994). Vertical, upward gas-liquid two-phase flow across a tube bundle. *Int J Multiphase Flow*, 20(2):249–272.

Weaver, D. S. (1993). Vortex Shedding and Acoustic Resonance in Heat Exchanger Tube Arrays. In Au-Yang, M. K., editor, *Technology for the 90's*, chapter 6, pages 776–810. ASME Press, New York.

Weaver, D. S. (2003). *Flow-Induced Vibrations: Lecture Notes.* McMaster University, Hamilton, Canada.

Weaver, D. S. and El-Kashlan, M. (1981a). The effect of Damping and tube Mass Ratio on the stability of a Tube Bank. *J Sound Vib*, 76(2):283–294.

Weaver, D. S. and El-Kashlan, M. (1981b). On the number of rows require to study Cross-Flow Induced Vibrations in Tube Banks. *J Sound Vib*, 75(2):265–273.

Weaver, D. S. and Feenstra, P. A. (2002). Flow-Induced Vibration of a Parallel Triangular Tube Array with asymmetric support Stiffness subjected to Cross-Flow of Two-Phase Refrigerant 11. Technical report, McMaster University, Hamilton, Ontario, Canada.

Weaver. D. S. and Fitzpatrick, J. A. (1988). A Review of Cross-Flow Induced Vibrations in Heat Exchangers Tube Arrays. *J Fluid Struct*, 2:73–93.

Weaver, D. S. and Koroyannakis, D. (1983). Flow-Induced Vibrations of Heat Exchanger U-Tubes: A Simulation to study the effects of Asymmetric Stiffness. *J Vib Acoust Stress*, 105:67–75.

Weaver, D. S. and Lever, J. (1977). Tube frequency effects on cross-flow induced vibrations in tube arrays. In *5th Biennal Symposium on Turbulence*, volume IV, Dept. of Chemical Engineering, University of Missouri-Rolla.

Weaver, D. S. and Yeung, H. C. (1984a). Approach flow direction effects on the cross-flow induced vibrations of a square array of tubes. *J Fluid Struct*, 87(3):469–482.

Weaver, D. S. and Yeung, H. C. (1984b). The effect of tube mass on the response of various tube arrays in water. *J Sound Vib*, 93(3):409–425.

Westermann, G. D. (1987). The design and construction of a flow loop for the study of two-phase crossflow-induced vibration of heat exchangers. Master's thesis, McMaster University, Hamilton, Canada.

Yetisir, M. and Weaver, D. S. (1993a). An Unsteady Theory for Fluidelastic Instability in an Array of Flexible Tubes in Cross-Flow. Part II: Results and Comparison with Experiments. *J Fluid Struct*, 7:767–782.

Yetisir, M. and Weaver, D. S. (1993b). An Unsteady Theory for Fluidelastic Instability of Flexible Tubes in Cross-Flow. Part I: Theory. *J Fluid Struct*, 7:751–766.

Ziada, S., Oengören, A., and Bühlmann, E. T. (1989a). On Acoustical Resonance in Tube Arrays, Part I: Experiments. *J Fluid Struct*, 3:293–314.

Ziada, S., Oengören, A., and Bühlmann, E. T. (1989b). On Acoustical Resonance in Tube Arrays, Part II: Damping Criteria. *J Fluid Struct*, 3:315–324.

Zuber, N. and Findlay, J. (1965). Average volumetric concentration in two-phase flow systems. *J Heat Transf*, 87:453–468.

APPENDIX A

Theory of Random Vibrations

The turbulence-induced vibration distinguishes itself from the other flow-induced vibration phenomena in that, like dust or noise or weed is to our everyday, it is a necessary "evil" in the power and process industries (Au-Yang, 2001). Unlike vortex shedding of fluidelastic instability, which can be eliminated or minimized by design standards, the turbulence buffeting cannot be avoided in virtually any industrial application, and in some cases, cannot even be reduced.

Figure A.1 represents the time history of the pressure in a fixed point within a turbulent flow. It clearly produces a random force that can be dealt only by probabilistic methods, although using this approach we sacrifice the possibility of determine the time history of the response. Instead, we are satisfied by computing the root mean square (rms) values of the responses, in order to devise the potential for damage on the structure.

The fluctuating forces induced over the tubes within the array are random functions of time and space. Convenient formulations for describing such an excitation field and for computing the tube response can be developed, starting with the classical random linear vibration theory (Axisa et al., 1990). Additional simplifications can also be made, i. e. the velocity profile (in cross-flow) is uniform, the fluid has a uniform density and only the fundamental mode of the tube is considered.

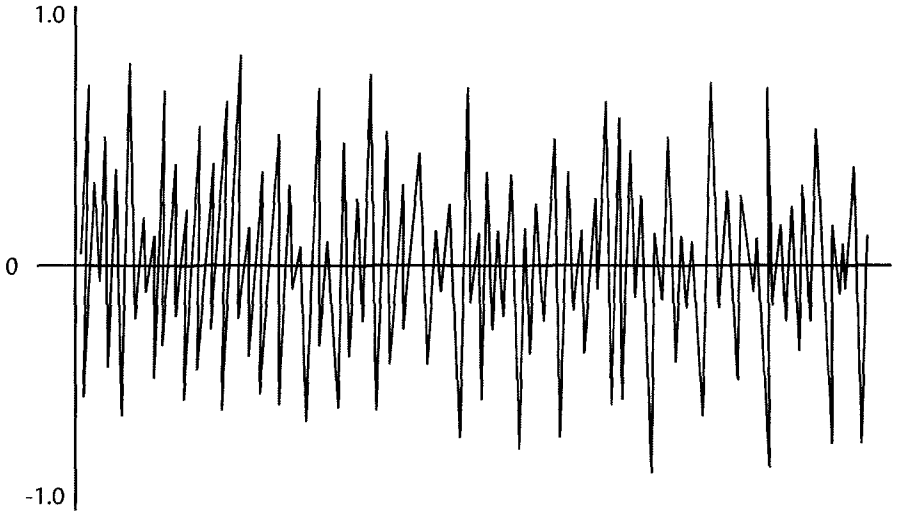

Figure A.1. Time history of fluctuating pressure in a turbulent flow (Au-Yang, 2001)

Let $\mathbf{F}(s,t)$ be the random force per unit length of the tube, acting at a location s along the latter. If this force is assumed to be stationary and ergodic, the it can be described by its cross-correlation spectrum, formally defined as the Fourier transform:

$$\psi_F(s_1, s_2, f) = \int_{-\infty}^{\infty} R_F(s_1, s_2, \tau) e^{-2i\pi f\tau}\, d\tau \tag{A.1}$$

In this case, R_F is the cross-correlation function between the locations s_1 and s_2:

$$R_F(s_1, s_2, \tau) = \lim_{\tau\to\infty} \frac{1}{2T} \int_{-T}^{T} \mathbf{F}(s_1, t) \cdot \mathbf{F}(s_2, t+\tau)\, dt \tag{A.2}$$

For practical applications, a dimensionless form is often preferred. The quantities used for the scaling can be defined as follows:

1. The steady cross-flow velocity V_o can be scaled using the pitch velocity ($V_p = V_o \frac{P}{P-D}$)
2. The fluctuating forces can be scaled using the dynamic head ($F = \frac{1}{2}\rho V_p^2 D$)
3. The frequency is expressed as a reduced frequency, ($f_r = \frac{fD}{V_p}$)

Substituting these scaling relations into equation A.1. we obtain the expression

$$\tilde{\psi}_F(s_1, s_2, f_r) = \left(\frac{1}{2}\rho V_p^2 D\right)^{-2} \frac{V_p}{D} \psi_F(s_1, s_2, f) \tag{A.3}$$

Since the tubes are subjected to an uniform flow, the fluctuations are not conveyed along the tubes. The cross-correlation spectrum can be rewritten as real function of the form:

$$\psi_F(s_1, s_2, f) = \phi'_F(f)\gamma(s_1, s_2) \tag{A.4}$$

It can be seen in equation A.4 that the space and time variables are separated. The quantity ϕ'_F represents the autocorrelation spectrum of the forces per unit length, which can be restricted to positive frequencies. The coherence function γ characterizes the degree of correlation of the forces along the tube, and can be approximated by

$$\gamma = \exp\left(-\frac{|s_1 - s_2|}{\lambda_c}\right) \tag{A.5}$$

The term λ_c represents the correlation length, a quantity difficult to determine, and for which the experimental measurements are very scarce (Axisa et al., 1990). When λ=1 means that there is a complete axial correlation.

The final form of the power spectrum per unit length of the tube can be written as follows:

$$\psi_F(s_1, s_2, f_r) = \left(\frac{1}{2}\rho V_p^2 D\right)^2 \frac{D}{V_p} \exp\left(-\frac{|s_1 - s_2|}{\lambda_c}\right) \left[\tilde{\phi}(f_r)\right] \tag{A.6}$$

From this point, the tube vibration power spectrum can be determined by the product of the forcing spectrum S_F and the square of the transfer function of the system. In general,

$$S_y(s, f) = \int_0^1 \int_0^1 |H(s, f)|^2 S_F(s_1, s_2, f_r)\, ds_1 ds_2 \tag{A.7}$$

For a single degree of freedom system, the transfer function can be estimated as (?):

$$|H(s, f)|^2 = \frac{\sigma^2(s)}{16\pi^4 f_n^4 (mL)^2} \frac{1}{\left[1 - (f/f_n)^2\right]^2 + \left[2\zeta(f/f_n)\right]^2} \tag{A.8}$$

Where m is the generalized mass of the tube per unit length, that is, the tube mass plus the hydrodynamic of added mass. The mode shape $\sigma(s)$ can be assumed as that of a cantilevered tube, given by (Blevins, 2001):

$$\sigma(s) = \cosh\left(\frac{\lambda_i s}{L}\right) + \cos\left(\frac{\lambda_i s}{L}\right) - \kappa_i \left[\sinh\left(\frac{\lambda_i s}{L}\right) + \sin\left(\frac{\lambda_i s}{L}\right]\right) \tag{A.9}$$

For the first mode, $\lambda_1 = 1.875$ and $\kappa_1 = 0.734$. Combining equations A.6, A.7 and A.8, we have:

$$S_y(s,f) = \left(\frac{1}{2}\rho V_p^2 D\right)\left(\frac{D}{V_p}\right)\frac{1}{16\pi^4}\frac{\left[\tilde{\phi}_F(f_r)\right]\sigma^2(s)J^2}{(mL)^2 f_n^4\left\{\left[1-(f/f_n)^2\right]^2 + \left[2\zeta(f/f_n)\right]^2\right\}} \tag{A.10}$$

In equation A.10, J is the joint acceptance. The physical meaning of this parameter is related to the matching between the spatial distribution of the forcing function and the mode shapes of the tube. In more rigorous terms, the joint acceptance can be expressed as

$$J^2 = \left(\frac{\pi}{2}\right)^2 \int_0^1 \int_0^1 \sigma(s_1)\sigma(s_2)\exp\left(\frac{|s_1 - s_2|}{\lambda_c}\right) ds_1 ds_2 \tag{A.11}$$

The joint acceptance can be also determined as $(L_{cn}/L)^2$, where L_{cn} is the modal joint acceptance and L is the length of the tube (Axisa et al., 1990). The rms amplitude of tube vibration (per unit length) can be derived from S_y as follows,

$$y_{rms}^2(s) = \int_0^\infty S_y(s, f_r)\, df \tag{A.12}$$

If the damping is considered small and the forcing spectrum is broadband and constant over the frequency range of the tube natural frequency, then we may write:

$$\left(\frac{y_{rms}(s)}{L}\right)^2 = \left(\frac{1}{2}\rho V_p^2 D\right)\left(\frac{f_n D}{V_p}\right)\frac{J^2\sigma^2(s)}{64\pi^3(mL)^2\zeta f_n^4}\left[\tilde{\phi}_F(f_r)\right]_n \tag{A.13}$$

For the particular case where the correlation length is less than 1% of the tube length, $\lambda_c \leq 0.01$, the joint acceptance can be approximated by

$$J^2 = a_n \lambda_c \tag{A.14}$$

The value of a_n depends on the tube geometry, and it is equal to 0.5 for the case of a cantilevered tube. For comparison purposes, it is common to express the forcing spectrum in a dimensionless form, in order to account for tubes with different lengths.

Remember that a shorter tube will be subjected to higher unbalanced forces than a larger tube, due to the change in the ratio of correlation length of the flow to the tube length (increases for shorter tubes). The final form of the root mean square amplitude is:

$$\frac{\bar{y}}{D} = \frac{1}{16\pi^{3/2}} \frac{\rho D^2}{m} \left(\frac{V_p}{f_n D}\right)^{3/2} \left(\frac{J}{\zeta^{1/2}}\right) \left[\tilde{\phi}_F(f_r)\right]^{1/2} \sigma(s) \tag{A.15}$$

The values of the dimensionless spectrum as a function of the reduced frequency can be determined based on the results of de Langre and Villard (1998).

APPENDIX B

Instrument Calibration

B.1 Strain Gauges

The strain gauges selected for this research and used both for the single-tube testing device for the electromagnets (see Chapter 4) and for the tube bundle, were general purpose Vishay gauges model ED-DY-062AK-350. The dimensions of the gauges were 4 x 1.57 mm, due to the size limitations of the cylindrical tube supports (6.35 mm in diameter). The gauges were designed to operate in a temperature range between -195 and 205 °C. Since they were going to be exposed to high-velocity gas-liquid freon, a special coating (M-Bond 43-B) had to be applied to protect them from the chemical attack caused by the fluid.

Both the transverse and streamwise strain gauges were calibrated in air by applying a known static deflection at the tip of the tube and measuring the corresponding output signal (voltage). The bundle was mounted perfectly horizontal on a heavy vise and the deflections were performed by using a height gauge. Figures B.1 and B.2 show the calibration curves for the transverse and streamwise strain gauges respectively.

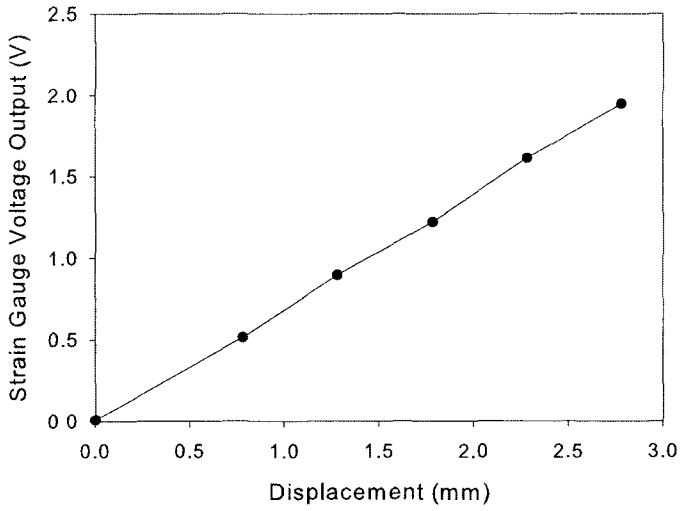

Figure B.1. Calibration curve for the strain gauge located in the direction transverse to the flow. The calibration constant was 0.685 V/mm.

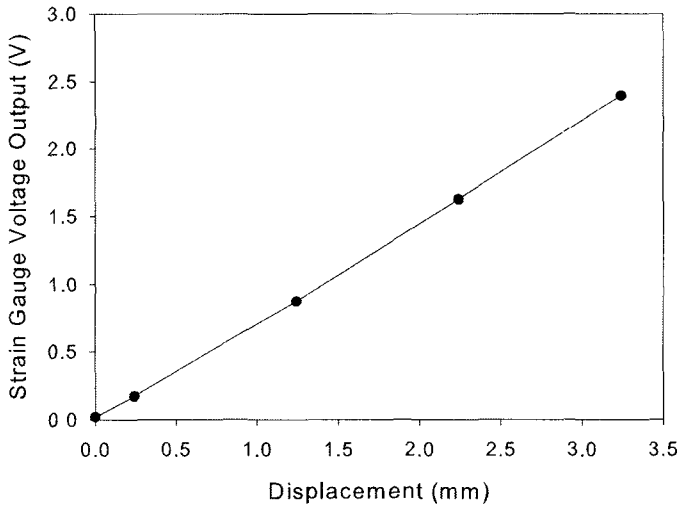

Figure B.2. Calibration curve for the strain gauge located in the direction parallel to the flow. The calibration constant was 0.695 V/mm.

B.2 Gamma Densitometer

The number of counts for the pure liquid and vapour phases was taken prior to performing every experiment. Before starting the experiment, the test section contained freon vapour at ambient temperature. This was achieved by closing the valve downstream the condenser in the previous experiment, causing the liquid freon to accumulate inside the condenser, and leaving the test section full of vapour. The gamma densitometer readings were taken and averaged over 300 seconds to obtain a more accurate estimate of the gas-phase count. Then, the test section was filled with liquid by opening the valve below the condenser, allowing the freon to level on both branches of the flow loop (condenser and test section). The recording process was initiated again. By proceeding this way, we ensure that the gamma densitometer reference counts are taken at the same temperature. At the end of some experiments, when the loop was warmer, the reading were taken again to evaluate the effect of temperature on the calibration of the gamma densitometer. The difference was never above 3%. This feature was taken into consideration by Feenstra (2000), who added a correction factor to the RAD void fraction to account for temperature change effects. The main parameters used for the calibration are summarized in Table A.1.

Table B.1. Main parameters for gamma densitometer calibration and operation.

Parameter	
Source	Barium 133
Scintillator Excitation	600 Volts
Coarse Gain	160
Fine Gain	1.0
Discriminator	3.0
Time Constant	0.1 sec

APPENDIX C

Uncertainty Analysis

This appendix discusses the experimental uncertainty of the variables used in this research. The uncertainties associated to the aforementioned parameters are based upon the following premises:

- The power transferred by the heaters was measured with a powermeter having a digital display measurement resolution of 0.1 kW. The uncertainty in this measurement is estimated to be ±0.05 kW, which represents half of the smallest division in the reading.
- The flow rate of R-11 circulating through the test section was measured with the orifice plates. The uncertainty in the pump motor speed is estimated to be ± 5 rpm, which corresponds to a flow rate uncertainty of about ±0.5 L/min. The uncertainty of the orifice-plate reading on the U-tube manometer is estimated to be ± 0.1" Hg, which is roughly the lowest resolution of the height difference of the mercury column that is discernable by eye. The E-type thermocouples have a measurement resolution of 0.01 mV, which corresponds to a temperature resolution of 0.16°C. A reasonable measurement uncertainty of this reading is half of the resolution which is ±0.005 mV or 0.08°C.
- The uncertainty in the thermodynamic quality was developed by combining the estimated uncertainties in three primary measurements discussed above: heater power (± 0.05 kW), flow rate (± 0.3 L/min) and thermocouple temperature

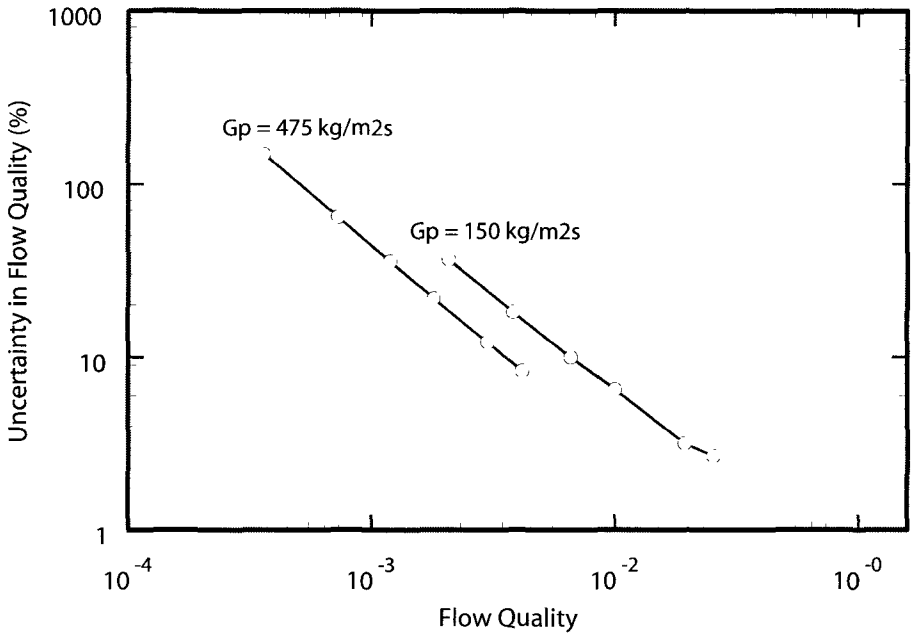

Figure C.1. Uncertainty in flow quality for R-11 data (Feenstra, 2000).

measurements (± 0.08°C). The curves in Figure C.1 represent the worst case combination of these three errors. Although the relative error seems excessive at low qualities, it must be remembered that the absolute value of the error is small, and of no great consequence to the accuracy of the fluidelastic data, which occurred at qualities at or above 0.01.

A guideline for estimating the uncertainty in void fraction measurements by radiation attenuation provided by Chan and Banerjee (1981), is based upon the error in the counting statistics, e_α, as follows,

$$e_\alpha = \left(S_n \sqrt{N_\alpha t}\right)^{-1} \tag{C.1}$$

For the Barium 133 source, the sensitivity, S_n, was 39%, the count rate in two phase flow, N_α, was between the count rates of liquid (2.841 mV) and gas (5.165 mV), and the counting period, t, was 300s. A conservative estimate of uncertainty using Equation C.1 is about ±2%. However, during the experiments the statistical behaviour of the counts was periodically monitored, and the worst case showed a standard deviation of about 4% of the mean count, N_α, over 5 samples. This leads to a 95% confidence interval for void fraction of about ±5% of the measurement. This

uncertainty is greater than that estimated by equation C.1, and is likely due to flow unsteadiness.

The uncertainty in the measurement of damping ratio, ζ_T, is difficult to determine because it depends upon several variables. For the half-power bandwidth method, it depends on the resolution of the frequency spectra compared with the bandwidth of the frequency peak and the goodness of fit of the least squares regression analysis. However, a practical estimate of this uncertainty was made assuming that the damping was independent of mass flux but dependent upon void fraction. A sample set of damping data was grouped according to void fraction over a range of mass flux conditions, and statistics were performed to determine the mean and standard deviation of these sets of samples. The 95% confidence interval was calculated for each data set and it appeared reasonable that an uncertainty of $\pm 15\%$ be assigned to the measured damping ratio. This relative uncertainty also applies to the log-decrement damping value, δ, since $\delta = 2\pi\zeta$. For the exponential fitting to the decay trace, the standard deviation of the results is shown in Chapter 4, Figure 4.9. These values are representative of the mass flux range studied.

APPENDIX D

Locally Weighted Polynomial Regression (LOESS)

LOESS (or LOWESS) denotes a method proposed by Cleveland (1994) that is known as "locally weighted polynomial regression". At each point in the data set, a low-degree polynomial is fit to a subset of data, with explanatory variable values near the point whose response is being estimated. The polynomial is fit using weighted least squares, giving more weight to points near the point of interest and less weight to points further away. The value of the regression function for the point is then obtained by evaluating the local polynomial using the explanatory variable values for that data point. The LOESS fit is complete after regression function values have been computed for each of the n data points. Many of the details of this method, such as the degree of the polynomial model and the weights, are flexible. The range of choices for each part of the method and typical defaults are briefly discussed next (NIST/SEMATECH, 2007).

The subsets of data used for each weighted least squares fit in LOESS are determined by a nearest neighbours algorithm. A user-specified input to the procedure called the "bandwidth" or "smoothing parameter" determines how much of the data is used to fit each local polynomial. The smoothing parameter (q), is a number between $(d+1)/n$ and 1, with d denoting the degree of the local polynomial. The value of q is the proportion of data used in each fit. The subset of data used in each weighted least squares fit is comprised of the nq (rounded to the next largest integer) points whose explanatory variables values are closest to the point at which

the response is being estimated. The reason why q is called the smoothing parameter is because it controls the flexibility of the LOESS regression function. Large values of q produce the smoothest functions that "wiggle" the least in response to fluctuations in the data. The smaller q is, the closer the regression function will conform to the data. The values of the smoothing parameter typically lie in the range 0.25 to 0.5 for most applications.

The local polynomials fit to each subset of the data are almost always of first or second degree; that is, either locally linear (in the straight line sense) or locally quadratic. Using a zero degree polynomial turns LOESS into a weighted moving average. Higher-degree polynomials would also work, but the results would not reflect the "spirit" of LOESS. LOESS is based on the ideas that any function can be well approximated in a small neighborhood by a low-order polynomial and that simple models can be fit to data easily. High-degree polynomials would tend to over-fit the data in each subset and are numerically unstable, making accurate computations difficult. Figure D.1 demonstrates a basic example of the application of LOESS to a given set of data, for a value of x equal to 8.

The first step is to calculate the nq parameter. This factor is equivalent to the number of points around the point of interest that will be used to perform the fitting. For the present example, q will be taken as 0.5, and the total number of data points is 20. A vertical strip, depicted by the dashed vertical lines in the upper left panel, is defined by centering the strip on x and putting one boundary at the 10th closest x_i to x.

Then, neighbourhood weights w_i are assigned to the points within the band, using the weight function shown in the upper right panel. The function has a maximum at $x = 8$ and decreases as we move from this value in either direction, becoming zero at the boundaries of the strip. The points closer to x receive the largest weight, and points further away receive less.

The next step is to fit a line to the data using least-squares with weight $w_i(x)$ at (x_i, y_i). The fit is shown in the lower left panel. The weight $w_i(x)$ determines the influence that each (x_i, y_i) has on the fitting of the line. The influence decreases as x_i increases in distance from x, and finally becomes zero. The initial LOESS fit at $x = 8$ is the value of the line at $x = 8$, represented by the filled circle. This value is shown as the result of the fitting in the lower right panel. The procedure is repeated for every value of x.

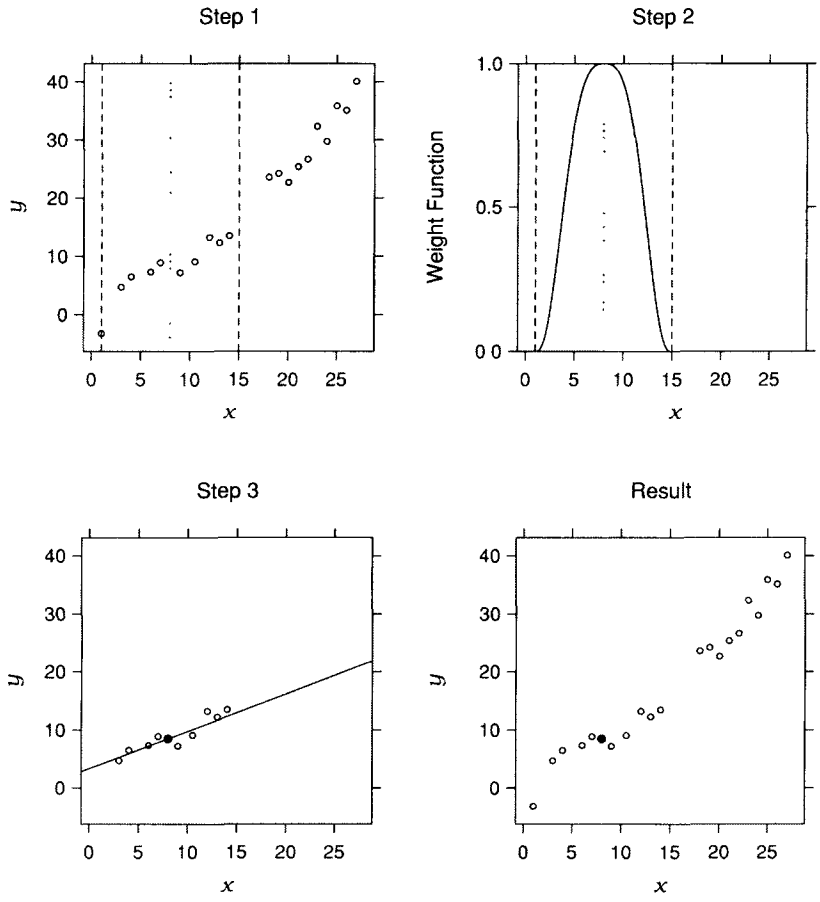

Figure D.1. Series of plots showing the LOESS fitting procedure Cleveland (1994).

APPENDIX E

Experimental Results

This Appendix presents the experimental results from the two series of experiments performed during this research. In test Series A, the tube bundle had one flexible tube surrounded by a fixed array. The purpose of this configuration was to obtain more reliable damping results, which can be affected by the hydrodynamic coupling between the tubes. In test Series B, all the tubes were flexible, allowing for the determination of the critical velocity and critical void fraction at the fluidelastic stability threshold.

The appendix is divided into three sections. First, the experimental data is tabulated for each experiment, indicating the mass flux utilized, RAD void fraction, natural frequency of the monitored tube, rms amplitude of vibration and total damping ratio where applicable. The second section includes representative raw frequency spectra obtained for three experiments in Series A. Finally, decay traces for different void fractions of two representative experiments are presented and its important features explained.

E.1 Frequency Spectra

As mentioned above, the behaviour of the natural frequency of the monitored tube in experiments TP-04, TP-02 and TP-11 (100, 250 and 500 kg/m^{2}s respectively) is

representative of the observations performed for all the mass fluxes studied. Only spectra from test Series A are shown in this section because these were subsequently used for determining the damping ratio, based on the half-power bandwidth method. It is important to note that for each experimental trial the true rms vibration amplitudes (shown for the larger peaks) were determined by integrating the amplitude peak over the frequency range of interest (40 to 60 Hz in most cases, see Feenstra, 2000). Even though the vibration amplitudes observed in the frequency spectra are not as large as those exhibited as a result of the electromagnetic excitation, the damping values obtained from both methods are still comparable. The validity of the assumption of linear-viscous damping up to amplitudes exceeding 5% of the tube diameter, has been demonstrated by the exponential fitting decay traces (see Figure 3.14).

It can be seen from Figures E.1, E.2 and E.3 that the broadening of the peak is strongly dependent on void fraction. The added mass fluctuations that occur as a consequence of density changes are more noticeable for voids below 50%, which correspond to bubbly flow and the transition to intermittent flows. These experimental frequency spectra look very similar to the frequency histograms presented in Chapter 4, in which the same effect of void fraction on frequency shifting was observed.

E.2 Decay Trace Responses

Figures E.4 and E.5 show representative decay traces at various RAD void fractions for a mass flux of 100 kg/m^{2}s (Experiment TP-04). In figure E.4 (top), the point in time where the electromagnets are shut-off is indicated. The maximum amplitude of vibration is around 9% of the tube diameter. As mentioned in Chapter 3, this initial amplitude was utilized with the objective of overcoming the excitation due to the flow, which can be significant, especially when approaching the fluidelastic stability threshold. Note that the amplitude of vibration is roughly constant while the electromagnets are operating.

In Figure E.4 (bottom), the amplitude seems to be varying prior to the shut-off of the electromagnets. This phenomenon occurs due to the strong frequency shifting observed during bubbly flows. The excitation frequency set-up for the electromagnetic device is based on the frequency obtained from the averaged frequency spectrum. Since the natural frequency of the monitored tube is constantly changing due to spatial and temporal changes in local void, the amplitude observed also varies. The amplitude of oscillation will be maximum when the frequency of the tube matches the frequency of the electromagnets, and it will diminish as the difference between these two increases. It is important to remark that the range of the decay trace used for the damping calculations was between 1 and 3% of the tube diameter, far from

the transient that occurs after the electromagnets are shut-off.

Figure E.5 shows the decay traces for void fractions of 61.8 and 74.7%. A change in vibration amplitude is also observed before shutting-off the electromagnets. For this trace, the maximum amplitude of vibration is larger than for the previous two decay traces. During the experiments, the electric current used for the electromagnet was set to 1A. After the transition from bubbly to intermittent flow regime, the same current produced larger maximum amplitudes, due to the combination of two effects. First, the fluidelastic forces start to become an important factor after a certain point during the experiment. Second, the increasing void fraction implies that the density of the flow is diminishing, reducing the resistance around the vibrating tube. Due to this effect, the current was adjusted down for some trials in order to avoid an excessive vibration of the monitored tube. Since we only used the decay trace between 1 and 3% of the tube diameter, the maximum amplitude produced by the electromagnets had no influence on the final results.

Figures E.6 to E.9 show the decay traces for mass fluxes of 250 kg/m^2s and 500 kg/m^2s respectively. While the amplitudes observed are slightly higher than for 100 kg/m^2s, the decay traces are similar in shape to those shown in Figures E.4 and E.5. The influence of mass flux on the shape of the decay traces does not seem to be as strong as that of the void fraction.

In some cases, the decay traces are not very smooth. Notice, for example, that in Figure E.9 (bottom) the decay trace is somewhat irregular. This is because it has been taken close to the stability threshold. Damping determined based on a single decay trace like this maybe unreliable which is why the results from several decay traces are averaged to estimate the damping ratio. We are confident that this methodology provides good estimates of the damping because the results are repeatable and agree well with those obtained using the half-power bandwidth approach at high void fractions.

These amplitude decay traces illustrate very well the value of the decay curve fitting approach. Turbulence excitation and frequency shifting create significant departures from the ideal decay of a simple sine wave, making the use of individual points of the decay traces unreliable for obtaining accurate estimates of damping. Fitting an exponential decay curve essentially averages out the irregularities in the amplitude and frequency of the experimental decay traces, thereby providing an improved estimate of the damping.

Damping Data
Series A: Fully Flexible Array

EXP.	Trial No.	Gp (kg/m^{4}s)	RAD Void	Frequency (Hz)	Exponential Fitting Damping Ratio (%)	Half-Power Damping Ratio (%)
TP04	1	104	0.045	40.75	0.54	1.300
TP04	2	104	0 268	45.00	1.48	2.270
TP04	3	104	0.493	48.00	1.21	1.540
TP04	4	104	0.618	48.50	0.65	1 010
TP04	5	104	0.693	48.50	0.67	0 870
TP04	6	104	0.693	48.50	0.60	0.770
TP04	7	104	0.712	48.75	0.61	0 760
TP04	8	104	0 747	48.75	0.52	0.580
TP04	9	104	0.763	48.75	0.42	0.630
TP04	10	104	0.776	48.75	0.40	0.510
TP04	11	104	0.789	48 75	0.28	0.540
TP04	12	104	0.796	48.75	0.12	0.470
TP04	13	104	0.808	48.75	0.11	1 220
TP03	1	153	0.082	42.50	0 88	1.150
TP03	2	153	0 231	44.75	1 21	2.260
TP03	3	153	0.418	47.50	1.26	2.170
TP03	4	153	0.471	47.75	1.56	1 83
TP03	5	153	0.528	47 50	1.16	1 76
TP03	6	153	0.570	48 00	1.18	1 58
TP03	7	153	0.623	48 25	1.14	1 01
TP03	8	153	0.654	48.50	0.75	0.82
TP03	9	153	0 683	48.50	0 77	0.87
TP03	10	153	0.711	48.75	0.62	0.81
TP03	11	153	0 752	48 75	0.56	0.6
TP03	12	153	0.776	48.75	0.47	0 55
TP03	13	153	0 780	48.75	0.40	0 53
TP03	14	153	0 813	48.75	0.22	0.44
TP03	15	153	0 833	48.75	0.14	0.34
TP09	1	203	0.138	42.75	1.72	1.904
TP09	2	203	0.268	45.00	1.53	2.164
TP09	3	203	0 375	45.50	1.71	2 192
TP09	4	203	0.472	46.50	1.23	1 745
TP09	5	203	0.521	46 75	1.55	1.563
TP09	6	203	0 569	47.00	1.29	1.404
TP09	7	203	0 618	47.25	1.29	1.128
TP09	8	203	0.642	47.25	1 08	1.027
TP09	9	203	0 656	47.25	0.97	0 915
TP09	10	203	0.685	47.25	0.91	0 842
TP09	11	203	0.701	47.25	0.94	0 863
TP09	12	203	0.720	47.50	0 76	0.843
TP09	13	203	0 735	47.50	0.74	0.714
TP09	14	203	0 753	47 50	0 52	0.678
TP09	15	203	0 763	47.50	0.56	0.558
TP09	16	203	0 775	47.50	0.47	0 526
TP09	17	203	0 792	47.50	0.45	0.486
TP02	1	256	0.161	43 00	1.54	2 04
TP02	2	256	0.265	45.25	1.74	2.56
TP02	3	256	0.340	46.50	1 92	2.43
TP02	4	256	0.404	47.00	2 08	2.24
TP02	5	256	0.456	47.25	1.78	2.08
TP02	6	256	0.506	47 50	1.75	1 87
TP02	7	256	0 524	47 50	1.55	1 75
TP02	8	256	0 548	47.75	1.50	1.8

Damping Data
Series A: Fully Flexible Array

EXP.	Trial No.	Gp (kg/m²s)	RAD Void	Frequency (Hz)	Exponential Fitting Damping Ratio (%)	Half-Power Damping Ratio (%)
TP02	9	256	0.597	47.75	1.46	1.41
TP02	10	256	0 624	48.00	1.46	1.25
TP02	11	256	0.645	48.25	1.16	1 19
TP02	12	256	0.677	48.50	0.91	1
TP02	13	256	0.683	48.50	0.77	0.87
TP02	14	256	0 711	48.75	0.73	0.94
TP02	15	256	0.736	48.75	0.67	0 75
TP02	16	256	0.753	48.75	0.61	0.69
TP02	17	256	0 769	48.75	0.44	0.62
TP02	18	256	0 798	48.75	0 40	0 51
TP05	1	300	0.034	41.25	0.35	0.5
TP05	2	300	0 031	41.25	0.50	0 5
TP05	3	300	0 112	41.50	1 28	1 693
TP05	4	300	0 242	45 00	1.87	2.911
TP05	5	300	0 343	45.50	1.35	2.49
TP05	6	300	0.425	46.50	1.57	1.992
TP05	7	300	0 479	47.00	1 32	1 583
TP05	8	300	0 527	47.00	1.55	1.517
TP05	9	300	0.562	47.25	1.29	1.416
TP05	10	300	0.577	47.25	1 12	1 358
TP05	11	300	0 598	47.50	0.95	0 99
TP05	12	300	0.624	47.50	0.88	1.214
TP05	13	300	0.648	47.50	1 01	0 95
TP05	14	300	0 659	47.50	0.69	1.044
TP05	15	300	0.687	47 75	0.94	1.006
TP05	16	300	0.704	47 75	0.76	0 769
TP05	17	290	0.723	47.75	0.63	0.659
TP12	1	356	0.206	42.00	2.06	2.167
TP12	2	356	0.326	44.75	2 02	2 418
TP12	3	356	0 387	45 00	1.93	2.392
TP12	4	356	0 434	45.50	1.72	2.1
TP12	5	356	0.471	46.00	1.56	1 989
TP12	6	356	0.507	46.25	1.56	1.672
TP12	7	356	0.546	46.50	1.17	1.325
TP12	8	356	0.575	46.50	0.88	1.243
TP12	9	356	0 601	47.00	0 88	1 054
TP12	10	356	0 621	47.00	0.99	1.003
TP12	11	356	0 636	47 00	0.54	0.84
TP12	12	356	0.652	47 00	0.59	0.876
TP12	13	356	0.672	47.25	0.47	0.759
TP12	14	356	0.691	47.25	0.66	0.724
TP12	15	356	0.713	47 25	0.42	0.54
TP12	16	356	0.732	47.25	0.40	0 429
TP12	17	356	0 747	47.50	0.20	0 285
TP06	1	400	0.011	41 25	0.50	0 698
TP06	2	400	0 048	41 50	0 69	0 952
TP06	3	400	0 192	43 50	1.52	2 303
TP06	4	400	0.265	45.25	1.69	2.668
TP06	5	400	0.344	45 75	1 88	2 093
TP06	6	400	0.397	46.50	1.28	2 197
TP06	7	400	0 449	46.75	1.62	2.103
TP06	8	400	0.486	47.00	1 62	1.669
TP06	9	400	0 530	47 00	1.49	1 624

Damping Data
Series A: Fully Flexible Array

EXP.	Trial No.	Gp (kg/m^{2}s)	RAD Void	Frequency (Hz)	Exponential Fitting Damping Ratio (%)	Half-Power Damping Ratio (%)
TP06	10	400	0.550	47.25	1.24	1.242
TP06	11	400	0.579	47.25	1.20	1.253
TP06	12	400	0.592	47.50	1.24	1.103
TP06	13	400	0.623	47.50	1 06	1 048
TP06	14	400	0 629	47 50	0 68	0 98
TP06	15	400	0.642	47.75	0 86	0 977
TP06	16	400	0.657	48.00	0.69	0.797
TP06	17	400	0.662	48.00	0.83	0.759
TP06	18	400	0.669	47.75	0.55	0.713
TP07	1	450	0 052	40.75	0 65	0.362
TP07	2	450	0 031	40.75	0.65	0 332
TP07	3	450	0.200	43.75	1.76	2.577
TP07	4	450	0.240	44.25	1.45	2.996
TP07	5	450	0 279	44 75	1.45	2 634
TP07	6	450	0 331	45.50	1.37	2 6
TP07	7	450	0 382	46.00	1 42	2 318
TP07	8	450	0 428	46.50	1 46	2 21
TP07	9	450	0.455	47.00	1 48	2 14
TP07	10	450	0 501	46.75	1.25	1.704
TP07	11	450	0.523	47.25	1.36	1.711
TP07	12	450	0.544	47.25	1.25	1.127
TP07	13	450	0.560	47.25	1.27	1 146
TP07	14	450	0.580	47.25	1 24	1 082
TP07	15	450	0 589	47.50	0.84	1.339
TP07	16	450	0.603	47.50	0.81	1 16
TP07	17	450	0 611	47.75	0.64	0.952
TP07	18	450	0 622	47.75	0.66	0.951
TP07	19	450	0.638	47.75	0 68	0.766
TP07	20	450	0 638	47.75	0 47	0.816
TP11	1	498	0.235	44.00	1.69	2.698
TP11	2	498	0.294	45 00	1.79	2.737
TP11	3	498	0.345	45.50	1.91	2.692
TP11	4	498	0 395	46 50	2.03	2.403
TP11	5	498	0 438	46 50	1 96	1.974
TP11	6	498	0.476	46 75	1 36	1.585
TP11	7	498	0.514	46 75	1.17	1.683
TP11	8	498	0.539	47.25	1.18	1.377
TP11	9	498	0.560	47.50	1.24	1.349
TP11	10	498	0.577	47 50	0.86	1 376
TP11	11	498	0.593	47 50	0 89	1 094
TP11	12	498	0 613	47.50	0.72	0 901
TP11	13	498	0 625	47.75	0.67	0 869
TP11	14	498	0.641	47.75	0.77	0.717
TP11	15	498	0.652	48 00	0.37	0.587
TP11	16	498	0 661	48 00	0 49	0.626
TP11	17	498	0 672	48 00	0.12	0 493

Fluidelastic Data
Series B: Fully Flexible Array

EXP.	Trial No.	Gp (kg/m^{2}s)	RAD Void	HEM Pitch Velocity (m/s)	Interfacial Velocity (m/s)	Frequency (Hz)	Two-Phase ρ (kg/m^3)	RMS Trans. Amplitude (%D)
TP-23	1	77	0.506	0.979	1 055	47.25	707.82	0.34%
TP-23	2	77	0.617	1.602	1 535	47.75	549.43	0.35%
TP-23	3	77	0.711	2.328	2.094	47.75	418.31	0 36%
TP-23	4	77	0 753	2.888	2.525	48 00	358.63	0 40%
TP-23	5	77	0.785	3.373	2.898	48 00	314 09	0.45%
TP-23	6	77	0.820	3 807	3.233	48.00	264 83	0.52%
TP-23	7	77	0 834	3 999	3.380	47.75	244.95	0 77%
TP-23	8	77	0.865	4.385	3.678	47.75	201.52	1 55%
TP-23	9	77	0.900	4.793	3.992	48 25	152.98	3.94%
TP-14	1	105	0.502	0 936	1.022	46.75	718.10	0.39%
TP-14	2	105	0.621	1.487	1.447	47.50	548.61	0 37%
TP-14	3	105	0.635	1.809	1 694	47 50	528 38	0.40%
TP-14	4	105	0.656	2.061	1 889	47 75	499 85	0.40%
TP-14	5	105	0.709	2.317	2.085	47.75	424.01	0.40%
TP-14	6	105	0.723	2 715	2.392	47.75	403.50	0 43%
TP-14	7	105	0.735	2.979	2 595	47.75	386.84	0.46%
TP-14	8	105	0.759	3.186	2.754	47.75	352.74	0.48%
TP-14	9	105	0.769	3 403	2.921	48.00	338 48	0 48%
TP-14	10	105	0.782	3.665	3.123	48.00	320.24	0 53%
TP-14	11	105	0 788	3.827	3 248	48 00	311.90	0.54%
TP-14	12	105	0.797	4 078	3 442	48 00	298 14	0.55%
TP-14	13	105	0.806	4.332	3 637	48.00	285.25	0.64%
TP-14	14	105	0 815	4.442	3.721	47.75	272.56	0.71%
TP-14	15	105	0.824	4 642	3.875	47.75	260.32	0.97%
TP-14	16	105	0.837	4 889	4.066	47 75	241 72	2.31%
TP-17	1	155	0 324	0 582	0.750	45.25	970.76	0.41%
TP-17	2	155	0 496	1 109	1.156	46.75	727.14	0 40%
TP-17	3	155	0.570	1.506	1.461	47 25	620.86	0.41%
TP-17	4	155	0.617	1.912	1.774	47.50	554.68	0.43%
TP-17	5	155	0 659	2.280	2.057	47.50	494.41	0 42%
TP-17	6	155	0 695	2.617	2.317	47.75	443.36	0 45%
TP-17	7	155	0.701	2.914	2.545	47 75	434 11	0.46%
TP-17	8	155	0.718	3 267	2.817	47.75	410 20	0.49%
TP-17	9	155	0 726	3.416	2.932	47.75	399.28	0.53%
TP-17	10	155	0 736	3.535	3.023	47.75	384.64	0.54%
TP-17	11	155	0.746	3.779	3.211	47.75	371 35	0.59%
TP-17	12	155	0.758	4.094	3 454	47.75	352 89	0.61%
TP-17	13	155	0.780	4.418	3.703	47.75	322 30	0 72%
TP-17	14	155	0 794	4 782	3.984	47.75	303.32	1.57%
TP-17	15	155	0.800	5 020	4.167	47.75	294.00	7 49%
TP-18	1	203	0 373	0.759	0 886	46.75	904 74	0 44%
TP-18	2	203	0.468	1 138	1.178	46.75	767.58	0 44%
TP-18	3	203	0.539	1.479	1.440	47.25	667.52	0 43%
TP-18	4	203	0.572	1 780	1 672	47 25	620 20	0.46%
TP-18	5	203	0.626	2 307	2.078	47.75	543 21	0.49%
TP-18	6	203	0 660	2 931	2.559	47.75	493.84	0.56%
TP-18	7	203	0.699	3.396	2.916	48.00	438.22	0 64%
TP-18	8	203	0.710	3.769	3 203	47.75	423.38	0 80%
TP-18	9	203	0.722	4.077	3 441	47.75	406 19	1.29%
TP-18	10	203	0 747	4.570	3.820	47 75	369 50	6.97%
TP-15	1	255	0.423	1.016	1 084	48.00	830 90	0 46%
TP-15	2	255	0.487	1 411	1.388	47.50	740 36	0.47%

Fluidelastic Data
Series B: Fully Flexible Array

EXP.	Trial No.	Gp (kg/m^{2}s)	RAD Void	HEM Pitch Velocity (m/s)	Interfacial Velocity (m/s)	Frequency (Hz)	Two-Phase ρ (kg/m^3)	RMS Trans. Amplitude (%D)
TP-15	3	255	0.543	1.805	1.692	47.75	659 71	0.50%
TP-15	4	255	0.589	2.272	2.051	47.50	594 05	0.52%
TP-15	5	255	0.613	2.574	2.284	47.75	560.55	0 62%
TP-15	6	255	0.631	2 871	2 512	48.00	534.65	0.75%
TP-15	7	255	0.640	3.035	2.639	47.75	521 54	1.07%
TP-15	8	255	0 657	3 364	2.892	47.75	497 61	1.66%
TP-15	9	255	0 670	3.661	3.120	47.75	478 65	2.26%
TP-15	10	255	0.687	3 996	3.378	47.75	455.43	3.63%
TP-19	1	298	0 273	0 672	0.819	44.00	1047.97	0.47%
TP-19	2	298	0.456	1.316	1.315	46.75	784.25	0.49%
TP-19	3	298	0.525	1.694	1.606	47.25	685.05	0.51%
TP-19	4	298	0.581	2.270	2 049	47.50	606.40	0.61%
TP-19	5	298	0.608	2 634	2 330	48.00	567.61	0 89%
TP-19	6	298	0.618	2.835	2.485	48.00	553.12	1.35%
TP-19	7	298	0 633	3 132	2.713	47.50	531 55	1.79%
TP-19	8	298	0.650	3.428	2.941	48.00	507.84	2.19%
TP-19	9	298	0.673	3 947	3.340	48.25	474.59	5.00%
TP-20	1	356	0.217	0 552	0.726	43 50	1124.45	0.46%
TP-20	2	356	0 377	1.075	1 129	46.25	896 29	0.53%
TP-20	3	356	0 457	1.445	1.414	46.75	783.42	0.55%
TP-20	4	356	0.505	1.781	1.673	47.75	713.98	0.60%
TP-20	5	356	0.530	1 922	1.781	47.75	678.49	0 61%
TP-20	6	356	0 552	2.269	2.048	47.75	647.79	0.71%
TP-20	7	356	0 586	2.672	2.359	48.25	598.32	0.97%
TP-20	8	356	0.618	3.243	2 799	47.75	552.40	1.67%
TP-20	9	356	0.641	3 604	3.077	47.75	519.83	2 45%
TP-20	10	356	0.655	3.906	3.309	48.50	500.71	7 02%
TP-21	1	400	0 294	0.826	0 938	44.25	1018 57	0.52%
TP-21	2	400	0.405	1.297	1 300	46.50	859.10	0.57%
TP-21	3	400	0.453	1.598	1.532	46 50	790.36	0 60%
TP-21	4	400	0 504	1 964	1.814	47.00	717.21	0 66%
TP-21	5	400	0 534	2 286	2.061	47.50	674.44	0.77%
TP-21	6	400	0 563	2.682	2 366	47.50	632.96	1.02%
TP-21	7	400	0.594	3.094	2.684	48.25	588.36	1.30%
TP-21	8	400	0.615	3.526	3.017	48 00	558.46	1.98%
TP-21	9	400	0.630	3 782	3.213	48 00	536 42	4.75%
TP-21	10	400	0 653	4.058	3.426	48 25	503 23	8.00%
TP-22	1	455	0.252	0.783	0 904	44.50	1073.17	0.57%
TP-22	2	455	0.363	1 343	1.336	45 25	915.11	0.59%
TP-22	3	455	0.439	1.694	1.606	47 00	805 99	0.65%
TP-22	4	455	0 487	2.031	1 865	47.75	738.35	0.70%
TP-22	5	455	0 501	2.347	2 108	48.00	719.11	0.79%
TP-22	6	455	0.526	2.701	2 381	48.00	682.31	0.95%
TP-22	7	455	0.555	3 112	2 698	47.50	640.74	1 15%
TP-22	8	455	0 575	3.365	2.892	48.00	613 43	1.62%
TP-22	9	455	0.591	3 694	3.146	48 25	589 96	4.18%
TP-22	10	455	0.615	4 100	3.458	48.50	555.81	9.32%
TP-16	1	500	0.212	0 504	0 689	45.50	1127.82	0 48%
TP-16	2	500	0 336	1.008	1.078	46 50	953.12	0.55%
TP-16	3	500	0 414	1 393	1 374	47.50	841.67	0.58%
TP-16	4	500	0 460	1.696	1 607	47.50	775 95	0.65%

Fluidelastic Data
Series B: Fully Flexible Array

EXP.	Trial No.	Gp (kg/m^{2}s)	RAD Void	HEM Pitch Velocity (m/s)	Interfacial Velocity (m/s)	Frequency (Hz)	Two-Phase ρ (kg/m^3)	RMS Trans. Amplitude (%D)
TP-16	5	500	0.514	2.119	1 933	48.00	700 19	0.77%
TP-16	6	500	0.543	2 284	2.060	47.50	657.17	0.82%
TP-16	7	500	0.563	2 656	2.346	47.75	629 95	0.91%
TP-16	8	500	0.579	2.850	2 496	48 00	605.52	0.97%
TP-16	9	500	0.596	3.142	2.721	48.00	582.43	1.28%
TP-16	10	500	0.609	3 339	2.872	48.50	563.70	1.75%
TP-16	11	500	0.622	3 560	3.043	48 50	545.60	5.59%

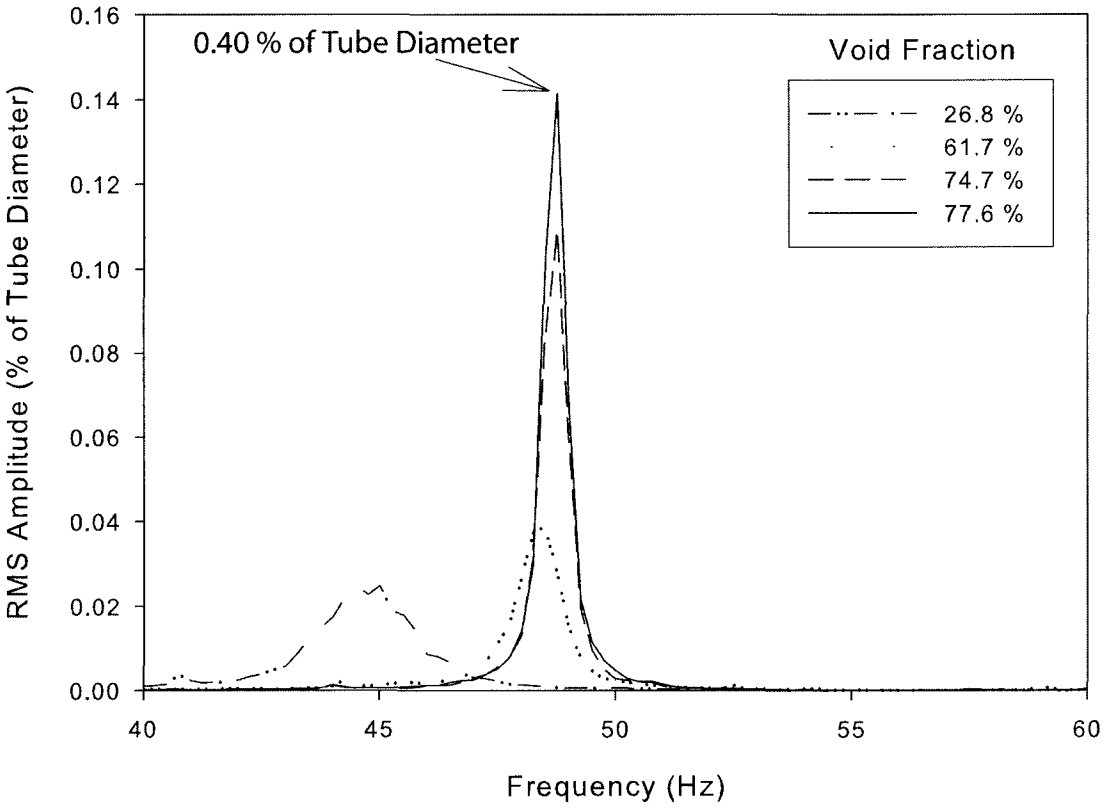

Figure E.1. Frequency spectra for various RAD void fractions at a mass flux of 100 kg/m^{2}s.

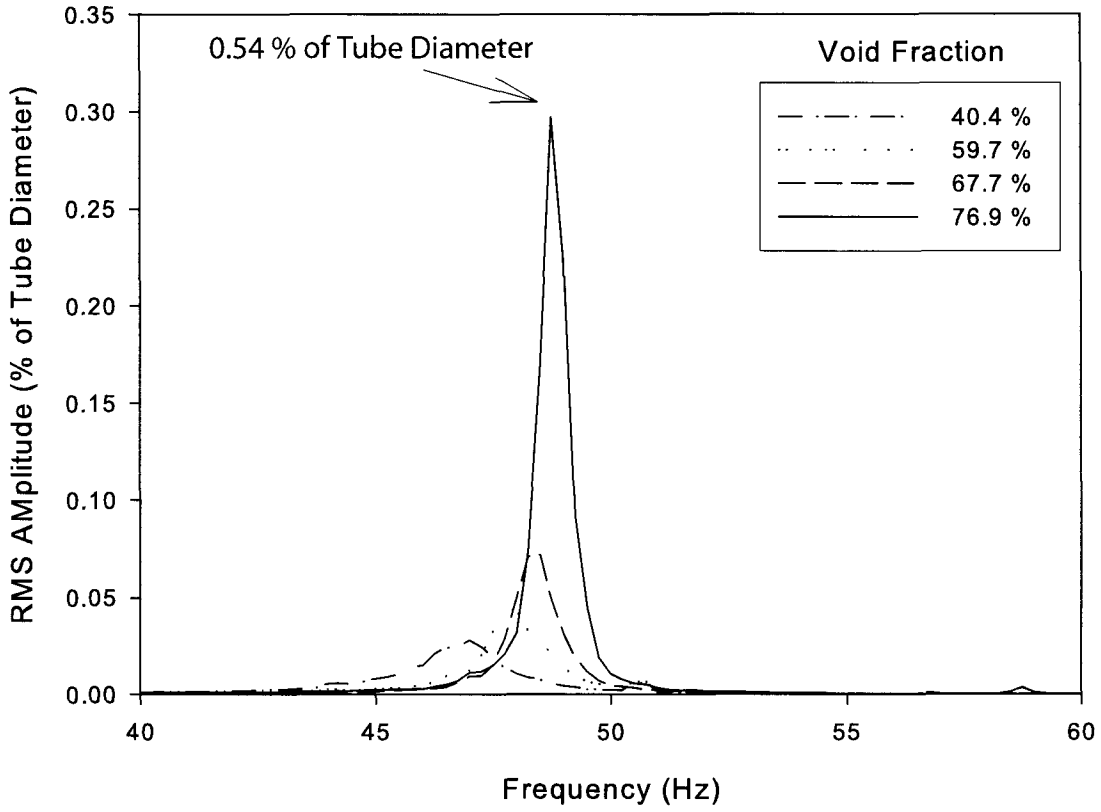

Figure E.2. Frequency spectra for various RAD void fractions at a mass flux of 250 kg/m^2s.

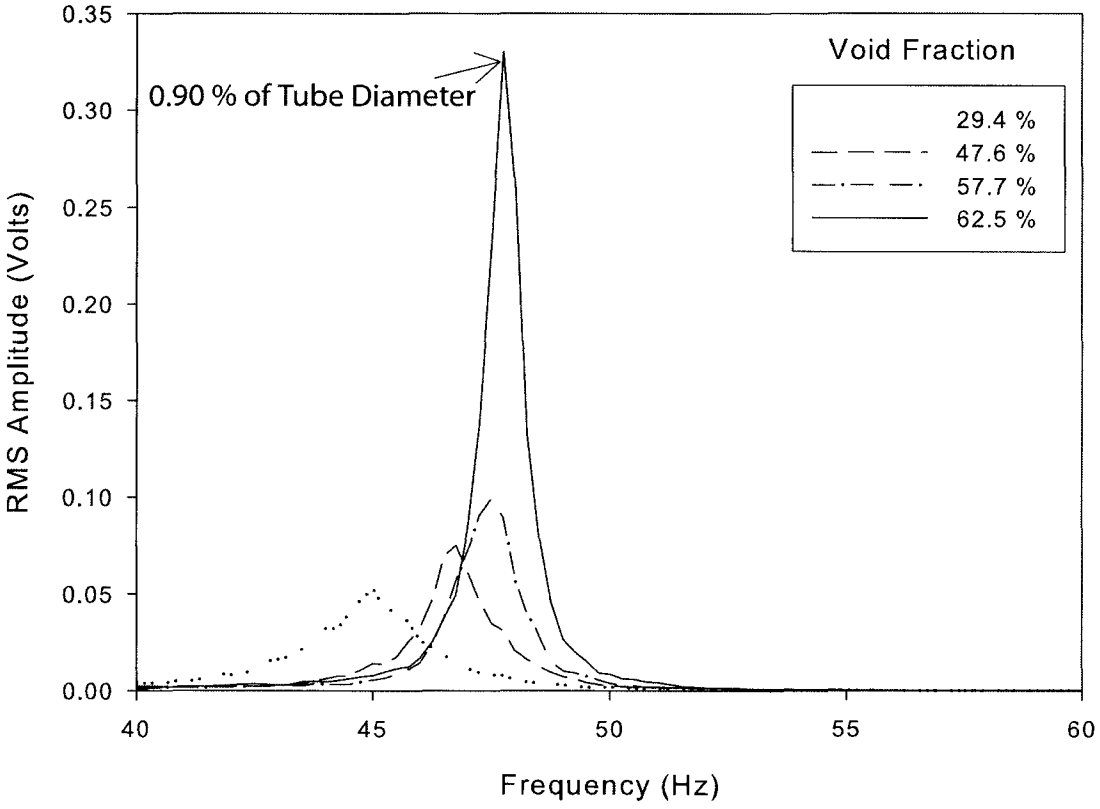

Figure E.3. Frequency spectra for various RAD void fractions at a mass flux of 500 kg/m^{2}s.

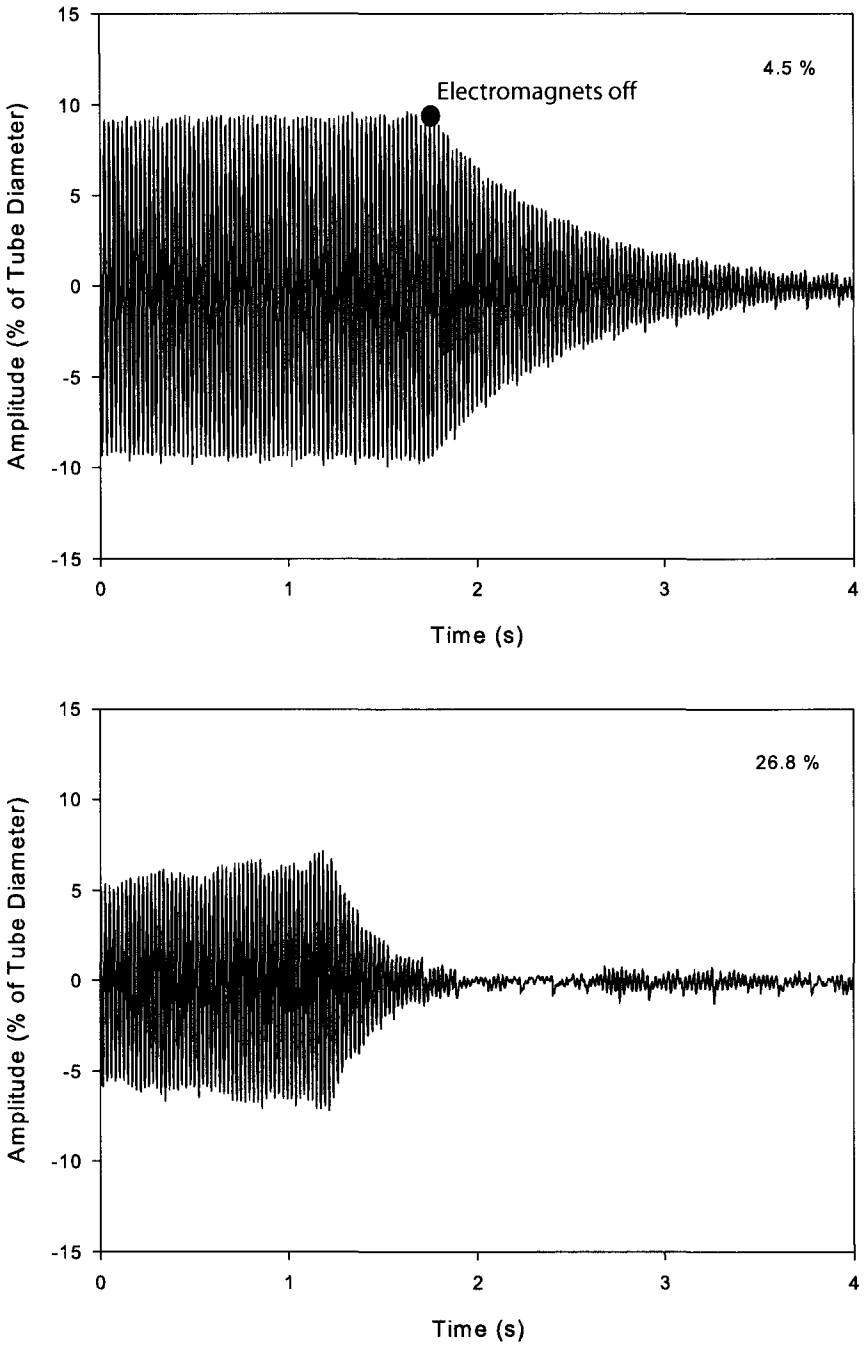

Figure E.4. Decay trace response of the monitored tube at 100 kg/m^{2}s for RAD void fractions of 4.5 and 26.8%

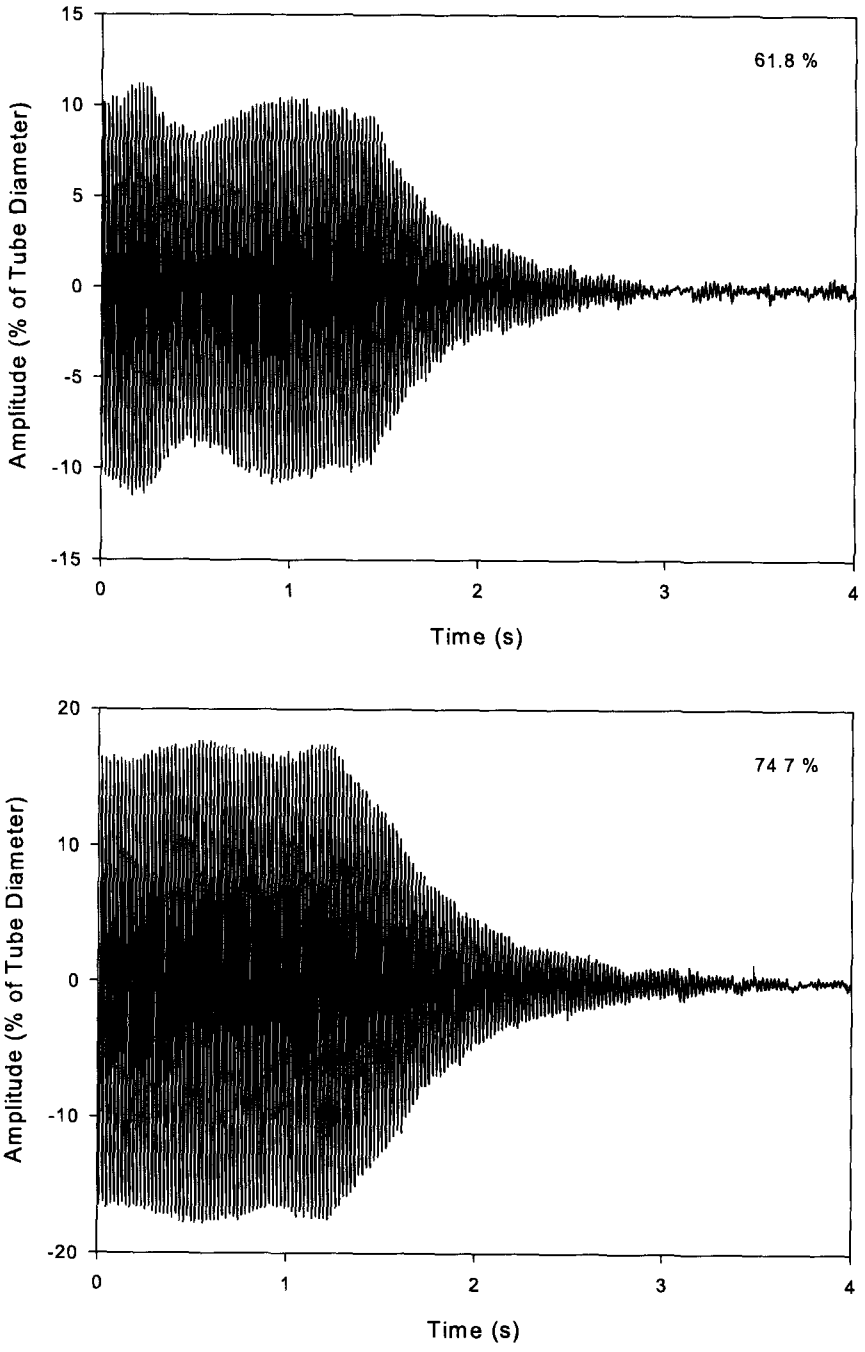

Figure E.5. Decay trace response of the monitored tube at 100 kg/m^{2}s for RAD void fractions of 61.8 and 74.7%

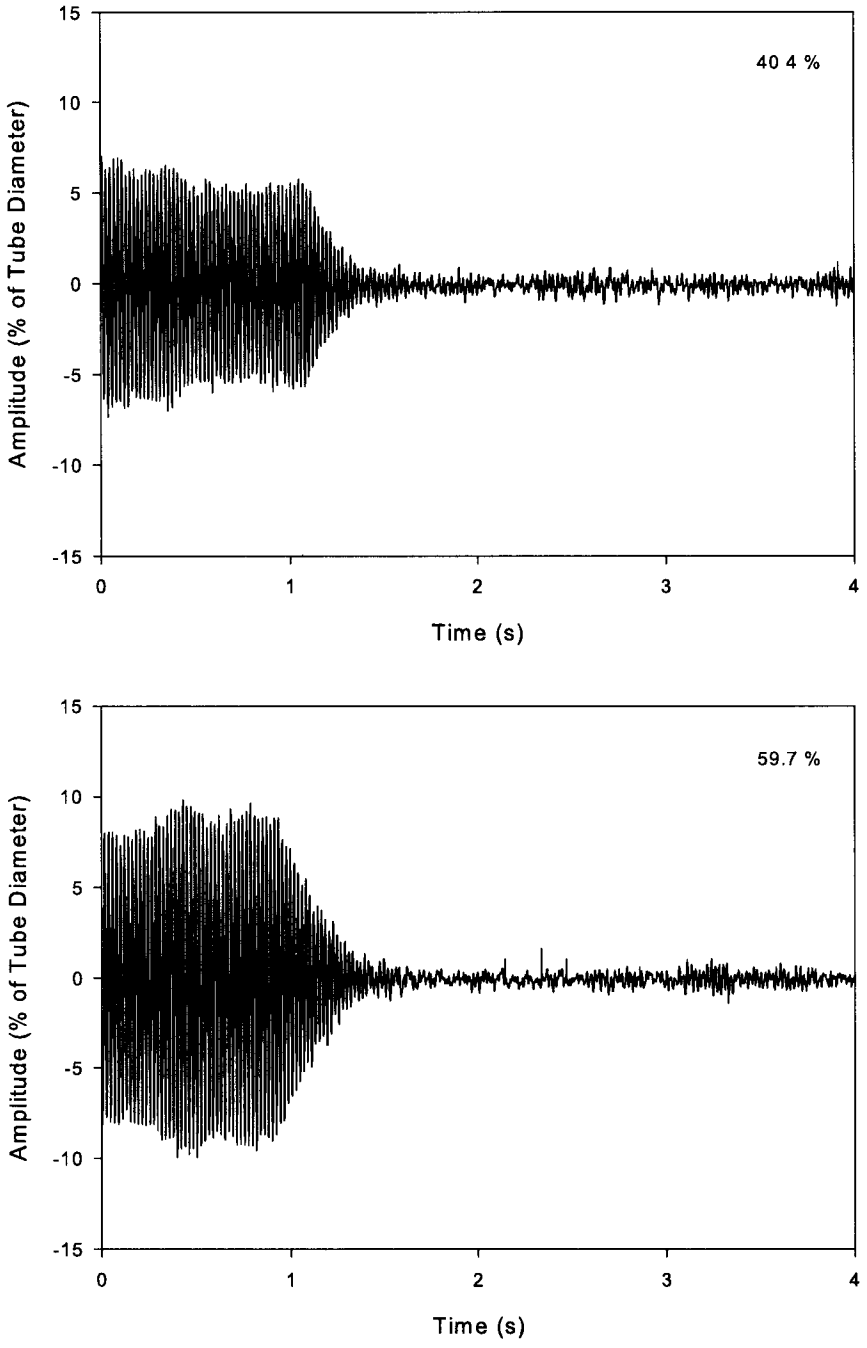

Figure E.6. Decay trace response of the monitored tube at 250 kg/m^{2}s for RAD void fractions of 40.4 and 59.7%

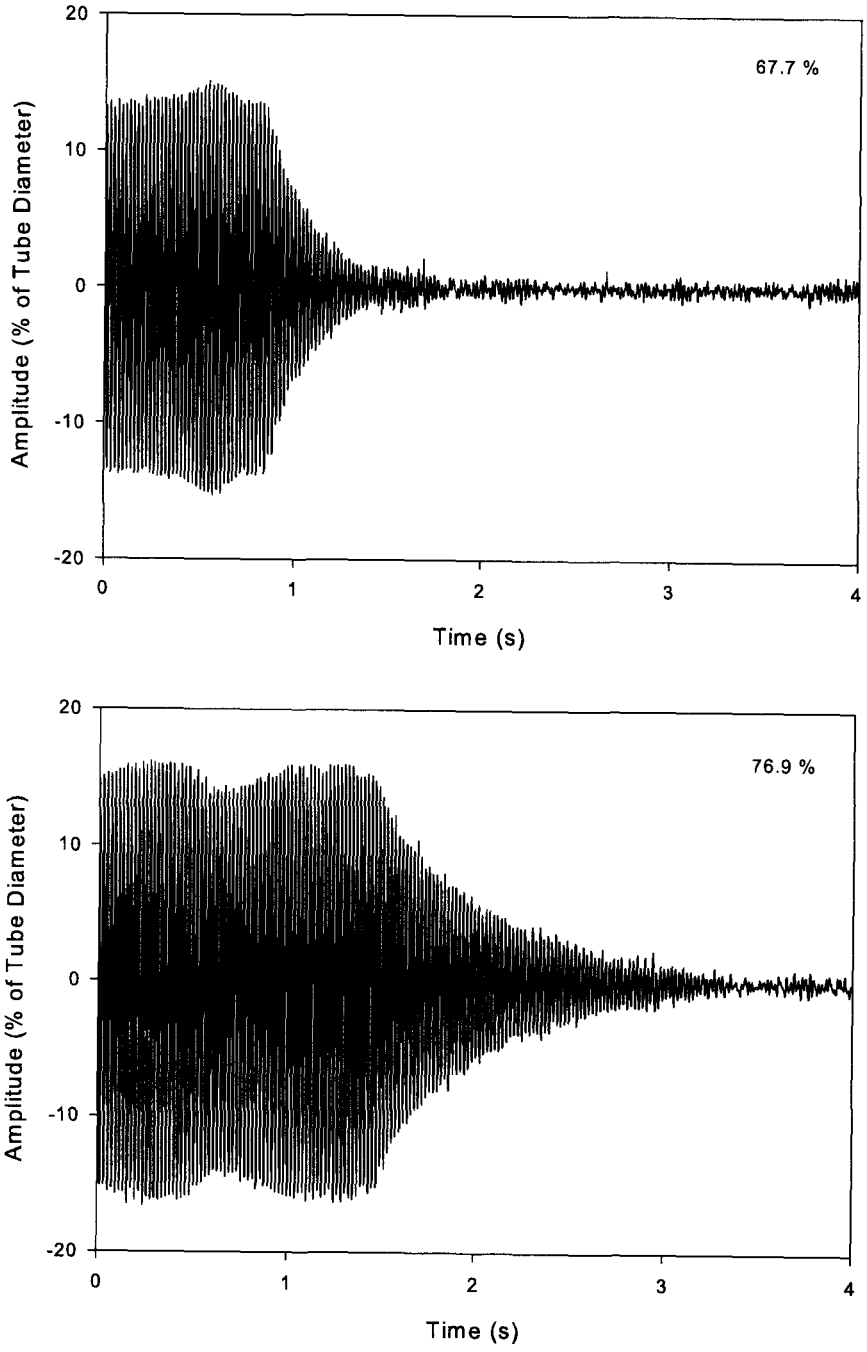

Figure E.7. Decay trace response of the monitored tube at 250 kg/m^{2}s for RAD void fractions of 67.7 and 76.9%

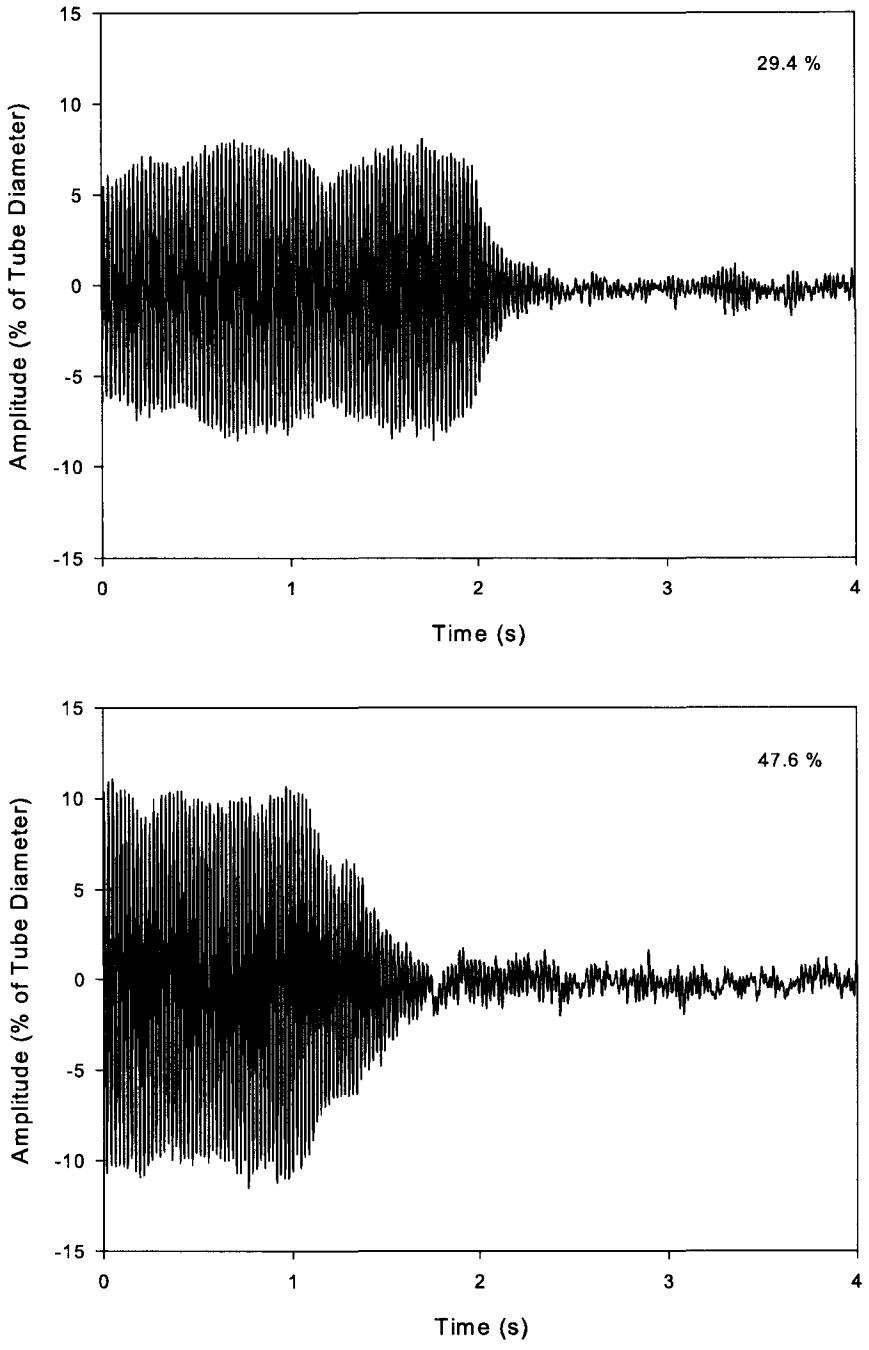

Figure E.8. Decay trace response of the monitored tube at 500 kg/m^{2}s for RAD void fractions of 29.4 and 47.6%

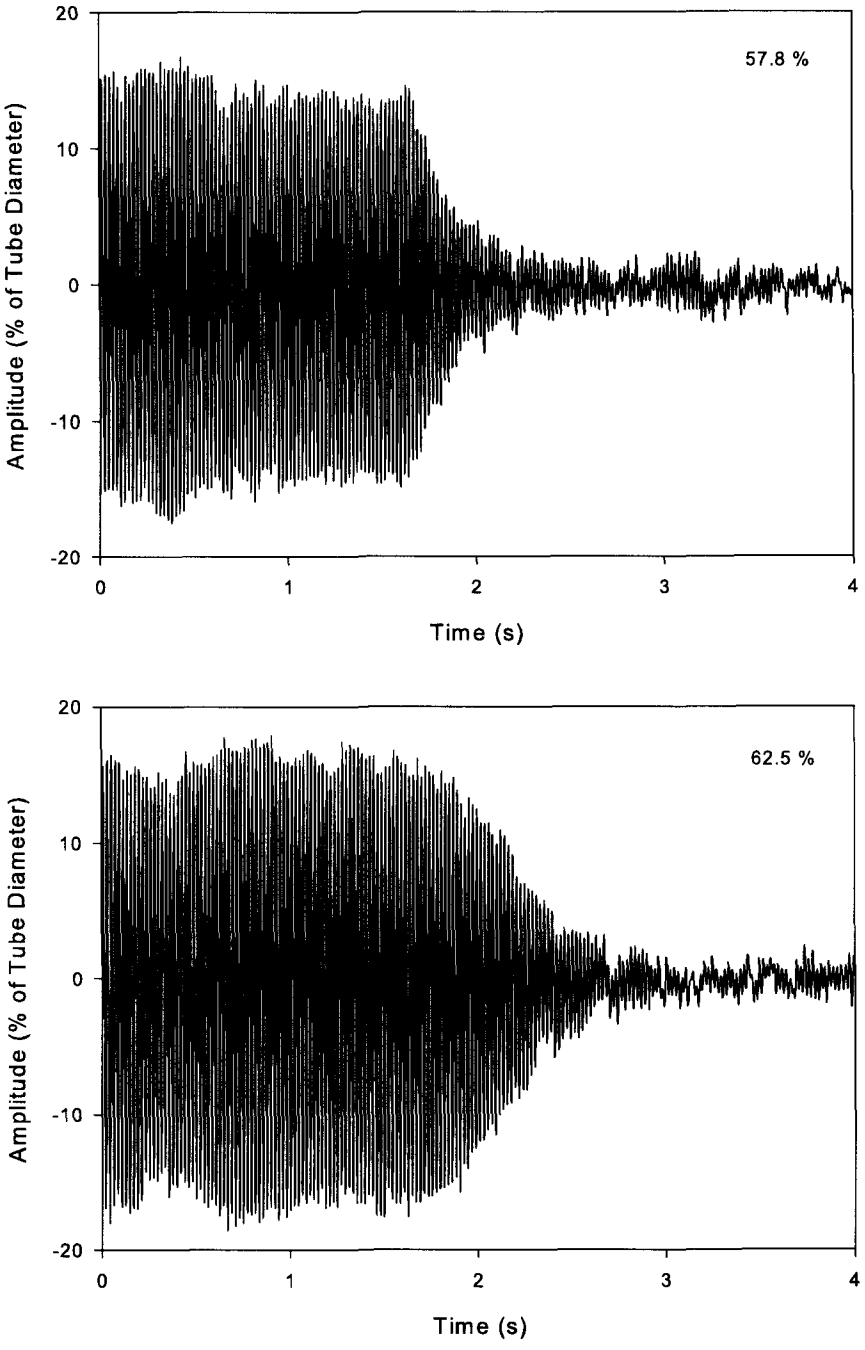

Figure E.9. Decay trace response of the monitored tube at 500 kg/m^{2}s for RAD void fractions of 57.8 and 62.5%